This item was submitted to Loughborough's Institutional Repository (https://dspace.lboro.ac.uk/) by the author and is made available under the following Creative Commons Licence conditions.

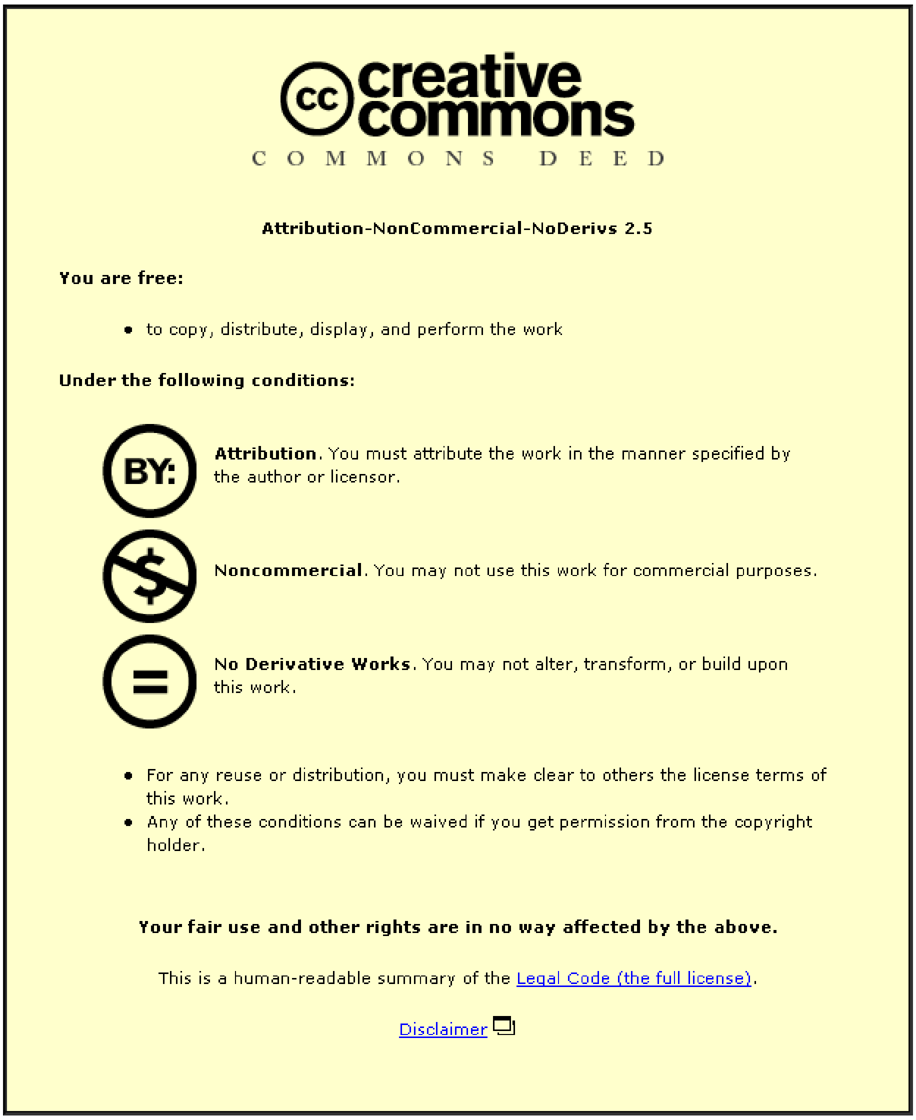

creative commons

COMMONS DEED

Attribution-NonCommercial-NoDerivs 2.5

You are free:

- to copy, distribute, display, and perform the work

Under the following conditions:

Attribution. You must attribute the work in the manner specified by the author or licensor.

Noncommercial. You may not use this work for commercial purposes.

No Derivative Works. You may not alter, transform, or build upon this work.

- For any reuse or distribution, you must make clear to others the license terms of this work.
- Any of these conditions can be waived if you get permission from the copyright holder.

Your fair use and other rights are in no way affected by the above.

This is a human-readable summary of the Legal Code (the full license).

Disclaimer

For the full text of this licence, please go to: http://creativecommons.org/licenses/by-nc-nd/2.5/

Oxidation of Austenitic and Duplex Stainless Steels during Primary Processing

by

Mark Alan Edward Jepson B.Eng (Hons)

Institute of Polymer Technology and Materials Engineering,

Loughborough University

Doctoral Thesis

Submitted in partial fulfilment of the requirements

for the award of Doctor of Philosophy of Loughborough University

February 2008

© Mark Alan Edward Jepson, 2008.

CERTIFICATE OF ORIGINALITY

This is to certify that I am responsible for the work submitted in this thesis, that the original work is my own except as specified in acknowledgements or footnotes, and that neither the thesis nor the original work contained herein has been submitted to this or any other institution for a higher degree.

……………………………………………… (Mark Alan Edward Jepson)

……………………………………………… (Date)

ACKNOWLEDGMENTS

I would like to take this opportunity to express my sincere gratitude to the following people without whom this work would not have been possible:-

Thanks must first be expressed to the Outokumpu Stainless UK Research Foundation and the Engineering and Physical Sciences Research Council for funding the project and the Institute of Polymer Technology and Materials Engineering and the Loughborough Materials Characterisation Centre for provision of research facilities.

I must also express my thanks to Dr Rebecca Higginson for her help, guidance and friendship throughout the project. She has given me many opportunities to present my work at various conferences and meetings, always had a kind word to say about my work and has always encouraged me to try to see the bigger picture.

Thanks must be given to David Dulieu and Staffan Hertzmann of Outokumpu Stainless for their valuable guidance and industrial viewpoint which enabled me to focus on particularly useful aspects without going off on a tangent. Members of the Avesta Research Centre must also be thanked for their friendly welcome during visits especially Cecilia Lille and Pasquelle Vangeli for their useful discussions.

All members of academic, research and technical staff of IPTME should also receive thanks for making the last few years as enjoyable as possible. Additional thanks must also be expressed to Geoff West for his guidance and assistance with focused ion beam and transmission electron microscopy techniques.

Finally I would also like to thank my family and my fiancée; Emma Spoor for their amazing support. It is also necessary to thank them for their subtle but still unrelenting nagging to finish my thesis. Although I may not have appreciated it at the time, it undoubtedly kept me on track and ensured that I finished in reasonable time.

ABSTRACT

During manufacturing, stainless steels will experience high temperatures at many steps: continuous casting, reheat, rolling and annealing. After continuous casting, it is usual for the as-cast metal to cool to ambient temperatures. In order to achieve successful hot forming, the metal must then be reheated to a suitable temperature. This process is called “reheat”, and commonly takes place in large, propane-fired walking beam furnaces at temperatures in excess of 1200°C for times of 2 or more hours. During reheat, a thick oxide scale will form which, if left in place during cold working, may cause damage to the surface of the final cold rolled product. As a result, manufacturers generally apply a mechanical descaling procedure immediately prior to rolling.

In order to study the effect of reheat conditions on the oxide scale formation, austenitic grades (Types 316L and 304) and duplex grades (Types S32101 and S32205) were oxidised. The temperatures used ranged from 700°C through to 1300°C for times up to, and including, 5 hours. The results of the heat treatments were investigated using a range of analytical techniques including: scanning electron microscopy (SEM), energy dispersive X-ray spectroscopy and site specific cross-section preparation using focused ion beam for both SEM investigation and transmission electron microscopy analysis. The use of these techniques has provided a thorough description of oxides that are expected to form at a variety of temperatures and conditions.

On austenitic grades a number of sub-surface oxide structures form, such as dendritic internal oxide particles and sub-surface oxide layering, which may pose great challenges to the mechanical descaling processes. External oxidation has not been neglected in this study and complex chemical and phase distributions within external oxide scales have been characterised. The presence of an as-cast oxide scale during reheat does not have a substantial effect on the reheat oxide formed, however, the as-cast microstructure may contribute to the formation of sub-surface oxide banding.

Duplex stainless steels produce oxides which are highly dependant on the phase distribution and surface finish of the substrate. Large scale oxide nodules have been found to form only on the austenite with an apparently protective thinner oxide present on the ferrite. The formation of these nodules has been studied from the initial stages of oxidation by the use of environmental SEM and site-specific preparation of important features to reveal that nodules form where the thin, protective chromium rich layer chemically fails during oxidation enabling local breakaway regions to form.

CONTENTS

1 INTRODUCTION

During production of stainless steel plate and sheet; slab, bloom, or billet is continuously cast, then cut to length and stacked to cool to ambient temperature. After stacking, the metal may, depending on final value, undergo a hot grinding operation or advance directly to the reheat furnace to be heated to an appropriate temperature for rolling operations. This so-called reheat operation usually takes place within walking beam furnaces heated to temperatures in excess of 1200°C by the combustion of propane in air. Reheat usually lasts for 2 - 3 hours, after which the metal is hydraulically or mechanically descaled before continuing to the hot rolling mill. It is crucial that the majority of the oxide scale (including internal and external oxides) is removed prior to the hot rolling operation since during this process any remaining oxide can cause surface defects on the final cold rolled products. As one of stainless steel's most desirable properties is its lustre, any imperfections on the surface are unacceptable to both the manufacturer and the consumer. These imperfections could lead to increased returns which necessitate melting and recasting that will inevitably lead to increased costs.

In terms of descaling, the ideal structure of an oxide scale is one which is thin and easy to remove. This not only ensures that the oxide scale is easily removed before any subsequent processing operations, but also that very little useful metal is lost during descaling. In reality, however, this is rarely the case, as less adherent oxides tend to be thick and thin oxides tend to be more adherent [Mougin, Dupeux, Antoni and Galerie (2003), Bamba, Wouters, Galerie, Charlot and Dellali (2006)]. On the other hand, if an oxide scale is grown during the service life of a component, then an ideal oxide would be one which is thin and adherent.

The aim of this project is to increase the understanding of the oxidation process which occurs during the industrial reheat procedure. Understanding how the oxide scale grows both during the initial stages and a full reheat procedure will lead to a greater appreciation of the mechanical properties of the oxide scale which will aid in the design of improved descaling operations.

Two families of stainless steels were chosen for this study: austenitic and duplex stainless steels. Austenitic stainless steels are the most widely used of all stainless steels [Lula (1986)]; 304 is regularly used for applications where thin gauges are required such as work bench top coverings, food preparation surfaces and medical surfaces. These applications require the steel to be flat rolled. It is therefore important to know how the material will oxidise prior to and during the rolling process. Type 316L finds uses in very similar applications but is also the main stainless steel used in marine environment due to its high corrosion resistance. 316L is also used in situations where high temperatures may be experienced such as heat exchangers in various applications. If the material is used at high temperature then it is important to know how it will oxidise in-service.

Duplex stainless steels are a family of stainless steels defined as a mixture of austenitic and ferritic structures, usually ~50:50 austenite : ferrite ratio. They were first discovered in the early 20th century with the first academic reference to duplex stainless steels published in 1927 [Bain and Griffiths (1927)]. After an extensive, ~50 year development programme they became common engineering materials in the early 1980s [Gunn (1997)]. The uses of duplex stainless steels are varied and include applications in the chemical, oil and gas industries with recent developments for use in construction where their properties are proving exploitable for structures such as foot and road bridges in a number of major world cities [Gedge (2006), Outokumpu (2006) $_1$] and in pressure vessels for the paper pulping industry [Outokumpu (2006) $_2$]. They are commonly used for their high strength, good corrosion resistance and high toughness. Due to the dual phase microstructure, duplex stainless steels have lower additions of nickel and molybdenum, allowing their purchase cost to be much less reliant on the price of these elements. LDX2101®, Outokumpu's low nickel duplex grade, inspired by traditionally high nickel prices, has recently found uses in the construction industry. The Siena footbridge in the city of Siena, Italy and the hydrogen peroxide reactor at Smurfit Kappa Kraftliner Piteå in Sweden are examples of recent use of LDX2101® [Gedge (2006), Outokumpu (2006) $_2$].

This thesis is divided into the following sections:- Chapter 2 is a review of the current literature, from continuous casting of steel through to the more specific topic of the oxidation of duplex stainless steels. In Chapter 3 the experimental procedures used to obtain the results presented are described including surface preparation techniques (both before and after oxidation), furnaces for production of oxides and the techniques to examine them. The results of preliminary studies on the oxide formation of austenitic grades in ambient air is given in Chapter 4, followed by Chapter 5, in which results of the oxidation of austenitic grades in simulated propane combustion products are presented. Chapter 6 is a discussion of the results obtained from the austenitic grade experiments. Chapters 7 – 10 are the results from oxidation experiments conducted on duplex grades of stainless steel. These experiments include :- in-situ observation of the growth of oxide scales on S32101 (Chapter 7), oxidation in simulated combustion products of propane (Chapter 8), reheat of duplex grades in a small-scale propane fired reheat furnace (Chapter 9) and finally, the effect of oxidation of polished duplex stainless steel (Chapter 10). The results of these studies are discussed in Chapter 11 followed by the conclusions of this work which are presented in Chapter 12 and suggestions for further work (Chapter 13).

2 LITERATURE REVIEW

2.1 Introduction

In this chapter the background literature to the project will be reviewed. This background will consider: processing of steel, principles of oxidation and a detailed review of the recent literature that is relevant to the specific study of oxidation of stainless steel. This review is divided into a number of sections including: processing of steel, mechanisms of oxidation, oxidation rates and section on the oxidation of specific steels. The oxidation of duplex grades and the effect of the addition of specific alloying elements is also discussed.

2.2 Processing of Steel

2.2.1 Continuous Casting of Steel

Before the development of continuous casting, ingots of steel were produced in a batch process where the metal was melted and then poured into moulds to cool. The ingots produced were then processed further to produce beams or slabs. This process, however, was expensive due to high operating costs. Continuous casting essentially allows this process to be automated and, as the beams, blooms or billets are produced directly from molten metal, the processing and handling costs associated with the much larger and heavier ingots are eliminated. Continuous casting also allows shapes that are much nearer to their final shape than ingot casting which further reduces the processing costs. Although continuous casting equipment may be in excess of 30 metres high, another advantage of their use is the reduction in size of equipment needed in comparison to ingot casting.

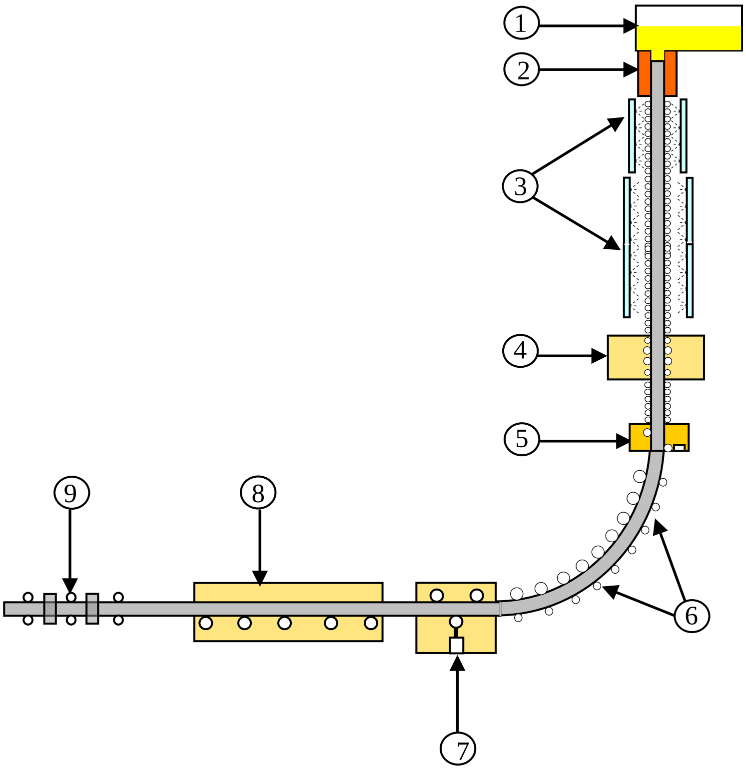

1	Tundish
2	Water cooled mould
3	Cooling water spray
4	Pinch rolls
5	Bending rolls
6	Curved guide rack
7	Slab straightening rolls
8	Reheat furnace
9	Sizing rolls

Figure 2.1:- Schematic of a cross-section of a continuous caster (following Beddoes and Bibby (1999))

Figure 2.1 shows a schematic representation of a continuous caster. Liquid metal which has been previously melted, in an electric arc furnace for example, is poured into the tundish where it may be left for up to ten minutes to allow any impurities present within the steel to float to the top and be collected as slag. The liquid metal from the tundish is allowed to flow into the water-cooled copper mould at a controlled rate and the depleted molten metal in the tundish can be replaced. This allows the process to be continuous. Once in the mould the outer “skin” of the metal will begin to cool and solidify. This can sometimes cause the metal to stick to the mould. So to avoid this, the mould is vibrated, which can cause marks on the outside of the cast metal called “reciprocation marks” (Figure 2.2). A number of factors including lubrication, temperature and the type of reciprocation system used, affect the appearance of reciprocation marks [Newton (1967)].

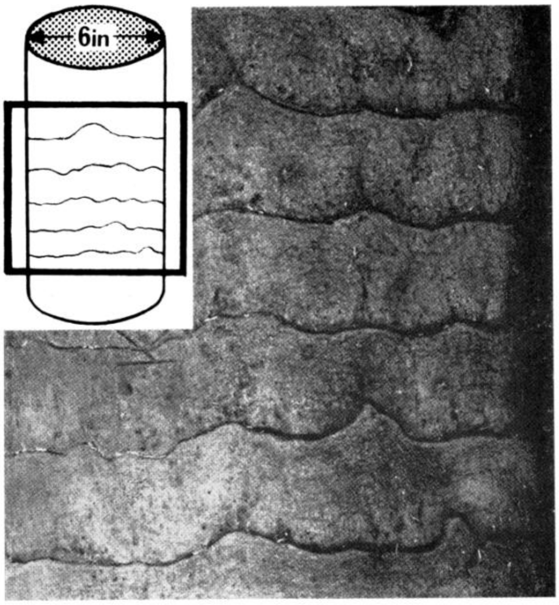

Figure 2.2: Reciprocation marks on steel after continuous casting (reproduced from Newton (1967))

Another method that can be used together with the reciprocation is a glass-based lubricant. Oil based lubricants have also been tried [Boichenko (1961)]. Once the metal has left the mould, water sprays are applied to remove further heat and to cool and solidify its core (Figure 2.3(a)). After the cooling process, the slab is then put through various rolls before being turned from a vertical to a horizontal position. This is intended to save space within the manufacturing plant i.e. the plant is built higher rather than longer.

The process of continuous casting has to be carefully monitored and controlled. If the molten metal was to be fed into the mould too quickly then the metal would not have enough time to form a thick enough “skin” to contain the molten core. This could cause the core to “break out” and cause significant and expensive damage to the surrounding equipment (Figure 2.3(b)). This situation can also occur when trying to continuously cast alloys which have a very long solidification period where solid and liquid phases exist simultaneously.

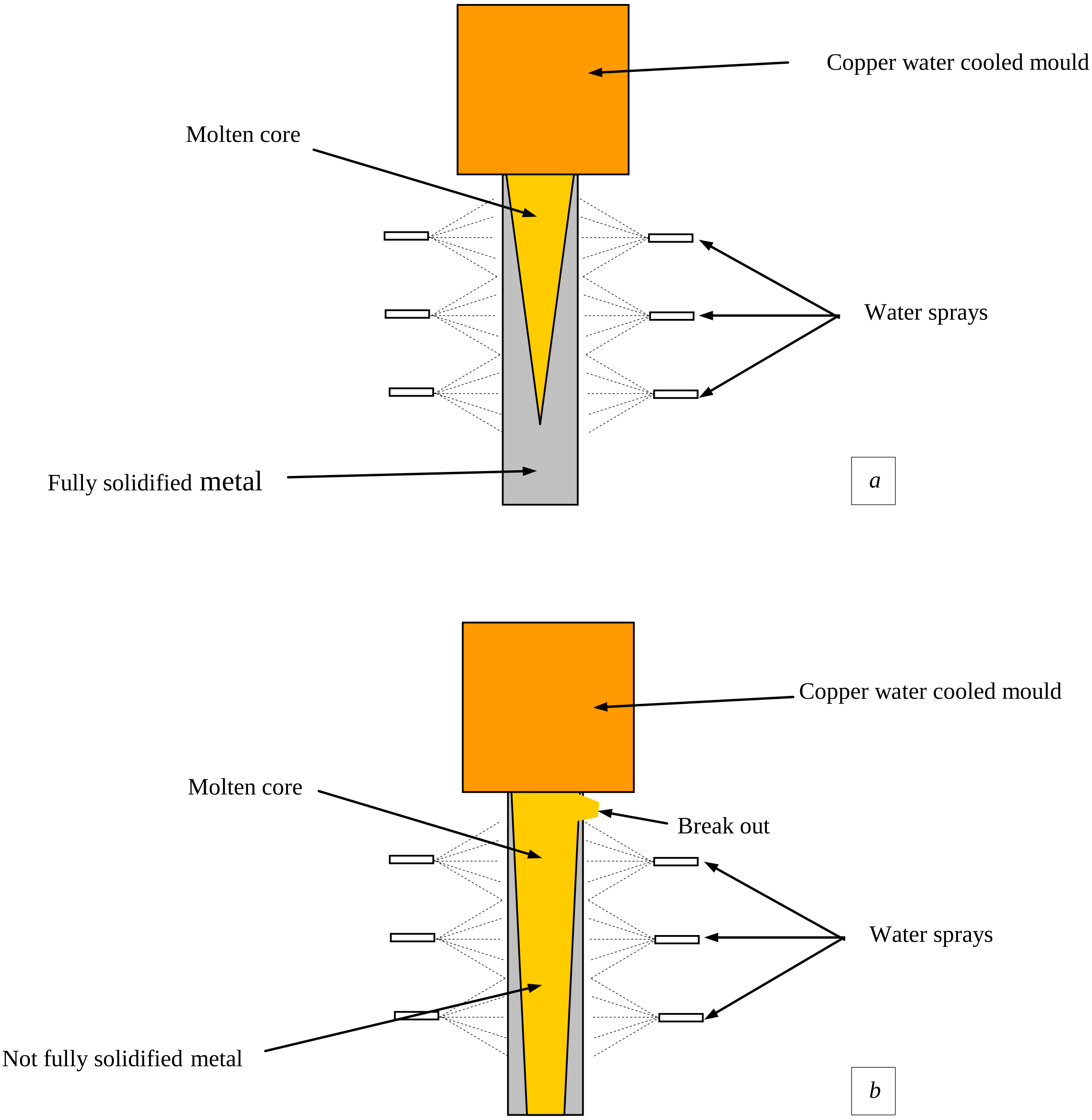

Figure 2.3: Schematic representation of a cross section of the cooling stage of continuous casting showing a) a successful cast and b) a break out

Another problem associated with these alloys is that the skin formed immediately after contacting the surface of the mould contracts, which separates the metal and the mould. This reduces the heat transfer rate that is occurring and so can cause metallurgical and process control problems [Beddoes and Bibby (1999)]. Doyle (1945) suggested that the basic stages of continuous casting are: pouring the liquid metal into a mould, cooling the surface of the metal and to complete metal freezing by cooling rapidly. A simple model of the heat exchange in continuous casting has also been presented by Boichenko (1961) and is shown in Figure 2.4.

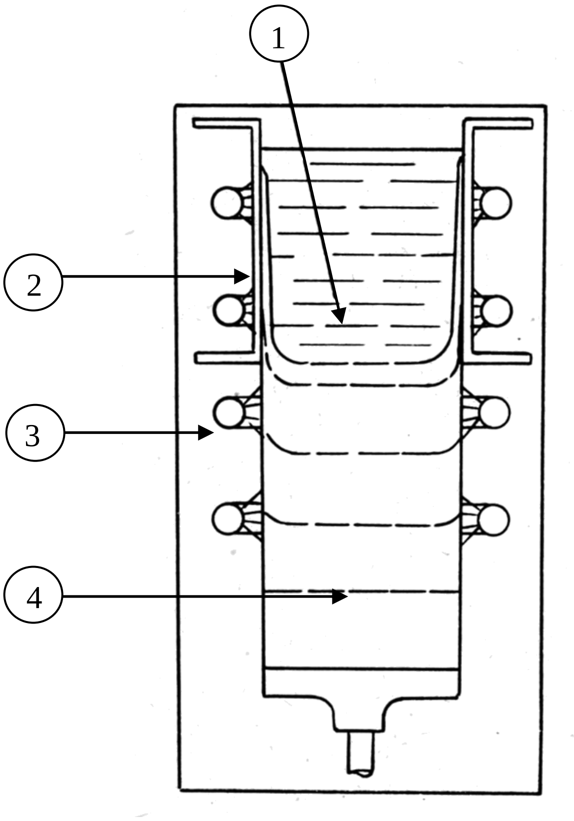

1	Liquid metal
2	Mould wall
3	Water sprays
4	Solid metal

Figure 2.4: Schematic representation of a cross section of the continuous casting optimum heat exchange (reproduced from Boichenko (1961))

2.2.2 Reheat

The area of interest for this report is the stage of processing before the rolling process, the reheat furnace. In this step the as-cast slabs, blooms or billets are placed into a furnace at a specific temperature for a set time. This is to homogenise the temperature of the metal before the rolling operations. An approximate heating profile is shown in Figure 2.5

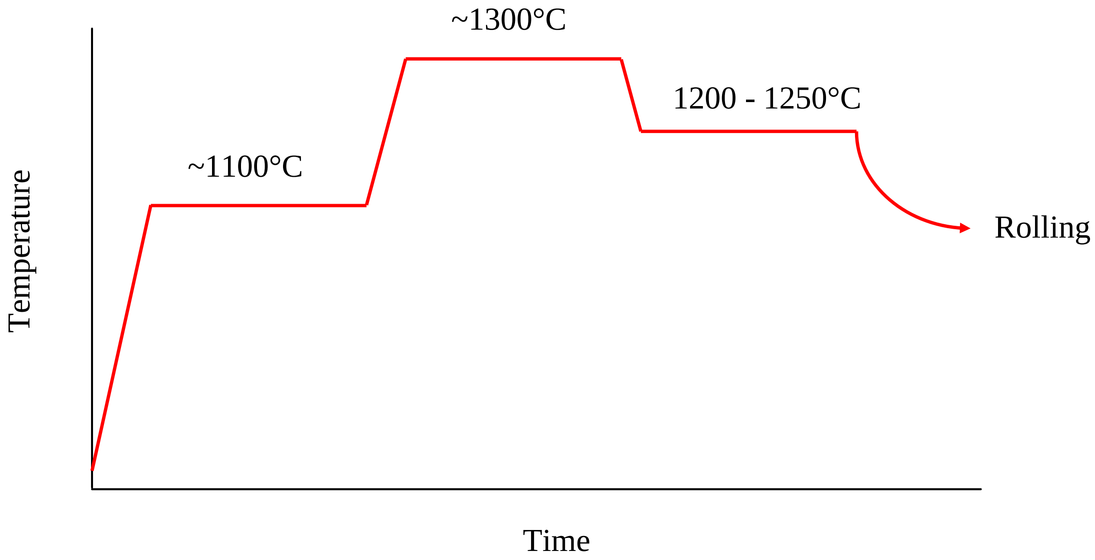

Figure 2.5:- Schematic showing the heating profile in a reheat furnace [McNee (2005)]

The purpose of the three-stage reheat is to ensure homogeneous heating of the slab. It is heated to below the final temperature before being heated higher than the target temperature, held there until it is homogeneously heated and allowed to cool to the final target temperature. For the stainless steels used for this project, a final reheat temperature of in excess of 1200°C is used. The furnaces used for the purpose of reheat in the stainless steel industry are usually fired by the combustion of propane gas in air. During the reheating procedure an oxide scale is formed which is called a “primary scale”.

2.2.3 Descaling

The oxide scale present after the reheat operation must be removed before any further processing can take place. During hot rolling, for example, oxide scale must be removed to ensure that the surface is clean. If oxide scale is still present then it can shorten tool life, cause irregular conditions and destroy the surface finish of the final product. Oxide removal is also necessary when the product is coated during future operations, as the surface must be clean to allow good adherence of the coating [Camp and Francis (1951)].

There are two types of descaling operations mechanical descaling and chemical descaling:

i) Mechanical descaling

The oxide scale is fractured from the surface by the introduction of an external stress. This stress can be produced in a number of ways which include: bending, shot blasting, high-pressure water jets and grinding. High-pressure water jets, for example, can be located after the two scale breakers and then after a number of roughing mills throughout the processing operation. Shot blasting is usually carried out on steel for zinc galvanising because it allows for better adherence between the zinc and the steel. As well as this, hydrogen embrittlement which is sometimes caused by chemical descaling, is avoided [Camp and Francis (1951)]. The use of mechanical descaling is affected by the adhesion of the oxide scale to the substrate. Mougin, Dupeux, Antoni and Galerie (2003) presented a method for determining the adhesion of oxide scales on ferritic stainless steel. They used a method called an inverted blister test (Figure 2.6). Distilled water was forced through the central hole until the foil specimen bulged and became detached from the oxide scale. It was found that as the thickness of the oxide increased, the adhesion energy and the spallation ratio decreased (Figure 2.7). It was also found that alloying additions of Ti increase the adhesion energy and that additions of niobium decreased it. So in production, it seems it is better for there to be a thick and therefore low adhesion energy scale before descaling, and in-service, a thin, protective, high adhesion energy scale should be present.

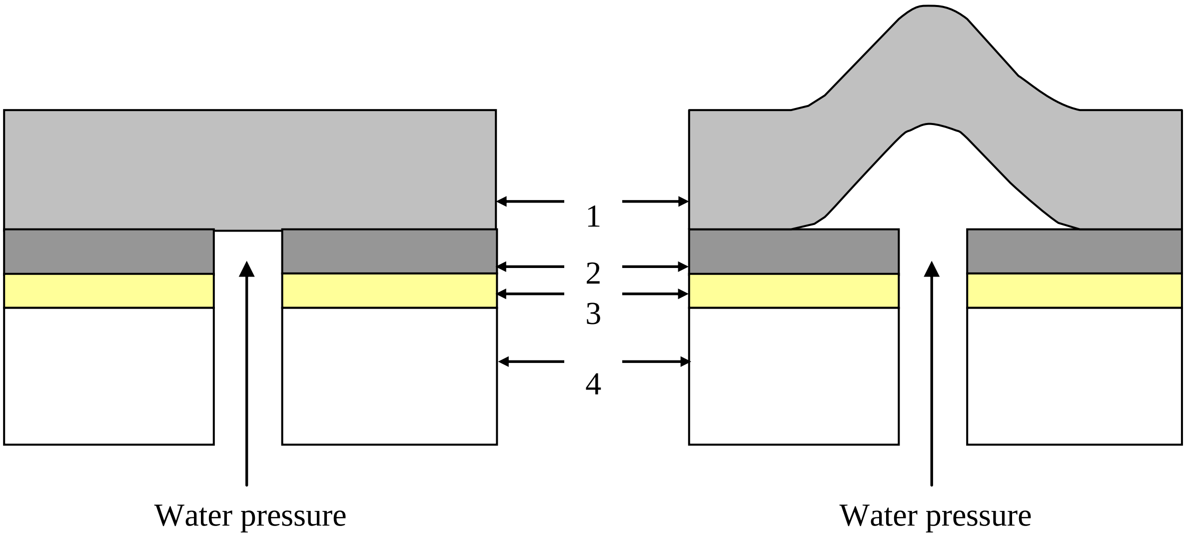

1 - Stainless steel foil, 2 - Oxide scale, 3 - Epoxy glue, 4 - Sample holder

Figure 2.6:- Schematic diagram of the inverted blister test (following Mougin et al. (2003))

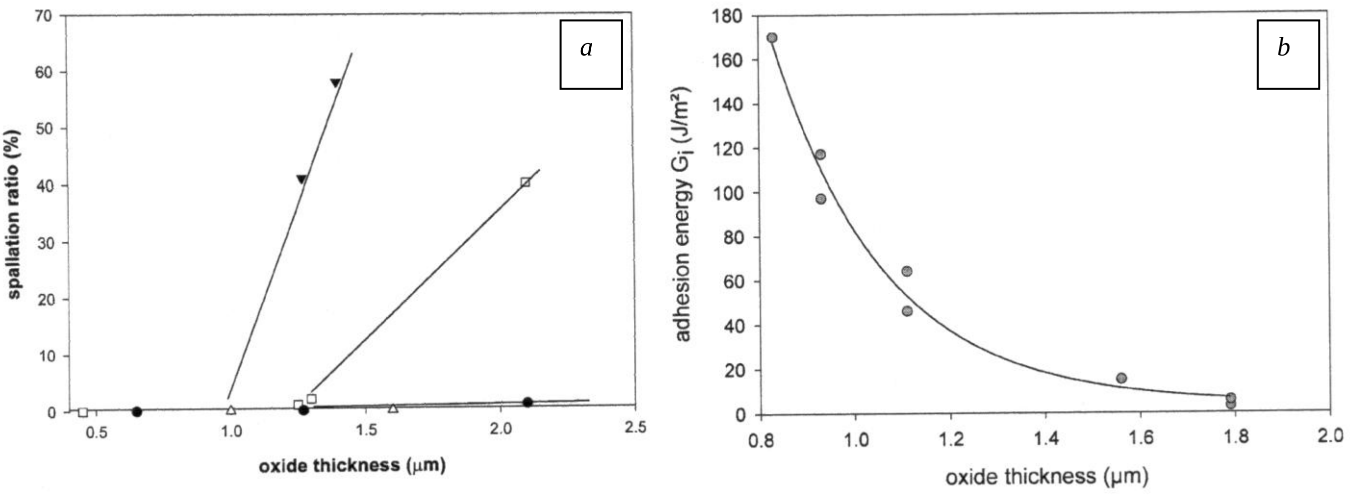

Figure 2.7:- Schematic graphs showing a) spallation ratio and b) adhesion energy (reproduced from Mougin et al. (2003))

Mechanical descaling has been studied by Krzyanowski, Yang, Sellars and Beynon (2003). They found that oxide scale spallation occurred by progressive cracking and then delamination along the metal scale interface. As the strain increased, the crack spacing decreased until a critical strain was achieved where spallation occurred. It was suggested that in order to improve descalability by mechanical means, the length of the oxide scale fragments must be reduced and the thickness of the fragments must be increased. Sherwood and Shatynski (1984) studied the effect of temperature on scale adhesion and it was found that the adherence of the scale depended on the oxidation time and temperature. Samples oxidised at 900°C and 1100°C showed poor adhesion and good descalability but samples oxidised at 1000°C were more adherent. The poor adherence of the scale formed at 900°C can be attributed to the relatively slow oxidation rate and the formation of a thin scale which is easily removed. At 1100°C the formation was much faster so the scale was thick and with many pores thus reducing adhesion. The scale formed at 1000°C was, however, well formed and showed some signs of plasticity. This study suggests that for mechanical descaling, oxidation conditions are very important with only 100°C making a significant difference to the adherence of the scale.

ii) Chemical descaling

Chemical descaling is a process consisting of moving the metal through an acid bath where the oxide scale is removed. It is often referred to as pickling. Pickling is defined as a process of chemically removing oxides from the surface of a metal by the action of solutions of inorganic acids. Steel is immersed in a tank containing approximately 3 – 8 % dilute sulphuric acid, hydrochloric acid or a mixture of both acids. An inhibitor is added which prevents the occurrence of pitting in the steel itself, thus economising on the amount of acid used and also protecting the steel from damage. For producing carbon steels, one of the main constituents of the scale is magnetite (Fe_3O_4) which is not easily dissolved in the acid. The acid will, however, act on the steel itself, producing a large amount of hydrogen which produces pressure and forces the oxide scale from the surface of the metal. The steel must be pickled under the right conditions and for the correct time; too long and the steel will end up pitted and damaged by the acid, too short and much of the scale will still remain attached to the surface of the steel. Another risk associated with pickling is hydrogen embrittlement. This is a process where the hydrogen gas becomes embedded in the grain boundaries of the substrate material which seriously weakens the structure and causes embrittlement. After the pickling process, the steel must be cleaned by water jets and immersed in a neutralising solution which in order to neutralise any remaining acid [Gregory and Simons (1964)].

In practice, both types of operation may be carried out in sequence with a mechanical descaling operation such as shot blasting being followed by pickling, for example. This ensures that the majority of the scale is removed before the next stage of production.

Outokumpu Stainless UK who have supported this work use three methods of descaling depending on what is being descaled;

Primary scale: Formed after the reheat operation is removed by the use of high-pressure water jets.

Secondary scale: Formed during the hot rolling procedure is removed by a combination of shot blasting and mixed acid pickling.

Final descaling: Carried out after the cold rolled product has been coiled and annealed and consists of an electrolytic nitric acid treatment followed by a mixed acid bath. [McNee (2005)]

2.3 Thermodynamics and Kinetics of Oxidation

2.3.1 Introduction

In oxidation studies it is important to understand what reactions are possible between gases and metals. Although oxidation is usually a simple reaction between a gas and a metal, things are often complicated by condensation or deposition of liquids and gases. So, although thermodynamics and kinetics are useful and powerful tools for determining the possible reactions and whether significant evaporation or condensation of certain species are possible, it is not always completely predictive.

In an oxidation reaction in its simplest form, oxygen is brought into contact with the metal and forms a metal oxide (Figure 2.8) It is clear to see from this case that once the oxide layer has initially formed, the metal must pass through the scale to the scale – gas interface and react there or the gas (oxygen) must pass through the scale to the metal – scale interface and react there [Birks and Meier, (1983)].

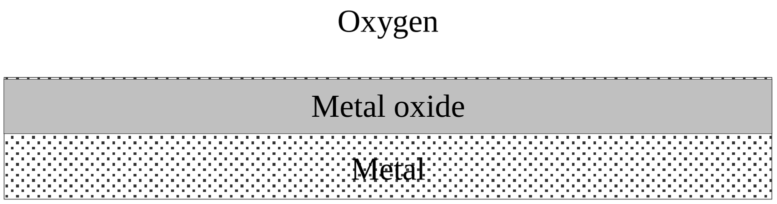

Figure 2.8:- Schematic diagram showing a cross section of a metal with an oxide scale

From this simple example the importance of the transport mechanisms of both oxygen and metal through the scale is emphasised, as without a transport mechanism present, an very thin scale would form causing little or no damage to the substrate which would also prevent further oxidation from occurring.

2.3.2 Initial oxidation

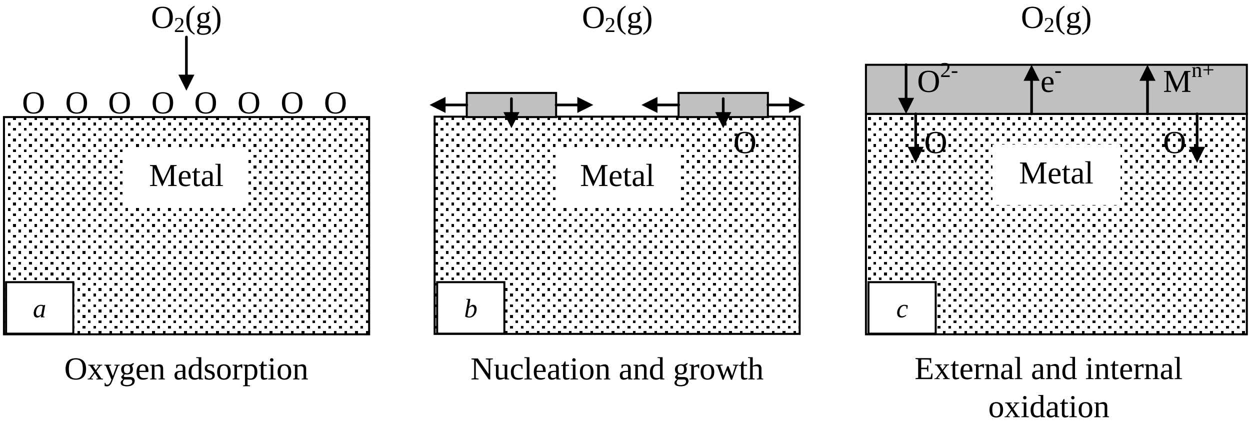

Figure 2.9:- Schematic diagram showing the stages of oxidation a) initial oxidation b) nucleation and c) scale growth (following Kofstad (1988))

The initial stage of oxidation is the adsorption of oxygen onto a clean metal surface (Figure 2.9 (a)). It can be estimated that if all the molecules impinging on a clean metal surface are adsorbed, then a single layer of adsorbed gas will form in approximately 1.5 seconds at 10^{-9} atmospheres at room temperature [Kofstad, (1988)]. There are two main types of adsorption: physisorption and chemisorption. In physisorption the molecules are bonded by weak van-der-Waals forces whereas during chemisorption, the molecules are bonded by a much stronger chemical bond. According to Stokkers, Van Silfhout, Bootsma, Fransen and Gellings (1983), chemisorption occurs on the chromium sites in stainless steel whereas the iron remains in the metallic state. As the reaction continues, the oxide forms by nucleation and growth (Figure 2.9 (b)). Nucleation and growth of oxides is suggested by Saeki, Konno and Furuichi (1996) to occur up to times of 120 s at temperatures of 1000°C on a ferritic stainless steel in an approximate reheat furnace atmosphere. Once a thin film on the surface of the substrate (Figure 2.9 (c)) has developed, it separates the metal from the atmosphere and the processes described in Section 2.3.3 commence.

Saeki *et al*. (1996), produced a model for initial oxidation similar to the one published by Kofstad (1988), however, the new model provided a time line and a more detailed explanation of initial oxidation on ferritic stainless steels (Figure 2.10).

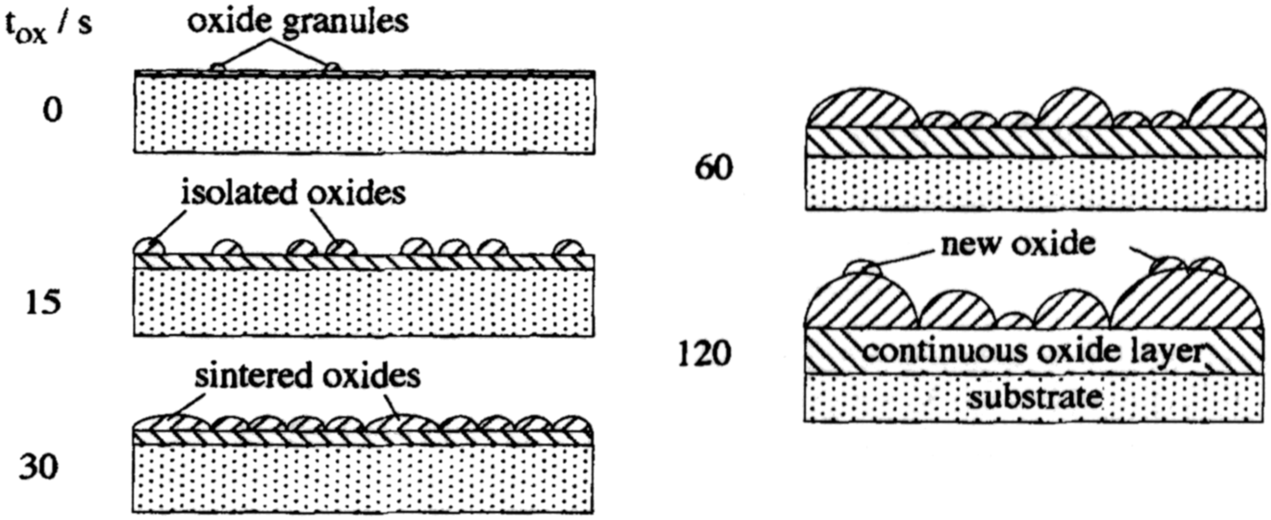

Figure 2.10:- Schematic diagram showing the stages of initial oxidation (reproduced from Saeki et al. (1996))

Before oxidation the surface is usually slightly oxidised due to exposure to the atmosphere and shows a thin oxide film. After 15 seconds the number of isolated oxide crystals increase but there is still some uncovered surface. After 30 seconds of oxidation the size and number of oxide grains has increased to the extent that they now start to merge together. After two minutes of oxidation the surface is fully covered in an oxide layer with large oxide crystals which have smaller new oxide grains on top.

2.3.3 Mechanisms of Transport

Metals are generally ionic in nature and so it is not appropriate to consider the transport of atoms of metal and oxygen but rather to consider the transport of metal and oxygen ions. The mechanisms of transport of metal and non-metal ions can be divided into two categories; mechanisms for stoichiometric compounds and mechanisms for non-stoichiometric compounds.

i) Stoichiometric Compounds

Shottky defects are one way by which ionic mobility in these types of materials is explained. The mobility of ions is made possible by the existence of ionic vacancies. It is assumed that electro-neutrality is maintained throughout so there must be an equal number of vacancies on both the anionic sub-lattice and the cationic sub-lattice. Since the vacancies are present on both the anionic and the cationic lattices both the anions and the cations will be mobile [Birks and Meier (1983)].

Frenkel defects are another possible explanation of ionic mobility. In this case, however, only the cation is mobile and the anionic sub-lattice remains perfect. In order to maintain the electro-neutrality of the crystal the cations form at interstitial sites leaving vacancies in the cationic sub-lattice [Birks and Meier (1983)].

These two types of defects provide mechanisms for the transport of ions through a material but do not provide a mechanism for electron transport which is required for the growth of an oxide (Figure 2.11).

There is one main difference between the two types of transport mechanisms; cation migration produces oxide growth at the oxide – gas interface whereas if the anion is the transport mechanism, the oxide forms at the metal – oxide interface.

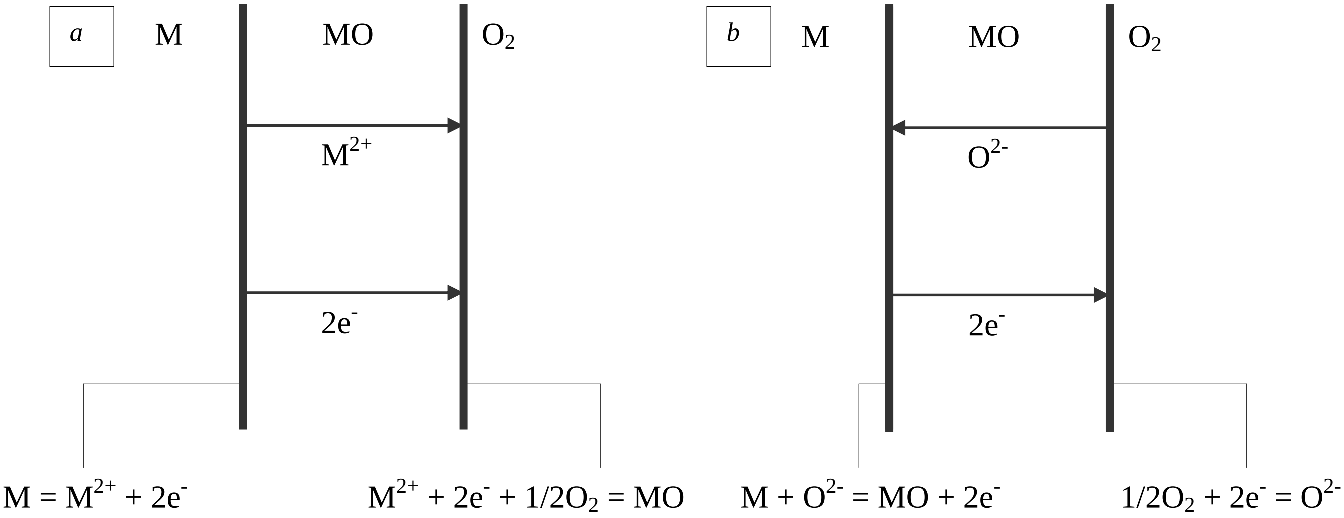

Figure 2.11:- Interfacial reactions and transport processes for high temperature oxidation mechanisms showing (a) cation mobile and (b) anion mobile (following Birks and Meier (1983))

ii) Non Stoichiometric Compounds

Non stoichiometric means that the compound does not contain the exact ratio of atoms shown by its chemical formula. These compounds are usually electrically neutral which can be explained by assuming that the cations or the anions have variable valency. It is much more likely that the cation (which is usually the metal) will show variable valency.

Electron transport has to occur in order for oxidation to proceed. Non-stoichiometric compounds are semiconductors, which means that electrons can be transported through them. Electrons can be carried either by negative carriers or by positive carriers. N (Negative) type semiconductors are non stoichiometric compounds which have either a metal excess or a non-metal deficit.

a) Metal excess;

The best-known example of an n-type semiconductor with metal excess is zinc oxide (ZnO) [Birks and Meier, (1983)]. In order for there to be an excess of metal in the structure, it is assumed that there are a number of cations at interstitial sites. In order to maintain an overall neutral charge there must also be an equivalent number of electrons in the conduction band.

b) Non – metal deficit;

If a compound is deficient in non metal then it can still be termed as an n-type semi-conductor. The way in which this is achieved is different to the metal excess case. The most simple way of explaining a non metal deficit is to visualise an oxygen ion being discharged from the compound and then evaporating. A vacancy is then left in the anion lattice and the electrons enter the conduction band [Birks and Meier (1983)].

Another way of explaining electron transport is to consider a positive carrier in the compound. Compounds which show this type of behaviour are called p-type semi conductors. Again there are two ways in which this can arise:

c) Metal deficit

In order for this type of deficit to occur, the metals must be able to exist on a number of valence states. Transition elements such as iron and nickel are able to exist on a number of valence states. The closer together the valence states are in terms of energy of ionisation, the easier a cation vacancy is formed.

A cation of a metal, M, can have a valence state of M^{2+} or M^{3+}. If an electron transfers from the M^{3+} to the M^{2+} ion then it reverses the valence state of the two cations and leaves an "electron hole" at the M^{3+} site. So if an MO is being formed then oxygen will chemisorb on the surface by attracting an electron the M^{2+} leaving an M^{3+}. Once the oxygen is fully ionised it leaves a hole in the cation lattice and forms a unit of MO on the surface of the oxide.

d) Non - metal excess

These are also termed as intrinsic semi conductors. There are very few metals which oxidise by this method. The concentration of electron defects greatly exceeds the ionic defects. In order to produce electro-neutrality electrons are excited into the conducting band and leave behind electron holes [Birks and Meier (1983)]

2.4 Crystal Structures of Oxides

Crystal structures of metals are usually found to be one of three structures; body centred cubic (BCC), face centred cubic close packed (FCC) or hexagonal close packed (HCP). Oxide ceramics, however, usually consist of a lattice of oxygen atoms arranged in either HCP or FCC structures with the metal ions occupying interstitial sites. There are two types of interstitial sites in a close packed crystal structure; tetrahedral sites, where the site is surrounded by four oxygen atoms, and octahedral sites, where the site is surrounded by six oxygen atoms.

2.4.1 Halite structure

The halite structure is the structure of FeO (Wüstite). It consists of an anion structure of FCC and the cations occupy the octahedral sites between the oxygen atoms. The structure is illustrated in Figure 2.12. A number of other oxides also have the halite structure: MgO, CaO, SrO, CdO, NiO, TiO, NbO and VO.

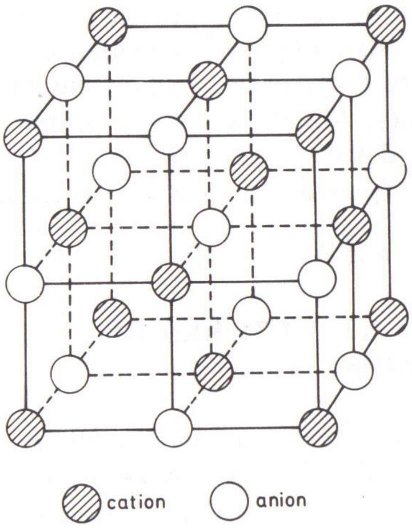

Figure 2.12:- The Halite structure (reproduced from Kofstad (1988))

2.4.2 Corundum structure

Haematite (Fe_2O_3) is made up of the corundum structure. It is a hexagonal close packing of oxygen ions with the metal ions occupying 2/3 of the octahedral sites. This means that the metal ions are surrounded by 6 oxygen atoms and the oxygen atoms are surrounded by 4 metal atoms. This is best described by considering Figure 2.13 which shows the location of the octahedral sites between two layers of oxygen ions (only one oxygen layer is drawn). The next cation layer has the same arrangement as this but is shifted by one atomic spacing by the vector marked 1. The third cation layer is shifted by the vector marked 2. A section of this crystal illustrated by the dashed line is shown in Figure 2.14. As well as haematite this structure is also possessed by: Cr_2O_3, Al_2O_3, Ti_2O_3, V_2O_3 and many other oxides with the formula M_2O_3. The corundum structure is so called as it is the crystal structure of the mineral corundum and is a member of the trigonal crystal system.

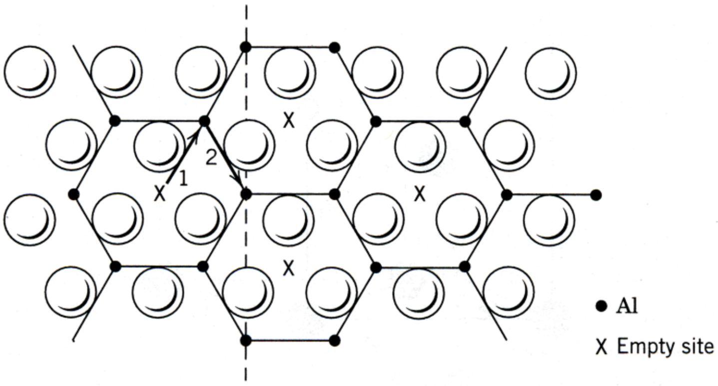

Figure 2.13:- The corundum structure (reproduced from Chiang, Bernie and Kingery (1997))

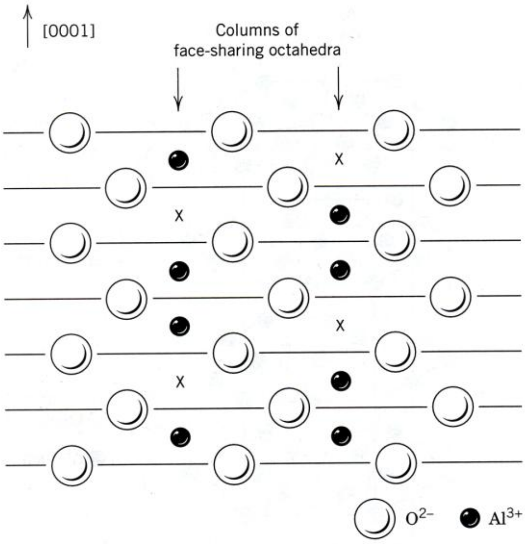

Figure 2.14:- The corundum structure (reproduced from Chiang, Bernie and Kingery (1997))

2.4.3 Spinel structure

The spinel structure is described as an oxygen lattice of an FCC type with the metal ions occupying both the tetrahedral and the octahedral sites. The unit cell of a spinel structure consists of 32 oxygen atoms with 32 octahedral sites and 64 tetrahedral sites. The divalent metal ions usually occupy only 1/8 of the tetrahedral sites with the octahedral sites being occupied by the trivalent metal ions. This is called a normal spinel. In the case of magnetite for example (Fe_3O_4), 1/8 of the tetravalent sites are occupied by the trivalent metal ions. This is therefore called an inverse spinel. Spinel structures can have many other arrangements of cation vacancies. Usually the formula is MN_2O_4 where M is divalent and N is trivalent, however, it is possible for any combination of valancies as long as the sum of cation vacancies is equal to 8. Spinel belongs to the cubic system of crystal structures.

2.5 Shape of oxide crystals

The shape of a growing oxide crystal can vary depending on the chemical composition of the individual crystal as well as the conditions of its growth. These may include pressure, temperature, any gradients of chemistry or temperature and the speed of growth both overall and in any particular direction. Differences in growth rate in a single direction can produce distortions of the ideal crystal shape [Bauer and Tvrz (1988)].

Figure 2.15 is a diagram detailing the expected crystal shapes for a particular crystal system. Of interest to the study of oxidation of stainless steels is the appearance of the corundum structure and those expected to form on the cubic system (e.g. magnetite). Figure 2.16 shows an example of crystal distortion of an ideal magnetite crystal. The magnetite shown here has grown preferentially in the direction of the arrow to produce an elongated crystal [Bauer and Tvrz (1988)]. This distortion is something which is very likely to be seen during the growth of oxides at high temperature due to local differences in supply of oxidising elements, temperature and oxygen partial pressure which will all produce gradients which the crystals will follow.

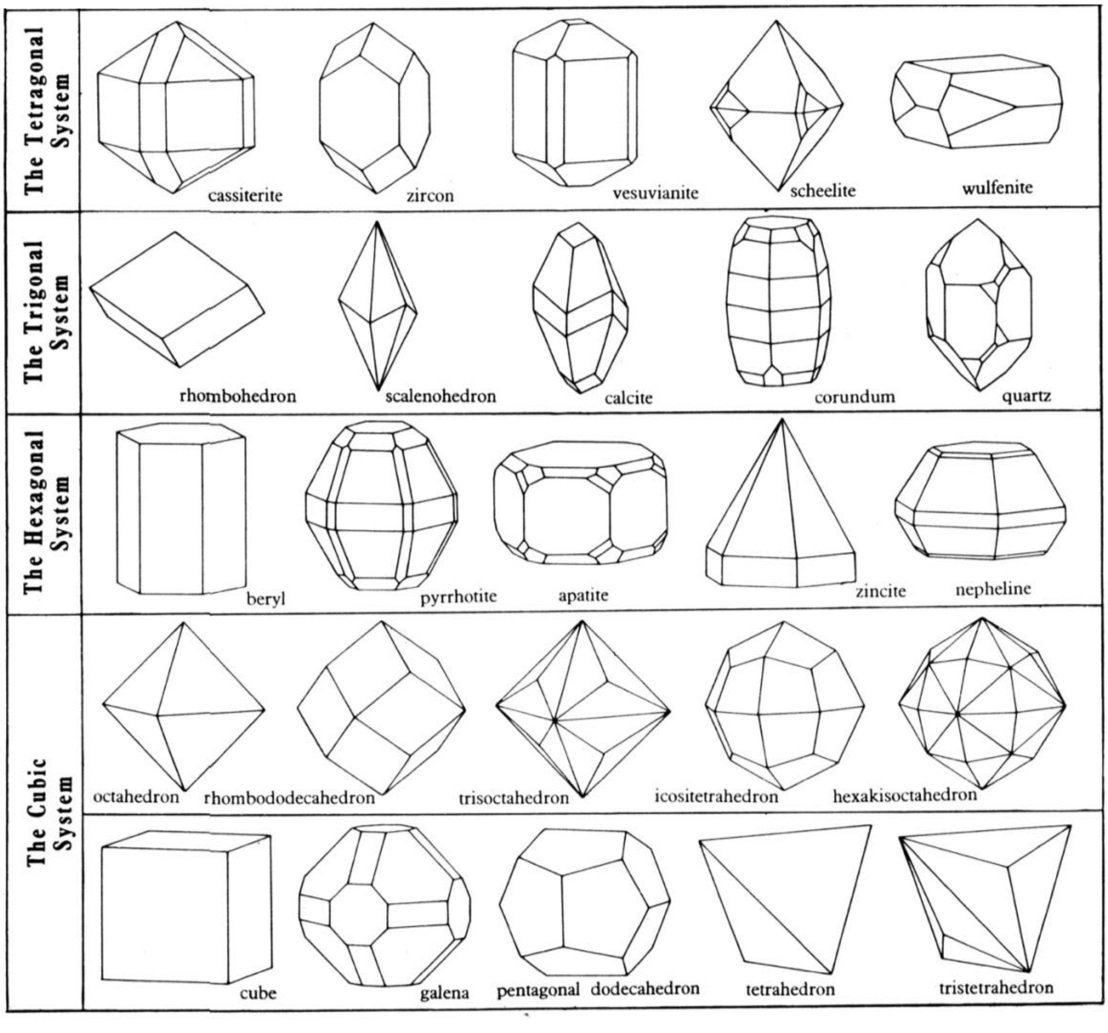

Figure 2.15:- Appearance of growing crystals of the crystal systems (reproduced from Bauer and Tvrz (1988))

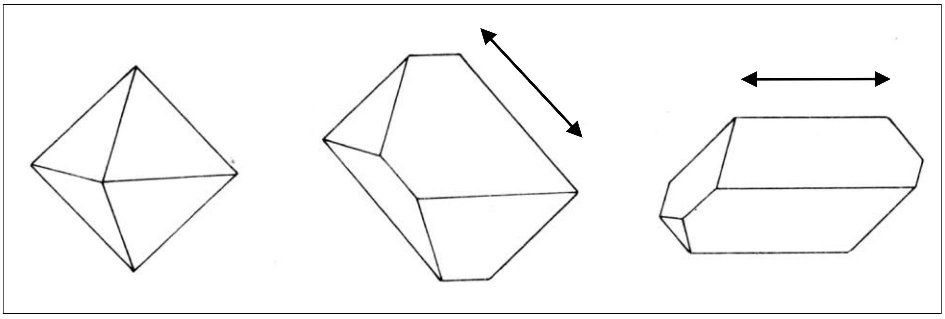

Figure 2.16:- Distortion of a magnetite crystal (reproduced from Bauer and Tvrz (1987))

2.6 Oxidation Rate

2.6.1 Linear Rate law

If the oxidation of a metal proceeds at a constant rate it is said to obey a linear oxidation rate law that is it obeys the equation:

$x = k_1 t$--[2.1]

where, x, k_1 and t represent the scale thickness, linear rate constant and the time respectively. If the scale is measured in scale thickness then the units for the linear rate constant becomes cm s^{-1}, if the mass gain of the sample is measured then the units for the linear rate constant become g cm^{-2} s^{-1}.

2.6.2 Logarithmic Law

When metals are oxidised below temperatures of approximately 400°C, they can show very fast initial oxidation followed by a slow oxidation rate (Figure 2.17). This behaviour has been found to conform to logarithmic rate laws:

$x = k_{log} \log (t + t_0) + A$ (direct log law)---[2.2]

$1/x = B - k_{il} \log t$ (inverse log law)---[2.3] where A and B are constants.

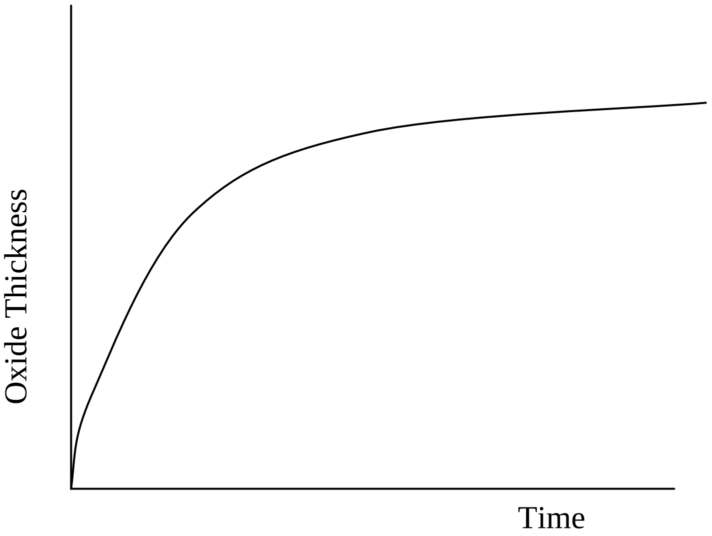

Figure 2.17: Schematic representation of the direct logarithmic law

2.6.3 Parabolic Rate Law

A scale growth that follows the parabolic rate law will grow with a decreasing oxidation rate with time. That is the rate at which oxidation occurs will be inversely proportional to the oxide thickness (Figure 2.18). This oxidation rate follows the equation:

$x^2 = 2k_pt + C$---[2.4]

Where, k_p is the parabolic rate constant, C is and x and t represents oxide thickness and time respectively. A parabolic growth rate is limited by the diffusion rate of ions or electrons through the oxide scale formed and was first derived by Wagner (1933).

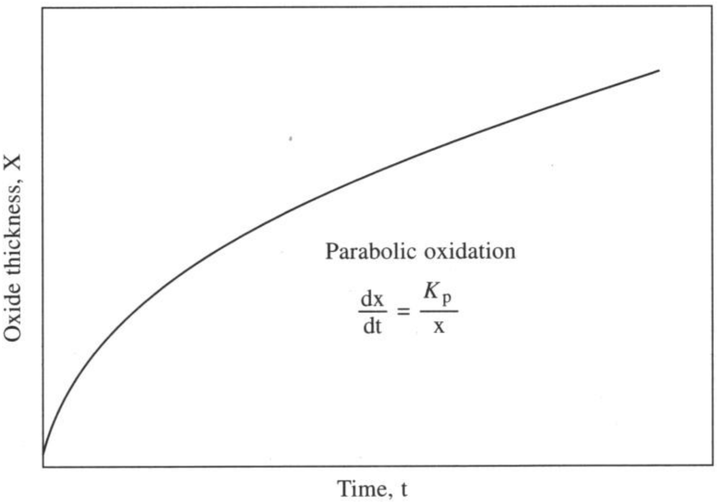

Figure 2.18: Schematic showing the Parabolic rate law of oxidation (reproduced from Khanna (2004))

2.6.4 Breakaway Oxidation

Many alloys, including stainless steel, rely on the formation of a protective layer of oxide to increase their oxidation resistance. In a breakaway oxidation situation, this protective scale layer may grow to a critical thickness where cracking and rupturing occurs. This cracking and rupturing effectively reduces the thickness of the protective scale and so growth continues. The scale then continues to grow at a near linear rate (Figure 2.19). This type of oxidation can be termed as breakaway oxidation or breakthrough oxidation. Breakaway oxidation is discussed in more detail in Section 2.8.7.

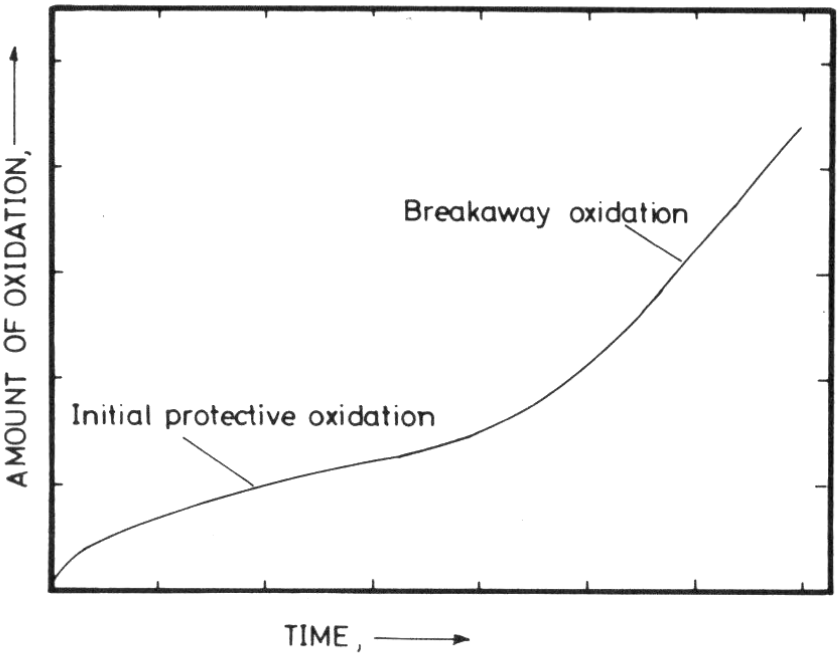

Figure 2.19:- Schematic diagram of the occurrence of breakaway oxidation (reproduced from Sedriks, (1979))

2.7 Oxidation of Iron and Mild Steel

2.7.1 Introduction

Iron is rarely used in high temperature applications because of its very poor oxidation resistance, even at room temperature. Mild steel, which is an alloy of iron and carbon, is occasionally used at elevated temperatures and steels with high chromium or aluminium contents are often used in high temperature applications such as heat exchangers in the power generation industry and are now being applied to fuel cell applications.

2.7.2 Formation of Oxide Scale

Iron is a perfect example of a metal which produces multi-layered oxide scales. It forms three layers: wüstite (FeO), magnetite (Fe_3O_4) and haematite (Fe_2O_3). The order of these scales is wüstite next to the metal with magnetite and haematite following towards the atmosphere.

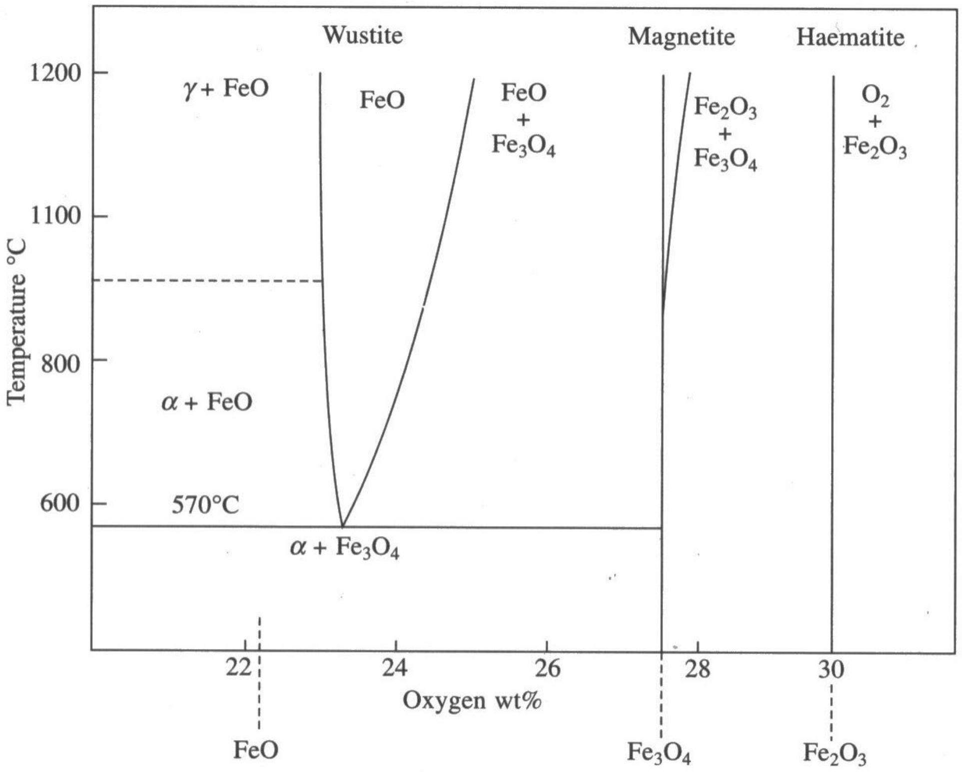

Figure 2.20: The iron – oxygen phase diagram (reproduced from Khanna (2004))

Wüstite is not stable at temperatures below 570ºC as is clearly shown in the iron – oxygen phase diagram shown in Figure 2.20. If iron was oxidised below this temperature then you would expect to find a two layer oxide scale; magnetite and haematite with magnetite next to the metal surface. West, Birosca and Higginson (2004) studied oxidation of steel using electron backscatter diffraction (EBSD) for phase identification. This work successfully distinguished between the magnetite and wüstite phases within the scale and showed magnetite precipitation in the wüstite layer of the oxide scale. This precipitation occurs because wüstite is unstable below temperatures of 570ºC and magnetite is stable. Therefore at slow cooling rates the wüstite will decompose into magnetite and iron as shown in Figure 2.20. The multi-layer scale occurs because the wüstite is metal rich and so requires a low oxygen partial pressure to form whereas magnetite is oxygen rich and requires a high oxygen partial pressure to form. Metal transport in the wüstite layer is extremely fast. This is due to the range of stoichiometry at which it exists ($Fe_{0.95}O$ to $Fe_{0.88}O$) at 1000°C [Kubaschewski(1982)]. The volume of cation vacancies and electron holes is extremely high so ions and electrons are extremely mobile.

The magnetite layer has an inverse spinel structure where defects occur on both the octahedral and the tetrahedral sites and so iron ions may diffuse over both sites. It behaves as a p-type semi conductor with metal ions diffusing outwards towards the scale / gas interface.

Haematite has two forms: α-Fe_2O_3 which has a corundum structure and γ-Fe_2O_3 which has a cubic structure. As γ-Fe_2O_3 oxidises to form α-Fe_2O_3, this is the only structure which needs to be considered for high temperature oxidation. In the corundum structure it may be expected that the cations would be mobile. However, this is not the case as it is only the anion lattice that shows disorder [Bevan *et al*. (1948)]. Therefore it is expected that only the oxygen ions are mobile through the haematite layer. However, a study by Bruckman *et al*. (1972) suggested that growth of the haematite layer may occur by cation migration towards the scale / gas interface.

From the knowledge of the multilayer structure of oxide scales formed on iron a schematic representation of the growth process can be produced (Figure 2.21).

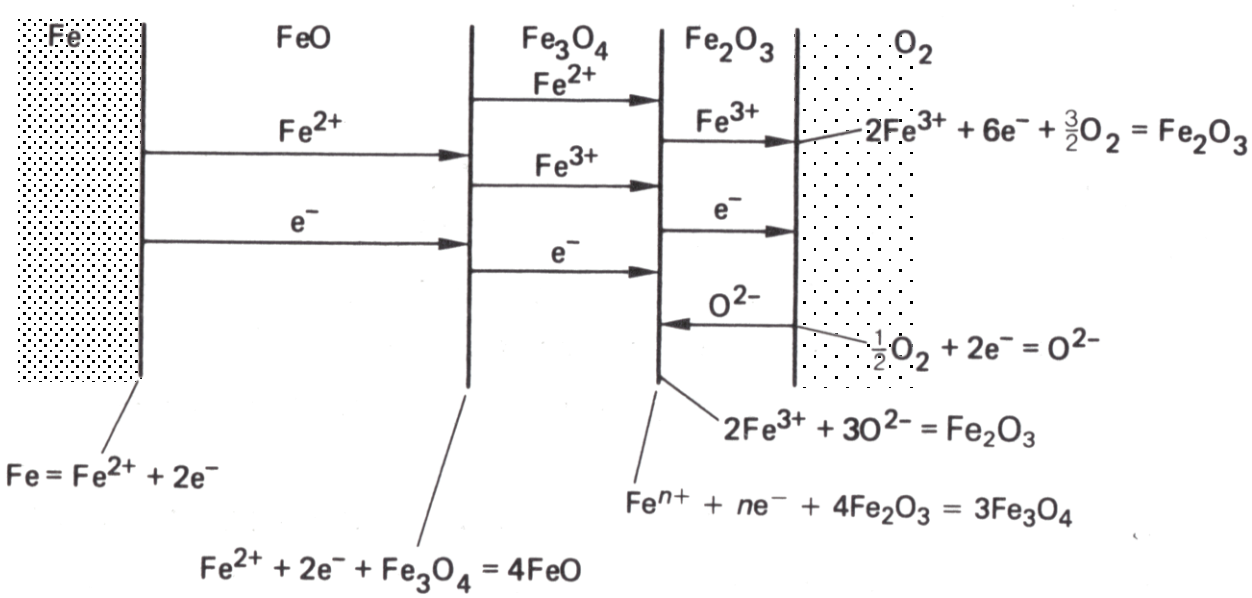

Figure 2.21: Schematic Diagram Showing Oxidation Mechanism of Iron Above 570°C (reproduced from Birks and Meier (2006))

The oxidation mechanism of iron at temperatures above 570°C after the initial oxidation stages explained in Section 2.3.2 is shown schematically in Figure 2.21. At the surface of the metal, iron ionises according to:

$$Fe = Fe^{2+} + 2e^{-} \text{--}[2.5]$$

The iron ions and the electrons move outwards over defects and electron holes to the wüstite / magnetite interface where new wüstite is produced by the reduction of magnetite according to the reaction:

$$Fe^{2+} + 2e^{-} + Fe_3O_4 = 4FeO \text{---}[2.6]$$

Excess electrons and iron ions then migrate outwards over the vacant sites in the haematite layer and the electron holes towards the interface between the magnetite and haematite layers where new magnetite is formed:

$$Fe^{n+} + ne^{-} + 4Fe_2O_3 = 3Fe_3O_4 \text{---}[2.7]$$

n in this case refers to the valency of the iron ions. 2 for Fe^{2+} and 3 for Fe^{3+}.

At the haematite / gas interface, further reactions occur between the iron ions and the oxygen to form new haematite:

$$2Fe^{3+} + 6e^{-} + \frac{3}{2}O_2 = Fe_2O_3 \text{--}[9]$$

Also at the haematite / gas interface, oxygen ionises to form O^{2-} which, if mobile, can react with the excess electrons and ions from the reaction at the magnetite / haematite layer to form new haematite. Defect mobility in wüstite is much greater than in the magnetite and haematite with this layer found to be much thicker by Mrowec *et al*. (1977). Usually the ratio of wüstite : magnetite : haematite is 95:4:1. Birosca, Dingley and Higginson (2003) also found a similar result with the ratio of wüstite: magnetite being 90:10.

2.8 Oxidation of Stainless Steel

2.8.1 Introduction

The oxidation and corrosion resistance of stainless steel is produced by the formation of a protective layer of chromia (Cr_2O_3). However, the chromia is usually not pure Cr_2O_3 as it may contain traces of other elements such as nickel and/or iron. It grows on low chromium stainless steels at low temperatures and can also form at higher temperatures on higher chromium steels. This protective scale grows very slowly due to low diffusion rates through it and, although other scale layers may form, Cr_2O_3 is considered the most protective. According to Sabioni, Huntz Silva and Jomard (2004), the formation of the chromia consumes oxygen from the atmosphere immediately adjacent to the oxide \ gas interface and so decreases the oxygen potential at the metal / scale interface and prevents other metallic alloying additions from oxidising. In this case, the chromia layer therefore, also plays a thermodynamic role in the protection of stainless steel.

At temperatures higher than 1200°C, the chromia may begin to volatilise. As stated by Khanna (2004), Cr_2O_3 has a tendency to dissociate at higher temperature into CrO_3 which is volatile and so effects the protection of the metal. Based on work done by Tedmon (1966), it can be concluded that when the oxide scale is very thin the amount of volatilisation of the

CrO_3 is negligible. This is because as the CrO_3 volatilises, it is very quickly replaced due to the high growth rates of the scale. As the scale thickness increases, however, the rate of volatilisation approaches the rate of scale growth which limits the thickness of the oxide scale (Figure 2.22(a)). Although the concept of the limiting scale thickness may imply that the metal has a continuous protective layer, the metal actually recedes and the consumption of the metal accelerates. (Figure 2.22(b)).

2.8.2 Oxidation of Fe-Cr alloys

Although the results may differ between the Fe-Cr alloys and stainless steels, the results are still relevant as they can give an idea of what can be expected from the chromium content in the stainless steel. An early study by Caplan and Cohen (1952) presented results that showed that scales formed on some Fe-Cr alloys consisted of Cr_2O_3 and Fe_2O_3 in solid solution. Caplan and Cohen (1952) did not use “pure” alloys of iron and chromium so some contents of other elements such as aluminium, copper, manganese and nickel were present making their study more relevant to stainless steel. These elements were detected in some of the scales. In an alloy containing 27 wt% chromium, for example, the scale consisted mainly of chromium oxides with small amounts of silica at the oxide – metal interface. They also found that iron and manganese were present within the scale with some aluminium and copper also detectable but no nickel was present. Seybolt (1960) gave some idea of the expected scale layers on Fe-Cr alloys. Studies were carried out on alloys containing varying amounts of chromium at a number of temperatures. One major conclusion from this work was that for chromium contents over 13wt% a two layer scale formed which consisted of Cr_2O_3 and Fe_2O_3 with the chromium containing oxide closest to the substrate which agreed with Caplan and Cohen (1952). At chromium contents below 13wt% a spinel scale was found with some Fe-Cr oxide. Wolff *et al.* (1998) presented data which showed that at high chromium content Fe-Cr alloys were resistant to breakaway oxidation.

They also showed that, if aluminium is added to the alloy then further increases in oxidation resistance are observed. This is due to the formation of a protective Al_2O_3 layer during initial oxidation and an additional layer of Cr_2O_3 once the aluminium becomes depleted. Mikkelsen and Linderoth (2003) conducted experiments oxidising Fe-Cr alloys in air and water vapour atmospheres as well as an atmosphere containing argon, hydrogen and water vapour. They concluded that scales formed in air showed the largest grains (2 – 3 µm) towards the top layer of the scale. They also found that increasing the water content in the atmosphere does not significantly alter the microstructure of the scale. The growth rate was also found to be independent of the oxygen activity in the atmosphere. This is due to the interstitial growth mechanism of chromium scale. An increase in the water content is reported to decrease the ultimate rate of oxidation, however, chromium would be lost due to vaporisation. A low oxygen pressure is able to protect the alloy from the breakaway oxidation that is observed at higher oxygen activities. An interesting conclusion from this work is that by tuning the oxygen activity the long-term oxidation of Fe-Cr alloys may be improved.

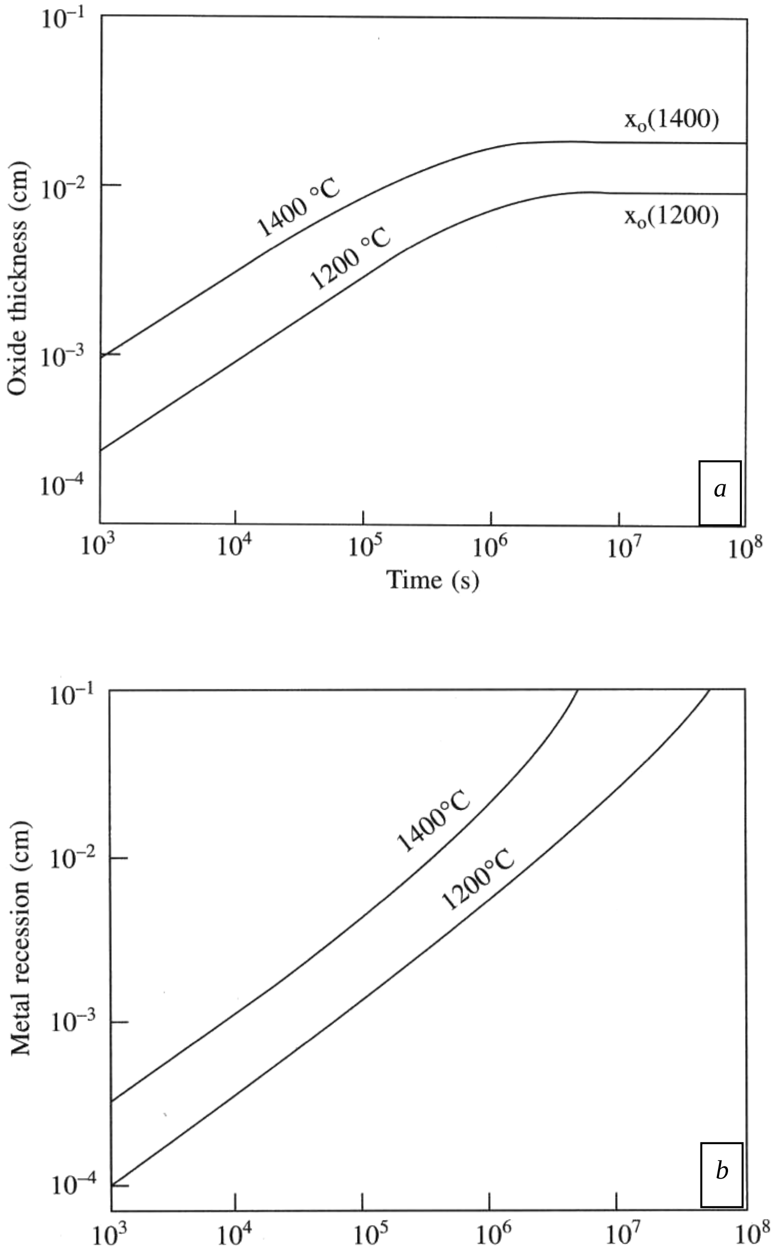

Figure 2.22: Schematic diagrams showing breakaway oxidation, a) oxide thickness with time and b) metal recession with time of an iron chromium alloy in a moist atmosphere (following Tedmon (1966))

2.8.3 Oxidation of Stainless Steel

McCullough (1951) carried out studies on 304, 430 and 410 stainless steels by weight gain measurements during heating at varying temperatures. It was found that the scale grew predictably until it was ruptured when breakaway oxidation began. They suggested that the composition of the scale was different after the scale had ruptured and that the protection of stainless steels was provided by the formation of an $FeO.Cr_2O_3$ spinel which tends to form at low oxygen partial pressures. Yearian, Randell and Longo (1955), presented findings from experimentation on chromium steels with varying chromium contents between 2 and 26 %. Two types of scale were suggested; the first is mainly Cr_2O_3 with an Fe_2O_3 upper layer which increases with increasing iron content in the alloy substrate, the second type of scale consisted of three layers of oxide. The outer layers of oxide were similar to Fe_2O_3 and Fe_3O_4 found on pure iron and the inner layer was a spinel of iron and chromium of the composition, $FeFe_{(2-x)}Cr_xO_4$ at the metal /scale interface with x equal to 2 and at the inner / outer layer oxide interface it was equal to 0. Yearian, Boren and Warr (1955) studied oxidation of nickel – chromium steels. Again two types of scale were present. Using X-ray diffraction techniques, one type of scale was found to consist mainly of Cr_2O_3 with the possibility of the presence of a mixed layer of Fe_2O_3 and Cr_2O_3. It was also noted that with small additions of manganese, a large amount of $MnCr_2O_3$ was present in the scale. This was reported to be replaced by a Fe-Cr-Ni spinel at increased temperatures. At higher oxidation rates it was observed that the Fe-Cr-Ni spinel became more common and that no pure Cr_2O_3 was present. Instead a large amount of the mixed Fe_2O_3 and Cr_2O_3 oxide was seen. Yearian, Derbyshire and Radavich (1956) followed the previous year's publications with a study of the oxidation of 18-8 stainless steel. It was reported that a thin layer of iron – chromium oxide formed very quickly over a very thin layer of Fe-Cr or Fe-Cr-Ni spinel oxide. As this scale grew the chromium contents of it increased. The scale then failed and small areas of localised attack produced thicker regions of oxide which consisted of haematite or the mixed Fe_2O_3 and Cr_2O_3 solid solution formed over a thin layer of Fe – Cr spinel. It was noted that small additions of silicon and manganese reduced the oxidation rate of these alloys. Wood and Hobby (1965) studied the oxidation of austenitic stainless steel for times varying between 30 minutes and 50 hours at 1200°C. It was found that a protective layer of either Cr_2O_3 or $MnCr_2O_3$ formed as the oxidation rate decreased and that a silicon rich layer forms which reduces diffusion of cations from the substrate into the scale. It was also found that an irregular scale forms after the first hour followed by very slow oxidation accompanied by internal oxidation. Occasionally rapid catastrophic oxidation was observed which resulted in metal being present within the scale layer. Perez *et al*. (2001) studied the oxidation behaviour of low nickel austenitic stainless steels. Their results partially agreed with the publication by Wood and Hobby (1965) as they found a scale layer consisting of $MnCr_2O_4$, $Mn_{1.5}Cr_{1.5}O_4$ or a mixed spinel of $(Mn, Cr, Fe)_3O_4$. It was suggested that this spinel allows faster diffusion of ions than Cr_2O_3 which would increase the oxidation rate.

Peraldi and Pint (2004) studied the scale formed on stainless steels after oxidation in air and 10%vol water mixture. After oxidation at 650°C and 800°C the oxide scales consisted of a corundum oxide of $(Fe,Cr)_2O_3$ for high nickel alloys and chromium contents above 16%. However, after longer periods of oxidation on an alloy containing iron, chromium and nickel a three-layer scale was produced. The layers were: a haematite (Fe_2O_3) layer, a $(Fe, Cr, Ni)_{0.8-1}O_1$ layer and an inner $(Fe, Cr, Ni)_{1.4-1.7}O_1$ layer. Previous studies conducted by McCullough *et al*. (1951) also found nickel contents in the scale layers, although they did not name it as a constituent part of the spinel. Caplan and Cohen (1959) also showed a content of nickel within the spinel layers.

2.8.4 Oxidation of Duplex Stainless Steels

Li, Jiang and Riquier (2005) showed the effect of oxidation on duplex stainless steels in atmospheres designed to simulate heating in combustion atmospheres. It was found that oxidation of a standard alloy resulted in the formation of oxide nodules on the austenitic regions and a suppression of oxide formation on the ferritic regions. The reason suggested for the occurrence of these different regions is localised breakaway oxidation of the austenitic region due only to a lower chromium concentration on the underlying region. As the material oxidises it depletes the underlying alloy of chromium, so if a crack forms in the oxide at some point during oxidation, it will become unlikely that there will be a sufficient supply of chromium to induce healing. Due to the austenitic region's lower chromium content before heat treatment, this effect occurs at an earlier stage to the ferrite region and an area of breakaway is observed as an oxide nodule on the metal's surface. The nodules' island regions are reported to be rich in iron with chromium rich craters. Although this process of breakaway oxidation is very well known, the authors do not present any chemical data from the phases before oxidation or give any indication of oxide cracking. Although the explanation of the occurrence of the oxide nodules presented in this publication is certainly feasible, it is possible that other factors may also be acting to produce the nodular oxides on duplex grades.

To further complicate the study of duplex stainless steels during oxidation, it has been suggested that the depletion of chromium from the underlying substrate also causes the ferrite phase to transform into austenite to a depth related to the oxidation time. It is unclear in this publication, however, how the samples were prepared prior to oxidation trials and so it cannot be concluded that the growth of the austenitic layer is due solely to the depletion of chromium. Instead it is possible, if the samples were cold worked prior to heat treatment (by surface grinding for example), that recrystallisation has occurred. As well as the production of nodular oxides, the authors also present results which show the formation of oxide “chains” and silicon rich oxides being produced along former phase / grain boundaries. The formation of oxide nodules will create a challenge when it comes to descaling as they are “deeply embedded in the underlying alloy” [Riquier and Zhang (2003)](Figure 2.23).

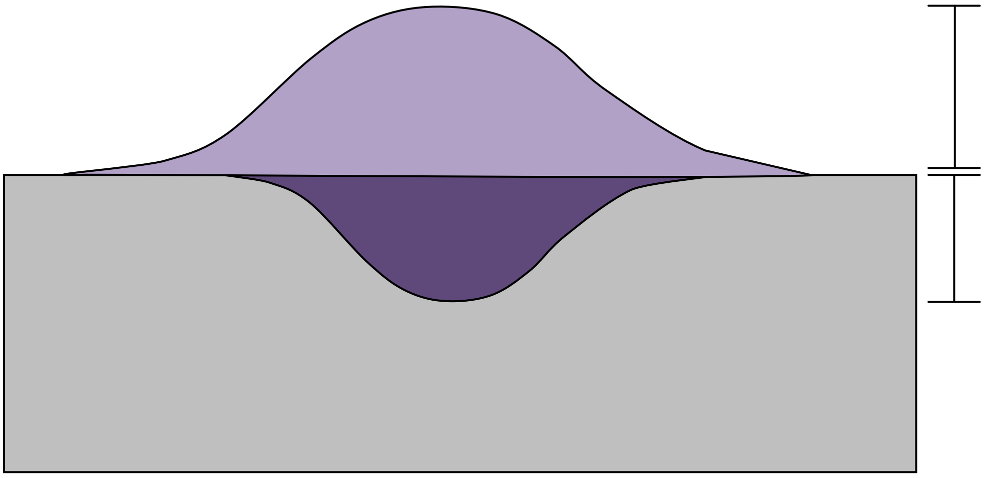

Figure 2.23:- Schematic showing the amount of metal which could potentially be lost through descaling of nodular oxides. Labels show 1) outer oxide which can easily be removed by mechanical descaling and 2) sub-surface oxide which would not be so easily removed

Although the top part of the nodule (1) would be relatively straight forward to remove using mechanical descaling procedures, the internal region (2) would require a large amount of metal to be removed to ensure complete oxide removal. This is unacceptable to a manufacturer as much of the useful and valuable metal is scrapped. The alternative to this is to simply remove the oxide in the crater region which will leave an impression in the surface which, if large enough, could effect the final product's surface finish.

2.8.5 Effect of the Addition of Manganese

Marasco and Young (1991) carried out an extensive study into the effect of manganese on the oxidation of iron – chromium alloys. A number of alloys were studied which fell into two main categories: high chromium alloys and low chromium alloys. The high chromium alloys had chromium contents of 20wt% Cr and are the best comparison to the stainless steels studied in this thesis. It was reported that with increasing manganese content the oxidation rate increased. The results of their study showed that nodule formation was likely with any manganese content over 6wt%. The nodules consisted of a dual phase outer region and an inner region also consisting of two phases. The outer region was a haematite layer and a manganese and iron oxide layer and the inner region consisted of chromia and a mixed spinel oxide. With higher manganese concentrations, the chromia was situated at the oxide / metal interface.

The reason for the outbreak of nodular growth was given to be the rapid transport of manganese and iron through the initial protective oxide scale in areas favourable to diffusion which produces a non-protective oxide layer. The chromia band formed at the perimeter of the internal region of the nodule is explained by the self-healing mechanism where the alloy surrounding the proceeding oxide front becomes depleted in manganese and so a chromium rich oxide can again form.

2.8.6 The Effect of Silicon on the Oxidation of Stainless Steels

Silicon is usually present in commercially available stainless steels as a residual impurity from the production process up to a value of ~1wt.%. Even at these low values, it can have a significant effect on the high temperature oxidation characteristics of an alloy. With this said and accepted within the literature, the effect that silicon has is still disputed. It is known that additions of silicon can have a beneficial effect on the oxidation resistance of stainless steels [Basu and Yurek (1991), Stott, Wood and Stringer (1995), Pettersson, Liu and Sund (2005)] but the reason for the benefits are unclear. The two main suggested methods are that the silica layer formed, acts as a diffusion barrier [Evans, Hilton, Holm and Webster (1980), Evans, Hilton, Holm and Webster (1983)] or that it acts as a structure which promotes the diffusion of chromium through the material and so encourages the formation of protective chromia [Francis and Jutson (1968)]. The reason that silica is a good diffusion barrier is that after oxidation at temperatures below 1000°C it is usually found to be amorphous in nature which, due to a lack of diffusion pathways (i.e. grain boundaries), hinders transport through it. It has also been suggested that the addition of silicon has detrimental effects on the spallation resistance of scales formed on stainless steels [Bamba, Wouters, Galerie, Charlot and Dellali (2006)].

Francis and Jutson (1968) investigated the role of silicon on the oxidation resistance of austenitic stainless steel with 20wt% chromium and 25wt% nickel. It was found that removal of the silicon from the steel was deleterious to oxidation kinetics (i.e. oxidation rate increases) indicated by the presence of an iron containing oxide on specimens containing no silicon. This is due to the fact that additions of silicon apparently increase the rate of diffusion of chromium within the substrate which favours the formation of protective chromia. As well as this interesting observation, it was concluded that the formation of a thin silicon containing layer is crucial for the most protective oxide at high temperatures. Evans, Hilton, Holm and Webster (1980) examined an identical alloy under similar oxidation conditions for a much greater time period (>6000 hours as opposed to 1000 hours). Of particular interest was the silica layer which formed where local nodule formation was evident. They suggested that the silica would still remain a diffusion barrier between the island and the pit but instead of hindering growth at this stage of the oxidation process would produce an elemental segregation in the oxide leading to an iron rich island and a crater containing iron, chromium and nickel rich spinels. Where no silica layer was present, the iron extended further into the crater and porosity was significantly reduced. Oxidation behaviour of a 14% chromium, 14% nickel alloy with additions of 0, 1 and 4% silicon was investigated by Kumar and Douglass (1976) who found that the base alloy (0% silicon) formed a thick outer scale similar to that formed on mild steel with an internal region containing a spinel type oxide of iron, chromium and nickel. They also found that the best performing alloy of the three they tested was the 4% silicon alloy with the 1% silicon alloy giving intermediate protection. They therefore concluded that for their alloy of interest, the ideal silicon concentration for oxidation resistance lay between 1 and 4%. Evans, Hilton, Holm and Webster (1983) also investigated the influence of silicon addition to the oxidation resistance stainless steel. They found that an ideal silicon content was 0.92 wt% for all of their presented results. These include: the lowest gross weight gain over a period of time (growth rate constant), tendency to spall (little difference between 0.92 wt% and lower contents suggesting that lower silicon contents are beneficial to spallation resistance) and growth rate of sub-surface attack. They suggest that the outstanding qualities of the 0.92 wt% silicon alloy is attributable to the formation of a continuous diffusion barrier of silica at the metal – scale interface which aids the reduction of the growth rate of external and internal oxidation. The next value of silicon content they investigated was 1.56% which showed an increase in oxide growth rate suggesting that there is a maximum value of silicon required for effective oxidation protection. Although a very different result to Kumar and Douglass (1976), this thorough investigation was carried out using many different silicon concentrations ranging from 0.05% to 2.35%. The difference in their results can be simply explained by the substantially lower chromium content available in Kumar and Douglass' alloy.

Basu and Yurek (1991) studied three different Si contents of 0, 0.6 and 1.5% in an 18Cr-20Ni-1.5Mn stainless steel at 900°C for both isothermal and cyclic oxidation trials. The grain size of the material was also varied by different heat treatment procedures prior to the oxidation procedure. It was found that an alloy with no silicon would form iron rich nodules, particularly in the large grained specimen, after periods of <100 hours isothermal heat treatment in pure oxygen. When the grain size was reduced the occurrence of the nodules was reduced. This is also the case if more silicon is added to the sample as it produces a continuous protective silica layer at the metal / oxide interface. It was therefore concluded that the fewest oxide nodules are produced when the silicon content is high and the grain size is small. This effect was explained by the increased number of diffusion pathways available with a smaller grain size (Figure 2.24).

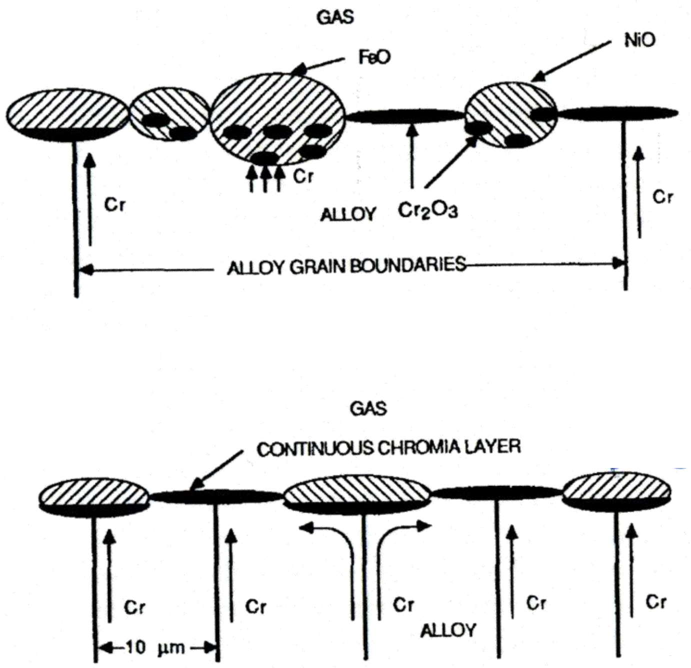

Figure 2.24:- Schematic showing the effect of grain size on the oxidation of a silicon containing stainless steel (reproduced from Basu and Yurek (1991))

Although describing the diffusion of chromium, this diagram could be adapted to show the transport of silicon via grain boundaries as Basu and Yurek 1991 state that “during the initial stages of oxidation, internal precipitates of silica form, which aid the internal precipitates of chromia in undercutting the transient oxides”.

Pettersson, Jiu and Sund (2005) tested two differing silicon contents: 0.5 and 2% Si in a 20Cr 35Ni specimen at 700 and 900 °C in dry and moist air. It was found that the high silicon material was less susceptible to breakaway oxidation due to a silica sub oxide layer between the chromia and the substrate which is in agreement with Evans *et al*. (1983) and Basu and Yurek (1991). Discolouration of the sample holders used for trials in water vapour containing gases suggests that chromium evaporation was occurring and the discolouration was lessened when high silicon samples were oxidised. This effect can be attributed to the slower diffusion of chromium from the bulk material when a silica layer is present within the oxide scale.

For the formation of a continuous silica band, Stott, Wood and Stringer (1995) produced a schematic showing the successive stages of formation for a generic alloy containing 15 – 30wt% chromium and sufficient silicon to form a continuous band of silica (Figure 2.25). As the chromia is faster forming than the silica, it will form an initial protective oxide layer.

During the formation of the chromia layer, silica precipitates will form simultaneously at the oxide / metal interface. As the oxide continues to grow, the silica layer will grow laterally (as suggested by Basu and Yurek 1991) until the internal oxide precipitates coalesce to produce a self healing silica layer which will hinder any further diffusion of chromium into the chromia and will therefore slow its growth.

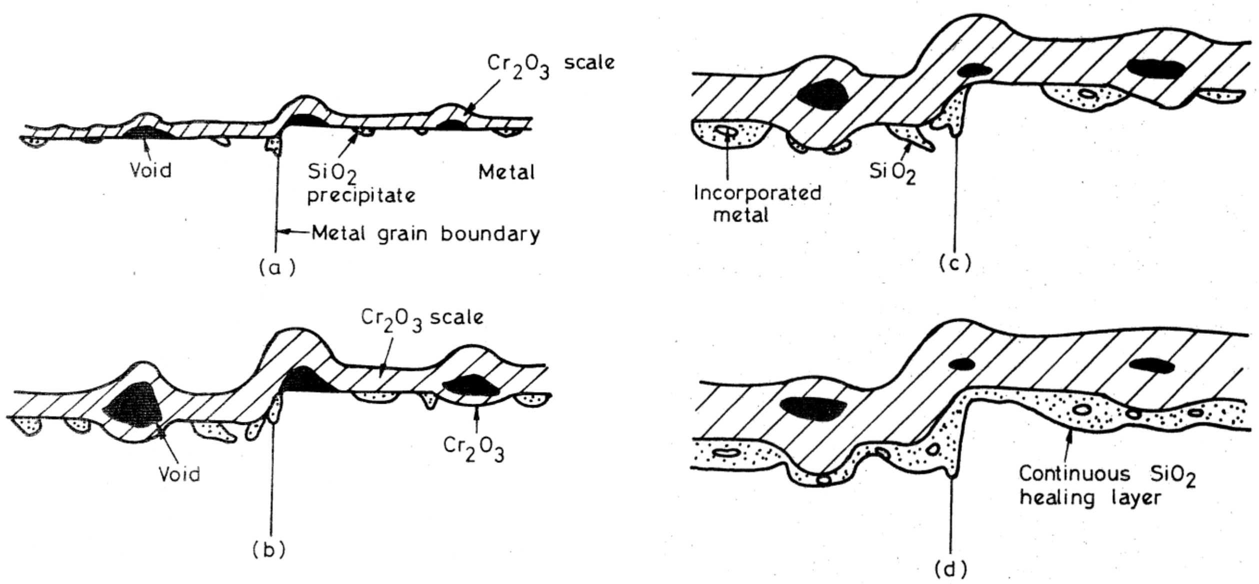

Figure 2.25:- Schematic showing the a timeline of growth of a continuous silica layer at the metal – oxide interface with (following Basu and Yurek (1991))

Bamba, Wouters, Galerie, Charlot and Dellali (2006) investigated the effect of small additions of silicon to a 15% chromium, iron alloy. It was found that an alloy with no silicon content produced breakaway oxidation resulting in iron rich nodules which agrees with much of the previous work on the effect of silicon. The thinnest oxide produced was found to be on the intermediate silicon content of 0.5% where a discontinuous network of silica particles formed which acted as a bulk diffusion barrier for chromium to the interface by restricting the movement of vacancies which reduces the flux of chromium. This is a very different mechanism to that proposed by previous authors although the same reduced oxidation rate is observed. It was also found that spallation was most severe in the 0.5% alloy a suggested reason for which, is that there is vacancy coalescence forming micro cavities at the scale / metal interface.

2.8.7 Breakaway Oxidation of Stainless Steel

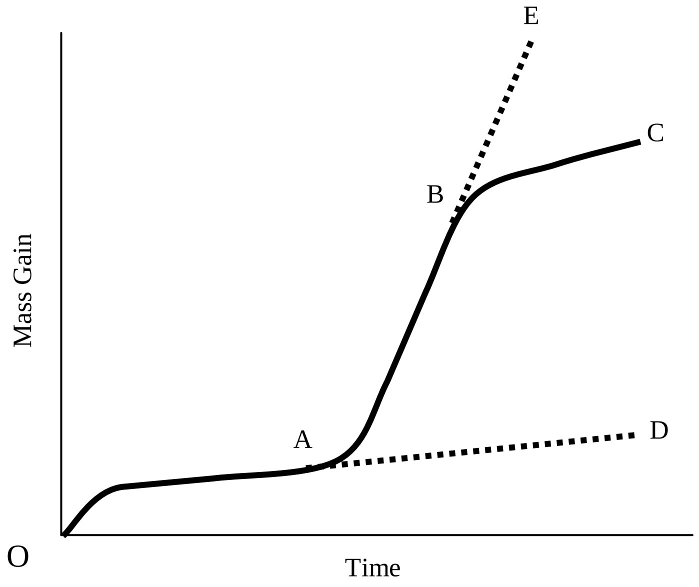

Figure 2.26: Illustration of typical growth curves for stainless steels showing OAD: protective oxide growth, OABE: protective growth followed by breakaway and OABC breakaway oxidation followed by re-healing(following Wood (1970))

Breakaway (or breakthrough) oxidation is a period of oxidation which can be described as a sudden and severe increase in the growth rate of the oxide scale after an initial growth of a protective layer (Figure 2.26) (OAB). After this breakaway period one of two routes can be followed; the scale can re-heal to follow the curve OABE, or re-passivate to follow the curve OABC. There are a number of reasons for which breakaway oxidation can occur. Breakaway oxidation is particularly evident in situations where cyclic heating and cooling takes place [Peraldi and Pint (2004)]. As the temperature is cycled, stresses produced in the oxide due to thermal expansion and contraction coefficient mismatches between the metal and oxide, cause the protective oxide to crack revealing a surface depleted of the protective oxide forming elements (e.g. aluminium or chromium) (Figure 2.27) [Pérez, Pedraza, Sanz, Hierro and Gómez (2002) and Peraldi and Pint (2004)]. This can also happen during isothermal heat treatments where vacancies coalesce at the oxide – metal interface and cause the protective oxide to spall [Howes (1968)]. Due to the nature of breakaway oxidation, it is reasonable to suggest that substrates with a higher concentration of protective scale forming elements (e.g. Cr) will be less prone to catastrophic oxide growth than those with lower levels, however, breakaway is also related to oxide scale adherence. An oxide formed on Fe-28% Cr during thermal cycling, for example, may spall and re-heal a number of times before breakaway occurs, but cyclic oxidation of an Fe -14% Cr alloy may not induce spallation as the scale is fairly adherent [Wood (1970)].

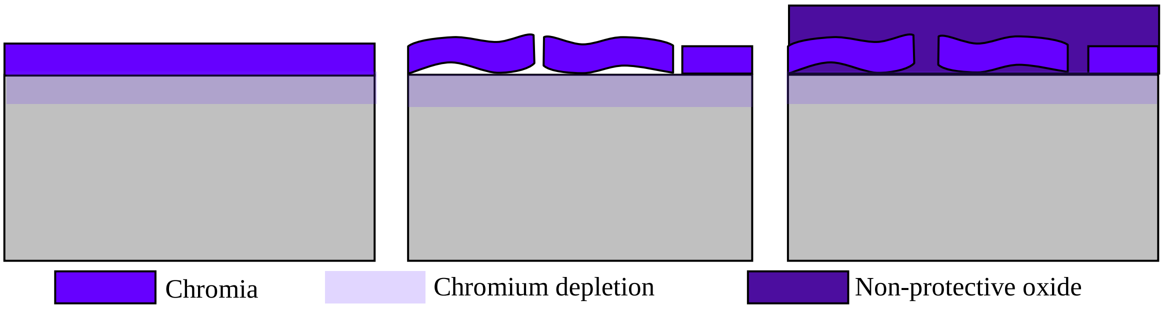

Figure 2.27: Schematic showing the occurrence of breakaway oxidation due to scale cracking produced from description by Perez et al. (2002)

Lloyd, Saunders, Kent and Fursey (1977), examined breakaway oxidation in Fe-Cr alloys at temperatures up to 600°C. It was found that for alloys of Fe-10%Cr and Fe-20%Cr, a thin protective scale forms consisting of two layers: Fe_2O_3 and a spinel layer. In-fact it was also suggested that there may be a Cr_2O_3 layer present. They stated that this layer would fail due to stress build-ups in the scale that deform the underlying substrate. The alteration in microstructure associated with the deformation encourages the growth of chromium rich oxide due to fast diffusion of chromium along slip planes. In-between these chromium rich bands of oxide were thin, patchy areas of low chromium scale. This leads to the onset of breakaway oxidation in these areas (Figure 2.28).

According to Morris (1977) breakthrough oxidation in stainless steels is accompanied by the formation of a scale consisting of an inner spinel ($FeCr_2O_3$) and an outer layer of haematite (Fe_2O_3). Kvernes, Oliviera and Kofstad, (1977), concluded that the breakaway oxidation of an Fe-Cr-Al alloy could be attributed to the depletion of chromium in the layer of the alloy just under the oxide scale. As oxidation continues, iron rich oxides form and break the protective chromium oxide. From this, a multi-layered oxide scale grows. This agrees with the study by Morris (1977) who found the formation of iron rich spinels and oxides during breakaway oxidation. Otsuka, Nishiyama and Kudo (2004), conducted experiments on a 310 stainless steel at temperatures of 1000 and 1050°C for 500 and 242 hours respectively and in an atmosphere calculated from the combustion of natural gas in air ($3\%O_2$–$9\%CO_2$–$16\%H_2O$–N_2). It was found that breakaway oxidation did occur on thinner foils of 0.11mm but did not occur on thicker foils of 1.2 mm. The breakaway oxidation was attributed to the depletion of chromium in the metallic substrate alone as opposed to mechanical spalling defects proposed by Lloyd *et al*. (1977). As the protective Cr_2O_3 layer grows it depletes the substrate of chromium and so stops growing. Once this layer has stopped growing, it allows breakaway oxidation to occur.

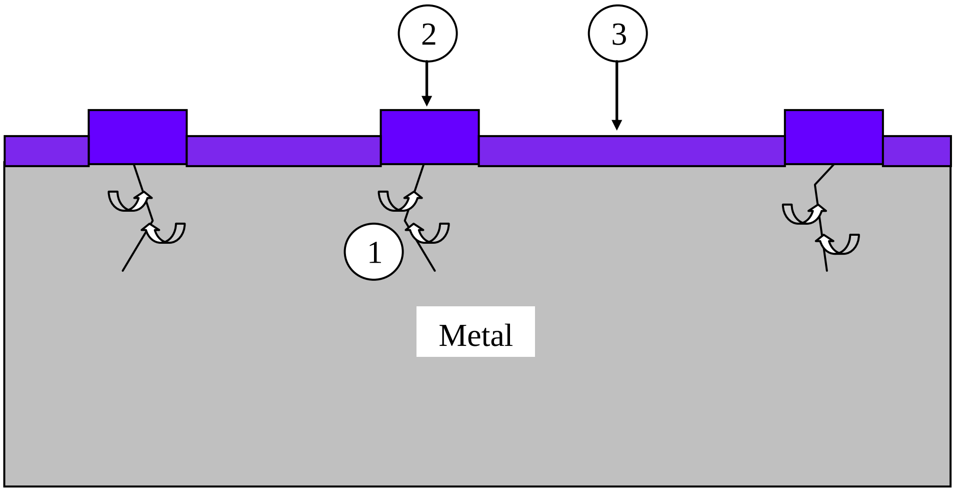

1 – Cr diffuses along slip planes, 2 – Cr rich protective scale produced, 3 – Fe rich non-protective scale formed

Figure 2.28:- Schematic Diagram of the Occurrence of Breakaway Oxidation on a Deformed Substrate produced from the description by Lloyd et al. (1977)

Thin specimens may fail due to chromium depletion but during the oxidation of samples of an adequate thickness to resist excessive chromium depletion, failure due to cracks forming in the oxide because of stress build up is far more likely. A mechanism for the formation of breakaway nodules on the surface of an Fe 14%Cr alloy has been suggested by Wood (1970) (Figure 2.29). It was proposed that after the initial formation of a thin protective oxide on the surface of the metal, buckling of the scale may occur which leads to stress build up and ultimately crack formation in the oxide. The presence of cracks in the outer edge of the oxide means that the underlying alloy (now depleted in chromium) is exposed to the oxidising atmosphere. The conditions of this exposure are sufficiently severe (and metal sufficiently depleted in chromium) to produce; an oxide consisting of an outer layer of iron rich oxide, an inner layer of iron – chromium oxides and internal chromium oxides. The iron based oxides will continue to grow until they are healed by coalescence of chromium based protective internal oxides at thier base [Evans, Hilton, Holms and Webster (1980) and Wood (1970)] or lateral growth of the original nodule will occur leading to a homogenous scale over the entire surface of the alloy.

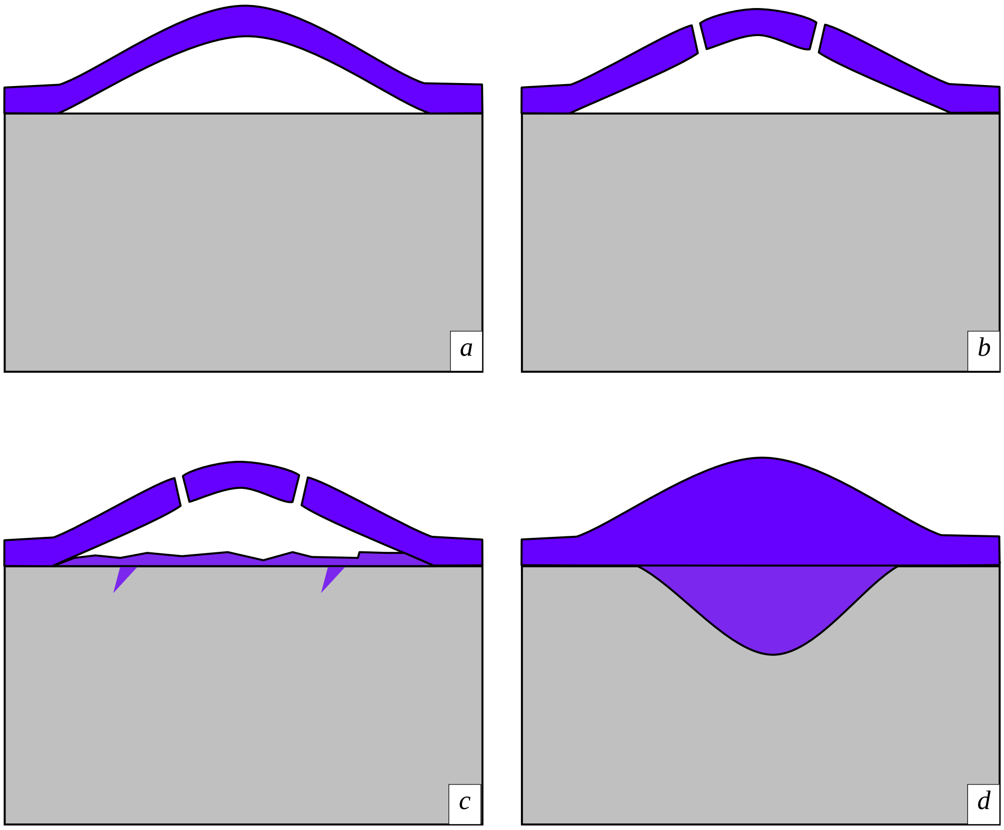

a – Protective oxide scale buckles
b – Stress build-up causes cracking
c – Exposed alloy forms oxide
d – Breakaway nodule is fully formed on the alloy's surface

Figure 2.29:- Schematic of breakaway nodule formation mechanism as proposed by Wood (1970)

Halvarsson, Tang, Asteman and Johansson (2006) suggested a method for breakaway nodule formation on 304 stainless steel. Due to the slow bulk diffusivity of chromium in austenite [Gunn, (1997)], the authors presented a model where nodules form in the centre of some grains (Figure 2.30). They suggest that the supply of chromium to the protective base oxide is provided by the grain boundaries which produces a base oxide in the centre of the grain, which has a lower chromium content near to the grain boundaries. This means that the base oxide in the centre of grains will lose its protective properties before areas near to the grain boundaries leading to the growth of breakaway nodules. Although Halvarsson *et al*. do not suggest that oxide cracking has any role in nodule formation [Wood (1970)], the mechanism of breakaway nodule growth has similarities. They both apportion blame to chromium depletion (or lack of chromium supply) leading to accelerated growth of iron oxides on the surface and chromium containing oxides in the crater.

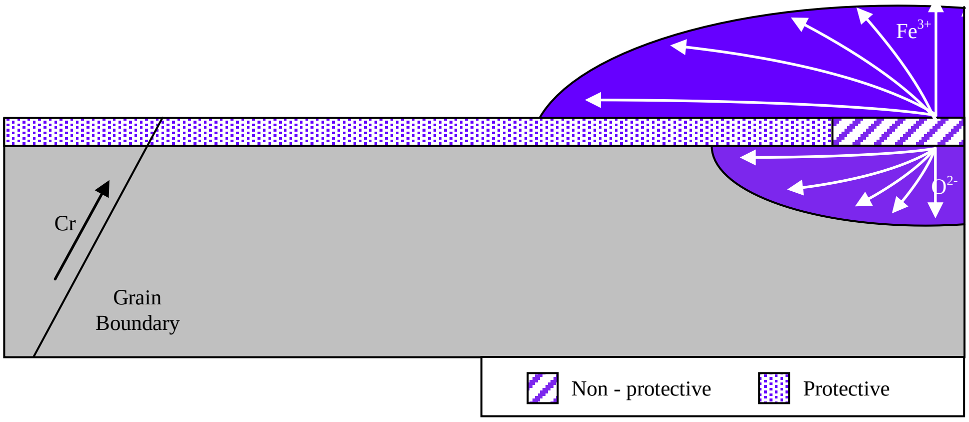

Figure 2.30:- Schematic of Breakaway nodule growth on 304 stainless steel following the breakdown of the protective base oxide. (Following Halvarsson et al. (2006))

Cheng, Kuan and Tsai (2005) investigated the effect of water vapour on the oxidation of 316 stainless steel. It was shown that at temperatures above 950°C, substantial breakaway oxidation occurred in a moist atmosphere which, over the same time period, did not occur in a dry atmosphere. An example of weight gain measurements at 1030°C is shown in Figure 2.31.

Figure 2.31 shows the two stages of oxidation in moist air. The accelerated region shown occurs between the times of 100 and 180 minutes of oxidation followed by a linear rate region. The breakaway oxidation is explained in this case by the fast outward diffusion of iron ions through the Cr_2O_3 which initially forms up to 30 minutes oxidation. After 1 hour of oxidation, nodules of iron oxide are formed on the surface. Further oxidation resulted in the formation of a thick, continuous, multilayered oxide scale of iron oxide at the outer edge and a chromium rich oxide at the substrate / scale interface.

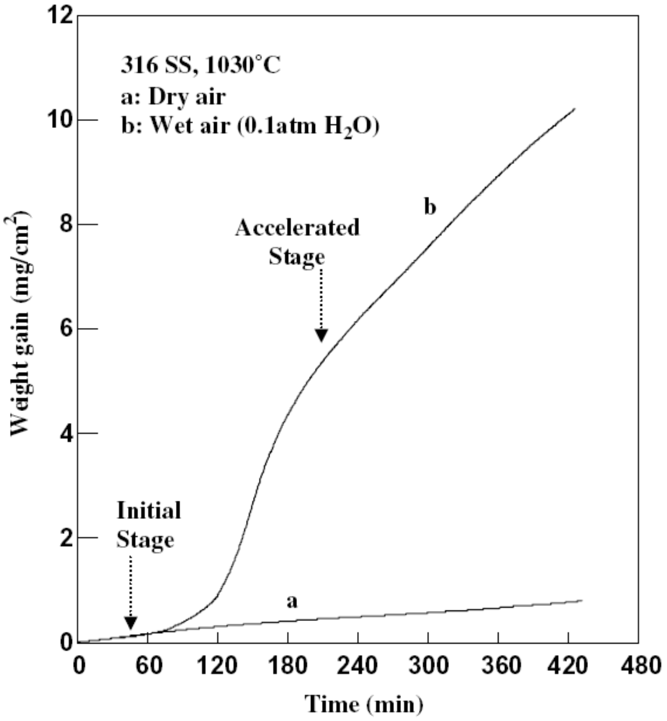

Figure 2.31:- Graph showing accelerated attack on 316 stainless steel (reproduced from Cheng et al. (2005))

2.8.8 Chromium Evaporation / Vaporisation

During oxidation at high temperature, chromium containing steels can form a gaseous oxide of chromium by the oxidation of chromia. The reaction for this formation is commonly published as [Caplan and Cohen (1961)]:

$$Cr_2O_3 + \frac{3}{2}O_2 \Leftrightarrow 2CrO_3 \text{---} [2.8]$$

This reaction can have a fairly noticeable effect on oxide scales produced on chromia forming alloys at temperatures of 1000°C or above. Menzies and Mortimer (1966) for example reported that as the chromia layer oxidises, it is succeeded by the formation of iron rich spinels which, once formed, stop the loss of chromium through evaporation. Although not mentioned by the authors, this would have a great effect on the protective properties of the oxide scales. The authors also give compelling evidence to suggest that increasing the oxidising gas flow rate increases the total loss of chromia in a given time. The reason for this flow rate dependence is best explained by Segerdahl, Svensson and Johansson (2002) who suggest that any volatile species will have to diffuse through a layer of stagnant gas separating the oxide surface from the bulk of the flowing gas. As the flow rate of the gas increases, the stagnant layer will reduce in thickness thus promoting the evaporation of any volatile species.

Tedmon (1966), carried out experiments into the oxidation of iron / chromium alloys and concluded that in order to fully appreciate the mechanisms of oxidation of chromia formers, formation of CrO_3 must be taken into account. It was found that a period of oxidation for 50 days at 1400°C and 100 days at 1200°C would result in maximum oxide scale thickness. This is due to the fact that evaporative losses and chromia growth rates will be equal. Although the data generated in this study suggested that oxides formed in late oxidation stages were protective, metal recession was still evident.

Although evaporation of pure chromium oxides (e.g. CrO_3) is common, it has been shown that the addition of water vapour to the oxidising gas increases the vaporisation rate of chromia, both in its pure state [Yamauchi, Kurokawa and Takahashi (2003)] and when produced on chromia forming alloys [Peng, Yan, Zhou and Wang (2005)].

This increase in rate is due to the formation of chromium oxide hydroxide ($CrO_2(OH)_2$) probably following the reaction [Astemann, Svensson, Johansson and Norell (1999)]:

$$\frac{1}{2}Cr_2O_3(s)+\frac{3}{4}O_2(g)+H_2O(g)\rightarrow CrO_2(OH)_2(g) \text{ --[2.9]}$$

Astemann *et al*. (1999), demonstrated that the increase in chromium evaporation was due to the presence of water vapour with a set of elegantly designed experiments. By the use of a cold finger and condensation products on a quartz furnace tube collected “downstream” from the sample, it was proven that chromium volatile species were emitted from the samples. It was also shown that samples in a “downstream” position were less likely to undergo chromium oxide hydroxide production as the gas would be closer to saturation than in an “upstream” position.

The exact effect of water vapour on the oxidation of chromia formers has been the subject of many subsequent studies. Studies have been carried with the focus of flow rate, water content and temperature with much of the work being carried out by Asteman and his co-workers ([Asteman, *et al*. (1999), Asteman, Svensson, Norell and Johansson (2000), Asteman, Svensson and Johansson (2002), Asteman, Svensson and Johansson (2004), Panas, Svensson, Asteman, Johnson and Johansson (2004)] with some valued contributions from others [Segerdahl, Svensson and Johansson (2002), Liu, Tang, Jonsson, Canovic, Segerdahl, Svensson and Halvarsson (2006), Young and Pint (2006)]. From these studies into the effects of water vapour on the oxidation of chromia formers, it is possible to produce a summary of their findings.

Asteman *et al*. (2000) compared the effect of oxidation of type 304L stainless steel in oxygen with varying quantities of water vapour. The results showed that with increasing water content and flow rate, localised breakaway regions started to appear at the grain centres. A mechanism for the formation of these breakaway islands was proposed and is shown in Figure 2.32.

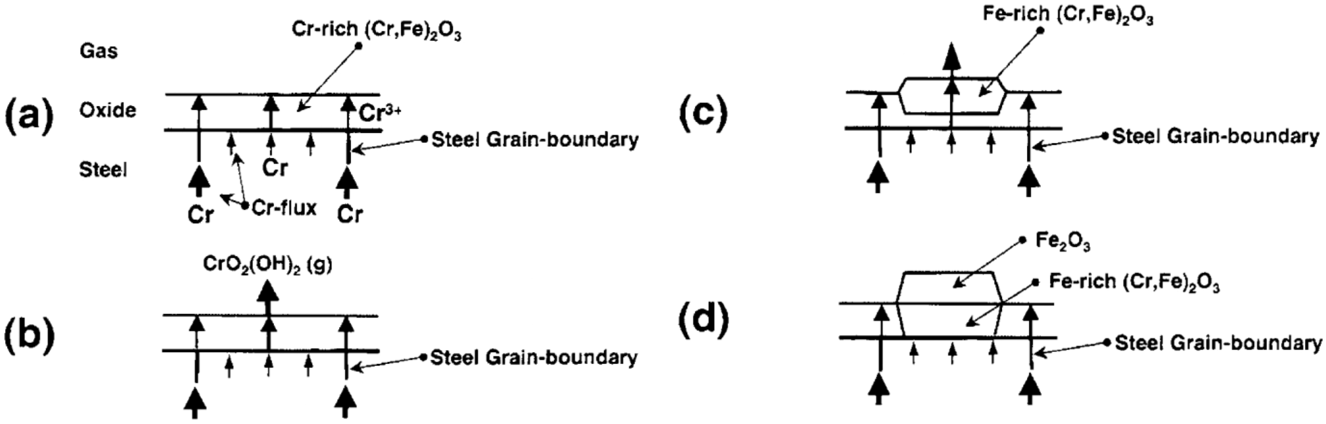

Figure 2.32: Schematic of a timeline of oxidation showing the effect of chromium evaporation on the oxidation of 304L stainless steel (reproduced from Astemann (2000))

Firstly a thin and protective oxide will form on the alloy's surface due to chromium diffusion to the surface of the substrate and then through the oxide scale itself. The greatest flux of chromium will be at the grain boundaries. Due to chromium oxide hydroxide formation, chromium will be lost from the surface of the oxide which therefore, becomes depleted in the upper layers. Iron will then diffuse through the oxide where it replaces the lost chromium in the outer edges producing a haematite-like oxide which is far less protective than the originally formed chromia. This transformation into a less protective oxide then gives rise to the production of a local breakaway region which may then grow up to the surrounding grain boundaries. This schematic can be viewed as a series of figures explaining the formation of oxide islands or as a set of individual figures describing the effect of flow rate on oxidation after a common time at a common temperature with (a) being the slowest flow rate and (d) being the fastest.

Yamauchi *et al.* (2003), studied the effect of oxidising pure chromia pellets in atmospheres containing various quantities of nitrogen (N_2), oxygen (O_2) and water (H_2O). The resulting mass losses during oxidation were recorded and revealed that during oxidation above 1100°C in an N_2-3%O_2 atmosphere, CrO_3 evaporation occurred at a rate of 1 order of magnitude lower than evaporation in the same atmosphere with H_2O included. This showed that H_2O content is an important consideration for chromium evaporation. However, when tests were carried out in atmospheres containing N_2-3%O_2 and N_2-H_2O, the differences in mass loss were negligible. This suggests that water alone is not significant and that water and oxygen together are required for substantial losses of chromium. It was also found during this study that a rate change occurs at temperatures above 1100°C where CrO_3 evaporation occurs, which implies that CrO_3 may contribute to the production of chromium oxide hydroxide according to the reaction:

$$CrO_3 + H_2O \rightarrow CrO_2(OH)_2 \text{ --[2.10]}$$

2.8.9 Protecting Stainless Steel

There are a number of ways that stainless steels can be protected from oxidation. Several researchers have used yttria dispersion, nitridation and addition of other elements with varying results. Wolff, Lorio, Rumpf, Scheers and Potgieter (1998), studied Fe-Cr alloys and Fe-Cr-Al alloys with minor alloying additions of ruthenium and other rare earth metals including lanthanum and cerium and found that the addition of Ru encouraged the growth of the protective Cr_2O_3. This provided extra oxidation resistance to the Fe-Cr-Al alloy but in the Fe-Cr alloy caused an increase in oxidation rate and an increase risk of spalling. Hoelzer, Pint and Wright (2000), examined scales formed on yttrium oxide dispersion strengthened iron-chromium steels. At 700°C a spinel of $(Fe,Cr)_3O_4$ forms at the gas / metal interface whereas at 800°C a layer of chromia was found at the gas / metal interface. The oxidation rate was slow in comparison to unprotected stainless steel and this was attributed to the yttria dispersion encouraging the formation of a fine grained substrate microstructure which increased the diffusion paths for the chromium. This then promoted formation of a protective Cr_2O_3 layer. A silica layer was also observed at the metal / scale interface which may have slowed the diffusion of anions and cations. The Cr ions would still have been mobile due to contact areas between the Cr_2O_3 and the metal acting as diffusion pathways. A similar result was obtained by Fujikawa, Morimoto and Nishiyama (2000) who found that a small amount of yttrium addition to the steel showed good oxidation resistance up to 1000°C with the scale composed of chromium oxide and silicon oxide. It was found that the most benefit was obtained when the yttrium was added to steel containing silicon as together they give good resistance to diffusion of cations and anions through the oxide grain boundaries. Work conducted by Riffard, Buscail, Caudron, Cueff, Issartrel and Perrier (2003) used a yttrium coating instead of yttrium addition or yttria dispersion within the alloy. It was found that during isothermal treatment at 1000°C in air the Y coated samples were more resistant to oxidation than one which was not coated. Issartrel *et al*. (2003) used a different method of oxide prevention; samples of 304 stainless steel were nitrided before oxidation was carried out. It was suggested that silicon was entrapped as Fe_7SiO_{10} in samples without nitridation which caused a non protective scale to form. After nitridation the silicon oxide phase does not form. This allowed the silicon to act as a diffusion barrier for iron ions. Fe_2O_3 was formed, however, but was quickly followed by the formation of protective Cr_2O_3 and $Mn_{1.5}Cr_{1.5}O_4$.

3 EXPERIMENTAL PROCEDURE

3.1 Introduction

In this chapter the materials chosen and reasons for their choice, the methods of sample preparation both before and after oxidation and the techniques used for the examination of the resulting oxides will all be described.

3.2 Materials

Experimentation has been carried out on Types 316L, 304, S32101 and S32205 stainless steels with the nominal compositions shown in Table 3.1. Specimens were supplied by Outokumpu Stainless in various forms. The 316L was supplied as slab in the as-cast condition and the 304 was as-cast billet. Both of these specimens were taken from production prior to the reheat operation and the oxide scale produced during continuous casting remained on both. The duplex grades: S32101 and S32205 were supplied as industrially ground slab specimens taken from production immediately following the grinding operation. The grinding procedures used in industrial practice are hot grinding (at ~800°C) to a finish of approximately 32 grit for the S32101 and cold grinding to the same finish for S32205.

Table 3.1: Nominal Compositions of Stainless Steels Studied (Wt %)

Type	C	Cr	Ni	Mn	Mo	Fe
316L	0.02	17.00	11.50	1.60	2.35	Balance
304	0.04	18.30	8.10	-	-	Balance
S32101	0.03	21.50	1.50	5.00	0.30	Balance
S32205	0.02	22.00	5.70	-	3.10	Balance

These grades of stainless steel were chosen for a number of reasons; 304 is the “standard” austenitic stainless steel and is the most produced austenitic stainless steel worldwide. It is regularly used for applications where thin gauges are required such as work bench top coverings and food preparation surface coverings. These applications require that the steel is to be flat rolled. It is therefore important to know how the material will oxidise prior to and during the rolling process. Type 316L finds uses in very similar applications but is also the main stainless steel used in marine environment due to its high corrosion resistance. 316L is also used in applications where high temperatures may be experienced in service such as heat exchangers in various applications. If the material is used in high temperature applications then it is important to know how it will oxidise in-service.

Duplex stainless steels were chosen as an additional area of study because of their recent increase in use, industrial interest in their oxidation characteristics and relatively few academic publications on the subject of oxidation of duplex grades are currently available.

3.3 Grain Size Determination

Samples were metallographically prepared by grinding using progressively increasing grit number silicon carbide paper up to 2400 grit followed by polishing on 6 and then 1 µm diamond polish. In order to reveal the grain structure of the material, it was etched using Kalling’s reagent for approximately 5 seconds. Micrographs were taken of the revealed microstructure using an MEF3 optical microscope with digital camera attachment.

The method used for the grain size determination was the linear intercept method as described in Higginson and Sellars (2003). The grain size of the 316L stainless steel substrate was found to be 8.5 ± 0.7 µm. The 304 was prepared in the same manner and, its microstructure was revealed to be dendritic as shown in Figure 3.1.

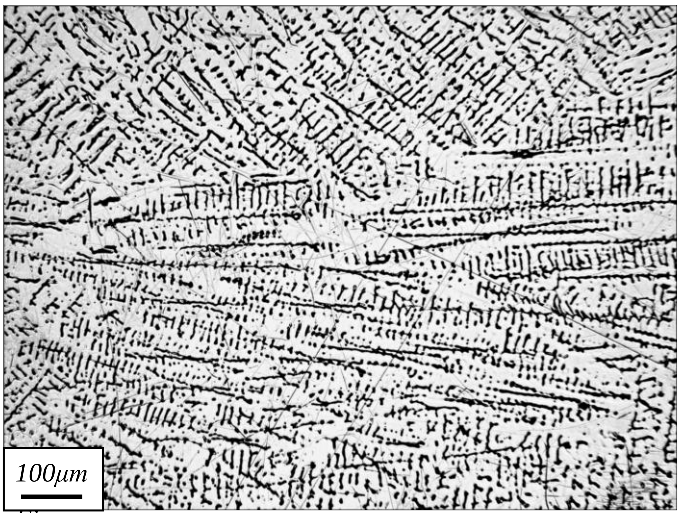

Figure 3.1: Optical micrograph of the microstructure of as-cast 304 austenitic stainless steel

Duplex stainless steels do not have a grain structure resembling that of austenitic grades. Instead they have a mixed structure consisting of approximately 50:50 austenite : ferrite. Due to this difference in microstructure appearance, the linear intercept method was not appropriate and due to the variation in shape and size of the austenite islands, numerical methods which provide equivalent circular diameter were also not applicable. Figure 3.2a) and b) are optical micrographs of the microstructures of S32101 and S32205 respectively. The microstructure of these two duplex stainless steel grades can be described as a matrix of ferrite with islands of austenite. When etched, the S32101 material tends to reveal only the phase boundaries with the austenitic region being the islands. In the S32205 material, the ferrite phase etch response is such that it remains bright and the austenite phase has a dark etch response.

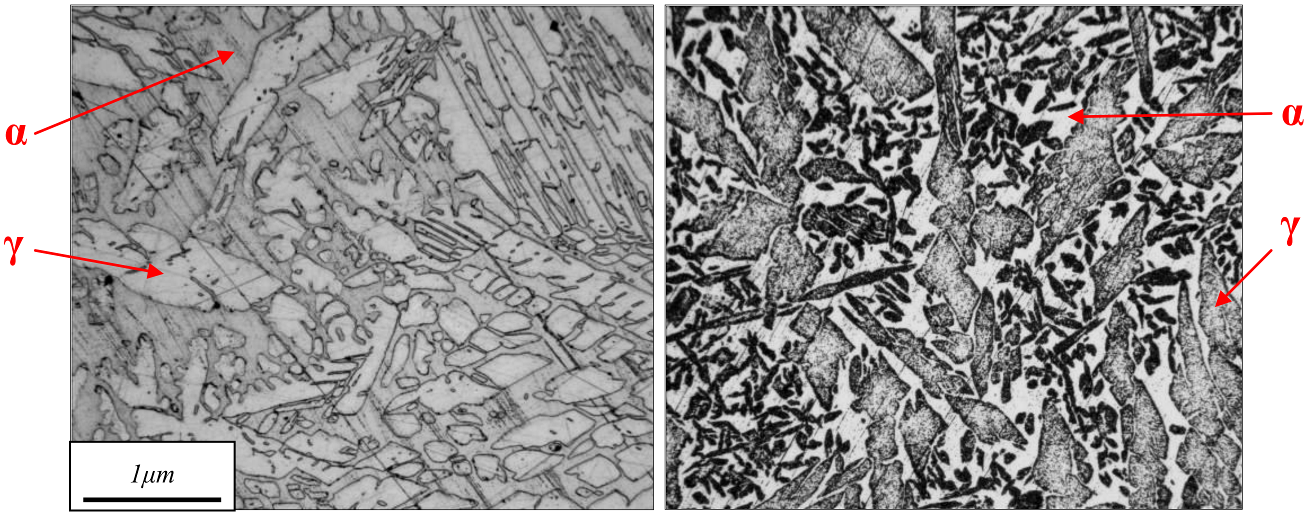

Figure 3.2: Optical micrographs of the microstructure of a) S32101 and b) S32205 duplex stainless steel with labels showing the austenite(γ) and ferrite(α) regions

As duplex stainless steel is a dual phase structure, each of the phases has a different composition. For example, the austenite phase will contain more of the austenite formers: nickel, manganese and molybdenum and the ferrite phase will contain more of the ferrite stabilisers: iron, chromium and carbon. The levels of these elements were measured in S32101 by taking the average of a number of area EDS measurements in the FEGSEM, to give the results shown in Table 3.2.

Table 3.2: Compositions of the Phases in S32101 Stainless Steel (Wt %)

	Cr	Ni	Mn	Si	Fe	Others
Austenite	21.6	1.4	5.0	0.8	70.6	C, Mo, N
Ferrite	23.1	1.1	4.6	1.0	71.1	C, Mo, N

3.4 Oxidation of Samples

3.4.1 Pre- oxidation Preparation

Samples were cut from as-cast billet or slab for 304 and 316L respectively or industrially ground slab specimens of S32101 and S32205. The samples were cut using a precision cutting machine to the dimensions of 10 x 4.5 x 4.5 (±0.5) mm. Before surface preparation, or oxidation if no surface modification was to be applied, a saw cut to a depth of approximately 1mm was made into one of the long faces (Figure 3.3). This allowed for the identification of the prepared face in the post oxidation examination stage. The face that was opposite to the saw cut was metallographically prepared using silicon carbide paper and diamond polish (if applicable) to the desired surface finish. After preparation, the samples were cleaned and finally rinsed with methanol.

A number of oxidation experiments have also been carried out in a small-scale propane-fired reheat furnace located at the Avesta Research Centre (ARC), Sweden (from this point referred to as the reheat furnace). These experiments were conducted using industrially ground (hot ground for S32101 and cold ground S32205) slab specimens measuring 120 x 75 x 30mm. Before oxidation, the slabs were cleaned using a mild abrasive to remove contaminants from the grinding marks and finally rinsed using acetone.

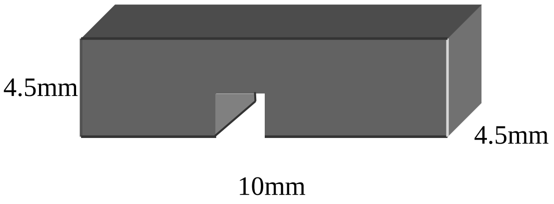

Figure 3.3: Dimensions of the cut bar of stainless steel showing the saw cut for oxidised face determination

3.4.2 Oxidation in Laboratory Air

For experiments in laboratory air box furnaces, the prepared samples were placed onto a ceramic “boat” with the prepared side facing upwards. The number of samples on the boats varied with no more than 4 on a single boat and a minimum separation of 10 mm. In any given heat treatment a maximum number of 8 samples were placed into the furnace. If 1 boat was used, it was placed into the centre of the furnace, whereas if two were inserted they were positioned with a minimum spacing of 50 mm. After oxidation, samples were simply removed from the furnace and allowed to cool to room temperature in air. This is the method which was used for the majority of the exploratory experiments carried out using the austenitic grades (304 and 316L).

3.4.3 Oxidation in the Reheat Furnace at ARC

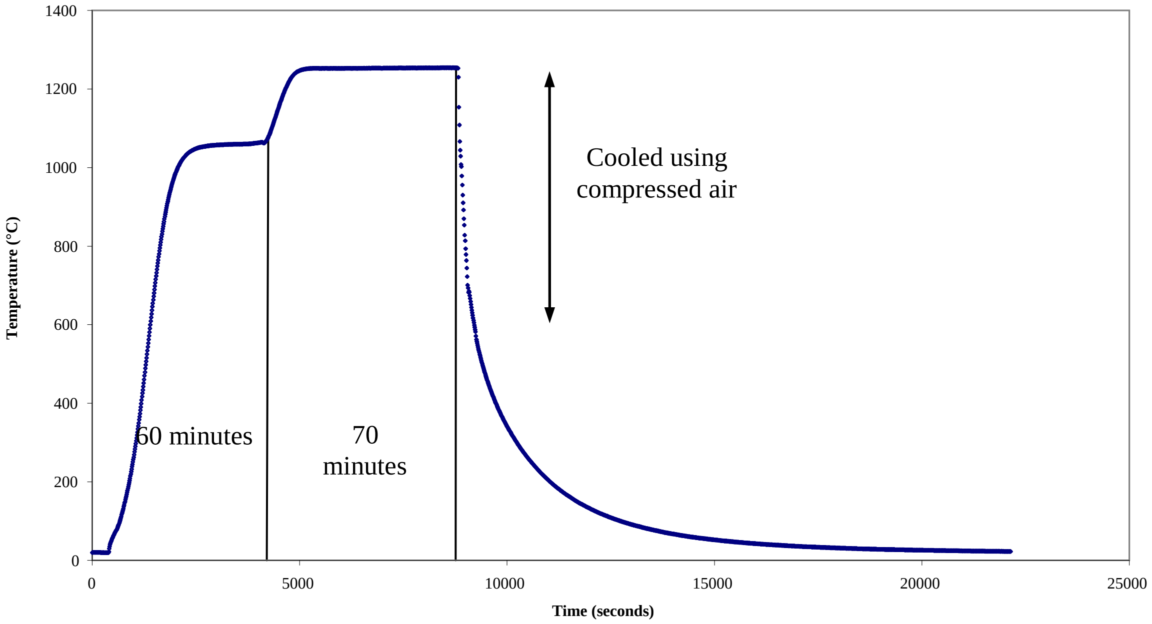

Figure 3.4: Temperature of the sample during oxidation in the Avesta Furnace

Prepared samples were placed into a cold furnace and then heated to 1050°C and held at that temperature for a total time of 60 minutes followed by a short heat to 1220°C or 1250°C together with a dwell totalling 70 minutes. Sample temperature was recorded by the use of a thermocouple attached to a reference piece of austenitic stainless steel. The heating profile of the reference block is shown in Figure 3.4. After oxidation, samples were removed from the furnace. Due to the samples' large thermal masses they were cooled using a compressed air gun until a temperature of ~600°C was reached. This was in order to prevent the materials oxidising any further than expected. It is necessary to note that the oxidation atmosphere experienced during these experiments was the product of this combustion.

Although this furnace is not completely representative of real reheat furnaces, members of the Outokumpu Stainless Avesta Research Centre have designed it to be as representative as possible of real reheat procedures.

3.4.4 Oxidation in Simulated Propane Combustion Products

During Industrial reheat, samples are heated in a large propane fired walking beam furnace. Therefore, although experiments carried out in laboratory air are useful, they cannot be said to be completely representative of the industrial reheat procedure. To overcome this, experiments have been carried out in a tube furnace with flowing simulated propane combustion products.

Due to the difficulties associated with collecting data from inside an industrial reheat furnace, a sample of exhaust gas was collected from inside the flue of an industrial reheat furnace and analysed by Outokumpu Stainless the results of which indicated a 2 – 6 % excess oxygen and a quantity of hydrocarbon (presumably propane which is the fuel for the reheat furnace) [McNee and Dulieu (2005)]

Using this data and the combustion of hydrocarbon equation [Heywood (1988)] it is possible to calculate an approximate combustion atmosphere inside the reheat furnace.

$$C_nH_m + \lambda\left(n+\frac{m}{4}\right)\left[O_2 + \frac{79}{21}N_2\right] \rightarrow aCO_2 + bH_2O + cN_2 + dO_2$$ -------------------------Eqn. 3.1

where

λ = Air to Fuel Ratio

$$a = n$$

$$b = \frac{m}{2}$$

$$c = \lambda\frac{79}{21}\left(n+\frac{m}{4}\right)$$

$$d = (\lambda - 1)\left(n+\frac{m}{4}\right)$$

So for propane in air:

5% excess (from data) ➔ ~15% excess air

λ = 1.15

$$C_3H_8 + 1.15\left(3+\frac{8}{4}\right)\left[O_2 + \frac{79}{21}N_2\right] \rightarrow 3CO_2 + 4H_2O + 21.63N_2 + 0.75O_2$$

From the above gas formula it is possible to determine the wt.% of the constituent gases which you would expect to find within the reheat furnace.

Table 3.2: Composition of the Reheat Furnace Atmosphere

	CO_2	H_2O	N_2	O_2
Moles	3.000	4.000	21.630	0.750
Atomic weight	44.009	18.014	28.014	31.998
	132.027	72.056	605.943	23.999
Wt.%	15.830	8.639	72.653	2.877

So the approximate reheat furnace atmosphere is calculated to be :

3 wt.% oxygen, 72 wt.% nitrogen, 9 wt.% water and 16 wt.% carbon dioxide

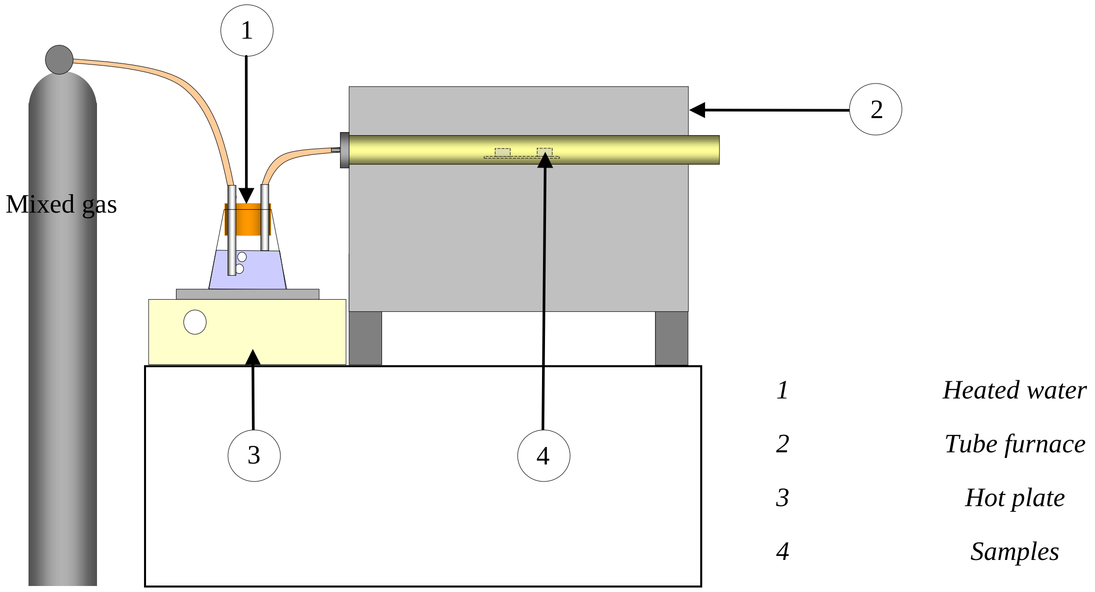

Figure 3.5: Schematic diagram showing the furnace apparatus

This atmosphere was produced by the use of a pre-mixed gas bottle containing oxygen, nitrogen and carbon dioxide to the stated wt.%. The gas was passed through a water bath heated to 55°C by a computer controlled hot plate. The flow rate of the gas was approximately 1 litre per minute (Figure 3.5). This produces a gas containing approximately 15 % water vapour of which some will condense in the feed tube. This gas is then fed into a non-porous furnace tube with an internal diameter of 25 mm which produces an average flow speed of 0.5 meters per minute (or 0.0083 m s^{-1}) through the furnace tube. Results obtained from this simulation were compared to results obtained from the Avesta Reheat furnace and were in good agreement (Appendix 3). Samples were placed onto an alumina boat with a spacing of 10 mm with their prepared surfaces positioned longitudinally to the flow of the gas.

3.4.5 In-situ Environmental SEM oxidation

In order to observe the differences in oxidation between the austenitic and ferritic regions of duplex grades during heat treatment, an environmental SEM (ESEM), with hot stage attachment was used. The instrument for this experiment was a Philips XL-30 FEG ESEM. The sample for this study was a 3mm diameter disk with a thickness of 1mm. A reference surface with a finish of 1µm was chosen to allow observation of an oxidising surface without the added complication of surface working. The sample was prepared using conventional metallographic grinding techniques on successively finer grades of silicon carbide paper followed by polishing routines using 9, 3 and 1 µm diamond polishing compounds. The atmosphere used was low pressure laboratory air at 266 Pa.

A schematic diagram of the heating routine applied is shown in Figure 3.6. All heating segments were carried out at a target heating rate of 100 °C / minute. The sample was first heated to 700 °C and held for 8 minutes to test for stability at high temperature. The sample was then heated to 900 °C and held for a dwell time of 120 minutes before being allowed to cool.

After heat treatment and in-situ examination, the sample was mounted on an aluminium stub using conductive silver paint ready for examination using FEGSEM and for Transmission Electron Microscope (TEM) sample extraction in a Focused Ion Beam SEM (FIBSEM).

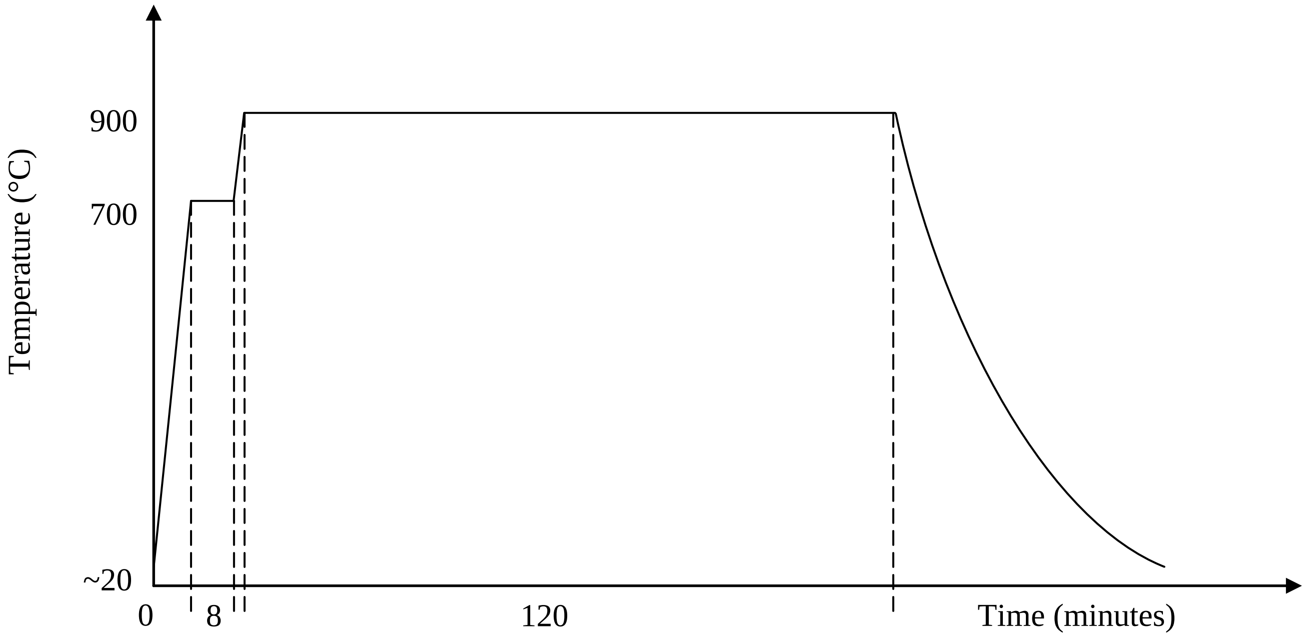

Figure 3.6: Schematic of the heat treatment applied to a sample oxidised in an ESEM

3.4.6 Post Oxidation Preparation

After oxidation and removal from the furnace, the samples were visually inspected. The samples’ prepared faces were examined using scanning electron microscopy (SEM) and any which had large features were mounted in electrically conductive Bakelite suitable for use in a SEM to produce a cross section. The mounted samples were ground to approximately the centre of the sample using 80 grit silicon carbide paper. The samples were metallographically prepared by grinding on progressively finer grades finishing on 2400 grit. The final procedure consisted of polishing using 9, 3 then 1 µm diamond solution. It is important to note at this point that the preparation of the sample is not only for the metal but, more importantly, the ceramic oxide scales. These tend to be much more delicate and require longer grinding at each stage of the preparation procedure [Birks and Meier, (1983)]. For Electron BackScatter Diffraction (EBSD), further preparation was required (see section 3.7).

3.5 Optical microscopy

The samples, prepared as described in Section 3.4.6, were examined using a Reichert MEF-3 optical microscope with a 10 mega pixel digital camera attachment and Qimaging QCapture image capturing software.

3.6 Scanning Electron Microscopy (SEM)

The SEM used to examine samples was a Leo 1530 VP field emission gun (FEG) SEM with an EDAX Pegasus EDS system and a TSL EBSD attachment. The working distances, operating voltages, apertures and currents were varied to give optimum conditions for imaging and EBSD. Examination was carried out using secondary electron imaging (with both a conventional secondary electron detector and an Inlens detector) and back scattered electron imaging. Typical working distances were 4mm, 5mm and 16mm for Inlens secondary electron imaging, backscattered electron and conventional secondary electron imaging respectively.

3.7 Electron Back Scatter Diffraction (EBSD)

Samples prepared as described in Section 3.4.6 were suitable for imaging in the SEM. For EBSD, however, further preparation is required. It is very important that any surface scratches are removed. If they are not, then the diffraction patterns can appear very faint or may even not be visible at all. Preparation of EBSD samples was carried out in the same way as preparation described in Section 3.4.6 with the additional step of 20 - 30 minutes of polishing using a colloidal silica solution.

The software used for collection and manipulation of the EBSD data obtained was the OIM 4.5 analysis package (OIM, EDAX UK, Cambridge, UK). This software enables the use of the data collected via energy dispersive x-ray spectroscopy (EDS) to be used as a filter to aid in phase identification. This is particularly useful when dealing with spinel phases that have almost identical crystal structure but very different chemical composition.

3.8 The Use of Focused Ion Beam Scanning Electron Microscopy (FIBSEM)

A FIBSEM is a system which consists of both a conventional field emission gun SEM and an ion source. Due to the instrument having both of these sources it is commonly referred to as a dual beam FIB. An FEI Nova Nanolab 600 dual beam FIBSEM system was used in order to produce site-specific cross sections and TEM thin foils of features in oxide scales. The main advantages of using this technique as opposed to conventional techniques are: site-specificity, a reduction in mechanical damage and speed of specimen production. There are, however, some disadvantages also such as ion induced damage.

3.8.1 Cross-Section Preparation

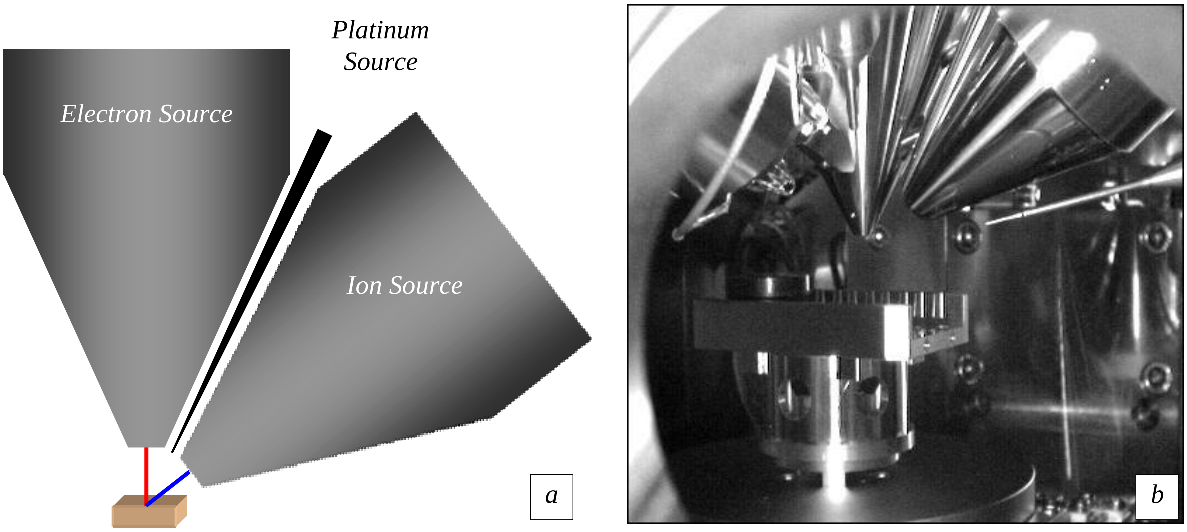

Figure 3.7: a) Schematic diagram of the focussed ion beam and b) photograph of the FEI Nanolab 600 FIB chamber

Cross sections are prepared in the FIBSEM by first selecting the area of interest using conventional SEM. The sample is then tilted to 52° to make its surface perpendicular to the ion source (Figure 3.7). Rough milling is then carried out with the ion beam current set at 3 nA. This rough cross-section is then polished by the use of a lower current (0.5 nA) ion beam. The finished polished cross-section can then be viewed using either the ion or electron beams. For cross-sectional cut throughs, this process is repeated with each cross-section being imaged so that a successive cross-section can be produced.

3.8.2 Transmission Electron Microscopy Sample Production

TEM sample preparation was carried out in a similar method as cross-sections. Rough milling is carried out from either side of the feature of interest. The remaining part of the feature was then polished on either side using the lower current probe (0.5nA). After the polishing procedure, the TEM sample was cut from the bulk of the sample by milling small boxes either side and on the lower edge. The TEM sample was then extracted using a micro manipulator and attached, using deposited platinum, onto a TEM grid (Figure 3.8).

3.8.3 Transmission Electron Microscopy (TEM)

The TEM used to examine samples depended on the results required. For standard examination, a Jeol 200FX was used with an accelerating voltage of 200keV used for all images. This machine was equipped with an Oxford Inca EDS analysis system. For EDS mapping and lower resolution imaging the Nova Nanolab's STEM attachment was used. This instrument used an EDAX Genesis EDS system and operated at a typical accelerating voltage of 30keV. For high resolution imaging and further EDS mapping an FEI Tecnai F20 FEGSTEM was used with an accelerating voltage of 200keV.

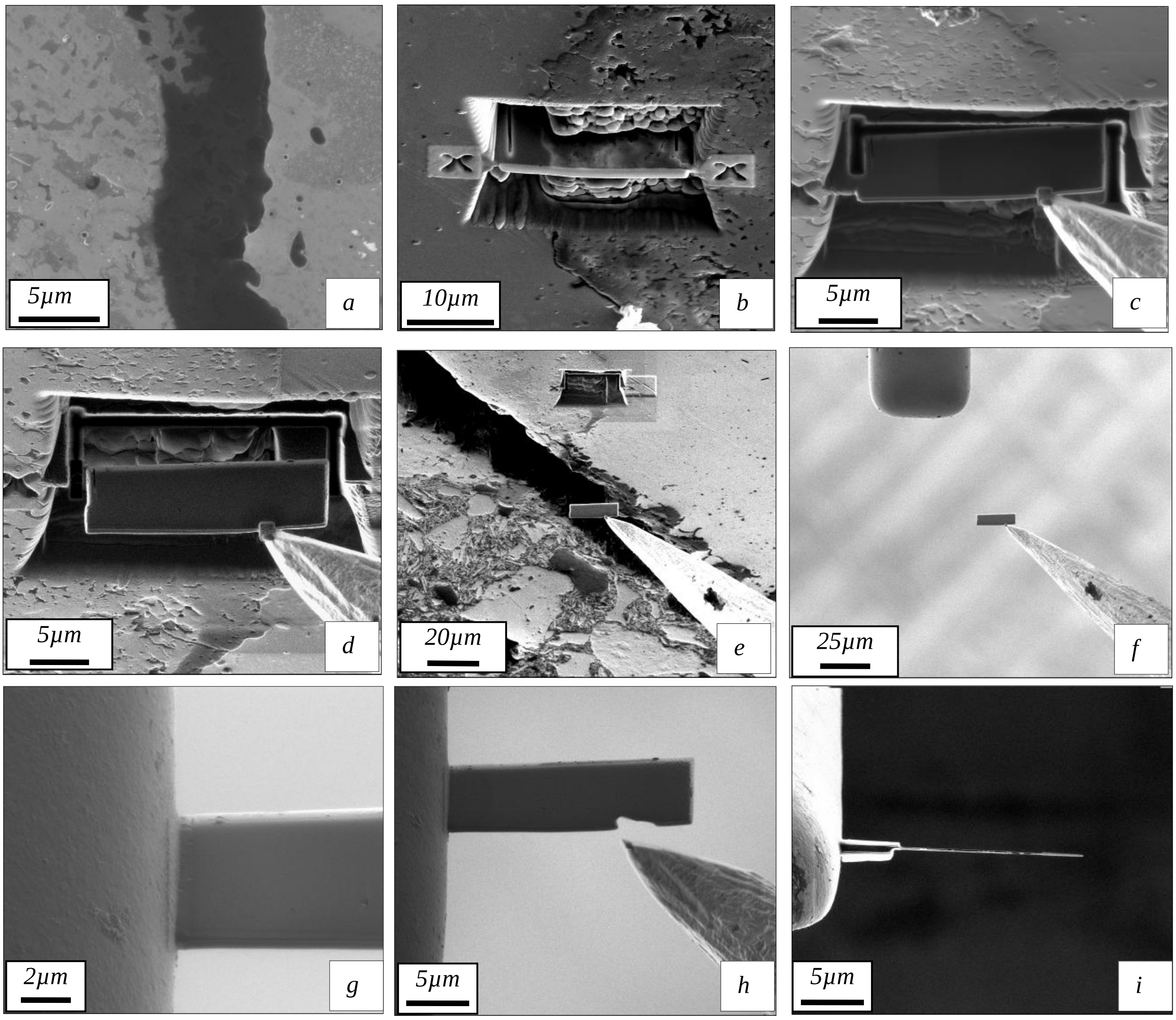

Figure 3.8: TEM sample preparation using FIBSEM. a) area of interest imaged using ion beam, b) Rough milled TEM sample, c) Micro-manipulator welded to the TEM sample ready for lift-out, d) Lift-out, e) Lift-out, f) Micro-manipulator with attached sample approaching TEM copper grid, g) Sample soldered to the copper grid, h) Micro-manipulator removal from sample, i) Final thinned TEM sample

4 OXIDE FORMATION – AUSTENITIC GRADES AMBIENT AIR

4.1 Introduction

As austenitic stainless steels are amongst some of the most globally produced stainless steels [Lula, (1986)], a large body of work presented in this thesis has been carried out on Types 304 and 316L stainless steels. As these grades are generally produced on a large scale, production costs are kept to a minimum. This means that processing steps such as grinding of the as-cast oxide scale, which is applied to some other grades, is not carried out. As a result, austenitic grades are usually reheated with an as-cast oxide still present on their surface. This as-cast oxide can complicate the study of reheat scales as they have a high degree of local variation. Due to this complication, the majority of the work has been carried out on surfaces finished to a ground surface of 80 grit with a number of trials also conducted using surfaces with an as-cast oxide still intact.

During the preliminary stages of this work, oxidation was carried out in standard ambient air box furnaces in order to obtain an overview of the oxide scales formed at usual reheat temperatures whilst negating the effects of combustion product atmospheres. This section will display results obtained from optical microscopy, SEM, EDS and EBSD studies of oxide scales formed on 304 and 316L stainless steels in this atmosphere at temperatures of 1000 °C and above for times of 1 - 5 hours.

Results within this thesis show examples of internal and external oxidation so it is necessary to define the term internal oxidation. “Internal oxidation is a process in which oxygen diffuses into an alloy and causes sub-surface precipitation of the oxides of one or more alloying elements” [Birks and Meier (2006)]. The oxide particles which are formed then grow to form an internally oxidised zone beneath the metal’s surface. Internal oxidation is difficult to interpret as, without appropriate marker studies, the position of the original metal’s surface is impossible to locate once an oxide scale has formed. In this thesis, the phrase “internal oxide” has been limited to circumstances where oxide is found within a recognisable metallic matrix or where metallic inclusions are a feature of the oxide. These circumstances include: oxide roots, oxide particles, crater regions of oxide nodule and oxides which have substantial inclusions of metallic particles within them. In all other situations, the oxide has been assumed to be an external oxide.

4.2 316L Stainless Steel

4.2.1 Oxidation at 1000°C

Figure 4.1 is a backscattered electron micrograph of a scale formed on 316L stainless steel after 1 hour at 1000 ˚C. A very thin scale can be seen which measures between 3 and 7 µm in thickness. The oxide is very disordered and damaged which has probably occurred during cooling. There are some root-like structures towards the bottom of the scale. At higher magnification it can be seen that cracks run from the surface of the oxide through to the substrate. The oxide roots extend to a depth of ~6 µm into the substrate. Unlike images of oxides at higher temperatures, this oxide is of one contrast which suggests that it is of a single phase.

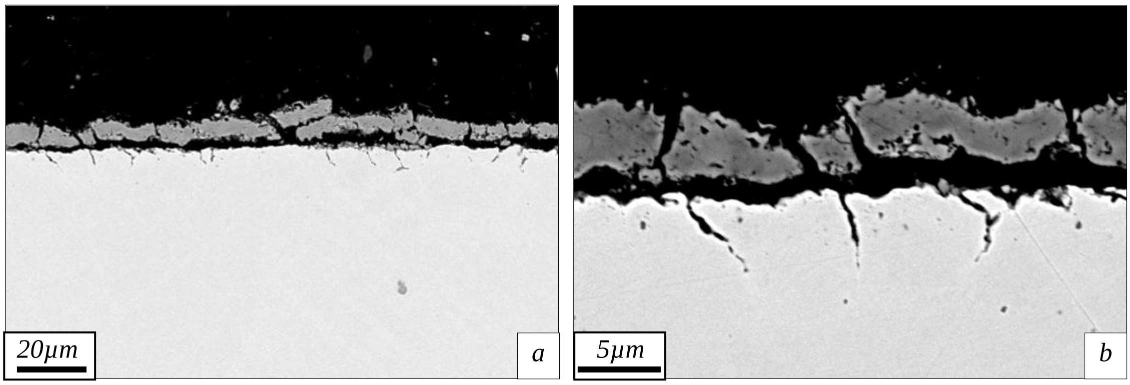

Figure 4.1: Backscatter electron micrograph of a) an oxide scale formed on 316L stainless steel after 1 hour at 1000˚C and b) at higher magnification

After oxidation at 1000˚C for 2 hours, the oxide shown in Figure 4.2 is produced. It can be seen from this image that the oxide scale is still relatively thin but unlike the oxide produced after 1hour at 1000°C, it does show 2 layers of oxide. The upper layer is of a brighter contrast and the lower layer is darker. The oxide roots structures seen in this image are similar in severity to that seen after oxidation for 1 hour at the same temperature and extend to a depth of approximately 5 µm and are fibrous in nature.

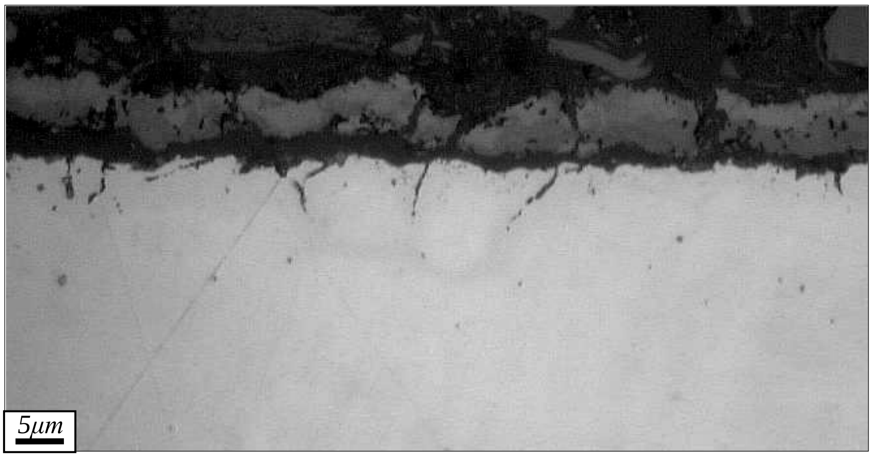

Figure 4.2: Optical microscopy image of an oxide scale formed on type 316L stainless steel after 2 hours at 1000˚C

Figure 4.3 shows a scale formed on 316L stainless steel after 3 hours at 1000°C. After three hours the scale is quite thin at ~15µm. Sub-surface oxidation extends to a depth of approximately 10µm and consists of both a fibrous root type structure and an internal oxide layer. The maximum depth of penetration of the sub-surface oxidation is ~20µm. There are two different layers; the lower layer is a lighter shade and the upper layer is the darker layer in Figure 4.3(b).

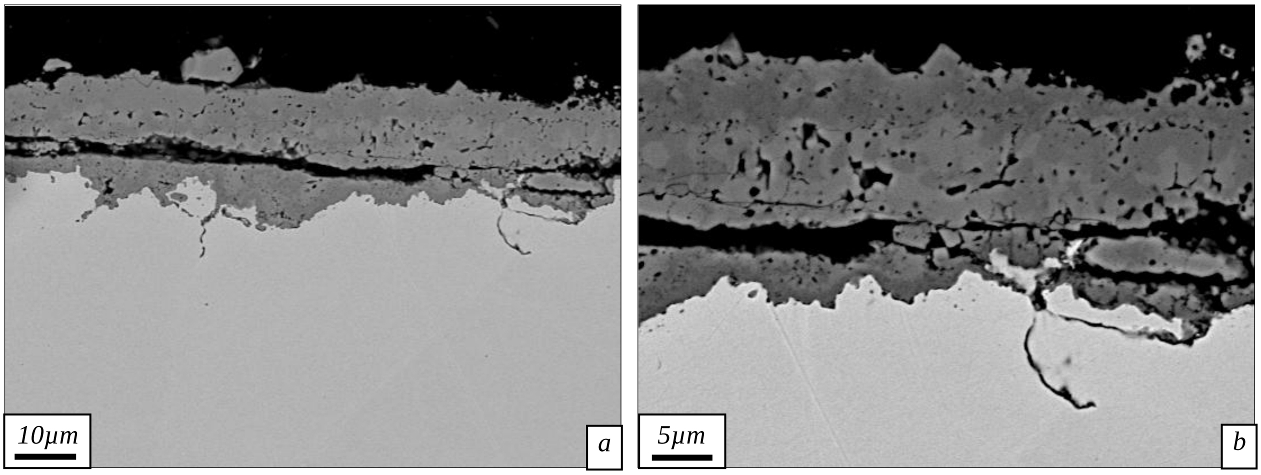

Figure 4.3: Backscatter electron micrograph of a) an oxide scale formed on 316L stainless steel after 3 hours at 1000˚C and b) at higher magnification

Figure 4.4 shows results of an EBSD scan of an area of oxide formed in the same conditions to that shown in Figure 4.3. The image quality map shows that the oxide microstructure consists of a fine-grained layer towards the metal – oxide interface and a coarser grained region towards the upper edge of the oxide with another fine grained layer at the outer extremity of the oxide scale. The simultaneously collected EDS maps show that the layers can also be distinguished by differences in chemistry. The coarse grained oxide is iron rich with very little of any other metallic element within it. The fine-grained regions, however, are enriched with chromium. The nickel map shows that there is no nickel present within the outer oxide. It does, however, show that there is a substantial nickel enrichment of the underlying substrate. This is shown to be true to a depth of ~5µm to the left of the image (i) and to a depth of ~15µm in between the two oxide roots (ii). As well as this enrichment of nickel it can also be seen that the substrate is also depleted in chromium. The region surrounding the grain boundary in the centre of the oxide has undergone the same nickel enrichment / chromium depletion as the upper part of the substrate (iii).

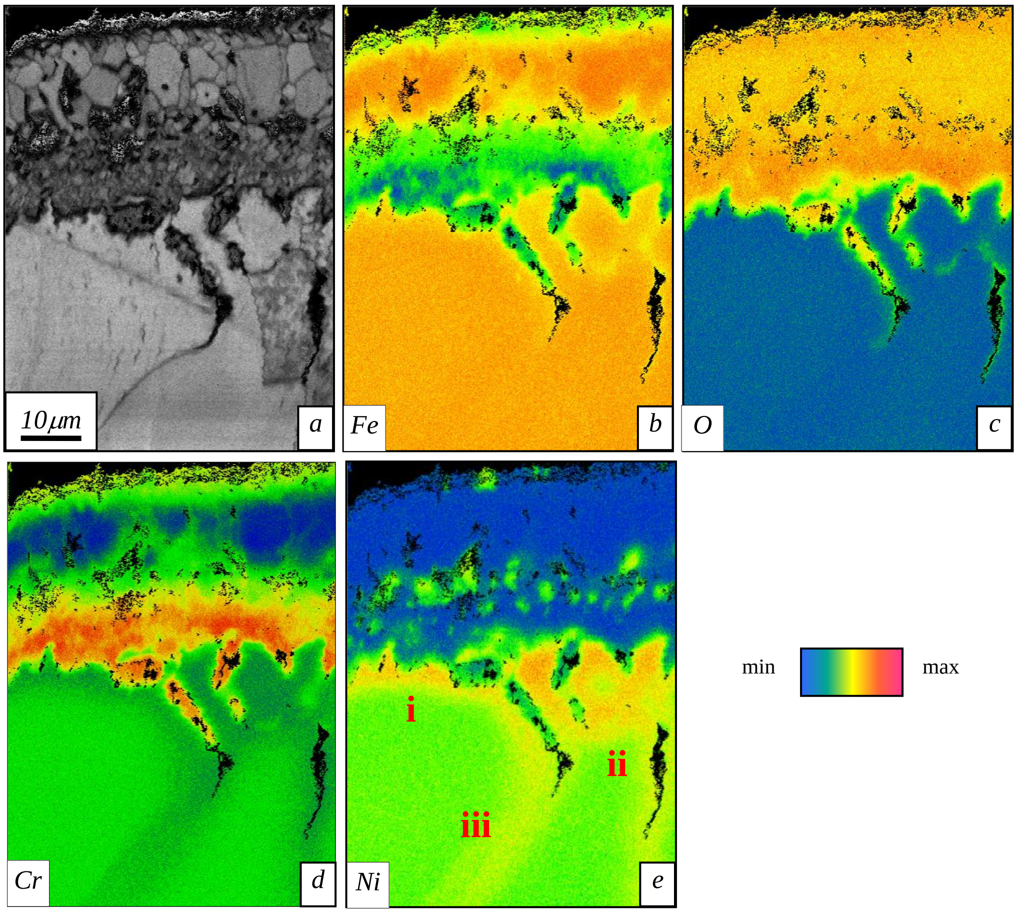

Figure 4.4: a) EBSD image quality map with simultaneously collected EDS maps of b) iron, c) oxygen, d) chromium and e) nickel of an oxide scaled formed on 316L stainless steel after 3 hours at 1000°C labelled with (i), (ii) and (iii)showing areas of nickel enrichment

Figure 4.5 is an optical micrograph of a scale formed on 316L stainless steel after 3 hours at 1000˚C and then cooled at a rate of 10˚C per minute to room temperature. This cooling rate was chosen in an attempt to reduce spallation during cooling. Contrary to what is seen after oxidation and fast cooling, a three layer structure is very clear from this image. The lower edge shows a mixed phase layer which is shown by the different shades contained within the layer. This first layer in the scale is also reasonably porous. Some of the pores seen in this image may well be from polishing damage. This is very clear in the second layer, which is a darker shade, as it has many damaged areas within it. The final layer, which is a lighter shade, is less damaged than the middle layer although it does still show some porosity.

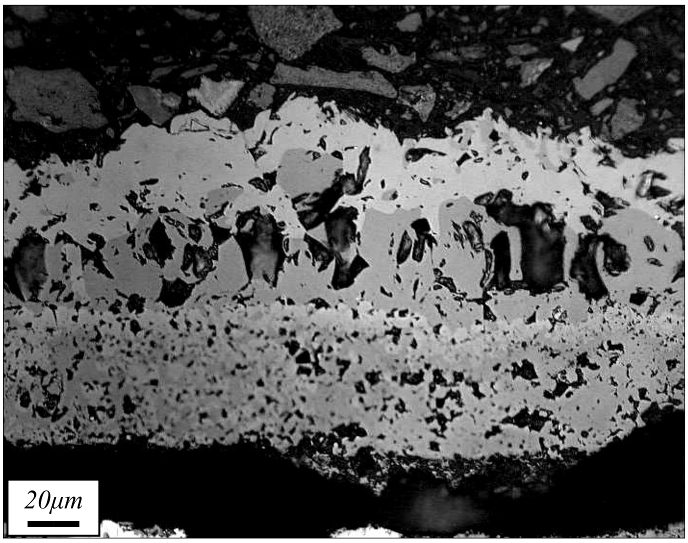

Figure 4.5: Optical microscopy image of an oxide scale formed on Type 316L stainless steel after 3 hours at 1000˚C and cooled at a rate of 10°C per minute to room temperature

4.2.2 Oxidation at 1200°C

As the reheating of austenitic stainless steels is usually carried out at temperatures in the range of 1200°C – 1300°C, it is important to understand what is expected at these temperatures. Due to the importance of oxidation at 1200°C, a large volume of results were obtained from experiments conducted at this temperature.

Figure 4.6 shows a scale grown on a 316L stainless steel substrate at 1200°C for 2 hours. The scale has a thickness of approximately 10 - 20μm and shows a low relative porosity or damage. There are some areas of sub-surface oxidation to a depth of approximately 5 - 10μm. There are two different phases within the scale. One has a lighter contrast (1) and the other is darker (2). In some areas of the scale the lighter phase extends from the top of the scale to the bottom of the scale. This would suggest that this scale is not multi-layer but rather mixed phase.

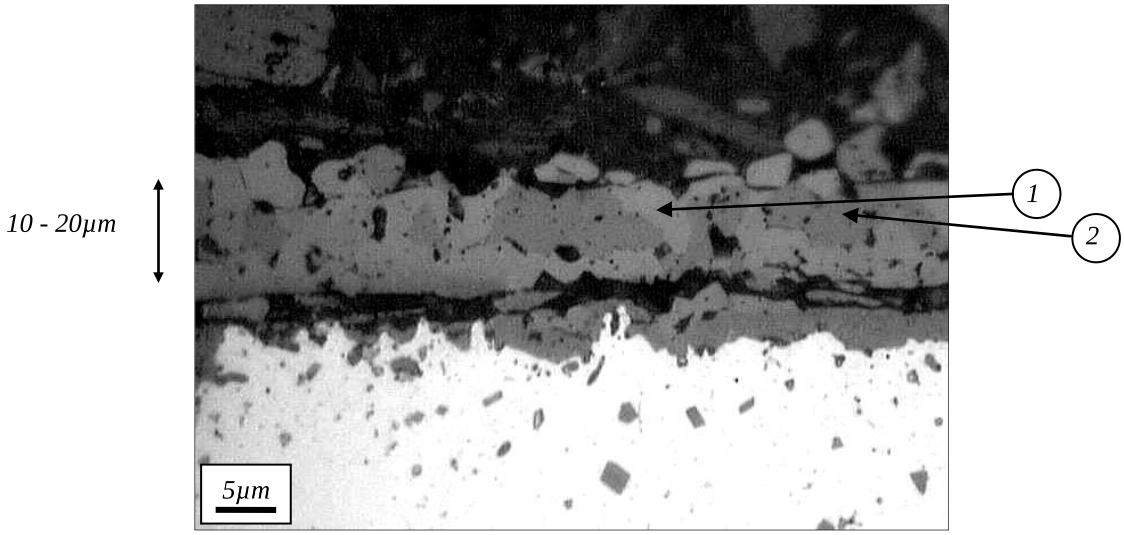

Figure 4.6: Optical microscopy image of a scale formed on type 316L stainless steel after 2 hours at 1200°C with (1) indicating a lighter contrast region and (2) indicating a darker contrast region

Figure 4.7 shows an EBSD image quality map of an additional area of a scale formed on 316L stainless steel after 2 hours at 1200˚C. As the oxide scale formed is not completely uniform, the oxide thickness is greater in this region. The grain structure is clearly shown and it can be seen that towards the bottom of the scale (closest to the substrate) the grain size is approximately 5 – 10µm. The top of the scale, however, shows a coarser grain structure with a grain size of approximately 15µm in length.

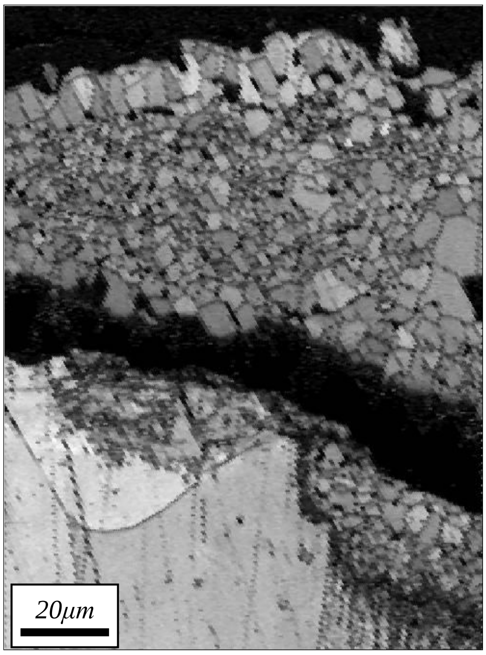

Figure 4.7: Electron backscatter diffraction (EBSD) image quality (IQ) map of an oxide scale formed on 316L stainless steel after 2 hours at 1200°C in air and cooled in air at room temperature

Figure 4.8 shows EDS maps of the oxide scale in Figure 4.7. The nickel map shows a scale which consists of at least two different types of oxide, one with a similar nickel content to the substrate metal (high nickel content) and one with a nickel content which is lower than the substrate metal (low nickel content). There is a region of oxidation to the right of the image (i) which is below the void and shows a mixed nickel content although the majority of the grains within it are lower in nickel than the surrounding metal. The metal shown in the image is enriched in nickel towards the scale – metal interface with the highest nickel content occurring around the metal - oxide interface to the right of the image (ii). The chromium map shows that the layer of larger grains at the top of the scale have a lower chromium content in relation to the substrate and the majority of the scale below this is higher than or equal in chromium content within the base metal. The substrate shows very little difference in chromium content towards the metal / scale interface apart from a thin very high chromium layer at the perimeter of the oxidation region seen at (iii). The iron map shows a graduation of iron towards the outer edge of the scale.

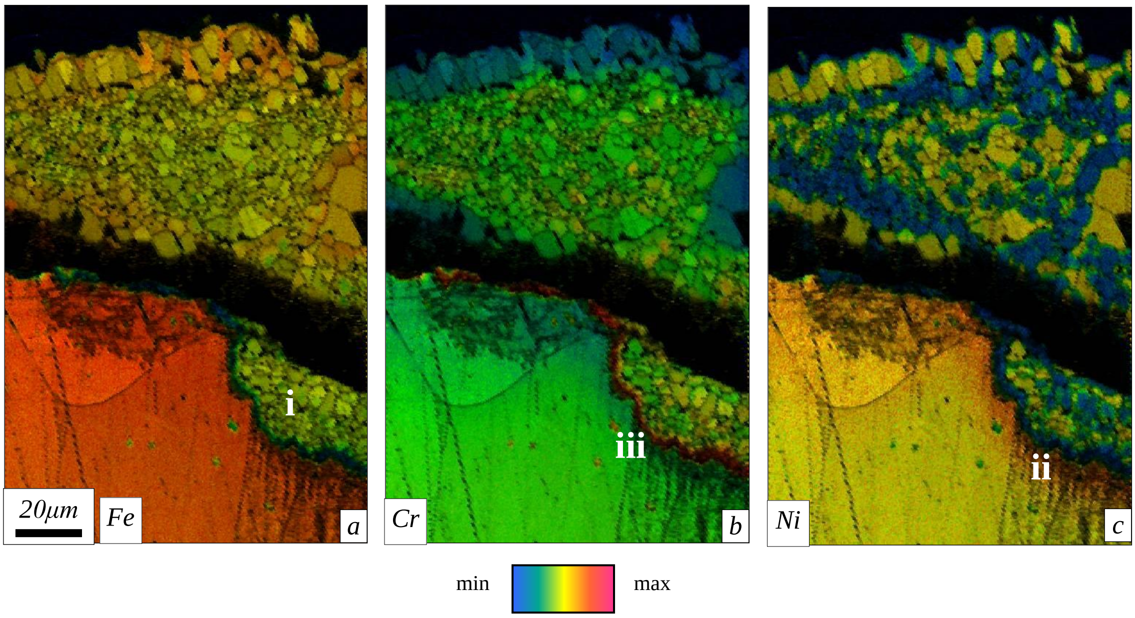

Figure 4.8: Image quality and energy dispersive x-ray spectroscopy (EDS) maps of a) iron, b) chromium and c) nickel in an oxide scale formed on 316L stainless steel after 2 hours at 1200°C in ambient air with labelled regions (i) oxide below the void, (ii) nickel enrichment at the metal – oxide interface and (iii) chromium rich oxide layer at metal / oxide interface

After oxidation for a further hour, the oxide shown in Figure 4.9 is produced. Three oxide layers are visible in this image: a bright layer (Layer 1), an intermediate darker layer (Layer 2) and a final layer which is a mixture of both the lighter and darker phases (Layer 3). The layer which is the darkest contrast in the image also shows the most porosity or damage. This suggests that it is the most brittle part of the scale. The mixed phase layer shows a lesser extent of porosity with the top lightest contrast layer showing very little porosity.

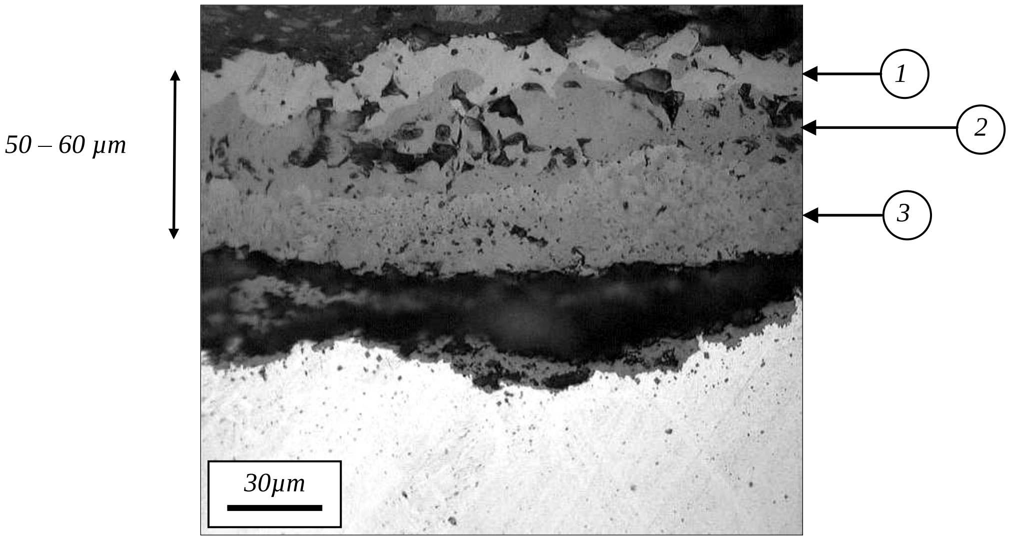

Figure 4.9: Optical microscopy image of a scale formed on type 316L stainless steel after 3 hours at 1200°C indicating (1) bright oxide layer, (2) intermediate darker layer and (3) fine-grained mixed contrast layer

Figure 4.10 gives semi - quantitative information obtained from a line scan through the scale. The line along which the EDS was taken is illustrated in Figure 4.10(b) by the dashed line through the image. The area on the chart without a plotted line is the gap between the substrate and the scale which can be seen in the micrograph. The results show that the iron content throughout the scale increases towards the outer edge where there is a maximum of approximately 70 at%. Chromium content changes significantly from the lower edge to the outer edge of the scale. It has a maximum value of just over 30 at% at the lower edge and decreases to approximately 20 at% at the top of the lower layer shown in the SEM image. It then decreases to a minimum value of approximately 1 – 2 at% at the outer edge of the scale. The oxygen trace remains fairly constant throughout the scale with the maximum value of approximately 35 at% being at the metal / scale interface, where the nickel trace shows the nickel content to be at a lower level than the majority of the scale which remains around 10 at% before decreasing to <1 at% at the outer edge of the scale. This decrease in nickel at the outer edge coincides with a dramatic increase in iron from just below 60 at% to just above 70 at%. The EDS from the top of the metallic substrate shows that the iron and nickel contents towards the metal / scale interface increase and the chromium content decreases slightly.

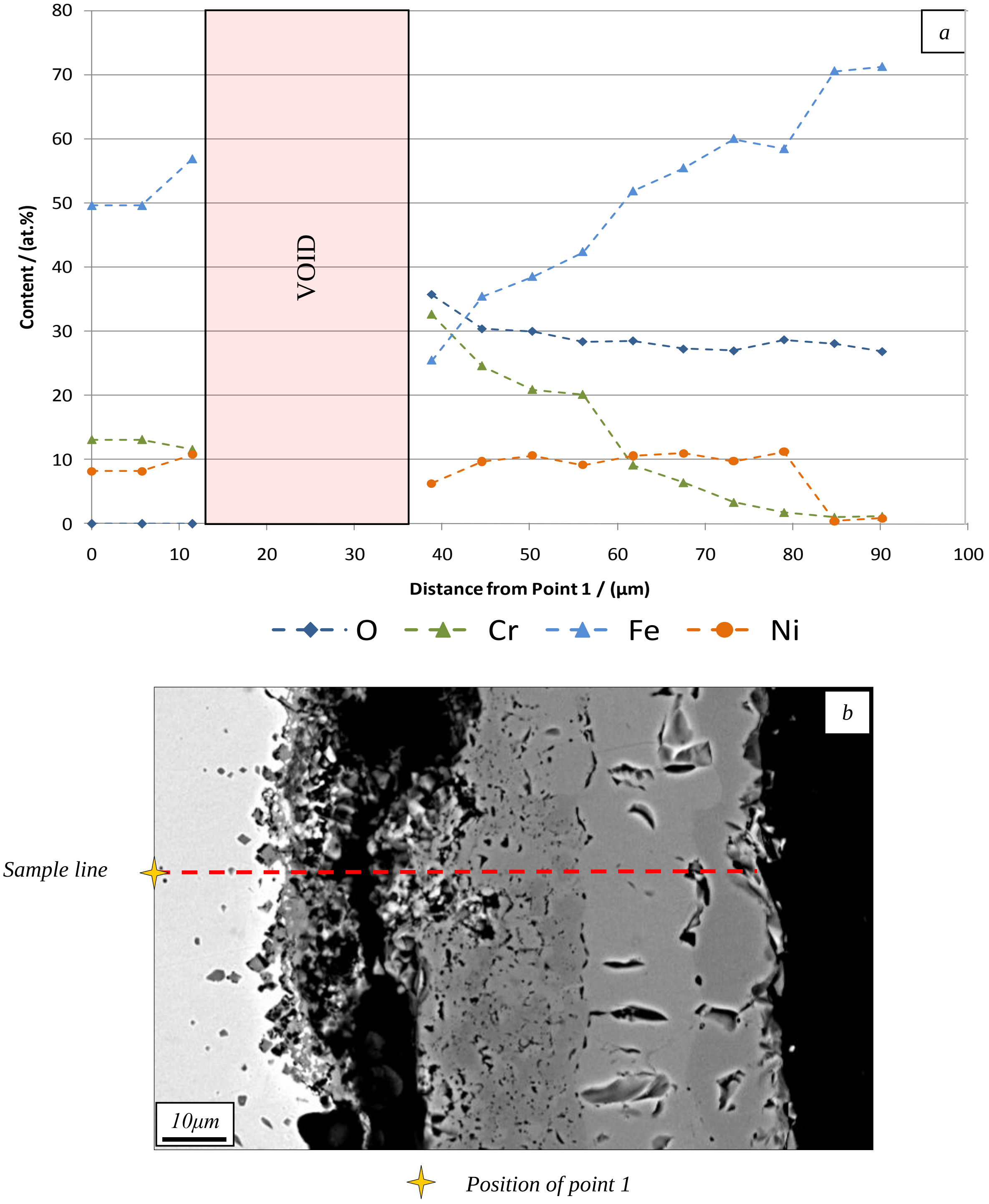

Figure 4.10: a) Elemental distribution through an oxide scale formed on 316L stainless steel after 3 hours at 1200°C and b) SEM micrograph of the area from which EDS was taken

In order to prevent scale spallation during cooling, a specimen was oxidised in the same oxidation conditions but was cooled at a slower rate. When oxidised for 3 hours at 1200°C and cooled at a rate of 10°C / minute, 316L produces the oxide shown in Figure 4.11. The oxide broadly consists of a ~350µm thick outer oxide scale with a deep internally oxidised region which penetrates to a maximum depth of ~250 µm. The particulate oxidation seen in this example is surrounded by a metallic matrix so can be referred to as internal oxide. The outer oxide scale consists of three distinct layers which can be distinguished by the contrast seen in the micrograph. EBSD / EDS maps of an equivalent area show that the internal oxide particles are low in iron and nickel and rich in chromium. The chromium map also shows that the lowest layer of external oxide is the only chromium rich layer in the external scale and that the metal which surrounds the oxide particles is depleted in chromium. The nickel map shows that the metallic regions are rich in nickel especially towards the scale / metal interface.

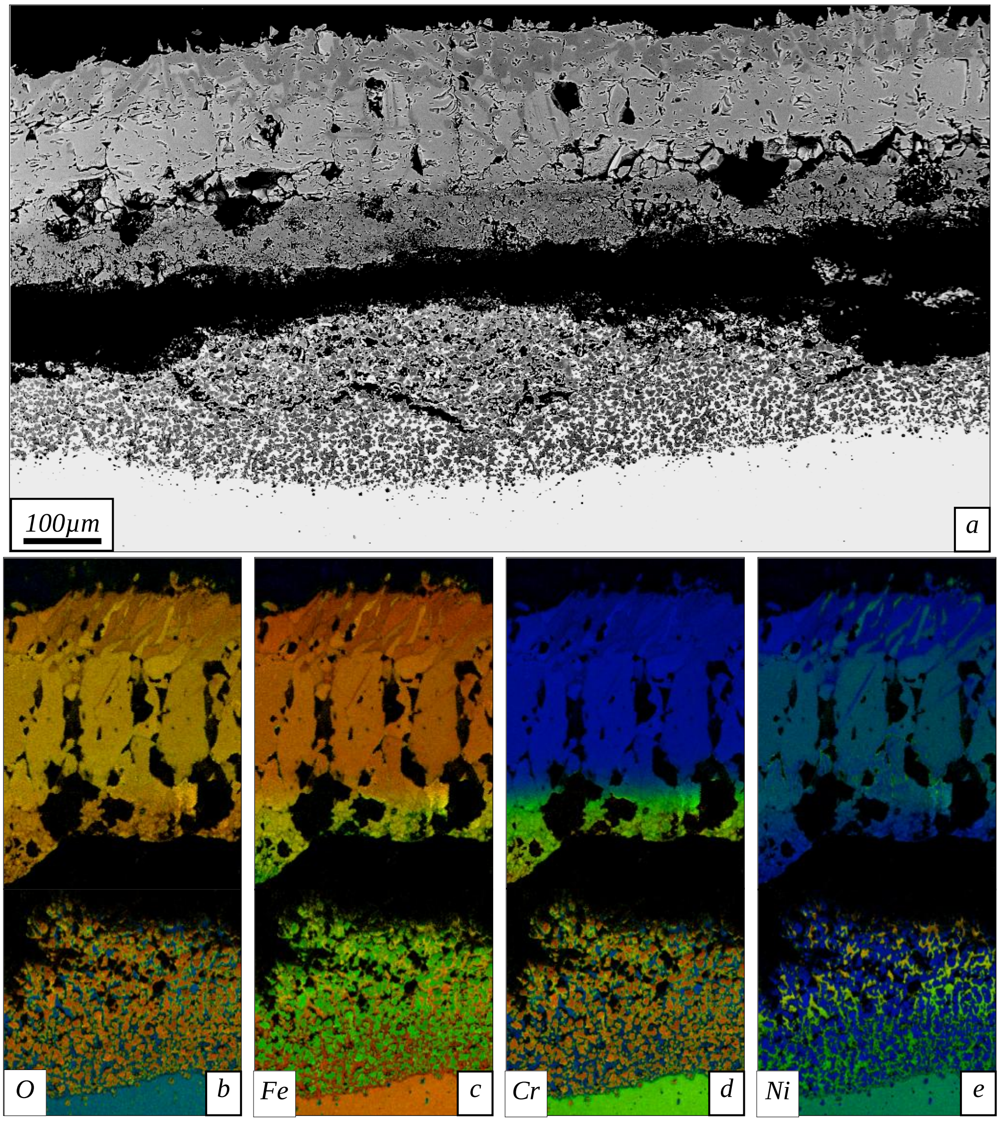

Figure 4.11: a) Backscattered electron micrograph with accompanying EBSD / EDS maps of b) oxygen, c) iron, d) chromium and e) nickel of an oxide formed on 316L stainless steel after 3 hours at 1200°C and a cooling rate of 10°C / minute

The sub-surface oxidation region is made up of oxide particles dispersed throughout the substrate with the occurrence of the oxide particles reducing with depth into the substrate. A higher magnification image of the oxide particles is shown in Figure 4.12(a). The oxide consists of small, isolated oxide particles contained within a metal matrix. It can be seen that as the depth of penetration increases, the occurrence of oxide particles decreases. The oxide particles measure 1 – 10 μm in diameter and are made up of a number of different regions. There are the lighter coloured areas (1) of which some are surrounded by an area of darker contrast (2) The lighter areas are spaced at random with areas of un-oxidised metal in between the oxidised areas. This figure clearly shows the slightly textured surface of the lower particles (3). Figure 4.12(b) is a high magnification image of an individual dendritic oxide particle. This example measures ~4-5μm across. The dendritic region is ~3μm and is made up of three individual dendritic arms measuring approximately 2μm in length and 500nm in width. The presence of these dendrites suggests that at some point during the oxidation process there was a molten phase within this internal oxidation region. The dark areas seen between the dendrites are probably voids in the structure.

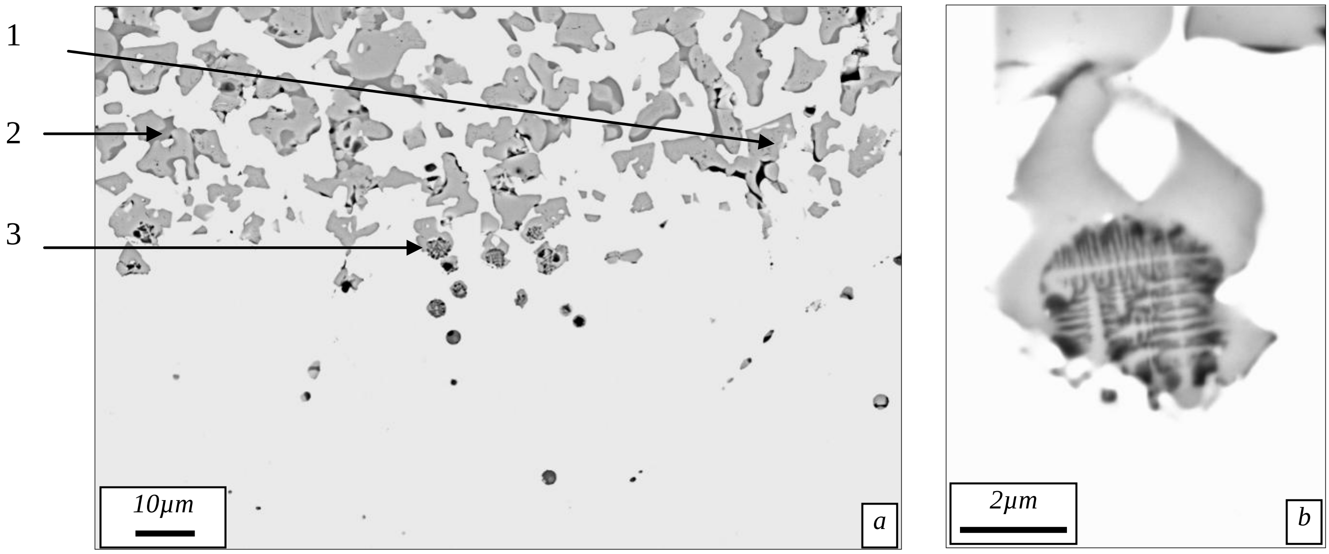

Figure 4.12: a+b) Backscatter electron micrographs of internal oxidation formed within 316L stainless steel after 3 hours at 1200˚C and cooled at a rate of 10˚C per minute to room temperature showing (1) non- dendritic oxide particle, (2) dark phase surrounding a particle and (3) a dendritic oxide particle

EDS maps of an equivalent area showing oxide particles are shown in Figure 4.13. It can be seen that the particles themselves are rich in chromium which has left the surrounding metal depleted in chromium. Nickel is absent from the composition of the particles whereas iron is present. The nickel map also shows that the substrate is slightly enriched towards the top part of the map which is closer to the scale – metal interface.

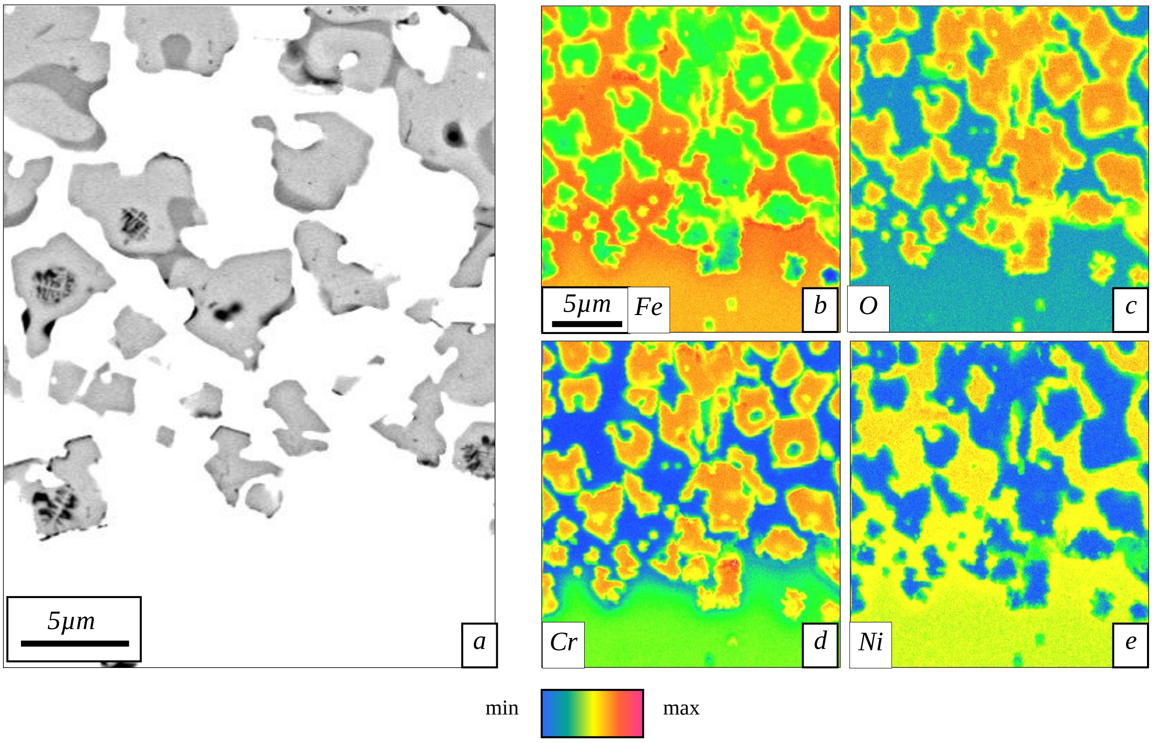

Figure 4.13:- a) backscattered electron image with accompanying EDS maps of b) iron, c) oxygen, d) chromium and e) nickel of internal oxidation of 316L stainless steel after 3 hours at 1200˚C and cooled at a rate of 10˚C per minute to room temperature

EDS of the individual dendritic particle in Figure 4.12(b) is shown in Figure 4.14. It revealed that the particles are rich in both chromium and oxygen and low in nickel and iron. This agrees with the result shown in Figure 4.13. The maximum or minimum values of all elements are shown to reach their peaks towards the centre of the particle.

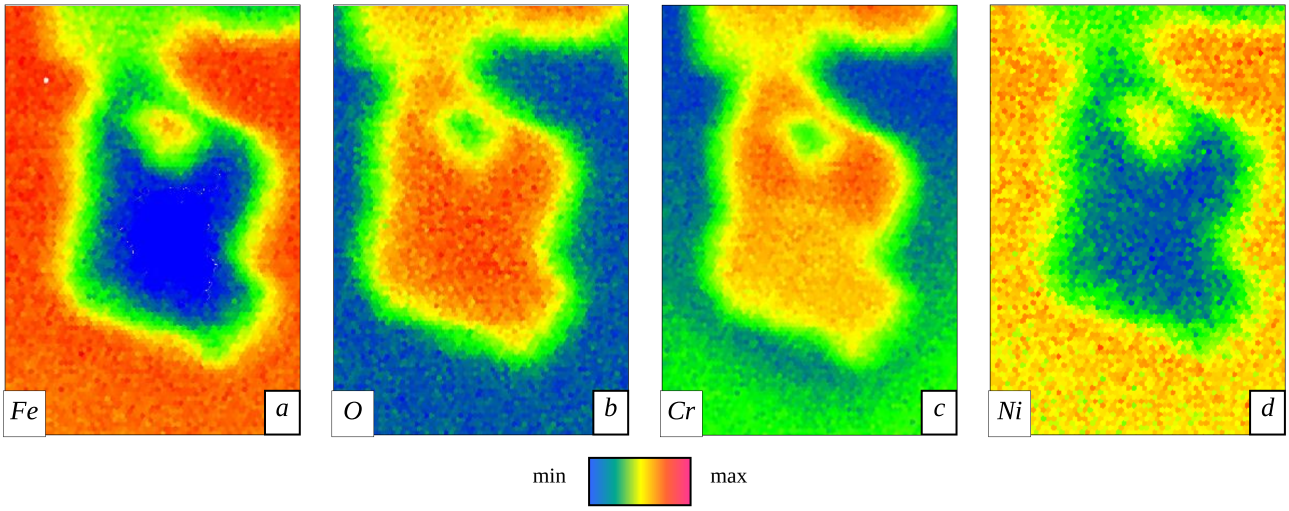

Figure 4.14:-EDS maps of a) iron, b) oxygen, c) chromium and d) nickel of a dendritic oxide particle shown in Figure 4.12 (b)

Figure 4.15 shows a backscattered electron image of an area of dendritic oxide particles with EDS spectra of a dendritic particle and a non-dendritic particle. It reveals that the dendritic regions have a large silicon peak as well as chromium, iron and oxygen. The non-dendritic particles, however, do not have a silicon peak.

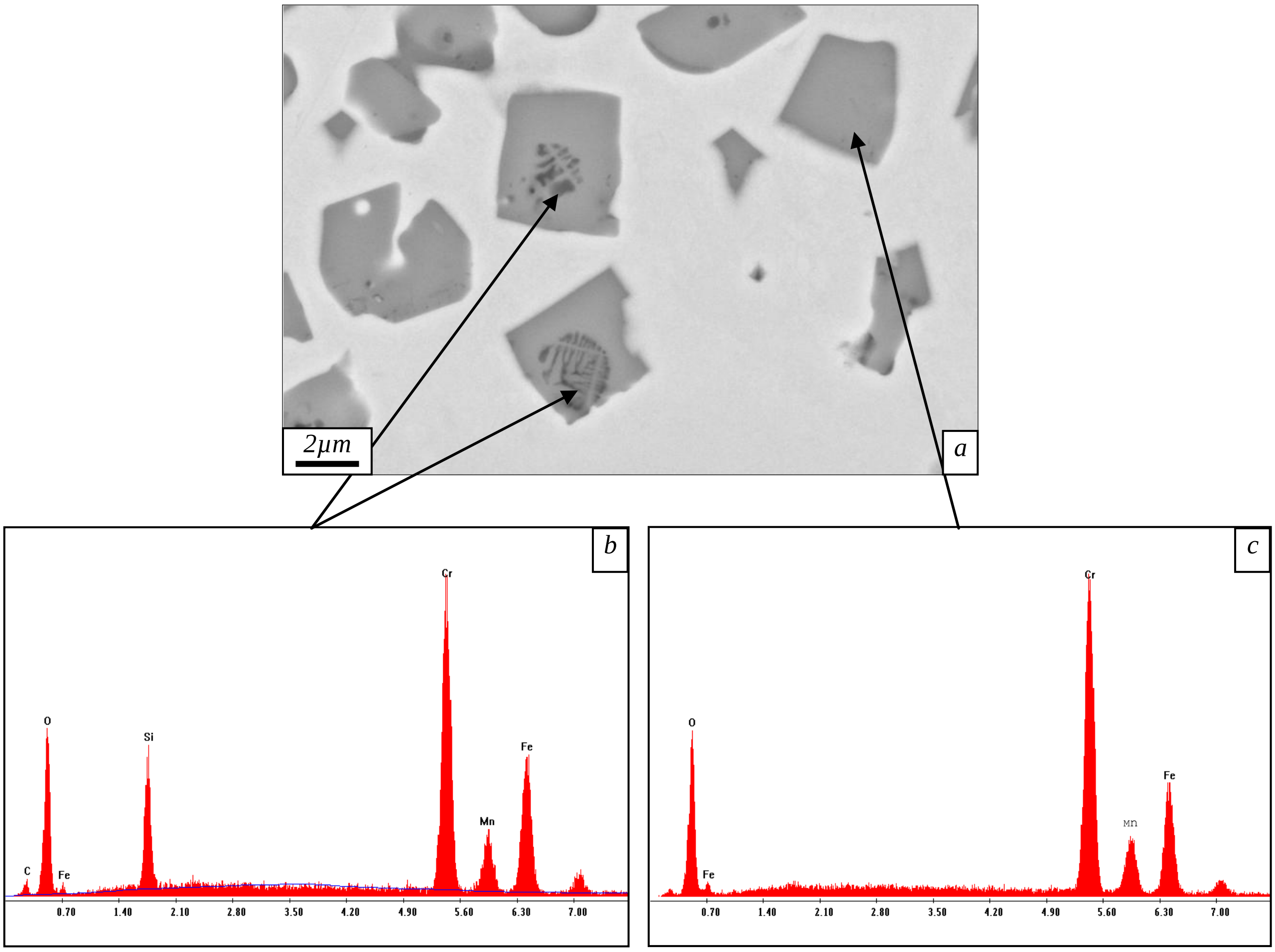

Figure 4.15:- a) backscattered electron image with accompanying EDS spectra of b) two dendrite containing particles and c) an oxide particle not containing a dendritic region formed in 316L stainless steel after 3 hours at 1200˚C and cooled at a rate of 10˚C per minute to room

Figure 4.16 shows the oxide produced on 316L stainless steel after 4 hours at 1200°C. It can be seen from this image that the layer structure and proportion of the layers remains fairly constant over the surface of the scale. The scale has a thickness of ~100 – 130 µm and a very clear layered structure. There is a layer at the top of the scale which is a lighter contrast (1) followed by a darker intermediate layer (2) and a mixed phase layer at the lower part of the scale (3). In layer 1 there is a crack running through it which stops at the layer 1 / layer 2 interface. Layer 2 shows a higher amount of porosity and damage which suggests that it may be more brittle than layer 1. Layer 3 also shows a high density of porosity but little damage.

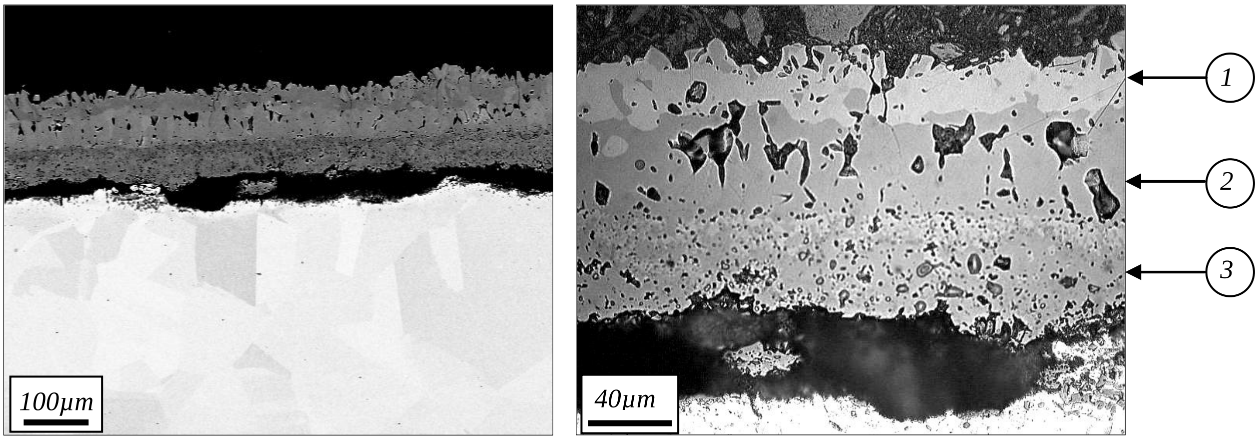

Figure 4.16: Backscatter electron micrograph of an oxide scale formed on 316L stainless steel after 4 hours at 1200˚C showing (1) upper bright contrast layer, (2) an intermediate darker contrast and (3) a fine-grained mixed contrast layer

Further examination using SEM (Figure 4.17) shows that the lowest layer of the scale is relatively fine-grained with a large degree of porosity. The top layer of the scale has a number of intergranular cracks which extend from the outer edge and come to an end in the intermediate layer. Also visible on this image are some grains on the top edge which are a lighter shade. This suggests that these grains are chemically different to the majority of the top layer.

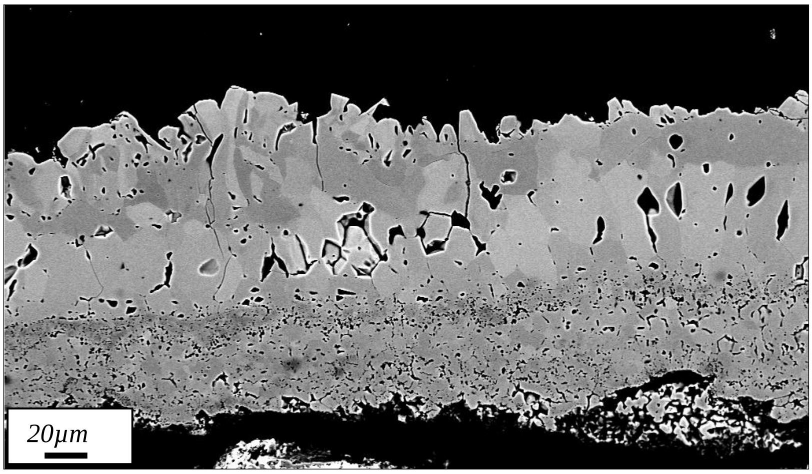

Figure 4.17: Backscatter electron micrograph of an oxide scale formed on 316L stainless steel after 4 hours at 1200˚C

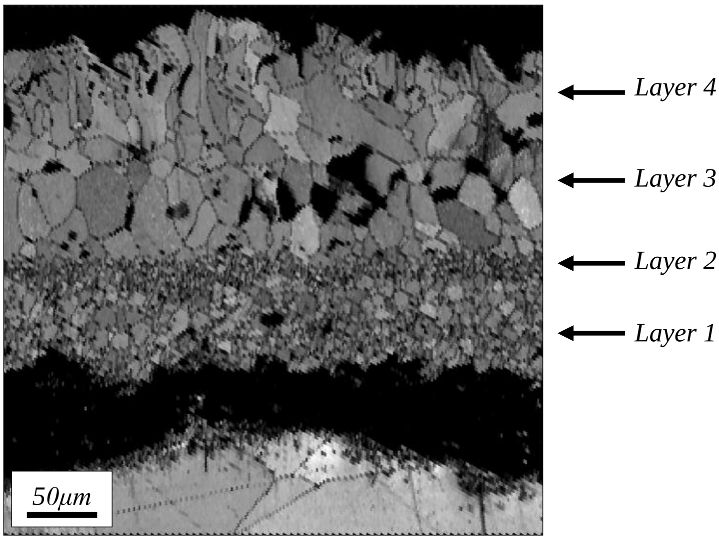

Figure 4.18: Electron backscatter diffraction (EBSD) image quality (IQ) map of an oxide scale formed on 316L stainless steel after 4 hours at 1200°C in air and cooled in air at room temperature showing Layer 1) fine-grained oxide, Layer 2) finer grained oxide, Layer 3) intermediate equiaxed grains and Layer 4) disordered upper oxide layer

Figure 4.18 shows an EBSD IQ map of the scale. It shows a minimum of four layers within the oxide scale which can be defined by grain size and / or morphology. There is a layer of relatively fine equiaxed grains closest to the substrate with a grain size of ~3 – 5 µm in diameter (layer 1). Above that is a layer of even finer grains (layer 2) followed by a layer of equiaxed grains which are ~10 – 30 µm in size (layer 3). The layer above this shows a somewhat disordered grain structure with grains which vary from 90 µm to 10 µm in length (layer 4). Within this layer there are also some columnar grains which extend from the outer edge of the scale to a depth of up to 80µm. Internal oxidation shown on this image is minimal but there is a small amount to a depth of approximately 5 – 10 µm from the metal - oxide interface.

EDS maps of the same region are shown in Figure 4.19. The nickel content of the oxide scale is fairly low in relation to the metal. The majority of the top layer of the scale shows a very low nickel content, however, there are a number of grains along the top edge which show a relatively high nickel content (i). The chromium map reveals a layer of scale which has a significantly higher content of chromium than the majority of the scale. There are two levels of chromium content within this layer; one with a relatively low chromium content which has a larger grain size (ii) and one with a finer grain size and a higher chromium content (iii). Along the metal / scale interface a very thin chromium rich layer can be seen. The iron map shows an increase of iron towards the outer edge of the scale with some grains at the outer edge being less rich than the surrounding areas.

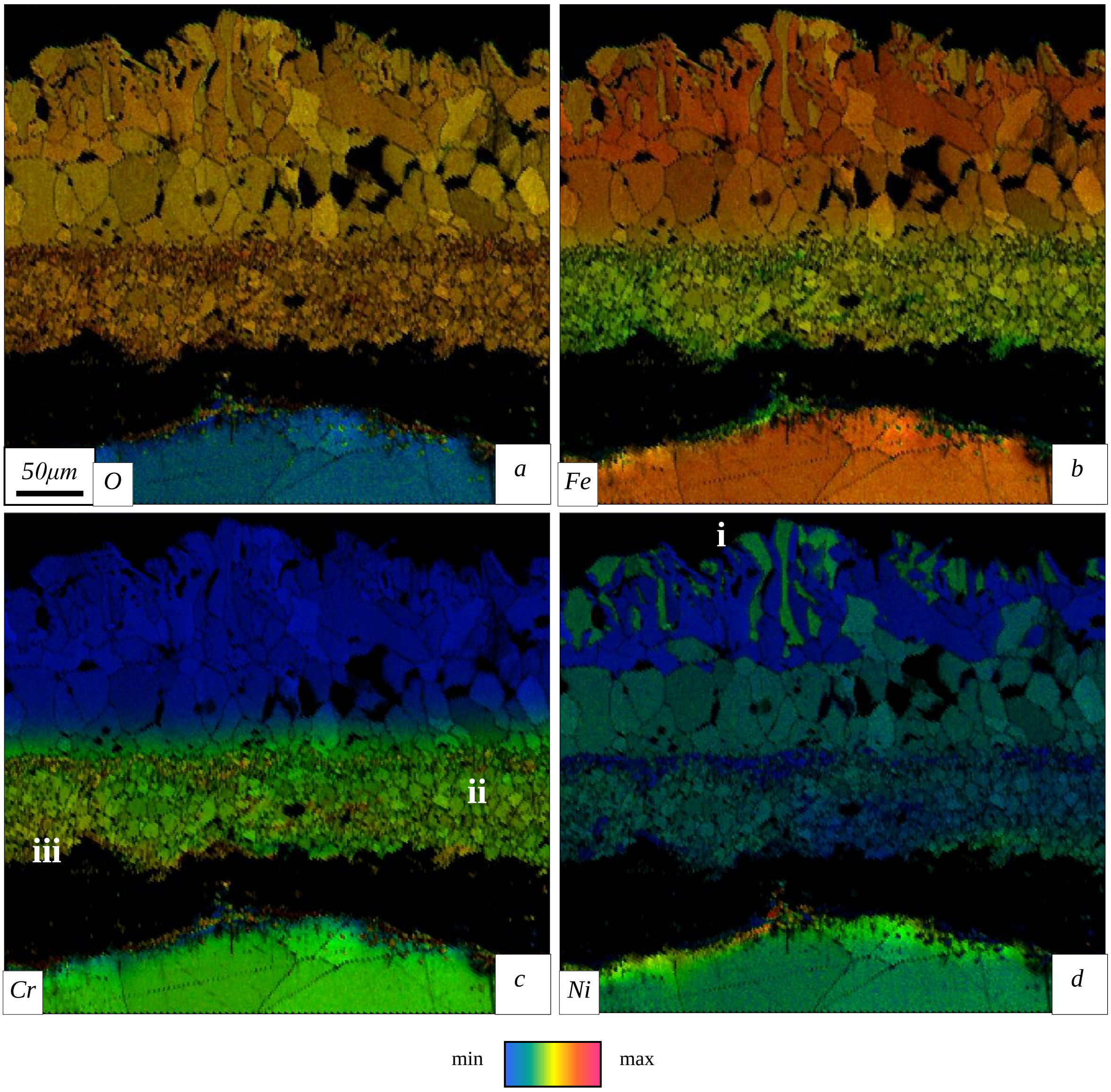

Figure 4.19: Energy dispersive x-ray spectroscopy (EDS) maps of a) oxygen and b) iron, c) chromium and d) nickel in an oxide scale formed on 316L stainless steel after 4 hours at 1200°C in air and cooled in air at room temperature showing (i) nickel rich outer grains, (ii) chromium rich grains and (iii) fine-grained chromium rich oxide

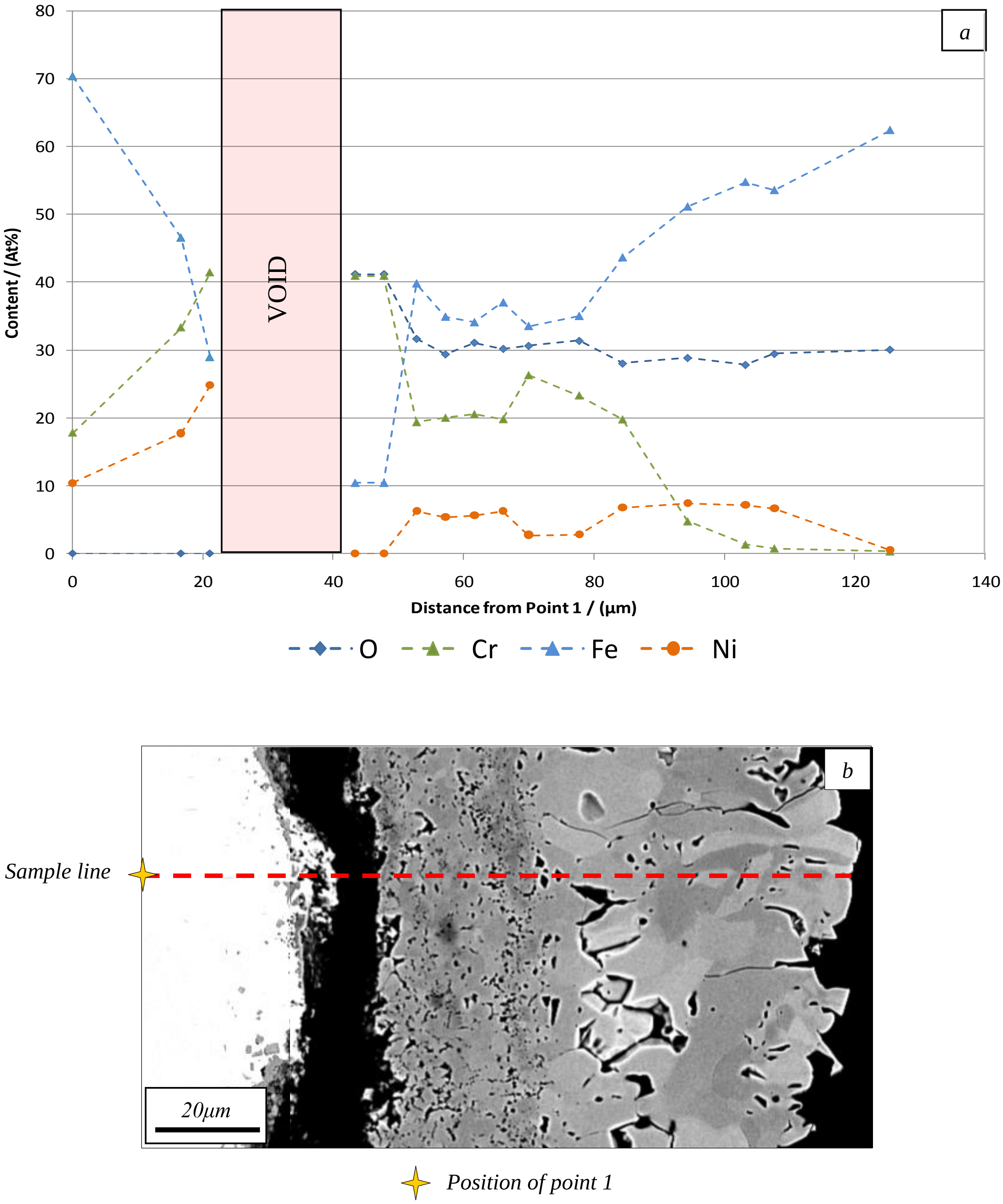

Figure 4.20: a) Elemental distribution through an oxide scale formed on 316L stainless steel after 4 hours at 1200°C and b) SEM micrograph of the area from which EDS was taken

Figure 4.20 shows semi - quantitative EDS data of a scale formed on 316L stainless steel after 4 hours of oxidation at 1200˚C. The sample line of the scan is illustrated in Figure 4.20 (b). The chart shows the elemental distribution throughout the scale. The gap in the data on the chart represents the gap between the metal and the scale shown in the SEM micrograph.

The iron content is seen to rise significantly from approximately 10at% at the lower edge of the first layer to over 60at% at the upper edge of the scale. There is a significant increase in iron content between 45 and 55 µm from point 1 (Far left of the sample line) to 40 at% where the content seems to settle slightly before increasing from 35 at% to 55 at% between 80 and 110 µm from point 1. The final point on the chart shows the iron content to increase from 55 at% to the maximum value of 62 at%. The chromium content's maximum value of ~42 at% is seen at the lowest edge of the first layer in the scale. The lowest content of <1at% is found at the outer edge of the scale. A second chromium peak of ~25 at% is seen at 70 µm from point 1. Again the iron and the chromium maps are almost mirror images of one another. After a low value at the metal / scale interface, the nickel content is fairly constant throughout the scale with the exception of a trough between 70 and 80 µm. This trough coincides with the secondary peak for chromium and a sudden decrease between 110 µm and 125 µm from point 1 which coincides with a rise in iron content. The oxygen content has a maximum of approximately 40 at% at the metal / scale interface after which remains reasonably constant at ~30 at%. The substrate shows the iron content dropping by 40 at% over 20 µm and the nickel and chromium contents rising towards the metal / scale interface.

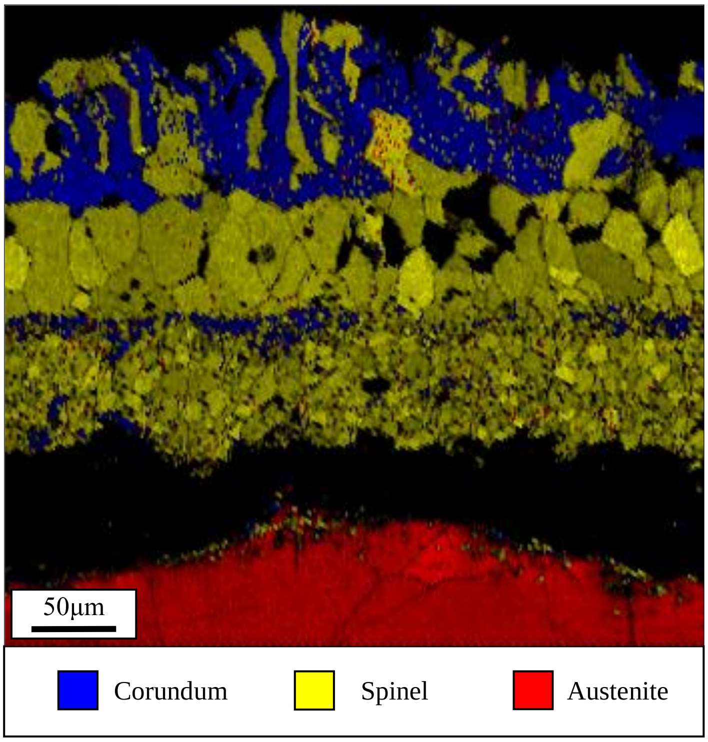

Figure 4.21: Phase maps of the possible phases present within a scale formed on 316L stainless steel after 4 hours at 1200°C in air and cooled in air at room temperature.

Figure 4.21 shows a phase map for the scale shown in Figure 4.18 The lowest layer in the scale is composed of a chromium rich spinel type oxide with additions of iron. The layer above is a layer of nickel and iron spinel type oxide up to the top layer which is haematite. Within the top haematite layer there are occasional grains of nickel iron spinel type oxide.

4.2.3 Oxidation at 1300°C

Reheat furnaces would be unlikely to ever reach this temperature unless an error was made during production. However, experimentation at this temperature is still useful so that it can be seen what oxide could be expected from an error resulting in furnace overheating.

Figure 4.22 shows the oxide formed after oxidation at 1300°C for 1 hour. It can be seen that excessive oxide growth has occurred which has resulted in an oxide which measures ~550µm thick. The entire oxide microstructure is disordered, cracked and difficult to interpret but many layers are visible in this microstructure. There is no internal oxide region visible after oxidation at this time and temperature. The lower half of the oxide is made up of equiaxed grains of a uniform size of ~10µm in diameter. This can be assumed from the inter-granular cracking which is visible throughout the thickness of the oxide. The upper half of the oxide is made up of alternating layers of fine-grained oxide and coarse grained oxide. The outer edge consists of coarse grained oxide and is shown at higher magnification in Figure 4.23. It can be seen that the upper edge consists of relatively large grains. The oxide is made up of at least 2 phases. There is a bright phase which makes up the majority of the grains and a darker phase which resides in the region of the grain boundaries. Within the dark phase there are also dark specks which are likely to be pores.

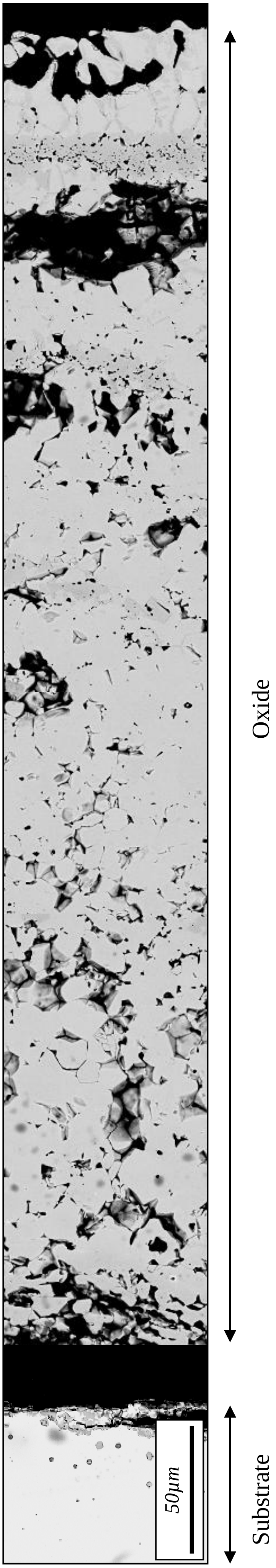

Figure 4.22:- Back scattered electron image of the cross-section of an oxide formed on 316L after oxidation at 1300°C for 1 hour

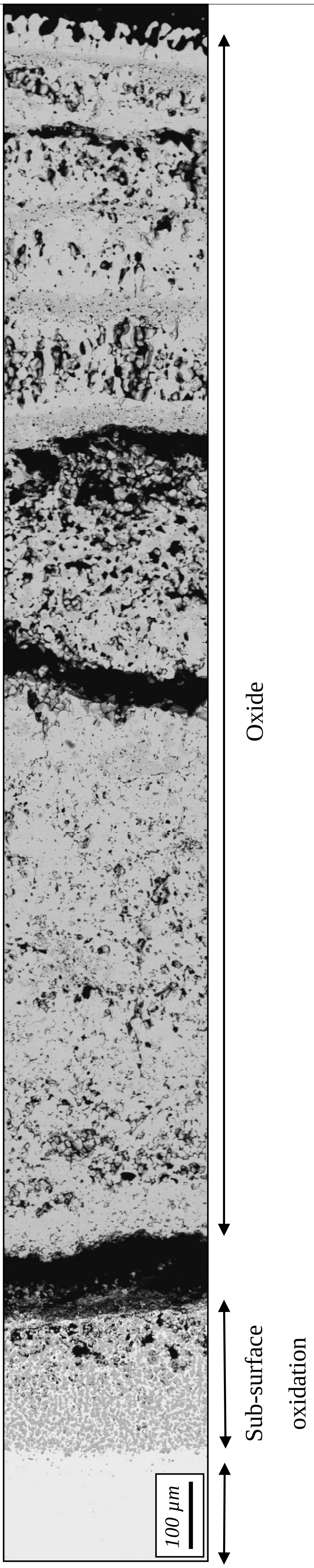

Figure 4.24:- Back scattered electron image of the cross-section of an oxide formed on 316L after oxidation at 1300°C for 4 hours

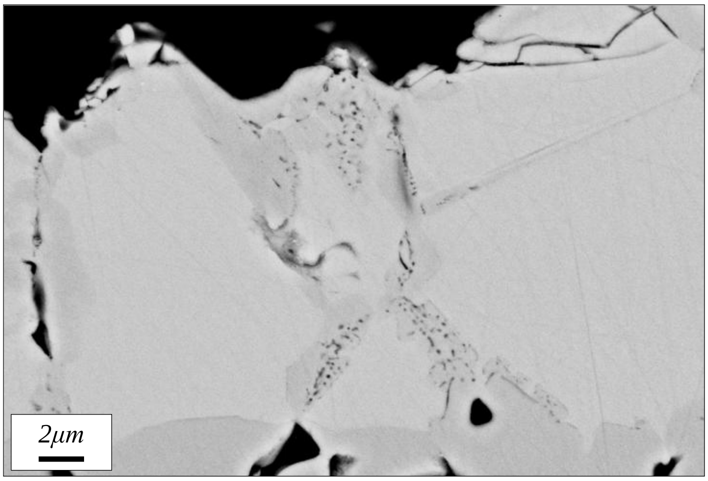

Figure 4.23: Backscattered electron micrograph of the outer edge of the oxide formed on 316L stainless steel after oxidation at 1300°C for 1 hour

After 4 hours at 1300°C, the oxide shown in Figure 4.24 is produced. As with the oxide produced after 1 hour, the oxide is extremely thick and measures ~1600 µm. The oxide is made up of many layers, with voids where layers have delaminated, fine and coarser grained layers. As well as the substantial external oxide layers, there is also an internal oxidation region which extends to a depth of ~150µm and resembles the internal oxidation region seen after oxidation at 1200°C and a slow cooling rate.

The outer layer of the oxide contains grains which are similar in appearance to those seen after oxidation at the same temperature for 1 hour. The optical micrograph shown in Figure 4.25 clearly shows the difference in contrast between the bulk of the grains and a bright needle-like phase. Here it can be seen that at the grain boundary regions, a bright oxide has formed which grows along parallel planes within the parent grains producing this structure. EBSD image quality, phase and EDS maps, of the structure are shown in Figure 4.26.

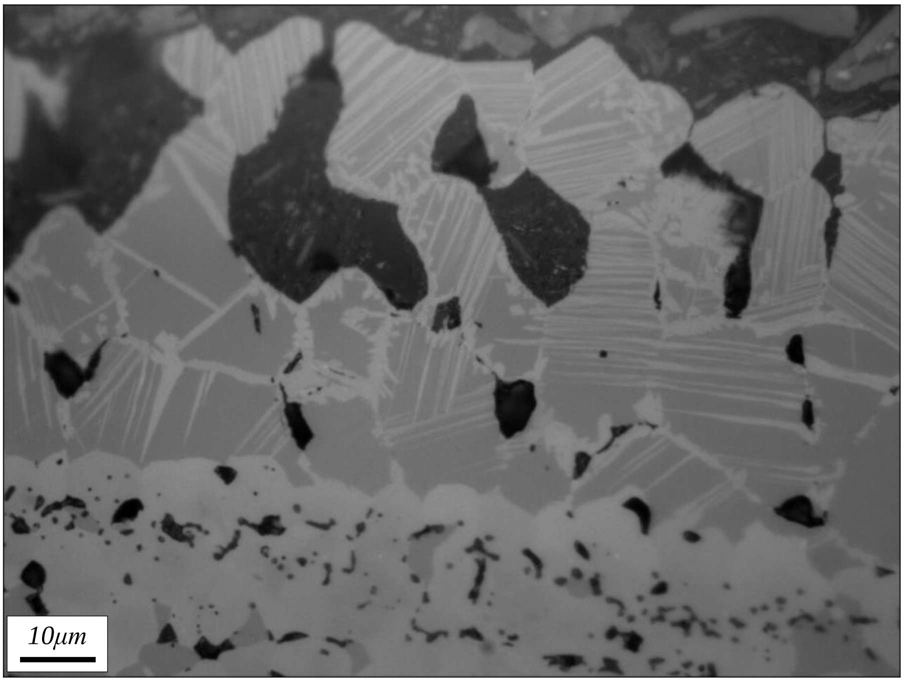

Figure 4.25: Optical micrograph of the outer edge of the oxide formed on 316L stainless steel after oxidation at 1300°C for 4 hours

The optical image of the un-etched oxide (Figure 4.26(a)) reveals a dual phase microstructure with dark areas and bright areas. The bright areas form two different regions: a granular region (1) and a needle-like structure residing within the upper most oxide grains (2). The EBSD IQ map of the same area reveals that the needles are individual grains. As well as the needles, there are small grains at the boundaries between the needle containing grains (as marked by the ellipse). The EBSD phase map shown in Figure 4.26(c) shows that the needles and the small grain boundary grains all have the corundum structure. This would suggest that formation of the needles and the grains at the grain boundaries are related. Below the needle containing spinel grains there is a region containing other grains of approximately 5 - 10µm in diameter which is also indexed as having the corundum structure.

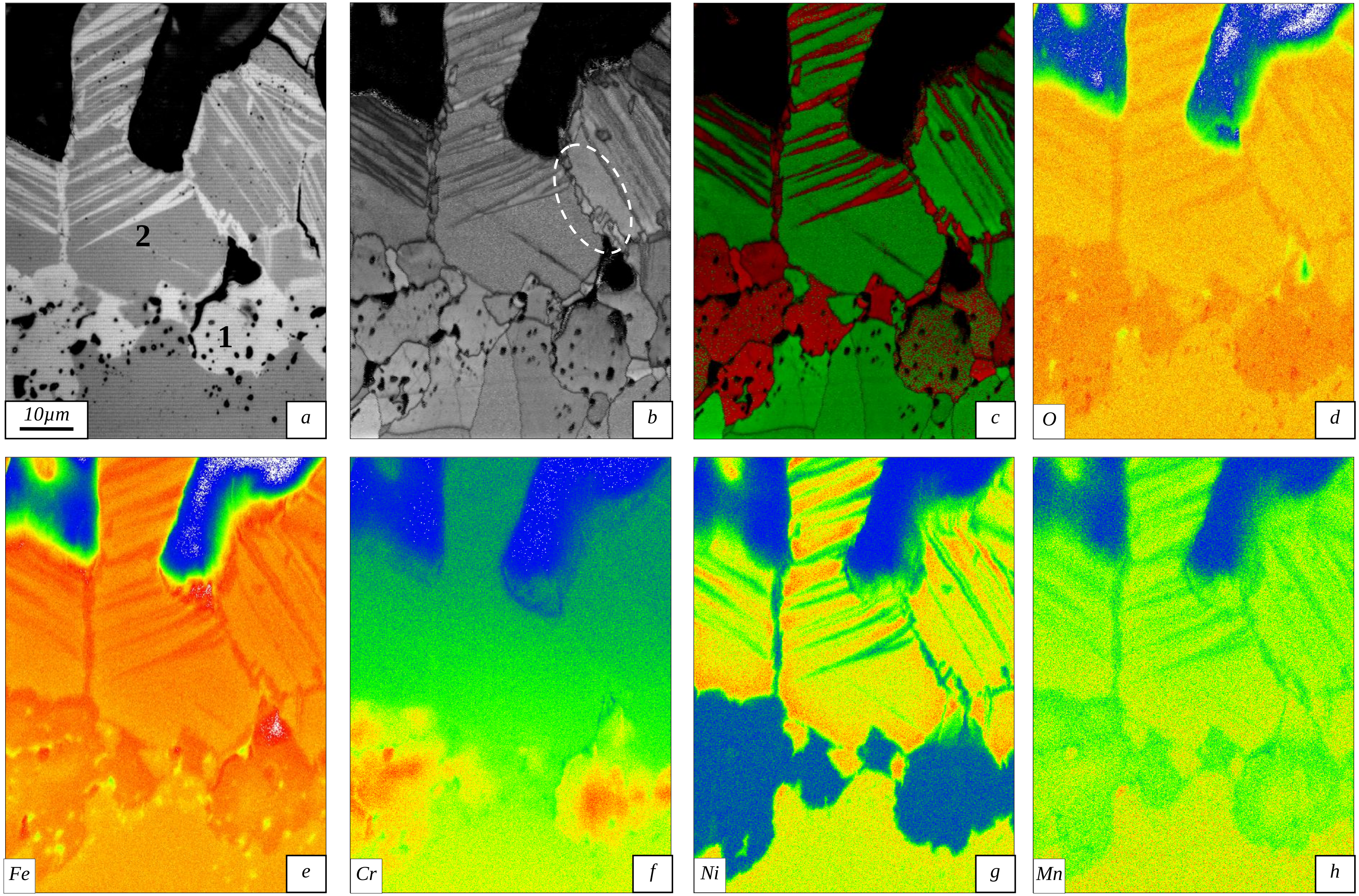

Figure 4.26:- a) optical micrograph, b) EBSD IQ map (with ellipse showing equiaxed grains at the oxide grain boundaries), c) EBSD phase map, d) oxygen EDS, e) iron EDS, f) chromium EDS, g) nickel EDS and h) manganese EDS of the outer edge of an oxide scale formed on 316L after oxidation at 1300°C for 4 hours

Figure 4.26(d-h) are EBSD EDS maps of iron, oxygen, chromium, nickel and manganese. Figure 4.26(e) clearly shows that the corundum needles contain more iron than the spinel oxide as well as slightly more oxygen (Figure 4.26(d)).The chromium map (Figure 4.26(f)) confirms the presence of chromium in the lower grains which, together with the discovery that these grains have the corundum structure suggests that they are chromium and iron-containing oxides of the corundum type (probably $FeCr_2O_3$). Figure 4.26(g and h) also shows some differences in chemical composition between the needles and the parent grain; the parent grain is rich in nickel and manganese and the needles show a lower content in both manganese and nickel.

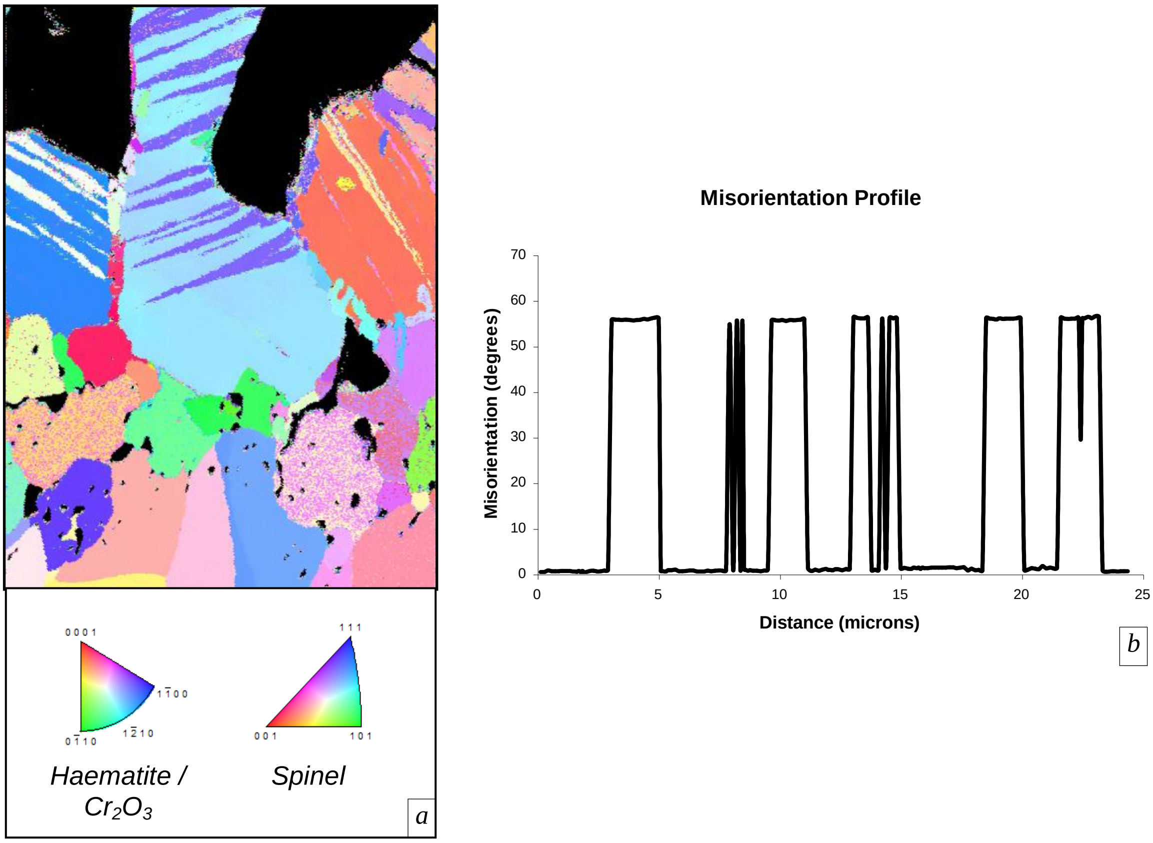

Figure 4.27:-a) Inverse pole figure and b) misorientation plot of the needle phase of the outer edge of an oxide scale formed on 316L after oxidation at 1300°C for 4 hours

Figure 4.27 is an Inverse Pole Figure (IPF) of the same area. It shows that the three needle containing spinel grains are of differing orientations to one another and that the needle like grains also differ not only to their parent grain but also to the needles formed in other spinel grains. They are, however, of identical orientation to the majority of the other needles within the same grain which suggests that they are forming along a preferred growth direction within the parent grain. The misorientation plot shown in Figure 4.27(b) shows that the needle like phase has a misorientation angle of ~55° to the parent grain.

4.3 Austenitic Stainless Steel with an as-cast Oxide Scale

Austenitic grades are generally produced on a very large scale due to their high demand. This means that the process has to be as fast as possible whilst also ensuring that a suitable surface finish is achieved. In order to produce the steel quickly, in many cases the as-cast oxide scale is left in place on the metal during the reheat procedure.

4.3.1 As-cast 304

Figure 4.28 is a photograph of the as-cast scale on 304 stainless steel. The lines which run from top to bottom in Figure 4.28(a) are the reciprocating marks of the continuous casting machine. The average spacing of these reciprocating marks is ~ 12 mm. This as-cast scale is very adherent and robust as it is still present even after handling in the production plant.

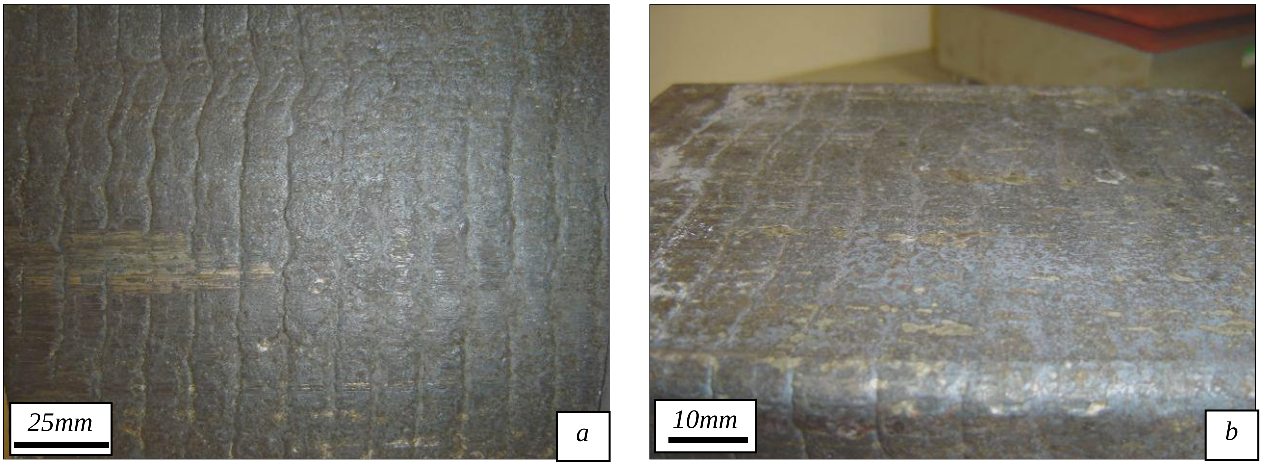

Figure 4.28: Photographs showing an as cast scale on type 304 stainless steel from a) plan view and b) from a corner

A cross-section of an as-cast oxide scale from a 304 stainless steel is shown in Figure 4.29 (a). It shows a scale that is approximately 50μm in thickness. The scale is disordered and damaged with no definite layers visible using optical microscopy. It is possible, however, to see what appears to be two pieces of metal within the as-cast scale. This is clearer in Figure 4.29 (b) which shows an image of the same scale at a higher magnification. The scale / metal interface in Figure 4.29 (b) shows a rough surface as though metal has been folded on top of the oxide. The higher magnification image of the as-cast scale shows that the oxide scale is a mixed phase scale showing one disordered layer.

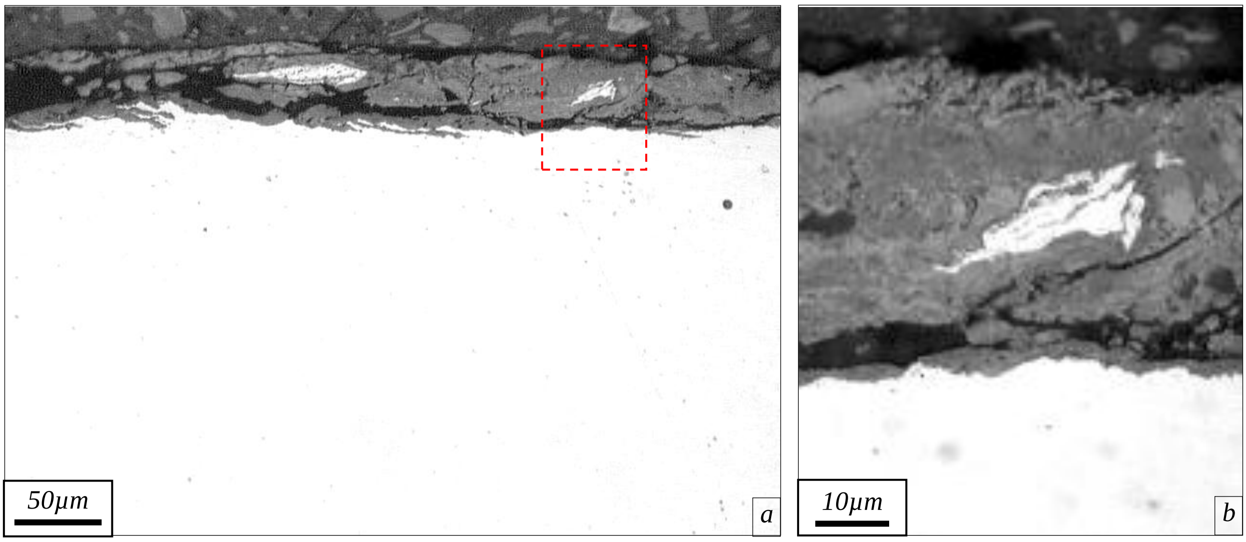

Figure 4.29: Optical microscopy image of an oxide scale formed on type 304 stainless steel after casting (as – cast scale). (The red box in Figure 4.29 (a) indicates the area shown in Figure 4.29 (b)

As the oxide is inhomogeneous, the structure varies over the length of the specimen as shown in Figure 4.30. Figure 4.31(a) is a backscattered electron micrograph of an alternative cross-section with accompanying EDS maps. The scale measures ~50 µm thick and is very disordered with many cracks present. There is a ~10 µm deep internally oxidised region immediately below the scale / metal interface. The EDS maps of this area reveal that there is a clear layered structure to the as-cast oxide scale. The upper regions of the scale consist of mainly iron rich oxides and the lower regions of the scale consist of chromium based oxides. The chromium rich lower layer measures approximately 20µm thick and the iron rich upper layer constitutes the remaining 30µm of the external scale. The internal oxidation region to the right of the image is indicated as being rich in chromium with a band between the oxide and the large crack being dense and with a high chromium count. The nickel maps show that there are a number of regions where nickel is present but only to a low level. Within the internal oxide region to the right of the image there are metallic particles present which are enriched in nickel. It also demonstrates that the upper part of the substrate has a greater concentration of nickel than the bulk of the substrate.

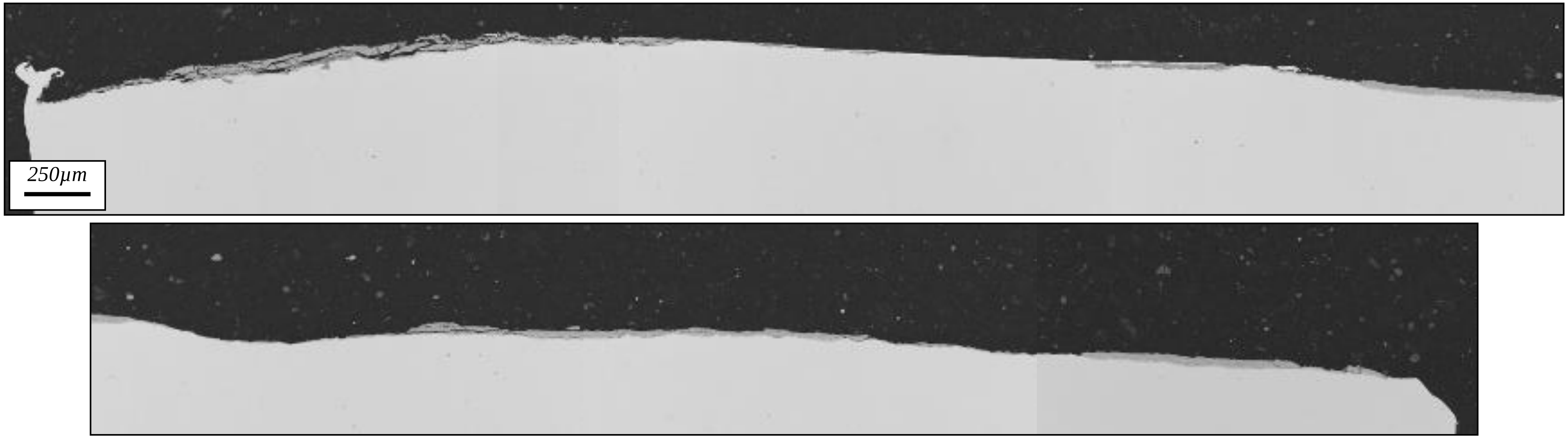

Figure 4.30:- Back scattered electron image of the cross-section of the entire surface of an oxide formed on 304 with an as-cast oxide

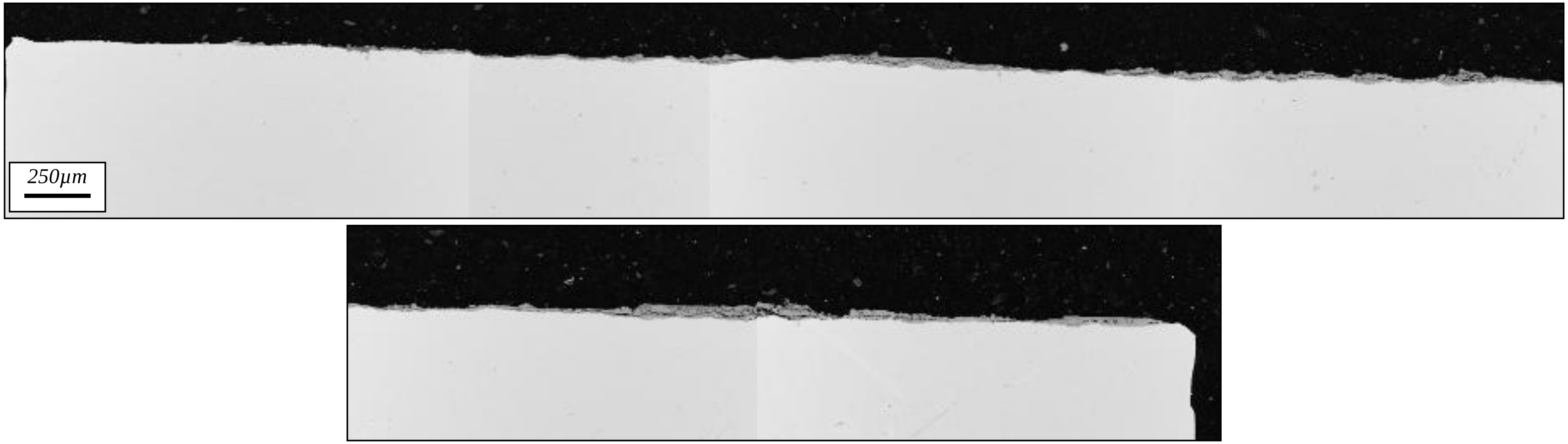

Figure 4.32:- Back scattered electron image of the cross-section of the entire surface of an oxide formed on 316L with an as-cast oxide

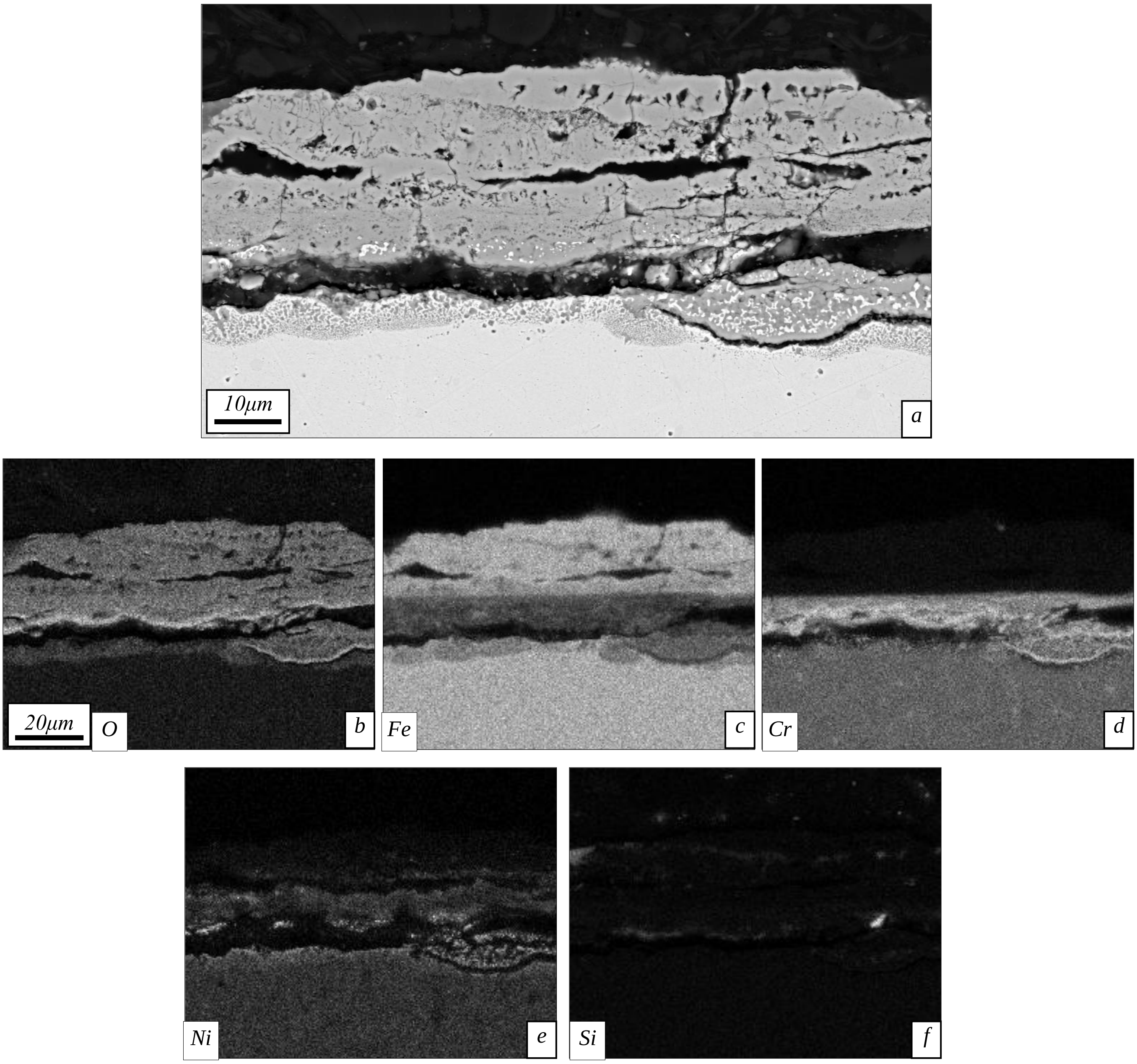

Figure 4.31:- a) Backscattered electron micrograph of the as-cast oxide formed on Type304 stainless steel with accompanying EDS maps of b) oxygen, c) iron, d) chromium, e) nickel and f) silicon

4.3.2 As-cast 316L

The as-cast oxide on 316L stainless steel is shown in cross-section in Figure 4.32. As with that on 304, the oxide varies in thickness over the entire length. At higher magnification, Figure 4.33, it can be seen that it is extremely disordered with major cracking evident in the through thickness direction and in the direction parallel to the metal's surface. As well as this major cracking, the upper most region of the oxide has a crumbled appearance. As with the as-cast oxide seen on the 304, there is a large area of sub-surface oxidation which extends to a maximum depth of ~30µm. The sub-surface region consists of an oxide with metallic particles distributed within it. At the interface between the substrate and the sub-surface oxidation region there is a crack which is similar to that seen in the 304. EDS maps of the as-cast oxide show that there are a number of chemically different layers within the oxide scale. Iron is revealed as residing mainly within the outer layers of the oxide with a slight enrichment in the centre of the oxide. The EDS signal from the upper crumbled layer may not be reliable as there are a large number of cracks within it. Iron has also formed oxide root type structures which penetrate the sub-surface oxide region. Chromium is mainly found in the sub-surface oxide region. Where the iron-rich roots have penetrated the surface, chromium is not present. At the perimeter of the sub-surface oxidation region there is a chromium rich band which is also observed in the 304 as-cast scale. Nickel is enriched at the scale / metal interface particularly in the region of the sub-surface oxide. As with other examples in this thesis this is likely to be present within the metallic particles in this area.

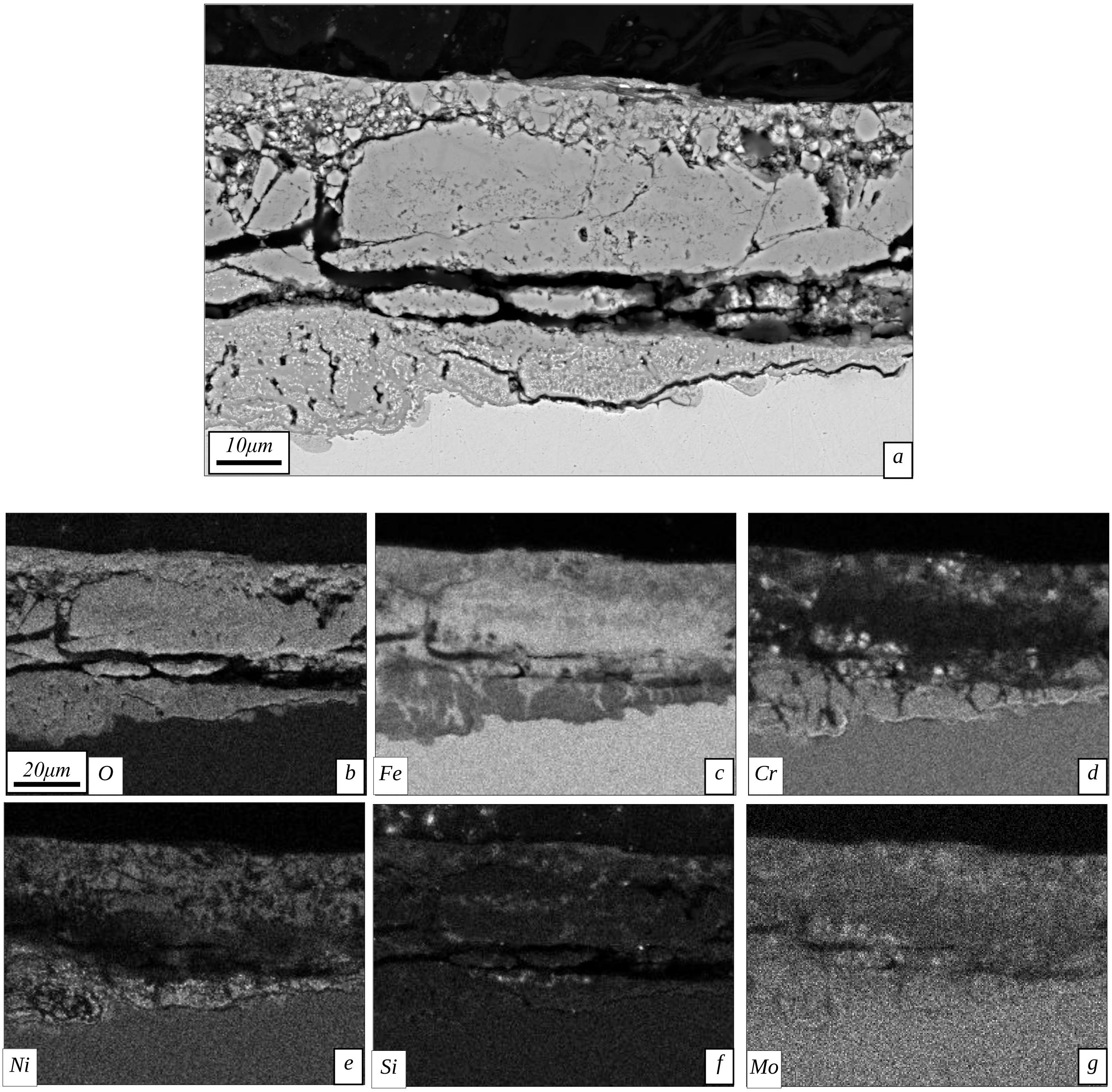

Figure 4.33:- a) Backscattered electron micrograph of the as-cast oxide formed on Type 316L stainless steel with accompanying EDS maps of b) oxygen, c) iron, d) chromium, e) nickel f) silicon and g) molybdenum

4.3.3 Oxidation of As-Cast 304 Stainless Steel

When oxidised with an as-cast scale, austenitic grades tend to suffer from large scale spallation during cooling. As a result, many of the results presented here consist of only sub-surface oxidation. Although this can generate difficulties during the study of the oxide growth, spallation is desirable during processing as the oxide then becomes more likely to be removed during mechanical descaling. The remaining oxide however, is of major interest to steel manufacturers as it is this which can remain after descaling and affect the surface finish of the final cold rolled product. This section therefore, presents results of the oxidation of as-cast 304 stainless steel with a particular emphasis on the differing types of sub-surface oxidation encountered.

4.3.4 Oxidation at 1000°C

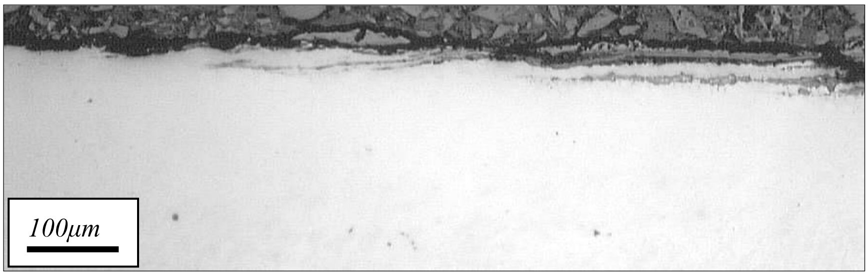

Figure 4.34: Optical microscopy image of an oxide scale formed on 304 stainless steel with an as-cast scale after simulated reheat at 1000˚C for 3 hours

After oxidation of the as-cast 304 stainless steel at 1000˚C for 3 hours the scale shown in Figure 4.34 was obtained. The external scale is thinner than before oxidation but this could be due to damage during heating or spalling during cooling. The external scale shows a two-layer structure which is distinguished by the contrast in the image. An interesting feature of the internal oxidation within this simulated reheat scale is that the metal folds seen in Figure 4.29 have elongated to form what can be described as bands at an almost constant depth of approximately 10µm below the scale / metal interface. The higher magnification image shown in Figure 4.35 shows 2 oxide bands; an area just below the scale / metal interface followed by a layer of metal and another oxidation band described above. The oxidation band seems to consist of two layers of oxide with metallic substrate sandwiched between them. There is a 3 – 4µm thick band of oxidation running underneath the main scale at a depth of ~3 – 5µm. The internal oxidation band also has some root type structures protruding into the substrate from it's surface. There is also a second oxidation band visible on this image which resides approximately 0.5µm below the main scale. It is less continuous and thinner than the main band. This image also shows the two layers of the external scale. One is ~2 – 3µm thick and is a slightly lighter shade whereas the scale which is darker is about half the thickness. Below this darker layer there is a layer of internal oxidation which is very disordered and mixed with metallic substrate material.

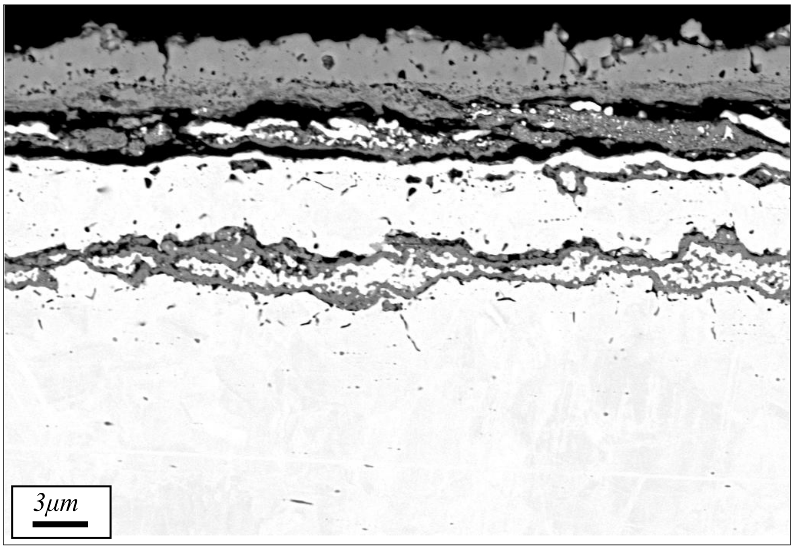

Figure 4.35: Backscattered electron micrograph of a scale formed on 304 stainless steel with an as – cast scale after 3 hours at 1000°C

Figure 4.36 is a higher magnification image of the scale displayed in Figure 4.35. This image gives a better view of the external scale layers and the internal oxidation. The darker shade layer in the external scale is porous whereas the upper layer is not. The internal oxidation has areas of metal contained within it which measure approximately <0.5µm in diameter. Also visible in this image is the secondary internal oxidation band. It is situated at an almost constant distance from the main scale and contains some metal.

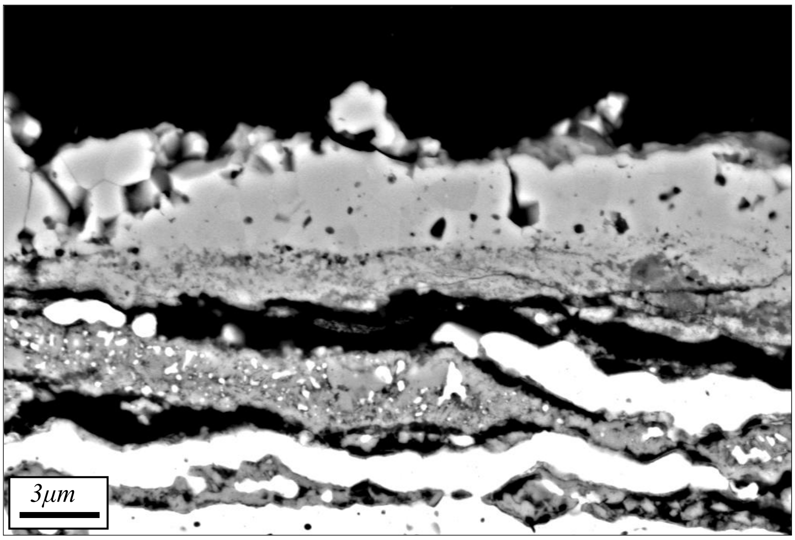

Figure 4.36: Backscattered electron micrograph of a scale formed on 304 stainless steel with an as – cast scale after 3 hours at 1000°C

Figure 4.37 is a high magnification image of the main internal oxidation band shown in Figure 4.35. The band consists of three layers. To the top and bottom of the band (1), there are oxide layers and sandwiched between them is a layer of a mixed oxide / metal (2). Clearly visible from this image are the root type structures protruding from the oxide layers (3).

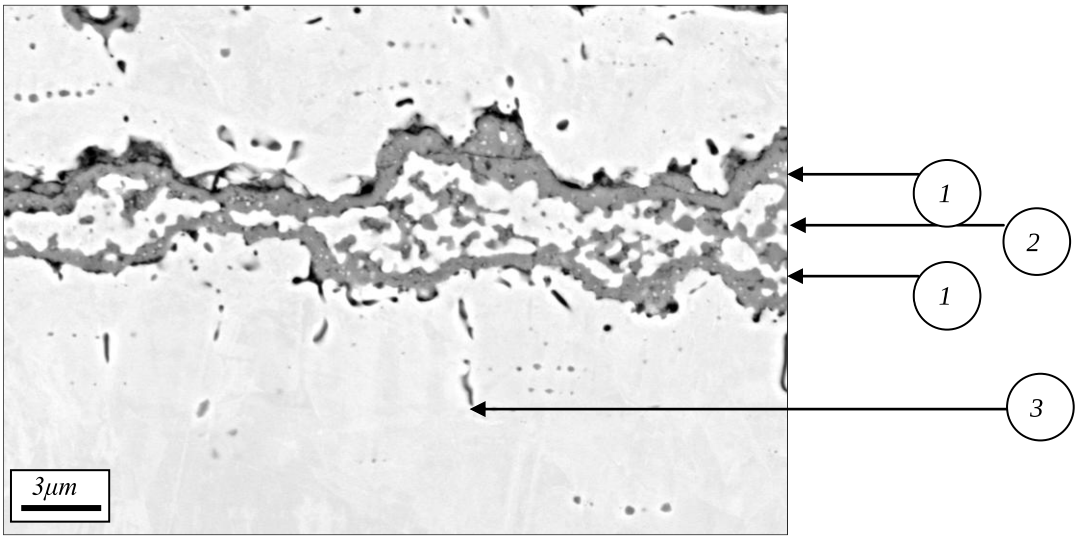

Figure 4.37: Backscattered electron micrograph of a scale formed on 304 stainless steel with an as – cast scale after 3 hours at 1000°C showing (1) continuous oxide at the top and bottom of the internal oxide bands, (2) a layer of mixed oxide and metal and (3) root type oxide structures extending away from the internal oxide band

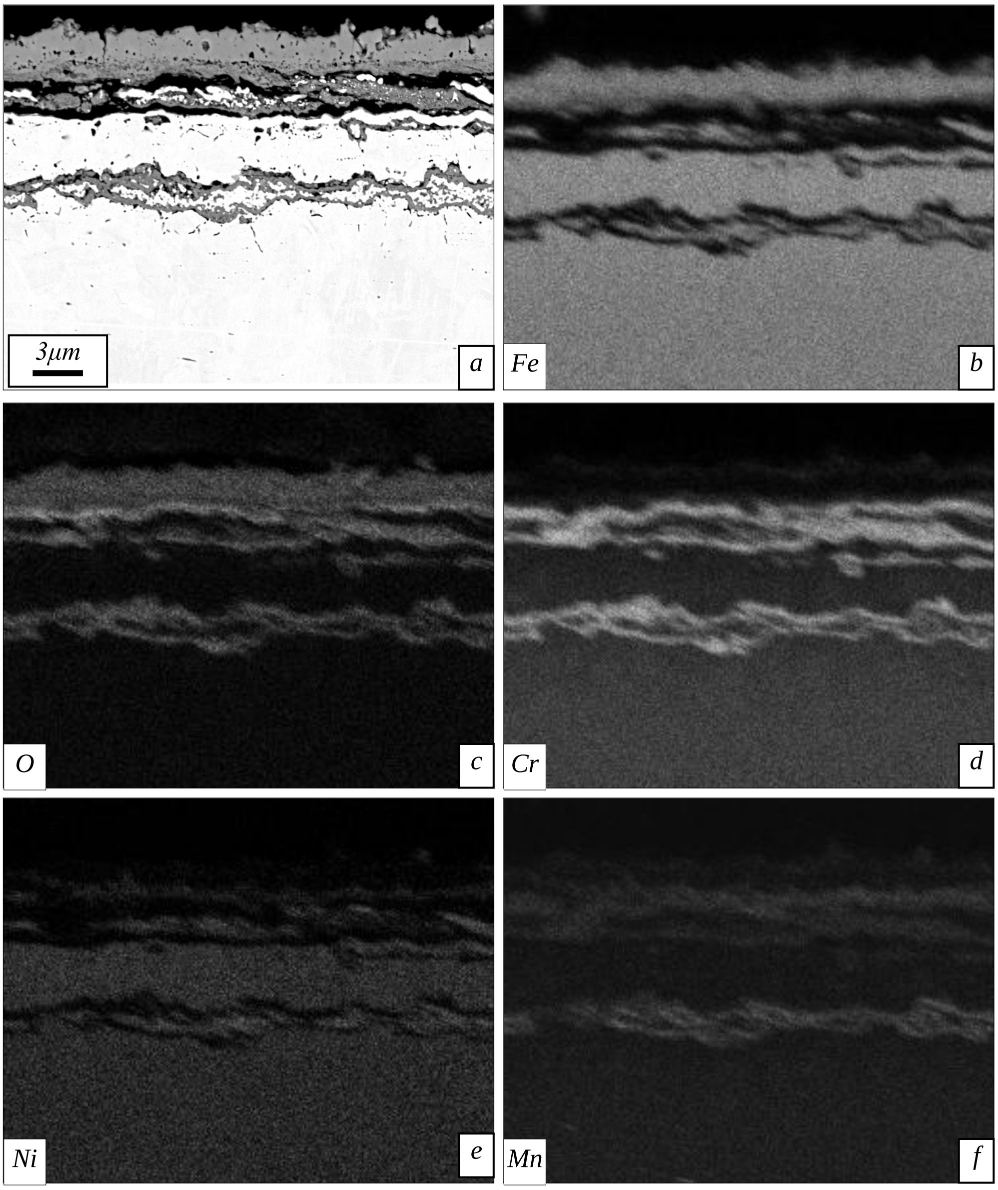

Figure 4.38: a) Backscattered electron micrograph with accompanying EDS maps of b) iron, c) oxygen, d) chromium, e) nickel and f) manganese of a scale formed on 304 stainless steel with an as – cast scale after 3 hours at 1000°C

EDS maps of the scale formed are shown in Figure 4.38. Iron is enriched in the upper parts of the external oxide scale but is not present in the internal oxide bands or the lower parts of the external scale. Chromium is enriched in the lower external scale and also in the internal oxide bands. The manganese map shows that it is present (albeit in smaller quantities), wherever chromium is present. The nickel map shows that it is not present in any of the oxide regions. Instead, there is a slight increase in the non-oxidised metal between the internal oxide bands.

4.3.5 Oxidation at 1100°C

Figure 4.39 shows the oxide produced on 304 stainless steel with an as-cast scale after heating to 1100°C for 2 hours. The oxide scale consists of two parts; an external oxide scale and sub-surface oxidation. The external oxide has three layers within it. The lowest layer is a fine-grained and highly porous layer and the second and third layers can be distinguished by the contrast difference with the upper layer which is darker in the micrograph. The sub-surface oxide region has a five-layer structure with rows of metallic particles separating each layer of oxide.

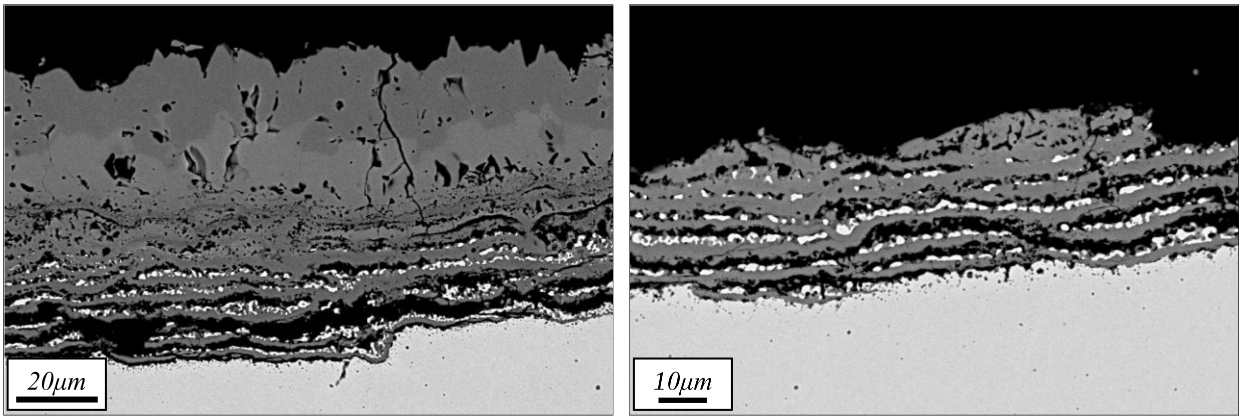

Figure 4.39: a) Backscattered electron micrographs of an oxide formed on 304 stainless steel with an as – cast scale after 2 hours at 1100°C showing a) a complete oxide scale and b) a scale with spalled external oxide

A montage of an electron micrograph, EBSD and EDS maps is shown in Figure 4.40. As shown previously, the BSE image shows a number of layers of sub-surface oxidation with small bright particles within them. The external scale is approximately 20µm thick and consists of two layers, which can be discriminated by contrast variation. The IQ map shows that the internal oxide is a very disordered, fine-grained microstructure and that the external scale has large grains.

The EDS maps show that the metallic particles within the sub-surface oxide region are high in nickel which suggests that most of the other elements have been consumed during the oxidation process. The external scale is an iron based oxide with small quantities of nickel within the lower layer. The upper external oxide contains only iron and oxygen and so it can be assumed that it is a haematite layer. The internal oxide bands are chromium and iron rich oxides and the upper layer of substrate material is nickel enriched and chromium depleted as seen in the majority of other conditions. This nickel enrichment / chromium depletion corresponds to the fine-grained substrate layer which is seen in the IQ map.

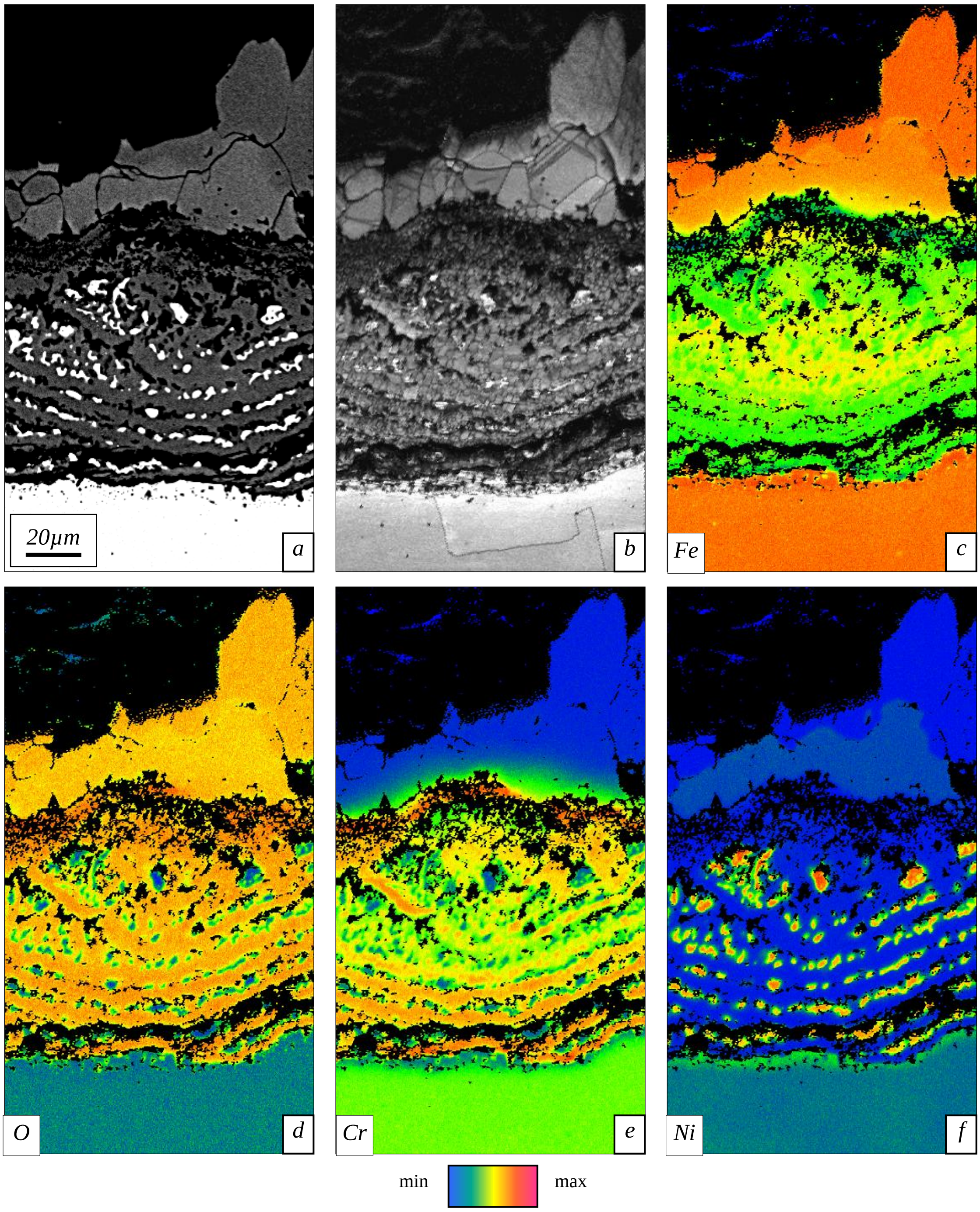

Figure 4.40: a) Backscattered electron micrograph with accompanying b)EBSD IQ map and EDS maps of c) iron, d) oxygen, e) chromium and f) nickel of a scale formed on 304 stainless steel with an as – cast scale after 2 hours at 1100°C

4.4 Oxidation of an as-cast 316L Stainless Steel

4.4.1 Oxidation at 1000°C

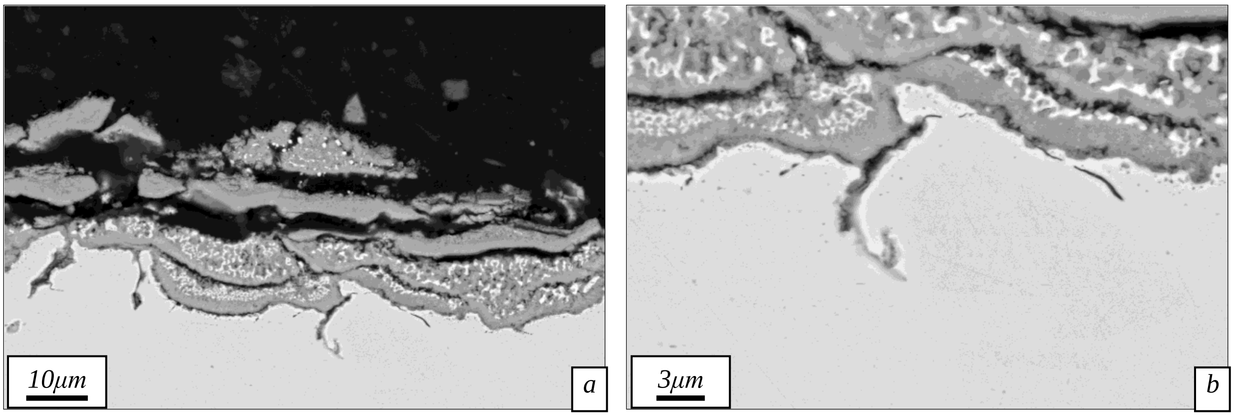

Figure 4.41: Backscatter electron micrographs of a) a scale formed on 3i6L stainless steel with an as – cast scale after 2 hours at 1000°C and b) at higher magnification

As-cast 316L stainless steel produces the oxide structure shown in Figure 4.41. As with the 304 stainless steel, the structure is very disordered with two sub-surface oxide layers visible, consisting of metallic particles and continuous oxide bands. Also within the substrate there are a number of oxide roots which extend to ~10µm from the oxide layers. In order to study these oxide roots further, a specimen was oxidised for the same time and temperature and a planar sample was produced. The oxide was carefully ground using 1200 grit silicon carbide paper from the top surface until the underlying substrate was just visible. The sample was then polished using 1 µm diamond to reveal the structure seen in Figure 4.42.

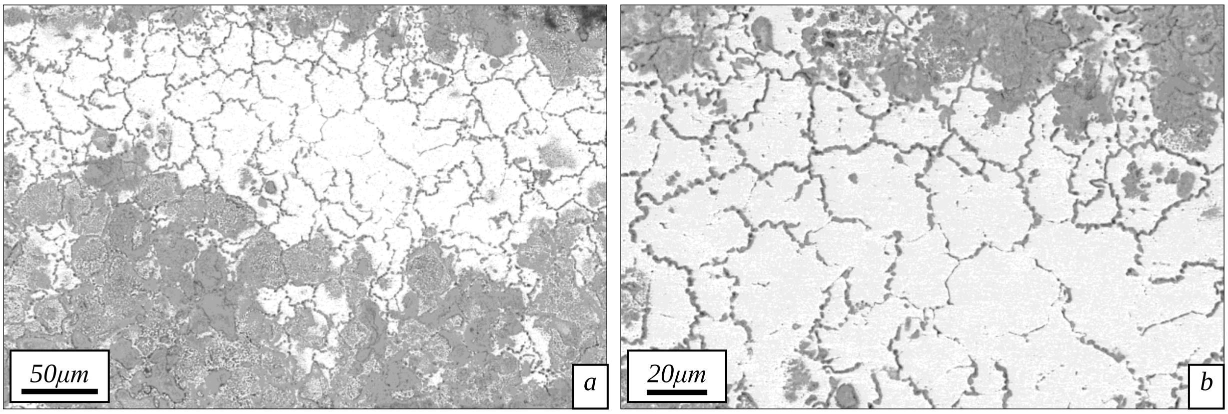

Figure 4.42: Backscatter electron micrographs of a) a scale formed on 3i6L stainless steel with an as – cast scale after 2 hours at 1000°C prepared to reveal the underlying root structure and b) at higher magnification

Where the root structure has been revealed it can be seen that they resemble the grain structure of 316L stainless steel. With very little additional oxidation observed in areas away from the grain boundaries. To confirm the correlation with the grain boundary distribution, the specimen was examined using EBSD the results of which are shown in Figure 4.43.

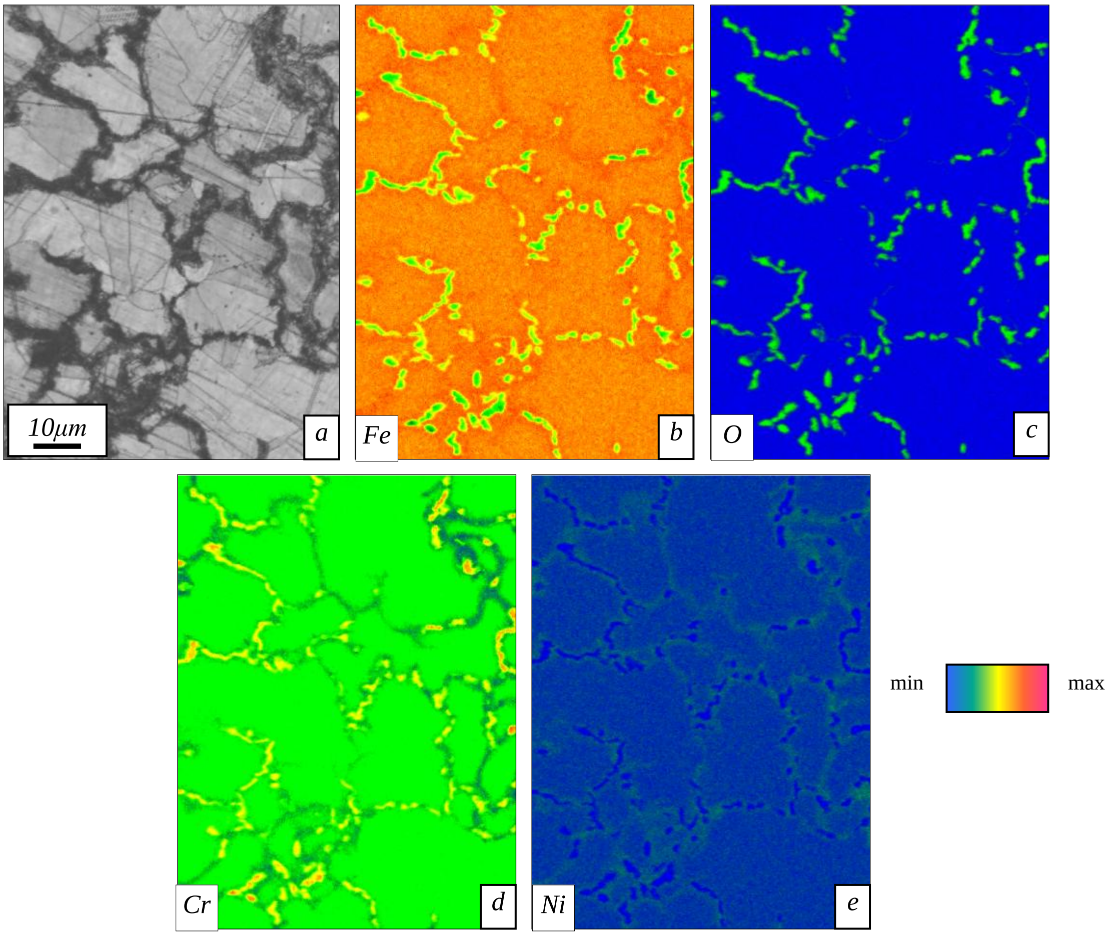

Figure 4.43: a) EBSD IQ map and EDS maps of b) iron, c) oxygen, d) chromium and e) nickel of a scale formed on 3i6L stainless steel with an as – cast scale after 2 hours at 1000°C prepared to reveal the underlying root structure

The IQ map shows that the oxide is very fine-grained and confirms that it tends to reside upon only the grain boundaries. The EDS maps of the area show that the oxide is rich in chromium with additions of iron whilst also being devoid of any nickel content. As well as the composition of the oxide, the EDS maps also show that the non-oxidised boundaries are slightly enriched in iron and nickel and also depleted in chromium. This is similar to the results observed after oxidation of ground 316L for 3 hours at 1000°C (Figure 4.4).

5 OXIDE FORMATION – AUSTENITIC GRADES CRACKED GAS

5.1 Introduction

As well as heat treatments in ambient air box furnaces, experiments were carried out in the tube furnace to examine the effects of a combustion product atmosphere. The use of this atmosphere also allowed a greater comparison to be made to the oxides produced on the duplex grades and is also more relevant to the industrial process of reheat.

In order to fully appreciate the stages involved in forming a full reheat scale, the initial oxide forming stages are of importance. Within this section, results are presented which show oxide scales produced on 304 and 316L stainless steels at temperatures comparable to industrial reheat operations but also at temperatures well below normal reheat temperature for times of 1 and 2 hours.

5.2 Type 304 Stainless Steel

5.2.1 Oxidation at 700°C

Oxidation of Type 304 stainless steel with an 80 grit surface finish after oxidation at 700°C for 1 and 2 hours in the tube furnace produces the oxide shown in Figure 5.1. After 1 hour (Figures 5.1 (a) and (b)), the majority of the surface oxide consists of a fine-grained oxide which makes up the dark contrast background in the images. As well as this fine-grained oxide there are facetted oxide grains which are brighter in contrast. These facetted oxide crystals are reasonably uniformly distributed over the surface of the metal and measure ~0.3 – 0.4µm. Following a further one hour of oxidation the situation shown in Figures 5.1 (c) and (d) is observed. The underlying dark contrast, fine grained oxide is still visible underneath an increased amount of the bright facetted grains on the surface. The facetted oxide crystals have grown (for example the crystals on the left of Figure 5.1 (c)) and new ones have nucleated producing a denser distribution on the metal's surface.

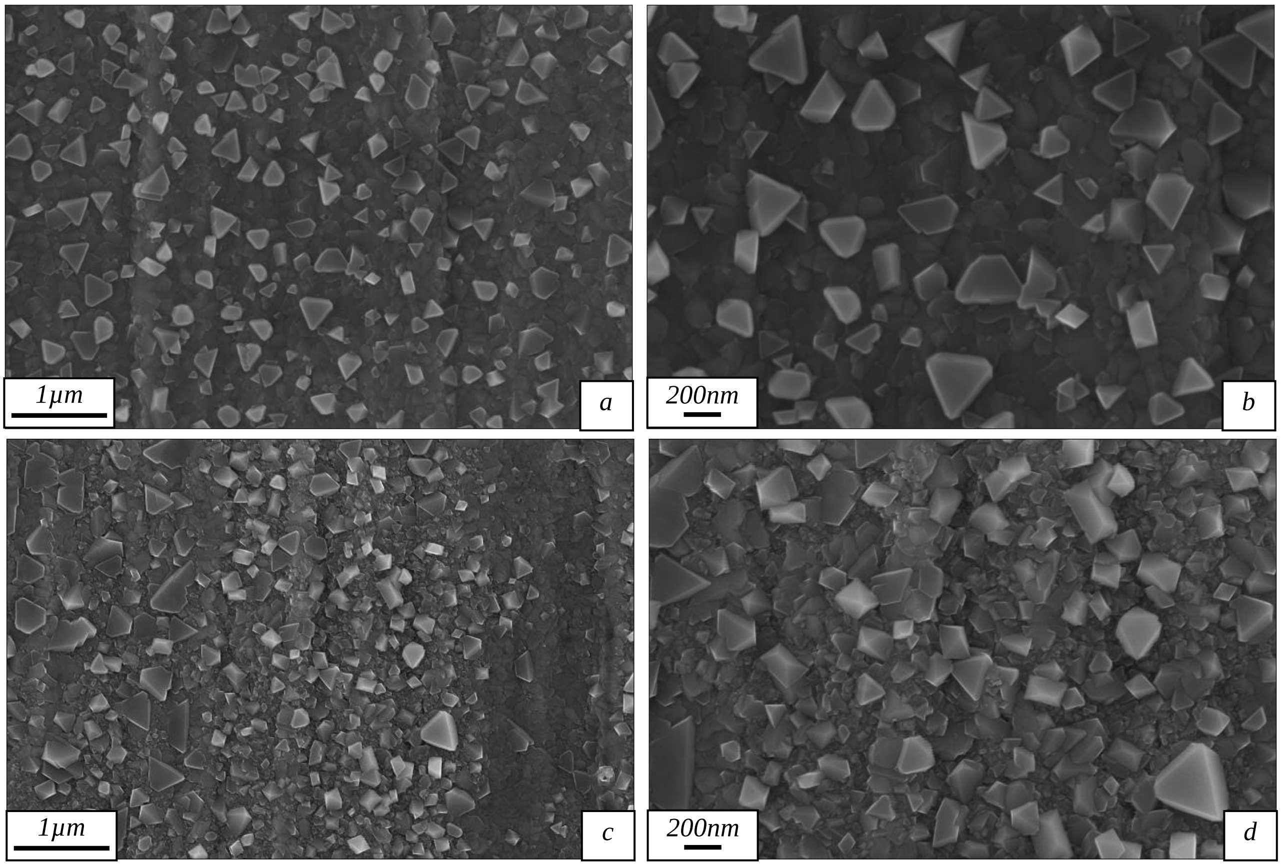

Figure 5.1:- Secondary electron images of the surface oxide formed on laboratory prepared (80 Grit) 304 after oxidation at (a+b) 700ºC for 1 hour and (c+d) 700°C for 2 hours in simulated combustion products of propane

5.2.2 Oxidation at 800°C

Increasing the temperature by 100°C to an oxidation temperature of 800°C for 1 hour substantially alters the appearance of the oxide produced. The resulting oxide is shown in Figure 5.2. The underlying fine-grained base oxide is no longer visible presumably due to it being completely obscured from view by facetted oxide grains which measure approximately 0.3 – 0.5μm in size. At higher magnification it is possible to see that some of the oxide grains are joined which is a progression from the isolated crystals seen after oxidation at 700°C. Figure 5.2(c and d) show secondary electron images of the oxide formed after oxidation at 800°C for 2 hours. The facetted oxide crystals on the upper surface of the oxide are larger than those produced on the same substrate after oxidation for 1 hour.

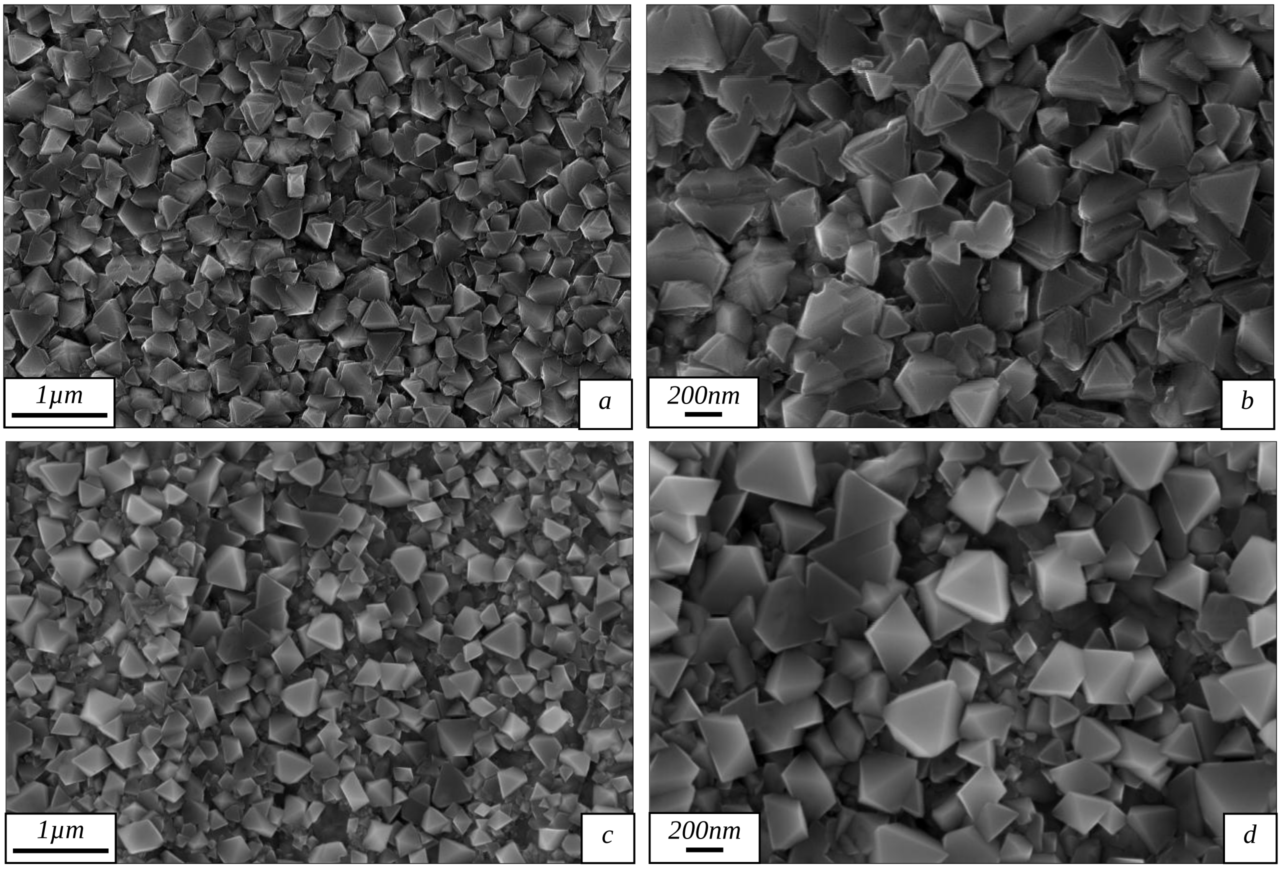

Figure 5.2:- Secondary electron images of the surface oxide formed on laboratory prepared (80 Grit) 304 after oxidation at (a+b) 800ºC for 1 hour and (c+d) 800°C for 2 hours in simulated combustion products of propane

Although no large scale oxide nodules are observed on the surfaces of 304 stainless steel after oxidation at 800°C, small features assumed to be initial nodule growth sites have been observed, some of which are displayed in Figure 5.3. Figure 5.3(a) is an initial oxide nodule formed after oxidation for 2 hours at 800°C. It is located within an area where the upper surface of the oxide consists of the facetted oxide grains and can be described as a small agglomeration of these surrounding grains. The initial nodule shown in Figure 5.3(b) is located in an area where the facetted grains are less densely distributed and the underlying base oxide is clearly visible. However, the nodule itself still consists of a number of agglomerated facetted oxide crystals. Both of the initial nodules measure ~1µm in diameter.

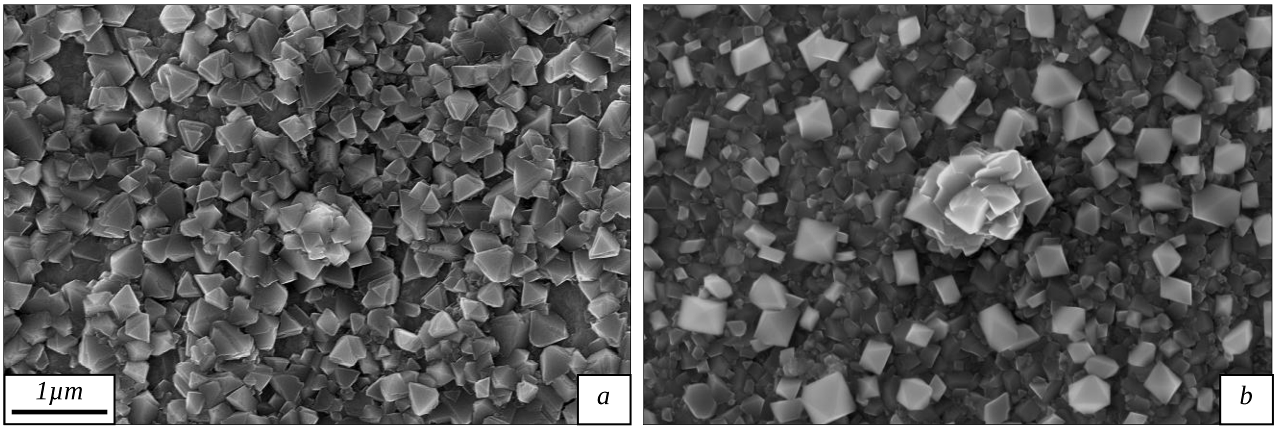

Figure 5.3:- Secondary electron images of the surface oxide formed on laboratory prepared (80 Grit) 304 after oxidation at 800ºC for 2 hours in simulated combustion products of propane of a) initial nodule formed amongst facetted oxide grains and b) upon a finer grained oxide region

5.2.3 Oxidation at 900°C

Figure 5.4 shows secondary electron images of the surface oxide formed after 1 and 2 hours at 900°C. These images show a further progression of the oxide growth on the surface. The large facetted oxide crystals found are of considerable size when compared to those seen in Figure 5.3 measuring ~0.6 - 1µm in size. On top of these large facetted oxide grains there is a scattering of finer facetted crystals. These resemble the shape and size of those seen after oxidation of the same substrate material at 700°C. After a further hour of oxidation, the dispersed fine facetted oxide grains have formed clusters on the surface of the oxide resulting in an inhomogeneous oxide surface with some areas being completely covered by the newly formed fine grains and other areas having only a light coverage.

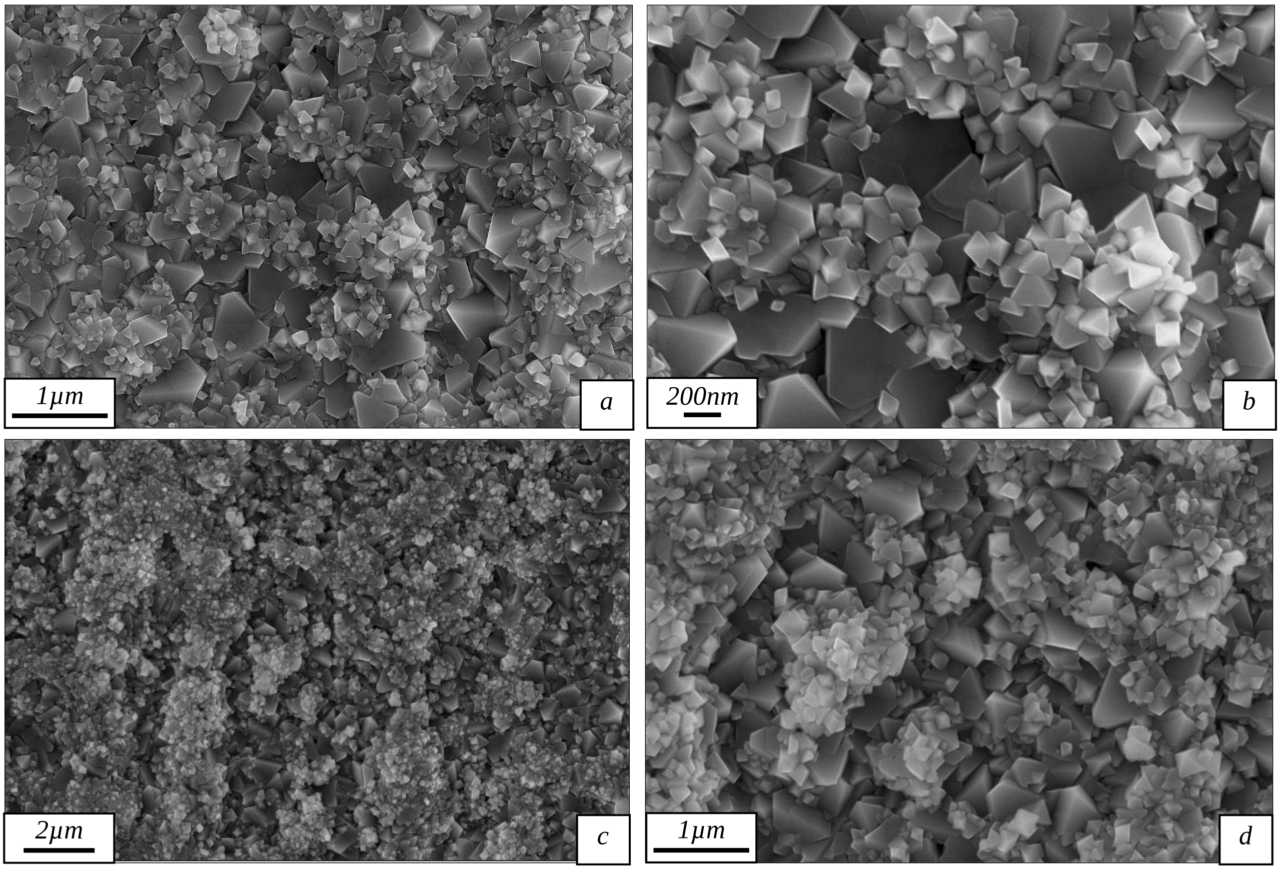

Figure 5.4:- Secondary electron images of the surface oxide formed on laboratory prepared (80 Grit) 304 after oxidation at 900ºC for (a+b) 1 hour and (c+d) 2 hours in simulated combustion products of propane

5.2.4 Oxidation at 1000°C

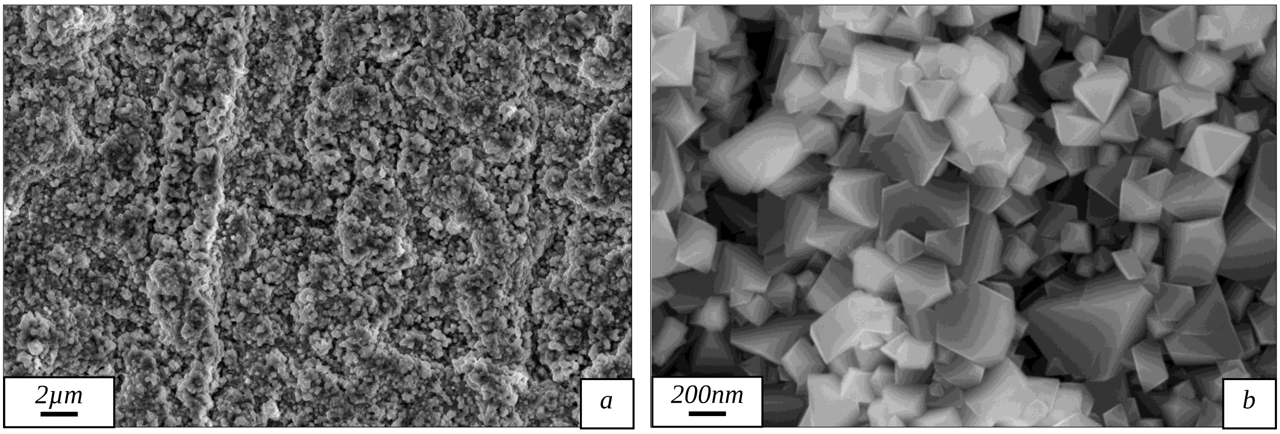

Figure 5.6:- Secondary electron images of the surface oxide formed on laboratory prepared (80 Grit) 304 after oxidation at 1000ºC for 1 hour in simulated combustion products of propane a) lower magnification and b) higher magnification

An increase in oxidation temperature of a further 100°C for a 1 hour heat treatment produces the oxide shown in Figure 5.6. The oxide surface is uneven (as shown in Figure 5.6(a)) with oxide features of which some seem to resemble the underlying grinding marks whilst others are oxide ridges with no clear relationship to the expected substrate microstructure. At higher magnification it can be seen that the surface only has facetted oxide grains (Figure 5.6(b)). This means that either the oxides observed in previous examples do not form at these higher temperatures or that this facetted oxide grows to obscure the previously described oxides from view. The oxide crystals seen after oxidation at this temperature for 1 hour can vary in size from ~0.1 – 0.5µm. After 2 hours at 1000°C, the oxide is still uneven with features which again follow the grinding direction of the pre-oxidised surface (Figure 5.7(a)). The oxide grains are the facetted type seen in previous examples and are shown in Figure 5.7(b)).

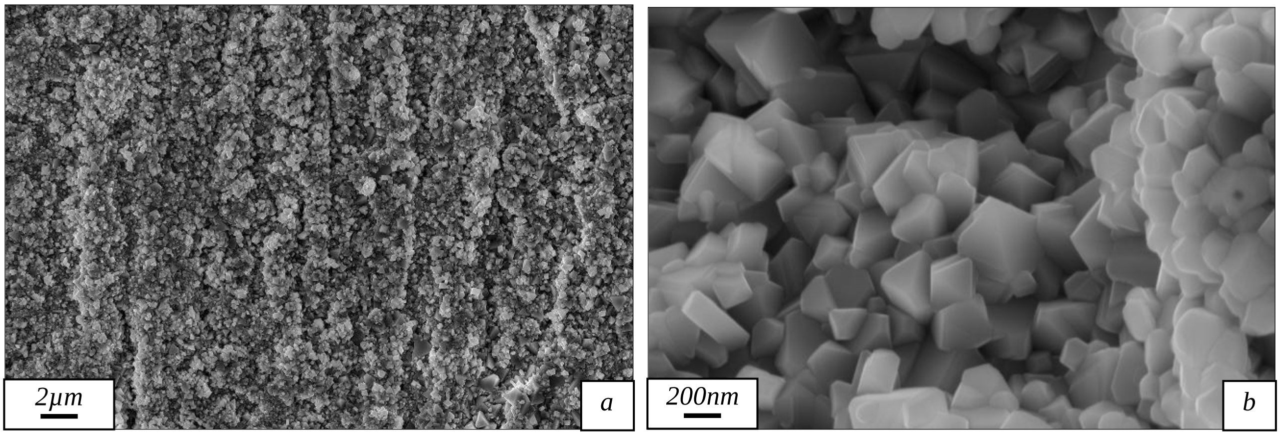

Figure 5.7:- Secondary electron images of the surface oxide formed on laboratory prepared (80 Grit) 304 after oxidation at 1000ºC for 2 hours in simulated combustion products of propane a) lower magnification and b) higher magnification

5.2.5 Oxidation at 1100°C

The oxide scale produced after oxidation at 1100°C for 1 hour is shown in Figure 5.8. At low magnification (Figure 5.8(a)), it can be seen that the surface is predominantly covered in a homogeneous oxide layer but also has a number of large oxide nodules on the surface. The nodules measure from ~200µm to ~ 600µm in diameter and bear no resemblance to any expected feature of the underlying substrate. The base oxide formed after these oxidation conditions has a rumpled structure similar to those presented for shorter oxidation periods and at lower temperatures. The base oxide consists of facetted oxide grains measuring ~ 0.5 - 1 µm (Figure 5.8(b)).

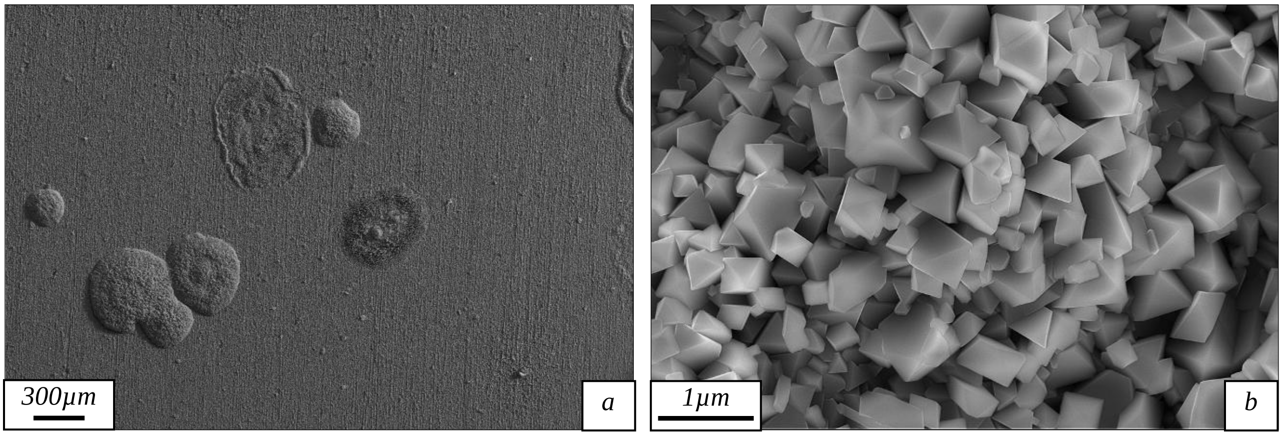

Figure 5.8:- Secondary electron images of the surface oxide formed on laboratory prepared (80 Grit) 304 after oxidation at 1100ºC for 1 hour in simulated combustion products of propane a) overview of the surface and b) high magnification of the base oxide

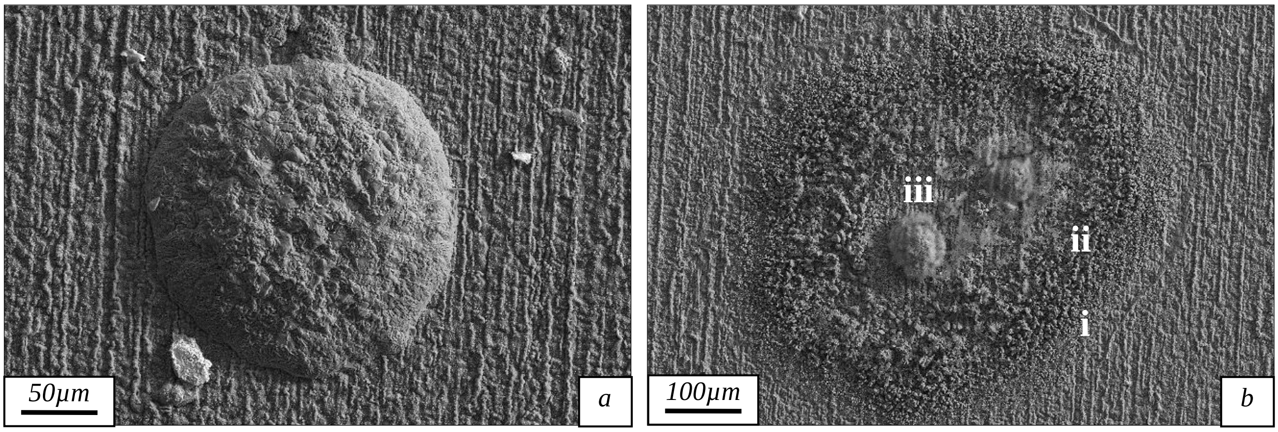

Figure 5.9:- Secondary electron images of nodular surface oxide formed on laboratory prepared (80 Grit) 304 after oxidation at 1100ºC for 2 hours in simulated combustion products of propane a) intact nodule and b) an oxide nodule which has spalled revealing the underlying oxide structure showing (i) fine-grained perimeter, (ii) larger-grained band and (iii) centre of the nodule showing underlying grinding marks

An example of one of the oxide nodules is shown in Figure 5.9 (a). This particular nodule measures ~200 µm in diameter and its surface is smooth. In a number of areas on the surface of the substrate, the top of the nodule has spalled revealing the inside of the growth. In the example shown in Figure 5.9(b), there are three regions: (i) is a fine grained oxide at the perimeter of the nodule, (ii) is a larger grained oxide which forms a band ~100 µm wide around the inside of the perimeter and (iii) is the centre of the nodule where the underlying oxide is still visible.

After a further hour of heat treatment at this temperature, an oxide such as that shown in Figure 5.10 is produced. A large proportion of the oxide produced on this sample has spalled during cooling. The spalled oxide mainly originated at the sample's edge leaving the centre of the specimen un-affected. The oxide found in the centre of the sample consisted of the same facetted oxide grains on a rumpled oxide surface which has been observed for many of the conditions presented (Figure 5.10(b)).

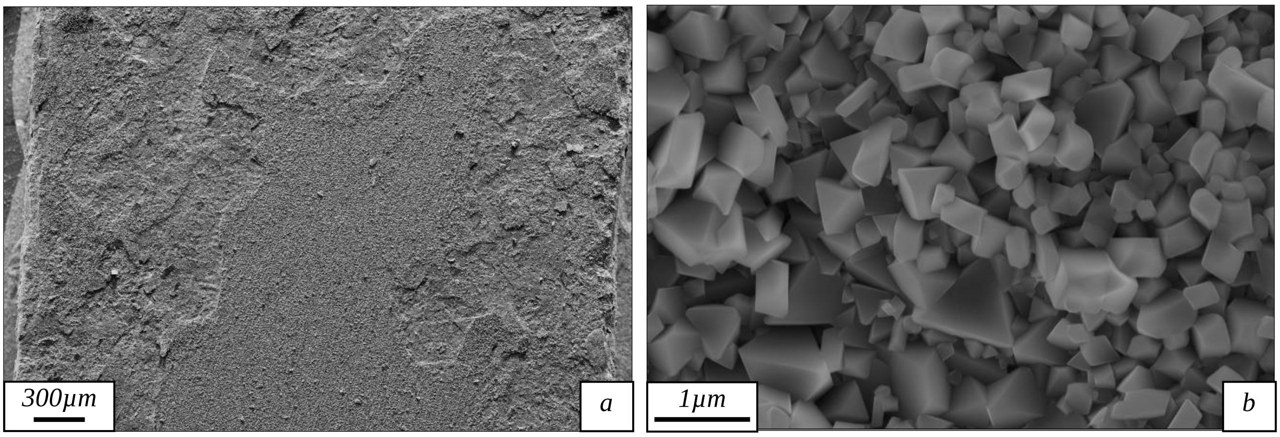

Figure 5.10:- Secondary electron images of the surface oxide formed on laboratory prepared (80 Grit) 304 after oxidation at 1100ºC for 2 hours in simulated combustion products of propane a) an overview of the sample's surface and b) high magnification of the base oxide

5.2.6 Oxidation at 1200°C

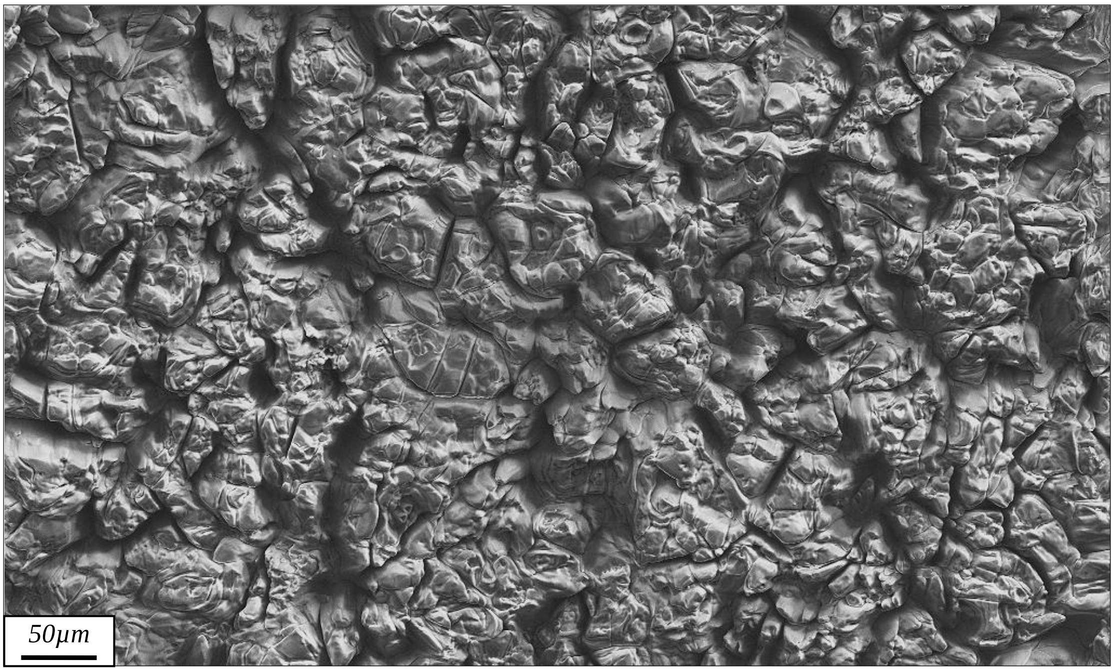

Figure 5.11:- Secondary electron images of the surface oxide formed on laboratory prepared (80 Grit) 304 after oxidation at 1200ºC for 1 hour in simulated combustion products of propane

Heat treatment of 304 stainless steel at 1200°C in the tube furnace produces a very thick oxide which tends to spall on cooling. Figure 5.11 is a secondary electron image of the top surface of a piece of spalled oxide which was collected for examination. When compared to the facetted oxides observed in the early stages of oxidation, the surface has a smooth appearance. However, the oxide is not fully dense in the upper regions with large crevices evident in the surface. In cross-section, the remaining oxide on the spalled regions has the structure shown in Figure 5.12.

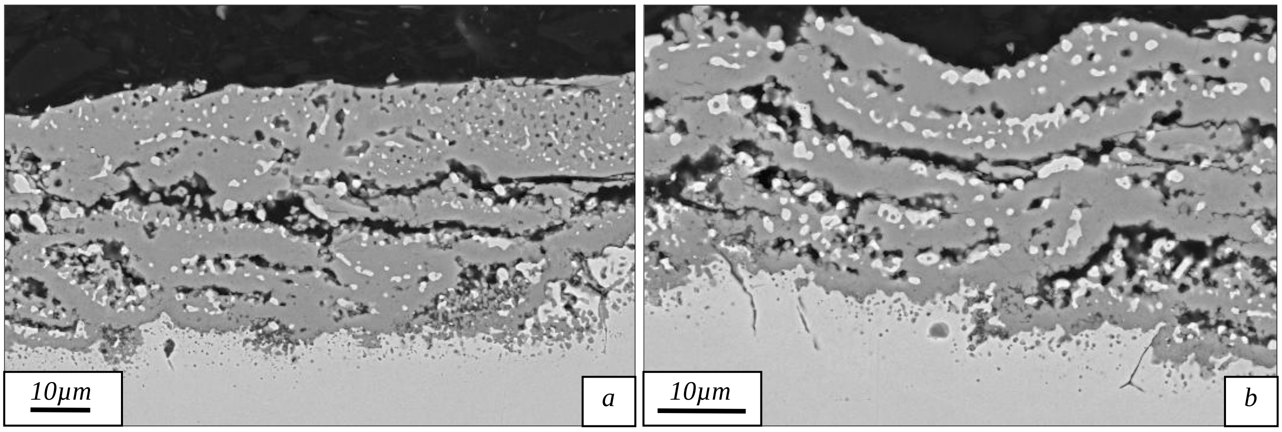

Figure 5.12:- backscattered electron images of cross-sections of the oxide formed on laboratory prepared (80 Grit) 304 after oxidation at 1200ºC for 1 hour in simulated combustion products of propane a) and b) show two separate regions

This particular area shows five layers of oxide scale which consist of oxide mixed with small metallic particles. The small metallic particles tend to reside in the top parts of the layers. The presence of these metallic particles suggests the remaining oxide on the surface of the metal after scale spallation, is in-fact a sub-surface oxide region. Results of oxide scales produced under other oxidation conditions but with similar internal oxide regions are shown elsewhere in this thesis (Chapter 4). EDS maps of an area similar to that in Figure 5.12 are shown in Figure 5.13(a-d). The chemical distributions reveal that the oxide consists of primarily chromium rich oxides with very low counts detected for iron. The metallic particles within the scale are enriched with nickel with no detectable presence of chromium or iron indicating that these metallic particles are almost pure nickel. As well as these metallic particles, a small level of nickel enrichment is present at the interface between the oxide and the substrate.

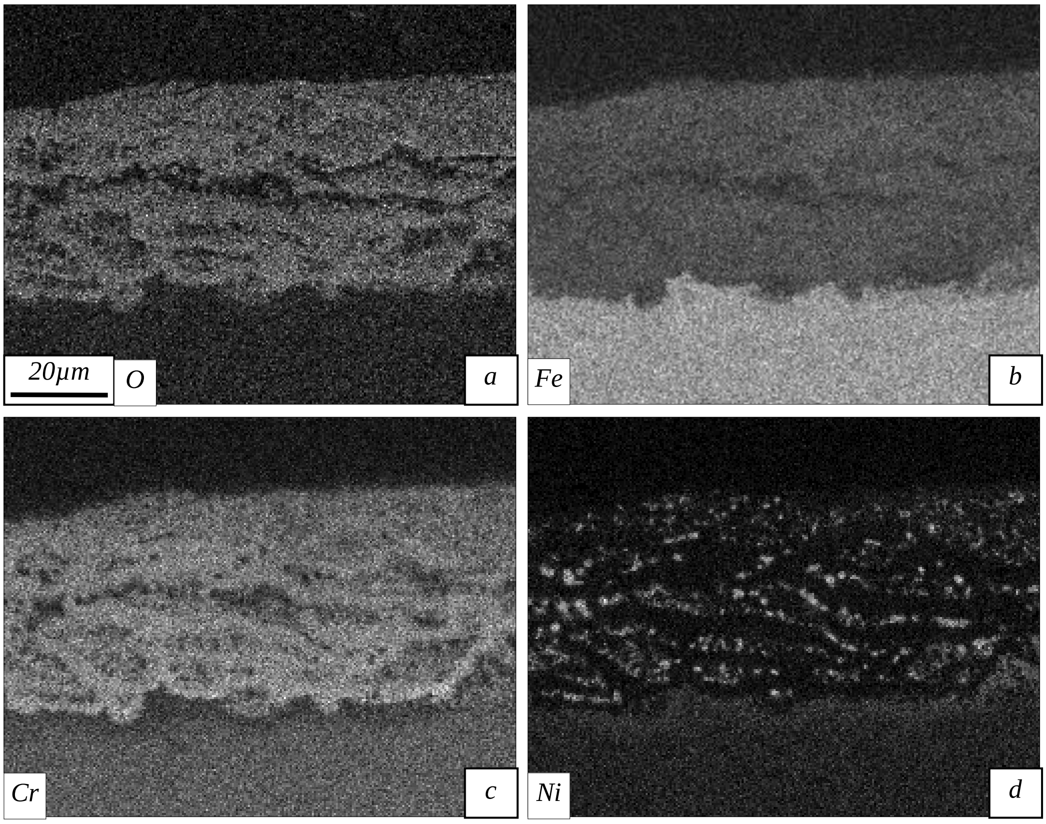

Figure 5.13:- EDS maps of the cross-section of the oxide formed on laboratory prepared (80 Grit) 304 after oxidation at 1200ºC for 1 hour in simulated combustion products of propane showing a)oxygen, b)iron, c)chromium and d) nickel

In an attempt to establish whether the nodules formed after heat treatment of 304 at 1100°C for 1hour also formed at 1200°C after shorter heat treatments, experiments were carried out for times of 5, 10, 20 and 30 minutes oxidation time at a temperature of 1200°C. Overviews of the resulting oxide scales are shown in Figure 5.14. After 5 minutes, the surface has a homogeneous oxide covering its entire surface. The scars on the surface of the oxide are related to the underlying surface finish. There are some small regions which can be said to have enhanced oxide growths which are assumed to be on grain boundaries. As well as these "macroscopic" details a higher magnification view is shown in Figure 5.15. The majority of the surface oxide consists of a fine-grained oxide with a size of <0.5 µm with protrusions of oxide creating a rumpled structure which suggests that the oxide formed is voluminous in nature. After this short period of oxidation, and chromium's high affinity to oxygen, the oxide making up this base oxide can be assumed to be chromia. In a number of other parts of the oxide, small oxide nodules have formed such as the one shown in Figure 5.16(b). This particular feature is an agglomeration of small octahedron shaped crystals which measure ~1-2 µm in diameter. The nodule itself measures ~10 µm in diameter. Nodules of this type are far more prevalent in the early-stage reheat of duplex grades and their formation will be discussed in detail in Chapter 11.

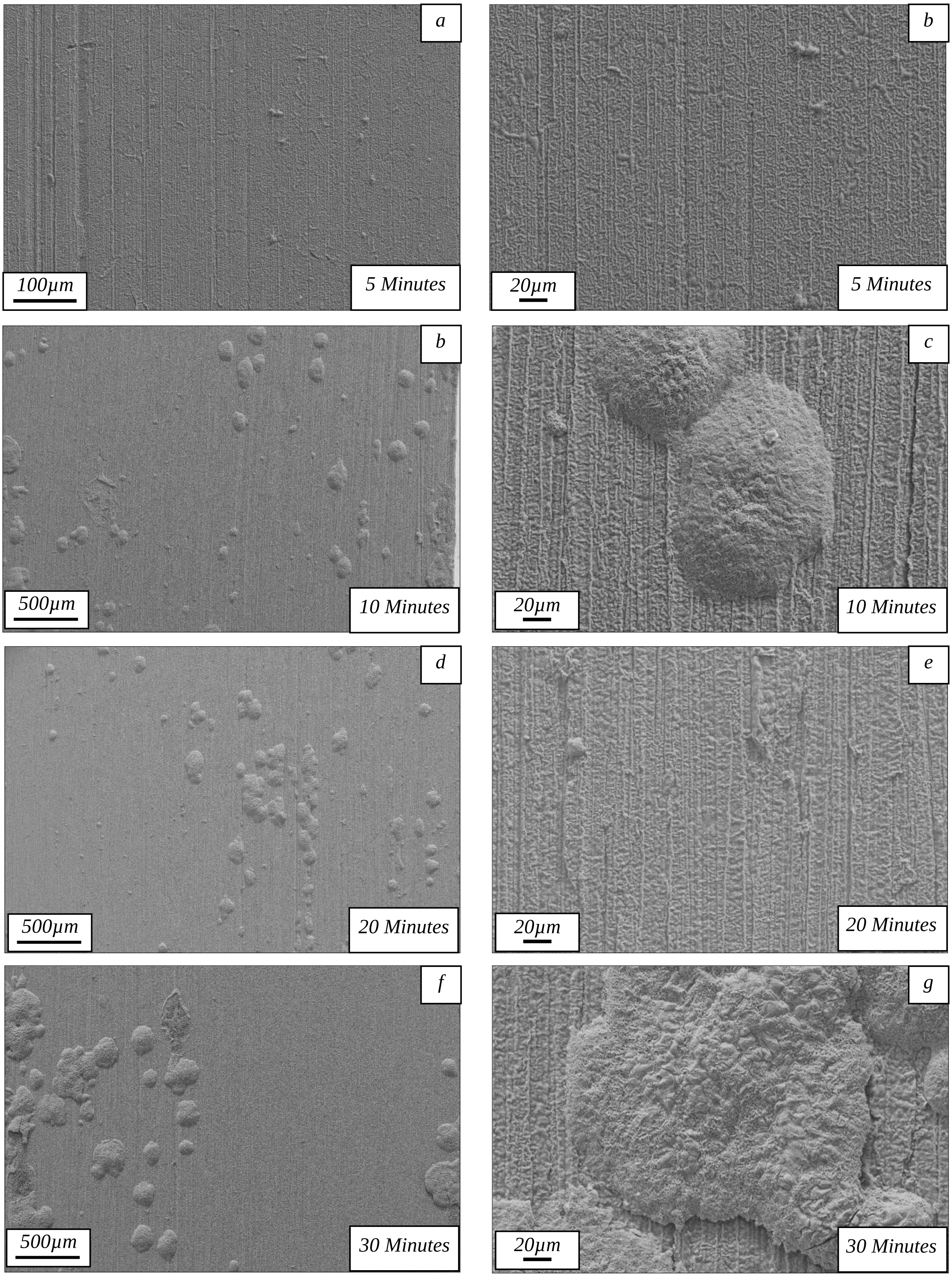

Figure 5.14:- Secondary electron images of oxide formed on laboratory prepared (80 Grit) 304 after oxidation at 1200°C for times of a+b) 5 minutes, c+d) 10 minutes, e+f) 20 minutes and g+h) 30 minutes in simulated combustion products of propane

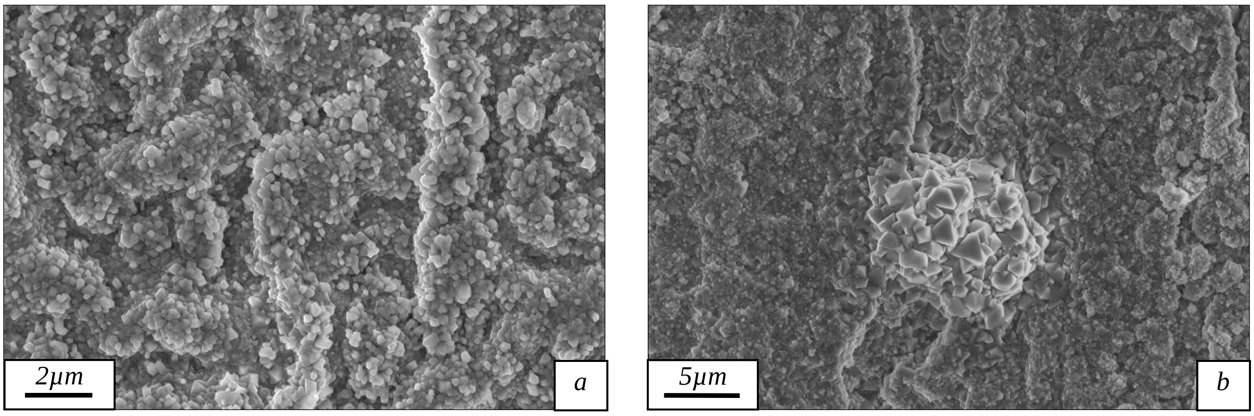

Figure 5.15:- Secondary electron image of the oxide formed on laboratory prepared (80 Grit) 304 after oxidation at 1200ºC for 5 minutes in simulated combustion products of propane a) lower magnification of the base oxide and b) high magnification of an oxide nodule

After 10 minutes at 1200°C, the material has developed large blisters on its surface. The example shown in Figure 5.14(c) measures ~100 μm in diameter and has a smooth surface. The nodules reside upon a base oxide which has scars which resemble the surface preparation marks present prior to heat treatment. A higher magnification image of the underlying base oxide is shown in Figure 5.16

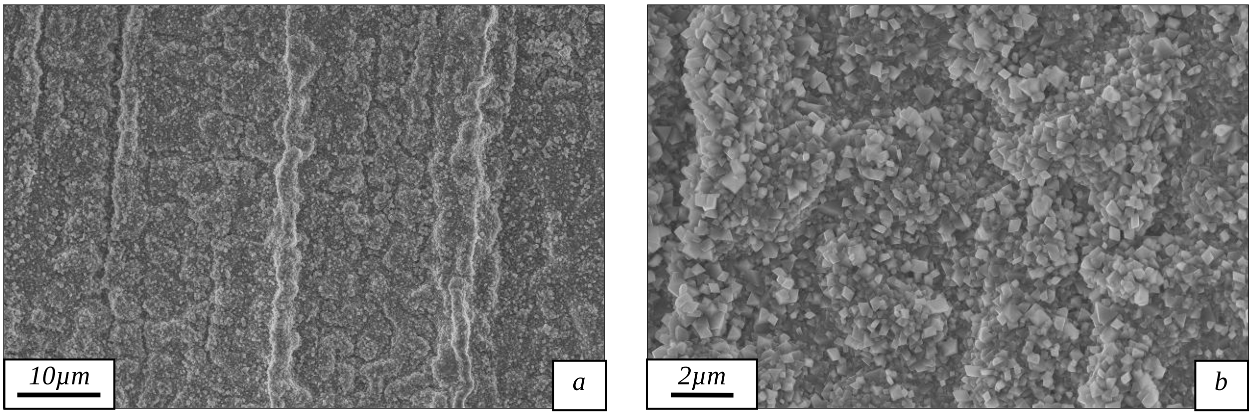

Figure 5.16:- Secondary electron image of the oxide formed on laboratory prepared (80 Grit) 304 after oxidation at 1200ºC for 10 minutes in simulated combustion products of propane a) lower magnification of the base oxide and b) high magnification of the base oxide

As with the example shown for the shorter time of 5 minutes, the base oxide consists of small oxide grains which form a rumpled oxide layer. However, differences are observed in the shape of the grains. In this example there are a number of facetted grains present within the oxide as opposed to the round grains seen in Figure 5.15.

The oxide formed on the substrate heated to 1200°C for 20 and 30 minutes show identical oxide structures. Large blisters are present on the surface of a base oxide. In general the oxide blisters are larger than those observed after shorter times. A number of regions were found where the blister had spalled revealing the underlying oxide (Figure 5.17).

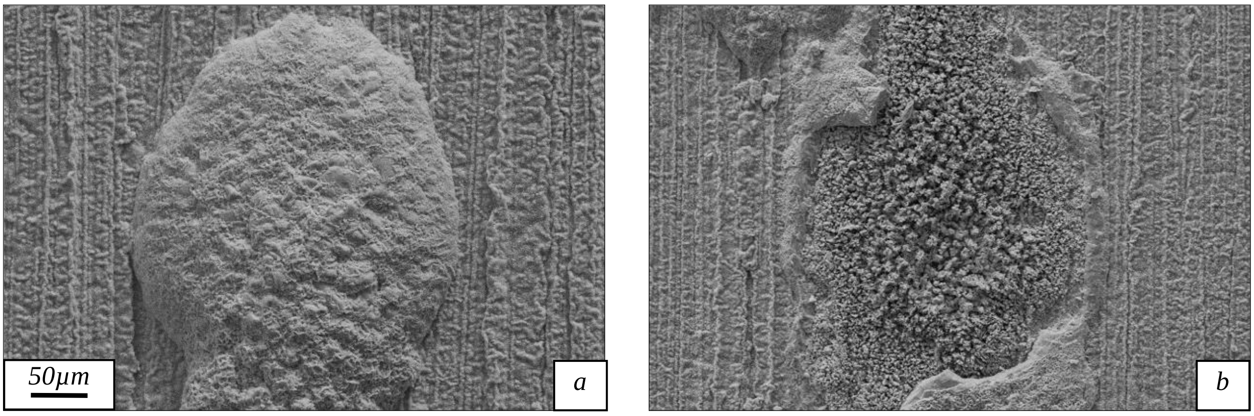

Figure 5.17:- Secondary electron image of a the oxide formed on laboratory prepared (80 Grit) 304 after oxidation at 1200ºC for 20 minutes in simulated combustion products of propane showing a) an oxide nodule and b) an oxide nodule which has spalled

The surface of the blisters is smooth in nature with a grain size in the region of 10µm. The oxide present within the centre of the spalled nodule is granular in nature and has grown independently of the blister i.e. it was not attached. The oxide grains revealed when the blister spalled are largest in the centre of the blister and their size decreases as they are found closer to the perimeter.

EDS maps (Figure 5.18) of the blisters reveal that they consist of mainly iron rich oxide. The base oxide surrounding the blisters has been confirmed as a chromium oxide whereas the blister itself does not contain any chromium. Manganese (although only present as an impurity in 304 stainless steel) is present within some parts of the base oxide and also in specific areas of the blisters' surface. These areas seem to follow oxide grain boundaries on the surface suggesting that manganese rich oxides are growing through the grain boundaries. Interestingly the region where the highest counts of manganese are situated in the base oxide (identified with the dashed circle) also correspond to a region in the chromium map where counts are at their lowest.

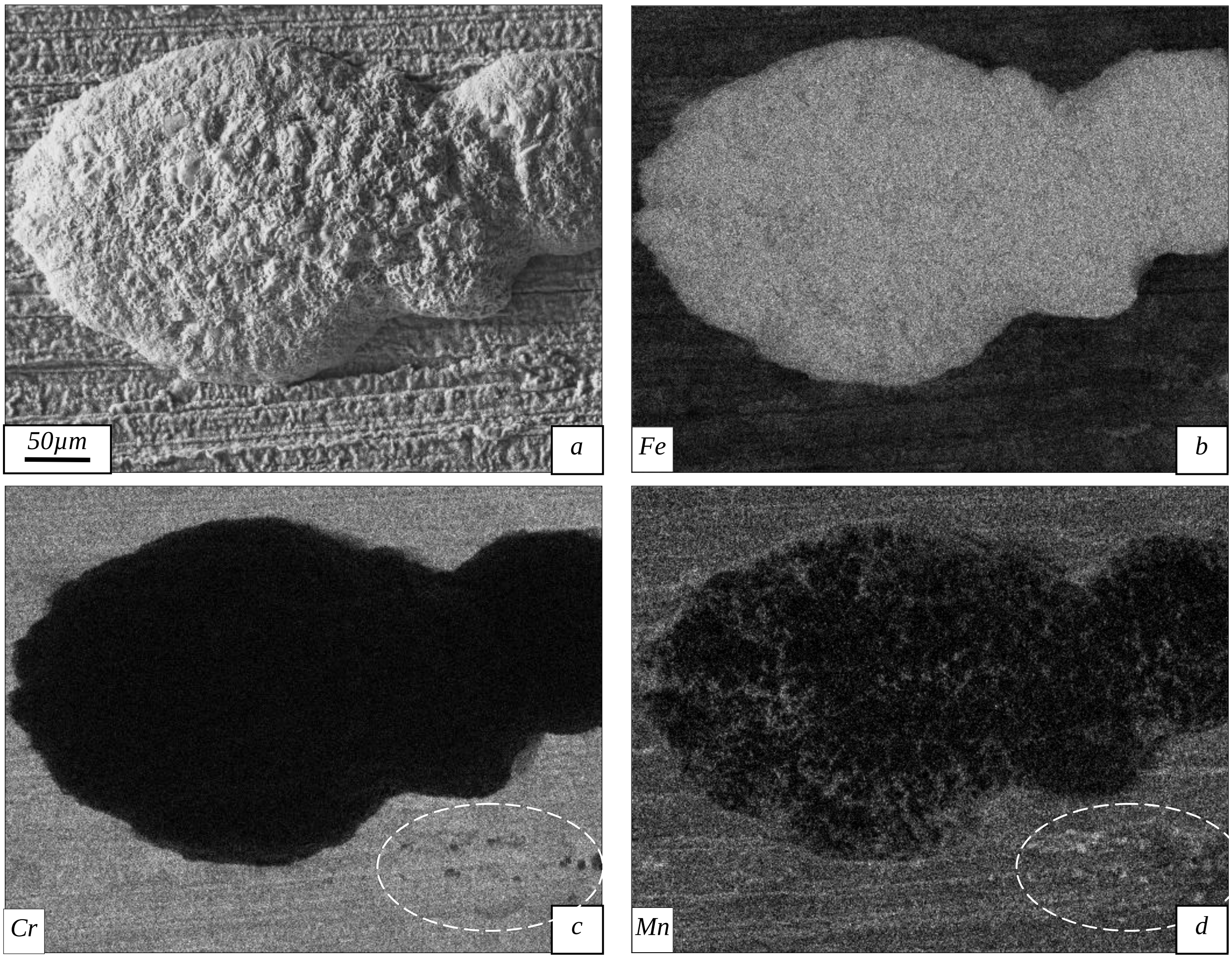

Figure 5.18:- a) Secondary electron image with accompanying EDS maps of b)iron, c)chromium and d) manganese of a nodule formed on laboratory prepared (80 Grit) 304 after oxidation at 1200ºC for 30 minutes in simulated combustion products of propane. The ellipse highlights a region of the oxide where there is a high manganese count in Figure 5.18(d) and a low chromium count in Figure 5.18(c)

In the spalled region, the chemical maps (Figure 5.19) show a similar pattern with the centre region shown as iron rich with little chromium and manganese present. However, the underlying oxide does have a small amount of chromium in the perimeter regions which is the fine-grained area shown in the SEM image. Here it is possible to distinguish manganese rich “veins” within the oxide of the intact blister (to the right of the image) but no manganese in the underlying oxide.

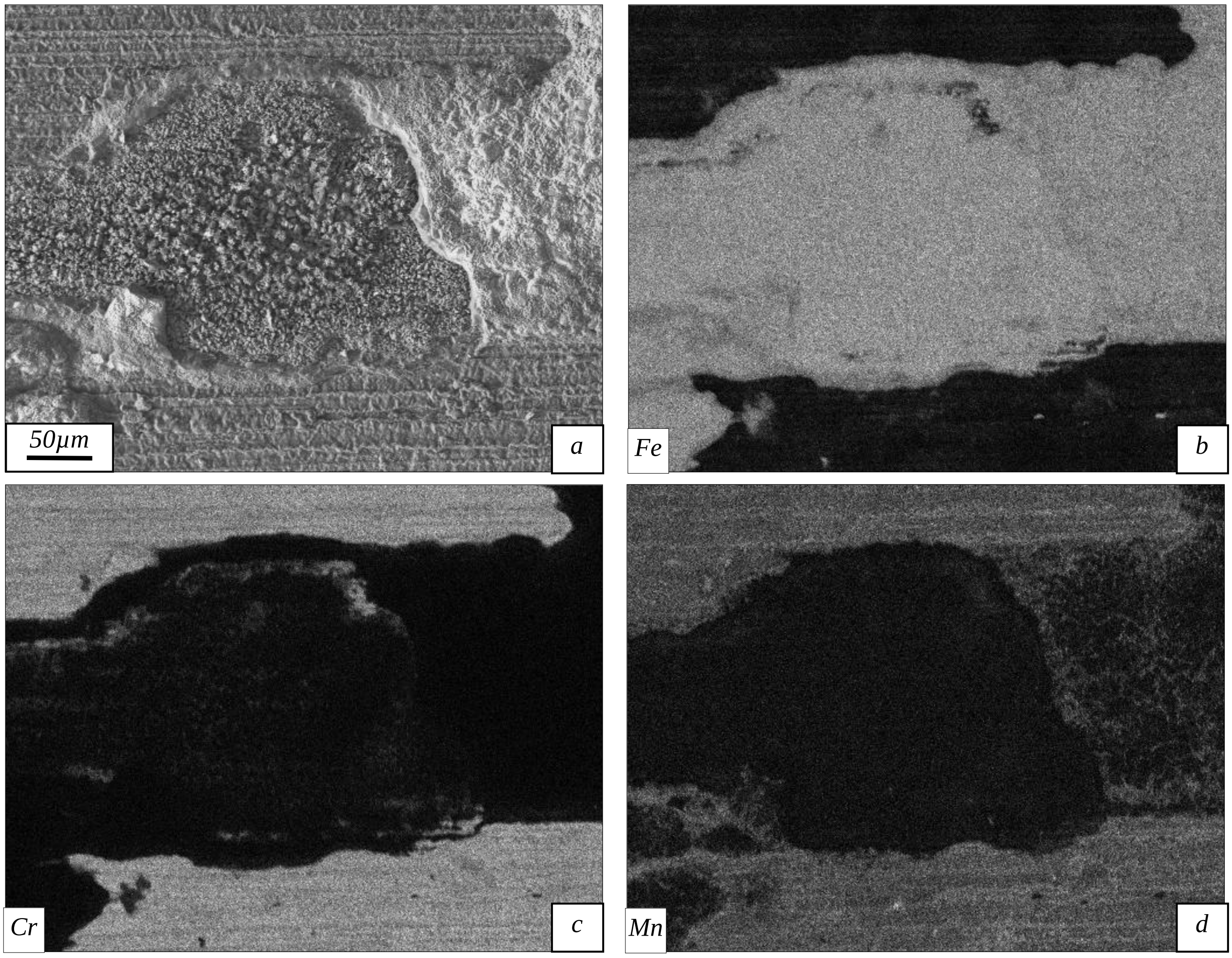

Figure 5.19:- a) Secondary electron image with accompanying EDS maps of b)iron, c)chromium and d) manganese of a spalled nodule on laboratory prepared (80 Grit) 304 after oxidation at 1200ºC for 30 minutes in simulated combustion products of propane

5.3 Type 316L Stainless Steel

5.3.1 Oxidation at 700°C

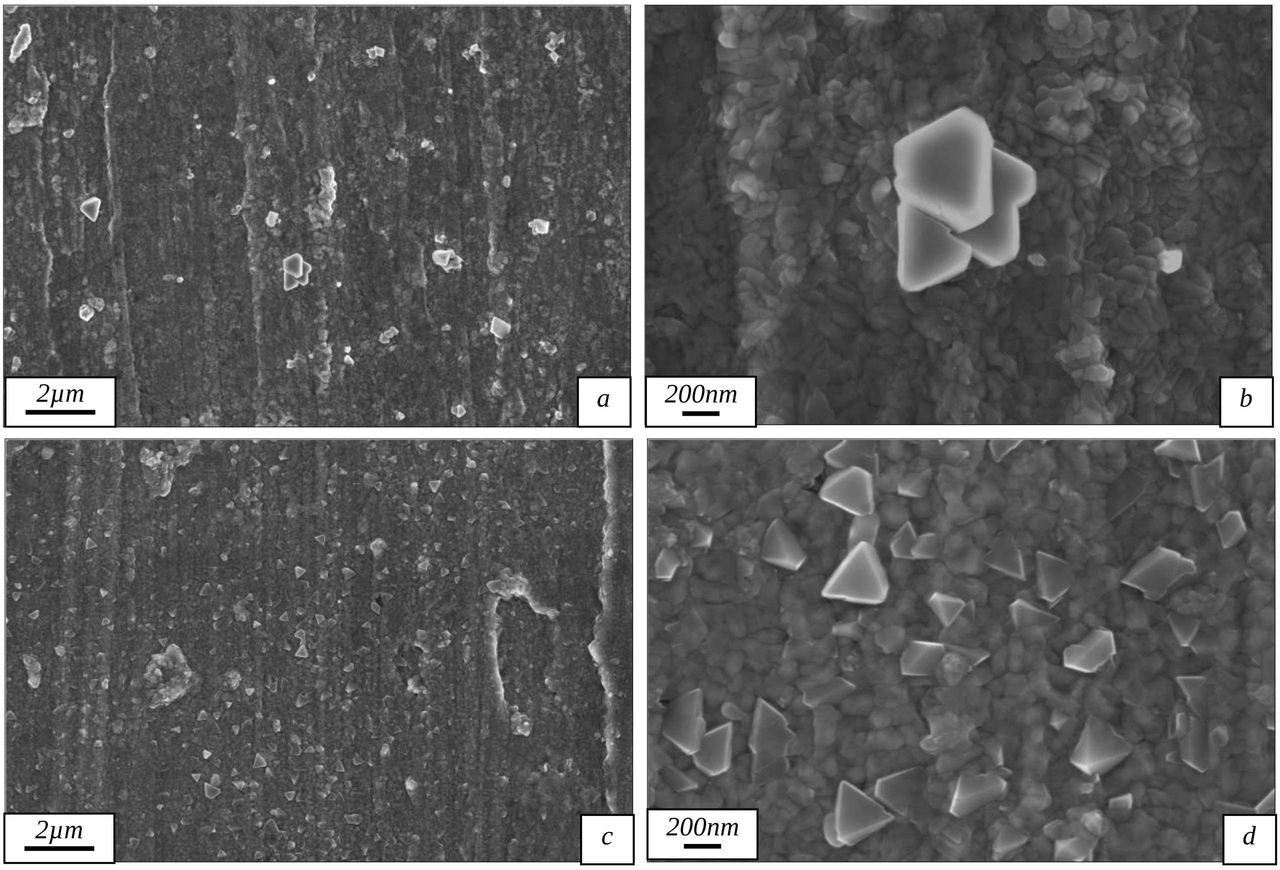

Figure 5.20:- Secondary electron images of the surface oxide formed on laboratory prepared (80 Grit) 316L after oxidation at a+b) 700ºC for 1 hour and c+d) 2 hours in simulated combustion products of propane

After oxidation at 700°C for 1 hour (Figure 5.20 (a and b)), the oxide scale on 316L consists of small globular type oxide grains (which are dark in the micrographs) with a number of larger more facetted oxide grains on the surface. In the area marked in Figure 5.20(b), three facetted grains have grown together. It is possible that this small agglomeration of facetted oxide grains is a nucleation site for the formation of an oxide nodule on the surface of the metal. After a further hour of oxidation, (Figure 5.20 (c and d)), the majority of the surface is covered in the globular type oxide crystal. Facetted oxide grains are present and there are a greater number on the surface than the shorter oxidation period.

5.3.2 Oxidation at 800°C and 900°C

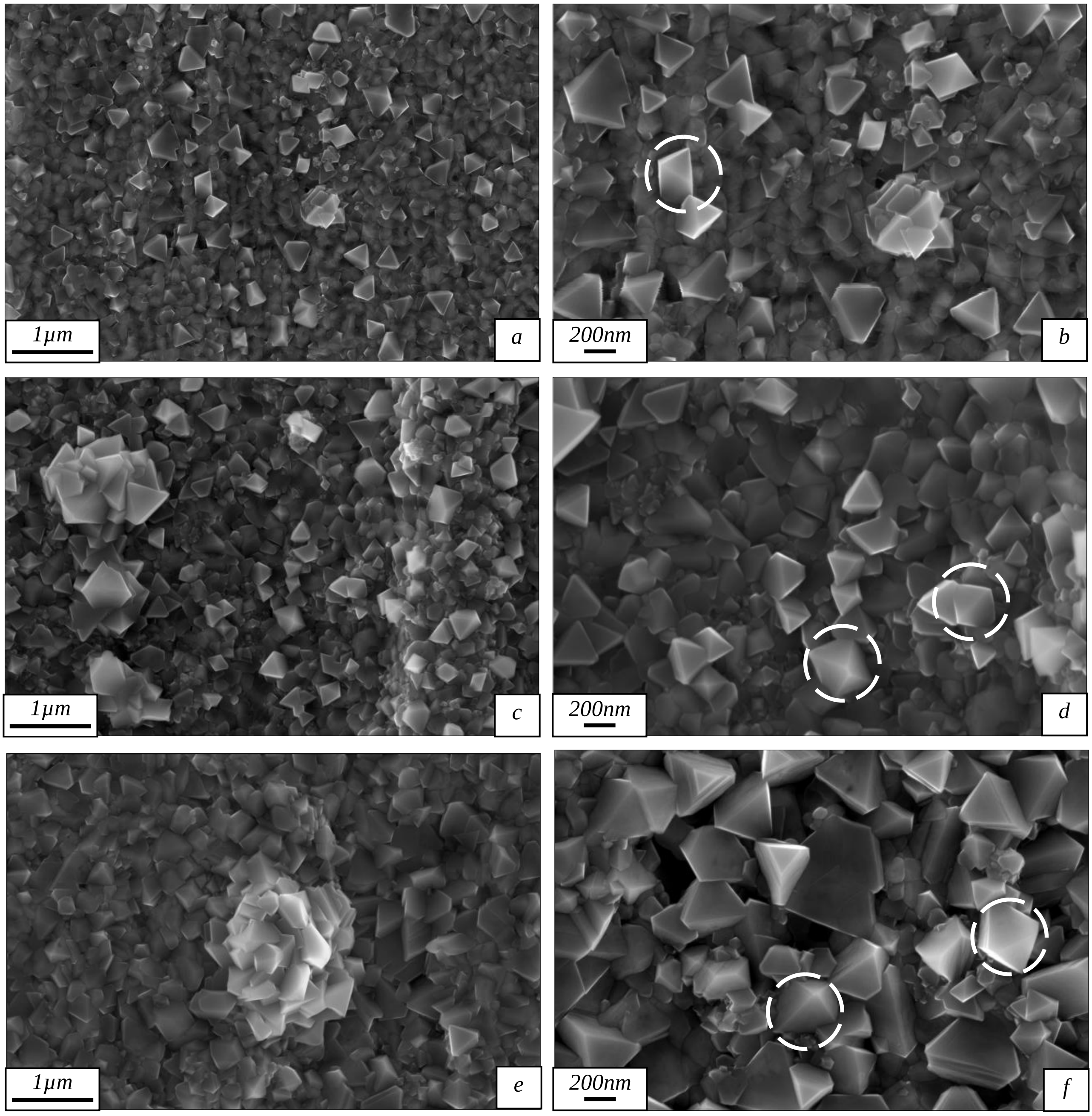

Figure 5.21:- Secondary electron images of the surface oxide formed on laboratory prepared (80 Grit) 304 after oxidation at (a+b)800ºC for 2 hours, (c+d)900°C 1 hour and (e+f) 900°C 2 hours in simulated combustion products of propane. The circles indicate oxide grains which are octahedral

Figures 5.21 (a – f) show the progression of oxide formation on 316L with an 80 Grit surface finish. The oxide produced at the least severe condition, i.e. at the lowest temperature and shortest time (Figure 5.21 (a and b)) consists of a base oxide of globular oxide grains with an even distribution of facetted oxide grains on its surface. By raising the temperature to 900°C, the oxide shown in Figure 5.21 (c) and (d) is produced. The surface is made up of facetted oxide grains only which have presumably grown on top of the underlying globular oxide grains. After the most severe heat treatment i.e. the highest temperature and longest time (shown in Figure 5.21 (e) and (f)), the oxide is made up of larger oxides crystals. All the facetted oxide grains in these images can be said to be tetrahedron in shape which can be confirmed by the crystals indicated by the dashed circles. As well as the base oxide, on each of the conditions shown, agglomerations of facetted oxide grains can be found within the oxide. These vary from small 400nm diameter agglomeration in Figure 5.21(b) to a fairly large feature shown in Figure 5.21(e). These agglomerations are likely to be the early stages of oxide nodules formed during the later stages of reheat.

5.3.3 Oxidation at 1000°C

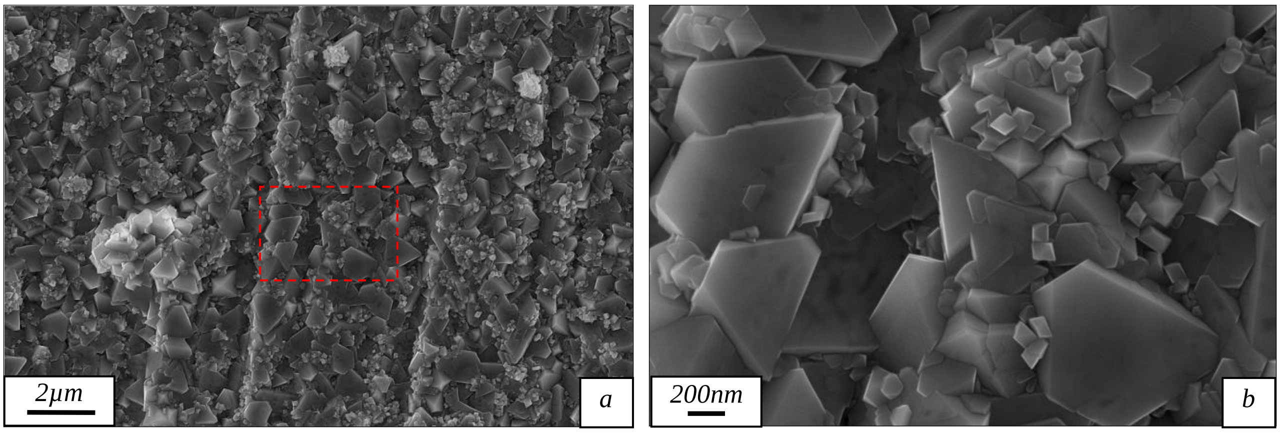

Figure 5.22:- Secondary electron images of the surface oxide formed on laboratory prepared (80 Grit) 304 after oxidation at 1000ºC for 1 hour in simulated combustion products of propane showing a) lower magnification with a red square showing the area in b) at higher magnification

Heat treatments at 1000°C produce the oxide which is shown in Figure 5.22. It consists of relatively large oxide grains measuring 1 – 1.5µm and smaller oxide grains measuring ~100nm in diameter on the surface. After 2 hours at this temperature, the oxide shown in Figure 5.23 is produced. The smaller facetted oxide grains have grown to cover almost the entire visible surface. As well as this, the oxide has also formed ridges indicating that it has experienced enhanced oxide growth.

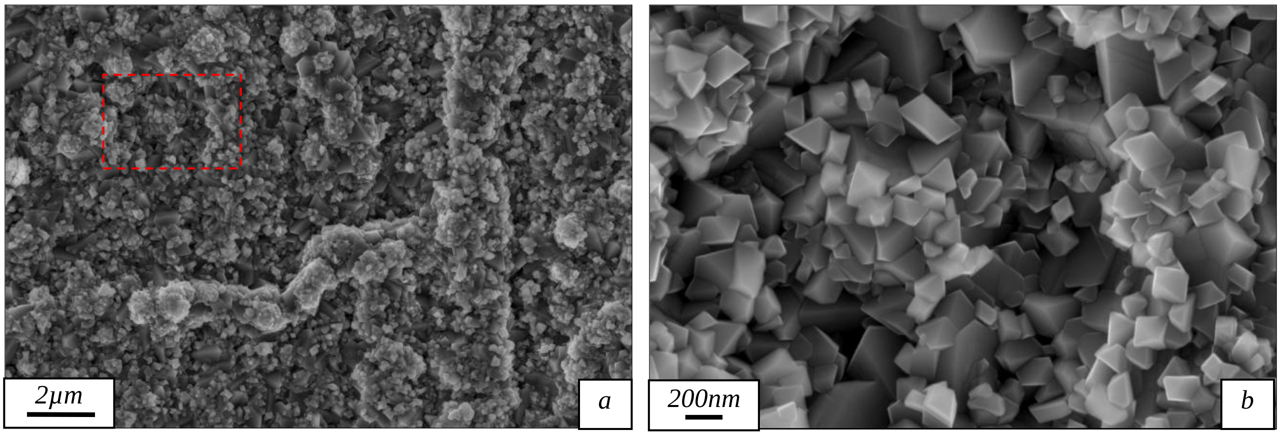

Figure 5.23:- Secondary electron images of the surface oxide formed on laboratory prepared (80 Grit) 304 after oxidation at 1000ºC for 2 hours in simulated combustion products of propane showing a) lower magnification with a red square indicates the area shown in b) at higher magnification

5.3.4 Oxidation at 1100°C

Oxidation of 316L stainless steel at 1100°C for 1 hour produces the oxide shown in Figure 5.24. At low magnification the oxide consists of a base oxide on the majority of the surface with areas where oxide growth is enhanced producing oxide nodules on the surface. At higher magnification, the base oxide has a rumpled surface with many oxide ridges on the surface which bear no resemblance to the underlying alloy microstructure or grinding scars.

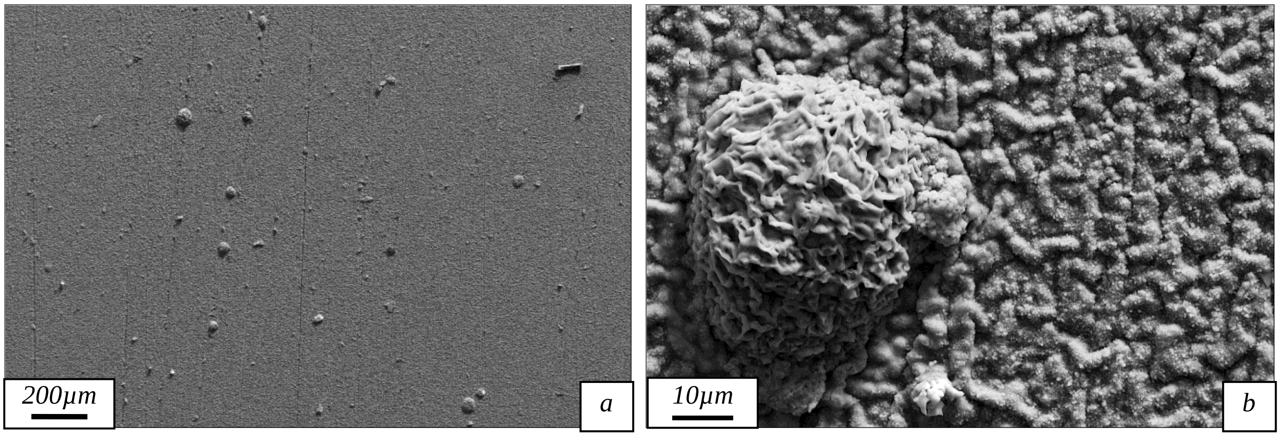

Figure 5.24:- Secondary electron images of the surface oxide formed on laboratory prepared (80 Grit) 316L after oxidation at 1100ºC for 1 hour in simulated combustion products of propane showing a) surface overview and b) higher magnification of the surface

Figure 5.25 shows TEM micrographs of a FIBSEM prepared cross-section of an oxide ridge. This particular oxide ridge is out of contact with the substrate due to a large void which has formed between the outer shell and the substrate. To the top-right of the image, an additional oxide ridge can be seen which is in contact with the substrate (i). It is unlikely that the formation of an oxide would cause deformation of the substrate to this extent so it must be assumed that this oxide ridge has formed on a substrate grinding mark. The oxide shown in this TEM sample is of a uniform thickness of ~1µm and has a homogeneous grain size apart from a small number of larger grains at the outer edge of the shell. Underneath the ridge, two areas of oxide are visible which are amorphous. EDS analysis of the oxide has shown that the amorphous oxide is silica, the fine grained oxide both in the ridge over the void and in contact with the substrate is chromia and that the outer oxide grains are spinel type oxides with chromium and manganese components.

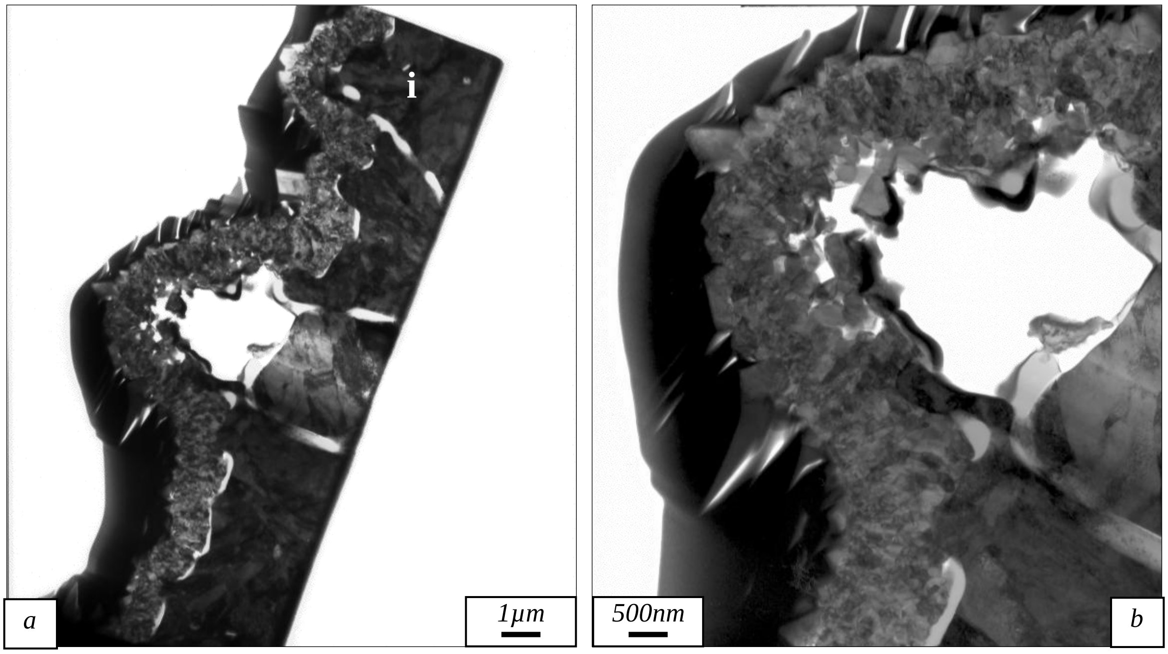

Figure 5.25:- Bright field TEM images of the a cross-section of the surface oxide formed on laboratory prepared (80 Grit) 316L after oxidation at 1100ºC for 1 hour in simulated combustion products of propane showing a) lower magnification and b) higher magnification

A further hour of heat treatment at a temperature of 1100°C produces the oxide shown in Figure 5.26. The nodules are much larger than those produced after 1 hour at the same temperature. The same base oxide is observed. The structure of the shell of the nodule is smooth with the grains appearing to originate from the centre of the growth.

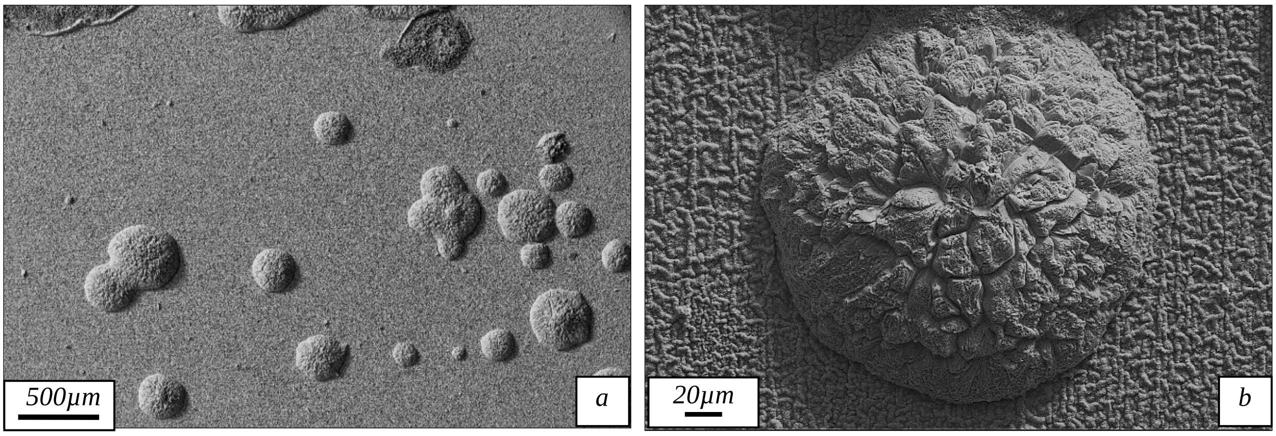

Figure 5.26:- Secondary electron images of the surface oxide formed on laboratory prepared (80 Grit) 304 after oxidation at 1100ºC for 2 hours in simulated combustion products of propane showing a) low magnification surface overview and b) higher magnification image of an oxide nodule

As with the examples shown for 304 stainless steel, in a number of areas the shells of the nodules have spalled revealing the underlying oxide structure (Figure 5.27). The figure shows that this particular nodule measures ~500µm in diameter and consists of (i) a perimeter where the shell was attached, (ii) an area measuring ~100µm wide where oxide grains have formed with their sizes increasing towards the centre of the nodule and (iii) a centre region which has a structure which resembles the base oxide formed on the surface.

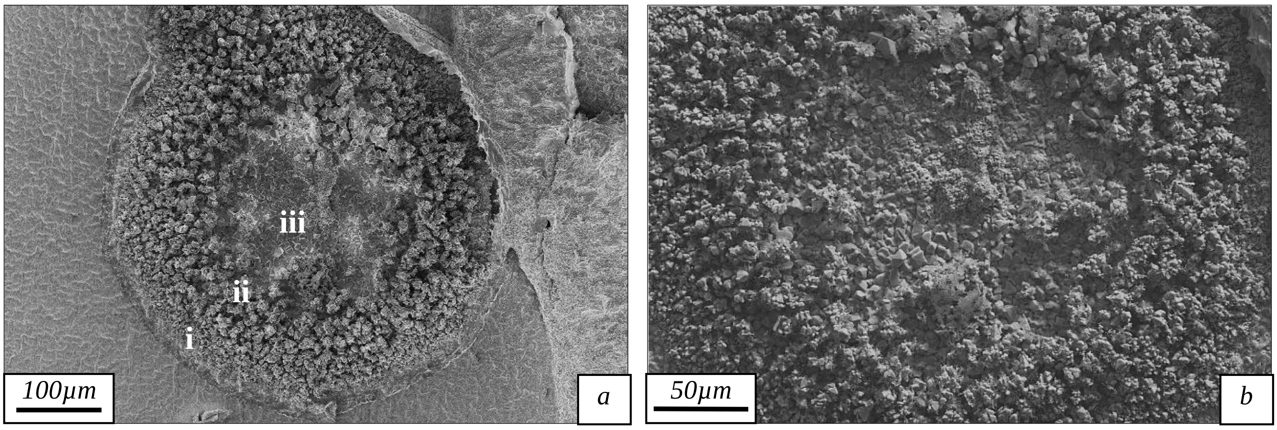

Figure 5.27:- Secondary electron images of a spalled oxide nodule formed on the surface of laboratory prepared (80 Grit) 304 after oxidation at 1100ºC for 2 hours in simulated combustion products of propane showing a) lower magnification with markers showing (i) perimeter grains, (ii) grain sizes increasing towards the nodule centre and (iii) the nodule centre and b) higher magnification of the nodule's centre

6 DISCUSSION – OXIDATION OF AUSTENITIC STAINLESS STEELS

6.1 Introduction

In this chapter, the results relating specifically to the oxidation of austenitic stainless steels will be discussed with reference to the literature. In this section, results obtained during heat treatment in both the tube furnace atmosphere and in ambient air will be discussed. These results include both the oxide produced in the early stages in the tube furnace and during the later stages in the tube furnace and the ambient air box furnace.

The phenomena treated here will include the formation of external oxide layers and resulting chemical distribution, sub-surface oxidation: including particle and dendritic types as well as sub-surface oxide layering, the effect of reheat on an as-cast substrate and finally the effect of oxidation of austenitic grades in a simulated reheat atmosphere which leads to the distribution of oxide nodules on the surface.

6.2 Chemical Distribution

Knowledge of the chemical distribution throughout the scale can allow a greater understanding of the kinetics of the elements through the scale and lead to an appreciation of the oxidation mechanisms involved.

Oxidation of 316L stainless steel at 1000°C for 1, 2 and 3 hours (Figures 4.1, 4.2 and 4.3 -4.4 respectively), produces an oxide which is initially a thin but highly damaged oxide scale which, after longer heat treatments, develops into a thicker multi-layered oxide scale. The oxide structure after oxidation at 1000°C for 3 hours is made up of two layers which can be defined by their chemical composition. The layer closest to the substrate is a chromium rich oxide (with a small iron content) and the outermost layer is an iron rich oxide (with a small amount of chromium). As well as these oxide scale layers, an apparent nickel enrichment forms within the substrate at the metal / oxide interface suggesting that the nickel is not oxidised at this temperature.

Oxidation of 316L at a temperature of 1200°C for 2, 3 and 4 hours (Figures 4.8, 4.10 and 4.19 respectively) results in a thin chromium rich oxide after 2 hours of oxidation and the formation of a multi-layered oxide after oxidation for longer periods of time. The layer closest to the substrate after oxidation for 4 hours at 1200°C is a fine-grained, chromium-rich oxide. In a number of areas, the oxide is identified as having the corundum structure (Figure 4.21) which suggests the presence of Cr_2O_3. The majority of the layer, however, is made up of a spinel type oxide rich in iron and chromium with some minor nickel content. Towards the outer edge of the scale, the oxide is rich in iron which, together with the fact that this also has the corundum structure (Figure 4.21), can be identified as haematite. The presence of these layers is consistent with the literature where a number of authors found a similar structure [Yearian, Randell and Longo (1955), Yearian, Derbyshire and Radavich (1956) and Peraldi and Pint (2004)]. EDS has revealed that this three-layer structure is also observed for the scale formed after 3 hours at 1200°C, however, after 2 hours the elements have very little organisation and the layer structure is not yet established. Instead a thin fine-grained layer has formed which is in the same order of thickness and with a similar grain size to the lowest layer of the oxides formed after longer times. As the chemical distribution here is very mixed, it can be suggested that this particular scale is at a transition between a protective oxide (i.e. a thin chromium rich oxide layer), and a non-protective oxide. This is further supported by the fact that a slight depletion of chromium is detected in the upper region of the substrate and that the small grains on the upper part of the oxide have a higher iron content.

The major differences observed with increasing temperature are that oxides produced after heat treatment at 1200°C are thicker than those produced at 1000°C, the outer iron rich oxides are dual layered and the nickel enrichment of the substrate is reduced. As well as this reduction in nickel enrichment, there is a small amount of nickel within the intermediate oxide layer of oxides formed at 1200°C. These differences arise because the temperature is sufficiently higher to increase the overall oxidation rate of the material. This increase in oxidation rate allows an oxide to form quicker which also means that at a given heat treatment time, more iron will have oxidised which allows the haematite layer to thicken. This explains why a haematite layer is visible after oxidation at 1200°C (Figure 4.21), but not visible after oxidation at 1000°C (Figure 4.4). The lack of nickel enrichment observed after oxidation at 1200°C is probably caused by an increase in diffusion rates of nickel, both in the substrate and within the oxide layers, at the higher temperature which has allowed it to be included in the intermediate oxide layer forming a spinel type oxide with iron and chromium.

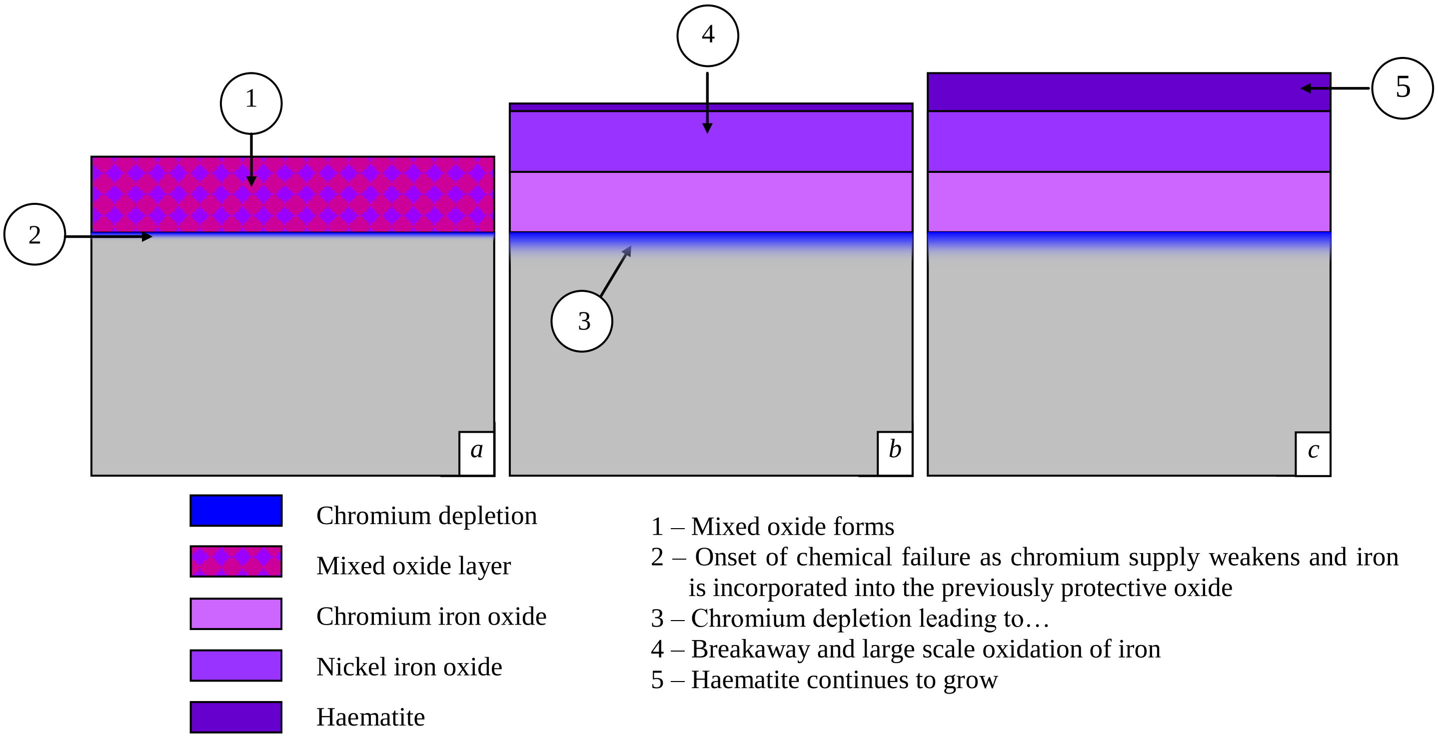

1 – Mixed oxide forms
2 – Onset of chemical failure as chromium supply weakens and iron is incorporated into the previously protective oxide
3 – Chromium depletion leading to…
4 – Breakaway and large scale oxidation of iron
5 – Haematite continues to grow

Figure 6.1: Schematic diagram showing oxidation of austenitic stainless steel in air at 1200°C showing a) formation of a mixed oxide layer, b) the onset of a multi layered growth and c) continued external layer growth

The structure formed after long heat treatments (at both 1000°C and 1200°C), agrees with the description for the oxidation of iron – chromium alloys by Birks *et al*. (2006) who give the following explanation for the formation of the external oxide layers: The formation of the predominantly spinel type layer is as follows, firstly a protective Cr_2O_3 will form which will grow slowly whilst consuming the chromium from the underlying alloy. As the substrate effectively then becomes iron rich, the Cr_2O_3 will react with iron to form the spinel $FeCr_3O_4$ which is less protective than Cr_2O_3 and allows faster transport of iron. As oxidation continues, iron diffuses through the $FeCr_3O_4$ where it forms almost pure iron oxides at the outer layer of the scale. Given this explanation, it can be suggested that the formation of the spinel type oxide seen after longer heat treatments begins shortly after 2 hours at 1200°C in ambient air. The presence of $FeCr_3O_4$ and the formation of a haematite layer towards the top of the scale were associated with breakaway oxidation by Morris (1977). The suggestion that breakaway oxidation has occurred after 4 hours is further supported by the fact that there is a chromium depletion at the metal / scale interface (Figure 4.19 (c)). A similar chemical depletion at the metal / scale interface during breakaway has been reported by Otsuka *et al*. (2004). From this knowledge of breakaway oxidation and scale layer formation, a simple timeline of events during the oxidation of stainless steel in air at 1200°C can be postulated and is presented in Figure 6.1.

In terms of industrial reheat at this temperature, it is therefore necessary to ensure that reheat does not continue for periods exceeding 2 hours as after this point, catastrophic oxidation will occur, possibly leading to a reduction in yield and an increase in production costs.

Figures 4.10 and 4.20 show a contradiction to this theory. The EDS graphs show that the chromium is increased towards the metal / scale interface and the iron is depleted. This may suggest that since breakaway has initiated, the iron has been consumed to form the iron oxides found in the scale layers. Chromium has consequently replaced the depleted iron and, because of this, it is very possible that, due to an increased supply of chromium, an additional period of oxidation may occur which could see the growth of further protective oxide layers consisting of chromium-rich oxides.

Although the oxide structures may change with cooling rate, it does not have a significant effect on the chemical distribution within the external scale. After heating to the same temperature and cooled at a slow rate (10°C / min), the same three discrete layers are present within the external scale. There is a chromium rich oxide, an intermediate layer higher in nickel than the other phases and a final iron rich oxide towards the top of the scale (Figure 4.11). This is the same layer structure as is seen in samples oxidised for 4 hours at 1200°C and fast cooled. The cooling rate does, however, have a noticeable affect on the internal oxide region which will be discussed in Section 6.3.1.

In a number of oxide scales produced on the surface of austenitic grades, a needle like structure was observed. Examples of this type of feature are shown in Figure 4.26, although many more examples were seen throughout the study. These needle type structures have been found to be of the corundum structure and reside within a spinel type oxide. A large percentage of the spinel oxide within the parent grains is iron and oxygen with some small quantities of other elements including manganese and chromium. These spinel grains therefore can be approximated to being very similar to magnetite produced during oxidation of pure iron or steel.

This approximation allows an argument for the mechanism of formation of the needles to be presented. The stoichiometry of magnetite varies with differing temperatures with its maximum range being at 1450˚C and its minimum below 650˚C. Between the temperatures of 900˚C and 1300˚C, as used in this study, it can exist within a maximum range of between 57.15 – 57.65 At.% oxygen (Fig. 6.2). The results agree well with this as many of the examples of needle like oxide structures occur at temperatures of 1200°C or above.

This means that when the spinel oxide forms at 1300˚C for example, it will become saturated with oxygen up to the maximum possible in the range of oxygen contents. When the sample is cooled at a relatively slow rate, haematite will begin to precipitate, initially at the grain boundaries where, due to the still elevated temperature, it will begin to grow. The formation of the needle structure occurs when the growing haematite grains encroach into the spinel grains and find a desired growth direction. In this case there appears to be a pathway along one specific atomic plane within the spinel grains which produces the result shown in Figure 4.26 where all needles within a particular grain have the same crystal orientation and same misorientation angle of ~56˚ to the parent grain.

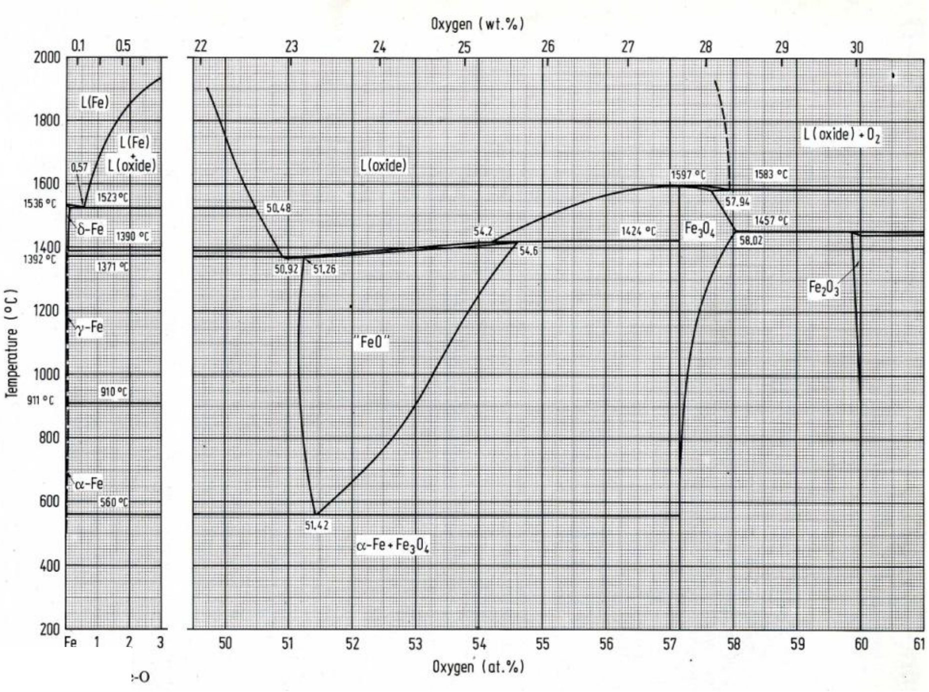

Figure 6.2: Iron-oxygen phase diagram showing varying stoichiometry of magnetite at high temperatures (reproduced from Kubaschewski (1982))

6.3 Sub-surface oxidation

6.3.1 Particulate and dendritic types

Figure 4.11 -4.14 and Figure 4.24 all show a large degree of internal oxidation which consists of particles of oxide to a depth of up to 250µm. This type of oxidation is particularly damaging if produced during industrial reheat as it would not be removed using conventional mechanical descaling techniques. As shown in the EDS maps of these oxide particles, they are generally chromium rich with small quantities of iron within them. Their density and size are reduced as depth into the substrate increases. This is due to the fact that an internal oxidation front will be present with the oxide particles precipitating when optimum oxygen and element concentrations are met [Birks *et al*. (2006)], with the previously precipitated particles experiencing growth as time progresses. The position of this oxidation front is also dependant on the outward diffusion of elements from the substrate.

This type of sub-surface oxidation does not occur at temperatures lower than 1200°C and is more likely to form if the metal is cooled at a slow rate. This dependence on the cooling rate could be due to the fact that at slower cooling rates the metal is held at elevated temperature for longer than it is during faster cooling (Figure 6.3). If the sample was heated to 1200°C and cooled at a rate of 10°C / minute for example, then it will remain above 600°C for 1 hour, this would be substantially longer than a sample cooled in air to room temperature. If t_1 is the time after the start of cooling that the sample is at an elevated temperature (600°C for example), for a fast cooling rate and t_2 is for the slow cooling rate then it can be seen that the sample is at an elevated temperature for a longer period of time. This gives more time for the oxidation process and for the diffusion of oxygen into the substrate. During the cooling process it is likely that the oxide will crack. As can be seen in Figure 4.11 a large crack is present within the oxide scale. In this case it is reasonable to suggest that the cracking may have occurred during cooling. This then allowed further oxidation of the substrate whilst at elevated temperature thus producing the differences between the slow cooled and fast cooled specimens. If the same type of cracking occurred during a faster cool, then there would be less time at elevated temperature so the internal oxidation zone would be less severe.

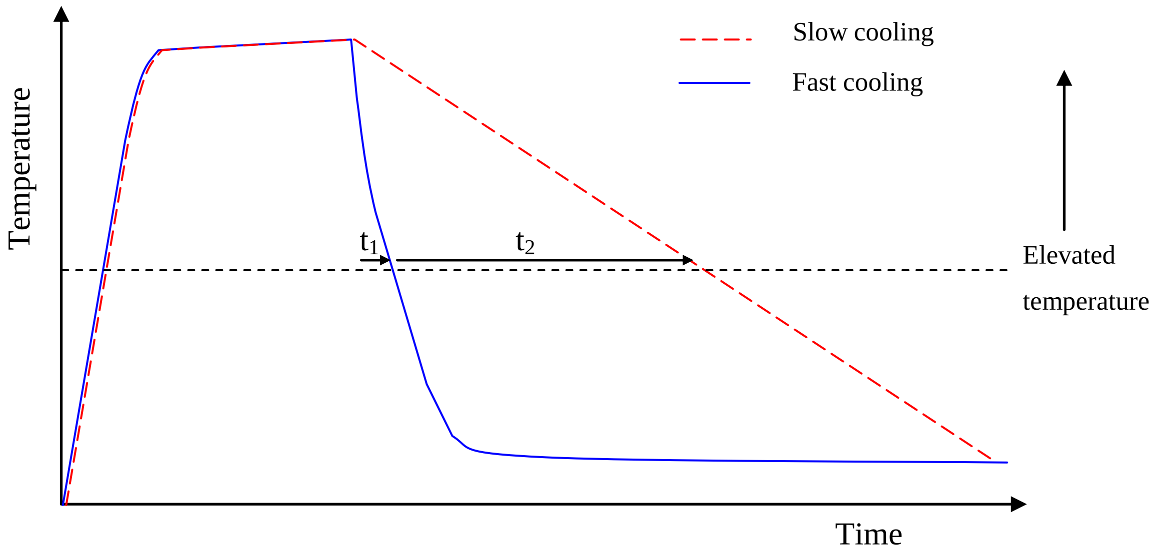

Figure 6.3: Schematic diagram showing temperature difference betwen fast and slow cooling rates where t_1 indicates the time at elevated temperature for a fast cool and t_2 indicates the time at elevated temperature for a slow cooling rate

This internal oxidation could also be explained by diffusion of oxygen along the grain boundaries accompanied by the diffusion of chromium to the grain boundaries (Figure 6.4). The figure shows a four-stage process that starts with the diffusion of oxygen along the grain boundaries into the substrate. It is known that chromium diffuses to the grain boundaries [Hänsel, Boddington and Young (2003)] where it meets the diffusing oxygen and carbon to form precipitates. The migration of chromium will lead to the depletion of chromium in the region surrounding the boundary which can be seen in Figure 4.13(d). If there is a lower concentration of chromium present then oxide formed on the external surface of the substrate will resemble that formed on mild steel. This is indeed the case as shown in Figure 4.11 where, apart from the chromium rich layer, the oxide scale consists of oxides similar to those found on mild steel [Birks *et al*. (2006)]. The process of chromium depletion can progress to greater depths than the oxidation front because chromium from within the grain will then diffuse to the depleted regions and leave an additional depleted area.

At the lowest extent of the internal oxide region, a number of dendritic particles are observed. According to Bolsaitis and Kahlweit (1967), dendritic oxide particles are observed in a copper – silicon alloy at the lowest extent of the internal oxidation region. As oxidation proceeded, however, these particles lost their dendritic structure and later, spherical particles existed in their place. The results presented in this thesis are in agreement with this effect as only the particles at the lowest extent contain dendrites whereas particles found closer to the metal / oxide interface (which are assumed to have formed earlier), do not.

As shown in Figure 4.15, many of the particles at the maximum extent of the internally oxidised region have formed dendrites and have compositions which are rich in silicon whereas the non-dendritic particles do not. It is therefore possible that the dendrites form due to the solidification of a molten oxide of silicon. A candidate material responsible for their production could be fayalite (Fe_4SiO_2) which has a melting temperature of ~1200°C [Zhao, Jak and Hayes (1999)]. This would explain why dendritic oxide particles are not found at temperatures below 1200°C.

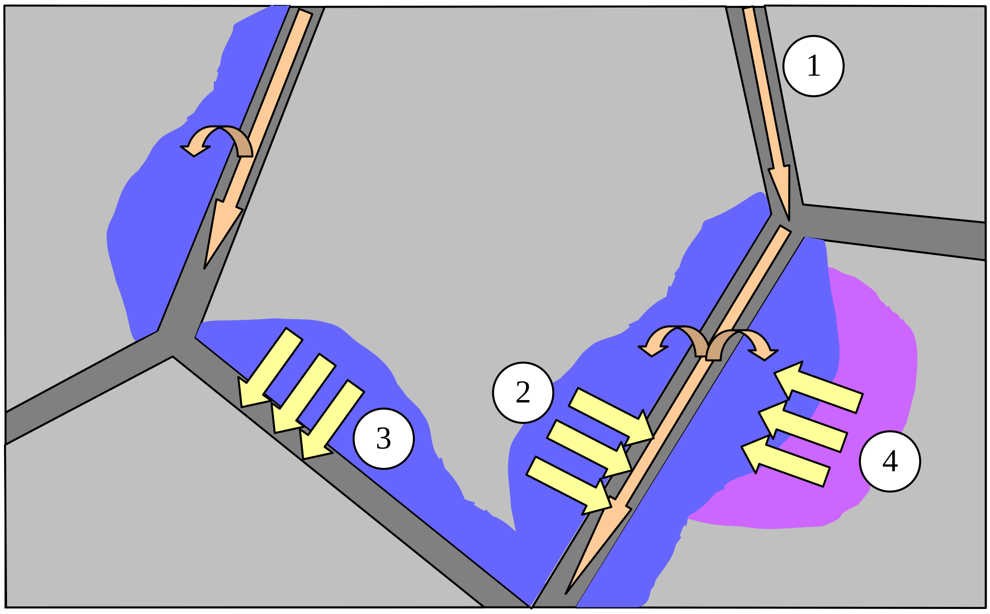

1 – Oxygen diffusion along grain boundaries ⇨
2 - Chromium depletion 🟦
3 - Internal oxidation
4 - Further chromium depletion leading to further oxidation 🟪

Figure 6.4: Schematic diagram showing possible process for internal oxidation at grain boundaries

6.3.2 Sub-surface oxide layering

Figures 4.39 and 4.40 are examples of oxides produced on austenitic grades of stainless steel which exhibit a layered, sub-surface oxide structure.

The mechanism of formation of the layered structure is similar to that described by Cheng *et al*. (2006) and is shown in Figure 6.5. The first stage of the process is the formation of the protective chromium rich oxide layer (a). The substrate immediately below this layer will become depleted in chromium and will approach the composition of an iron alloy. This will allow the formation of iron-rich oxides towards the outer edge of the oxide scale. This is clearly seen in Figure 4.4 where the inner layers are enriched in chromium and the outer layers are iron-rich oxides. At this stage, sub-surface oxidation would have commenced where the chromium in the substrate is below the value required for protective properties (b). As this chromium-depleted region is consumed, the oxidation front will eventually impinge upon areas of the substrate where the composition is sufficient to produce a more chromium rich protective oxide once more (c). This will enable the formation of a chromium-rich band which temporarily halts the oxidation front. This protective band will deplete the substrate immediately below it of chromium and the process continues. The nickel rich metallic particles have also been reported by Cheng *et al*. (2006) who attributed them to the fact that the iron and chromium would form oxides quicker than the nickel in the substrate. Evidence of this can also be seen in Figure 4.11 where there is an apparent enrichment of nickel at the scale / metal interface. The results presented by Cheng *et al*. (2006) suggest that the formation of this layered oxide is dependant upon oxidation in an atmosphere containing water vapour. This is further supported by the work by Vepulanont (2005) who found the layered structure down to temperatures as low as 900°C in a simulated combustion product atmosphere (with 10% water vapour). Here it was suggested that the layering produced continuous chromia layers in the substrate which temporarily hindered the growth of the external and internal oxides before experiencing chemical breakdown and allowing further growth into the substrate which had the effect of producing a series of layers. Figure 4.40, does show continuous chromium rich layers which is in agreement with Vepulanont (2005).

Work presented in this thesis shows these bands to be present after oxidation both in laboratory air and in simulated propane combustion products which contains a small amount of water vapour (Figure 4.40 in air, 5.12 and 5.13 in simulated propane combustion products). This is in disagreement with Cheng *et al*. who found them to only exist in moist air. The reason for this is that they carried out their tests at temperatures no higher than 1030°C; below the temperature required for this structure to form in dry air. Results presented in this thesis, however, continue to temperatures of 1300°C. At temperatures below 1200°C, this type of oxidation has not been observed within the current study which gives evidence to show that the addition of water vapour does accelerate the formation of the layered oxide structure. As the production of the structure relies heavily on the depletion of chromium from the underlying substrate, it is perhaps no surprise that its formation is promoted by an oxidising atmosphere containing water. Flowing gases which contain water are known to increase the oxidation rate of chromia formers by the increased evaporation of chromium in the form of volatile compounds such as CrO_3 and $Cr_2O_3(OH)$ [Khanna (2002), Astemann *et al*. (1999)].

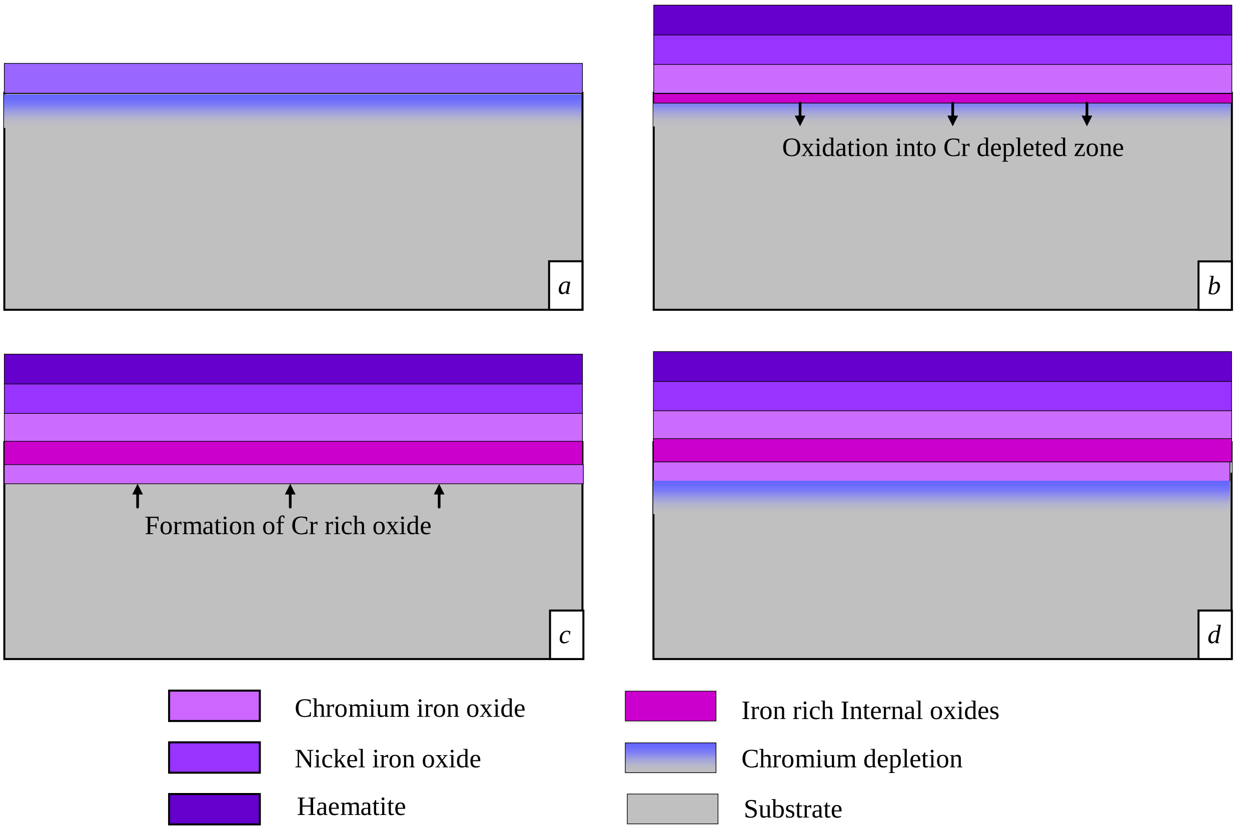

Figure 6.5: Schematic diagram showing possible process for the formation of internal oxide layering. (a) chromium rich oxide forms, depleting the substrate of chromium, (b) external iron rich oxides on the surface and internal oxides form in the chromium depleted metal, (c) depleted region consumed by internal oxidation so a chromium rich oxide is formed once more and (d) new chromium rich oxide consumes further chromium from the substrate producing a layered structure

6.4 Oxidation of as-cast substrates

The as – cast scales produced on both 304 and 316L stainless steels are extremely disordered and damaged (Figure 4.30-4.33). Obviously this is to do with the processes involved in the continuous casting procedure itself. The scale will form throughout the process as the metal is hot from pouring until it exits from the casting machine. During the process, rolls are used to pull the strand (Figure 2.1) thus producing the damaged scale that is evident from the figures. As the continuous casting machine is in operation, the mould has to vibrate to prevent sticking. This vibration causes the reciprocation marks visible on the as-cast sample in Figure 4.27. It was suggested by Lloyd, Saunders, Kent and Fursey (1977) that causing damage to the substrate might cause an increase in diffusion of chromium along the lines of dislocations and hence cause both oxidation within the substrate and breakaway oxidation in the external scale. Figures 4.34 and 4.35 show the scale produced after a laboratory simulated reheat and there is some sub-surface oxidation evident. On comparison with the as –cast scale (Figure 4.26) it seems that these areas of internal oxidation are in some way related to the metal folds at the metal / scale interface (Figure 4.29) as the internal oxidation is similar to the folds observed before oxidation has occurred, Figure 6.6. It is therefore possible that the reciprocation in the continuous casting process causes deformation of the substrate material and hence introduces dislocations. This in turn will then cause the internal oxidation evident in the micrographs.

Alternatively, as the substrate is dendritic in nature, the structure will be deformed at the substrate's surface (again due to the casting process) and has a curved appearance at the outer edge of the material. Oxidation may follow the dendritic structure within the substrate as reported by Tholence and Norell (2008) and so the cause the internal oxide banding.

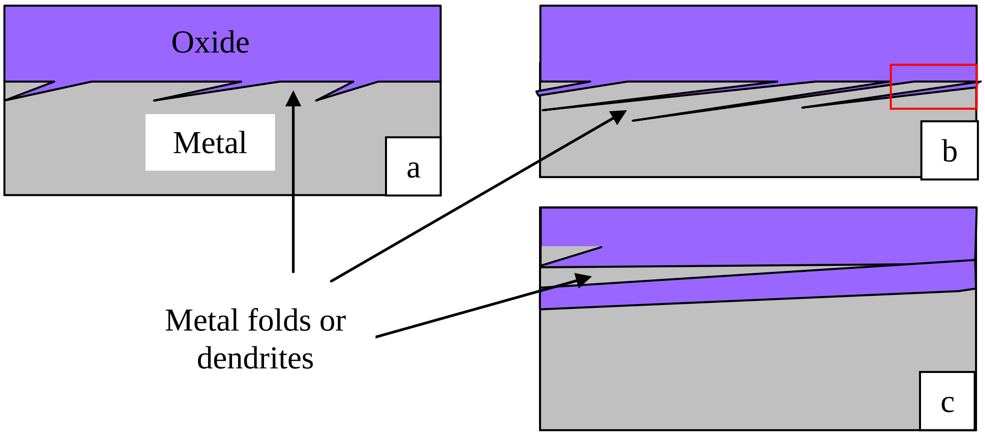

Figure 6.6: Schematic diagram showing how the growth of internal oxidation may occur and how this may be related to Figure 4.28 a) 304 with as-cast oxide scale, b)304 with as-cast scale after simulated reheat, c) 304 with as-cast scale after simulated reheat expanded section

Apart from the internal oxide banding observed in the 304 stainless steel, no other differences are evident. This is possibly due to the fact that many of the cracked and highly damaged as-cast oxides spalled when heated to reheat temperatures. This will leave a surface which, although of varying roughness, will be chemically uniform. Therefore, the only effect that the casting procedure will have on the reheat scale would be that caused by the as-cast microstructure. Although this may sound ideal for industrial reheat (as as-cast oxides will then not effect the reheat oxide), this effect may be limited to laboratory scale specimens which tend to heat at a far greater rate than the slab, bloom or billet produced in large scale steel production. In this case, the oxides may not spall as readily and will certainly effect the reheat oxide produced.

6.5 Initial oxide formation in simulated cracked gas

The initial scale formed on 304 after 1 or 2 hours at the relatively low temperature of 700°C (Figure 5.1) consists of a fine grained oxide which is typical of chromia. This scale would be slow growing and protective to the underlying alloy. However, as oxidation progresses many facetted grains are produced on the surface. These facetted grains are of a shape which is consistent with the crystal structure of spinel [Bauer and Tyrz (1988)] and continue to dominate the surface structure until a temperature of 1100°C is reached. At this temperature, the surface base oxide on both the 304 and 316L stainless steel is more uniform. The base oxide has a rumpled structure which is typical of highly stressed chromia oxide layers [Hansson and Somers (2006)]. Although this chromia layer can generally be considered protective, in cross-section (Figure 5.25) it can be seen that the “rumples”, of the base oxide form ridges under which large voids are present. The radius of curvature of the chromia ridge is very small and will be liable to cracking. After 2 hours at 1100°C both the 304 and 316L stainless steel grades have formed large scale oxide blistering on their surface (Figure 5.8 and 5.26). These nodules are more prevalent after oxidation of duplex grades (As discussed in subsequent chapters) but they are an important factor in the oxidation of austenitic grades as well. Their presence on the surface of austenitic grades has been observed on both type 304 and 316L stainless at all temperatures above 1100°C with size depending on oxidation time.

Nodules have previously been observed on austenitic and ferritic grades of stainless steel by other authors [Halvarsson *et al*. (2006) and Wood (1970)]. The formation mechanism put forward by Halvarsson *et al*. (2006) suggests that the nodules will always form in the centre of substrate grains as the faster diffusion at the grain boundaries will enable a protective oxide to remain protective for a longer period of time than an oxide formed over the grain which will subsequently experience chromium depletion. In this thesis however, many of the observed nodules measure in excess of 50µm in diameter which is many times more than the size of the individual grains measured prior to oxidation. Although no cracking of the oxide ridges is visible in Figure 5.25, it is plausible that following continued oxide growth, stress build-up would cause cracking to occur. Therefore from the results obtained, it is more likely that the mechanism of formation agrees with that suggested by Wood (1970) where nodule formation begins when the protective oxide buckles and cracks revealing the now chromium depleted substrate to the oxidising atmosphere allowing an iron oxide to form as a local breakaway region.

Oxidation at 1200°C for times in excess of 1 hour causes thick oxides to form on the surface which are prone to spallation (Figure 5.11). In an attempt to establish the formation steps of the thick oxide layer, short term experiments were carried out (Figure 5.14). The results show that after 5 minutes the surface resembles that produced after oxidation at lower temperatures, however, this oxide quickly loses its apparent protective nature and nodules are seen to form in increasing amounts until the surface is covered in a thick oxide layer.

7 ESEM OXIDATION OF S32101

7.1 Introduction

In order to study the oxide scale formation on duplex grades at the early stages of industrial reheat, an ESEM was used. This technique allows in-situ experiments to be carried out in an atmosphere at limited pressure. This, when coupled with the ability to operate at a variety of temperatures, allows a controlled experiment to take place with the focus being solely on the early stages of oxidation of S32101. The procedure used for this experiment is detailed in Section 3.4.5.

7.2 In-Situ Oxidation of S32101

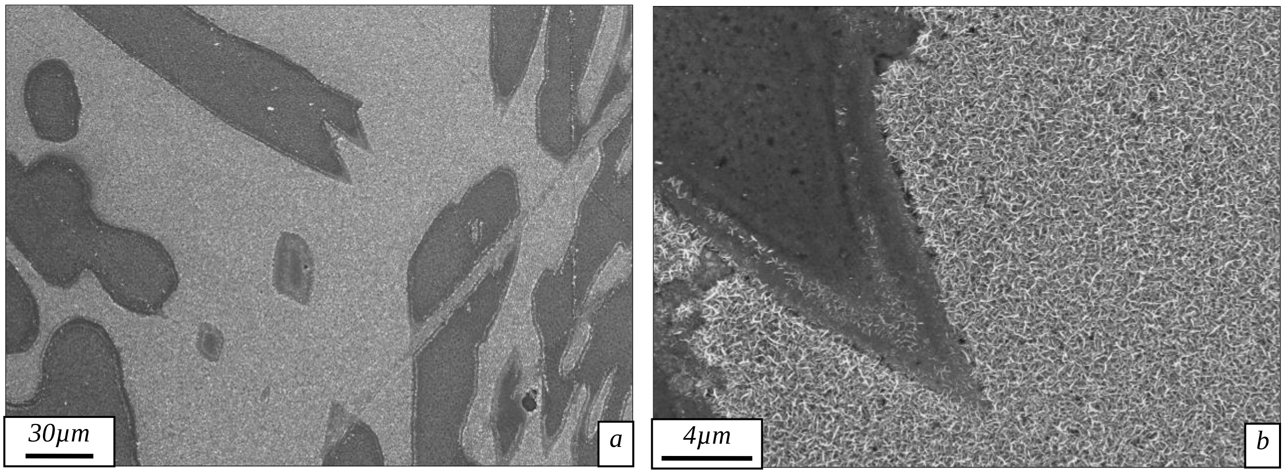

Figure 7.1:- Secondary electron micrographs of a) the surface oxide formed on S32101 with a 1µm surface finish at 700°C for 5 minutes in laboratory air at 266Pa and b) at higher magnification

Figure 7.1(a) shows a secondary electron image of a polished surface of S32101 during in-situ heating in a FEGESEM. The time elapsed was 5 minutes at a temperature of 700°C. Even after this short time and low temperature of oxidation there is a clear contrast difference between the oxides formed on each phase: the oxide formed on the austenitic regions is a darker shade than the bright oxide formed on the ferritic regions. At higher magnification (b), the oxide produced on the ferritic regions is fibrous whereas the oxide on the austenitic region is almost featureless apart from a band of oxide situated approximately 1-2µm from the edge of the region which is similar to the oxide produced on the ferritic region.

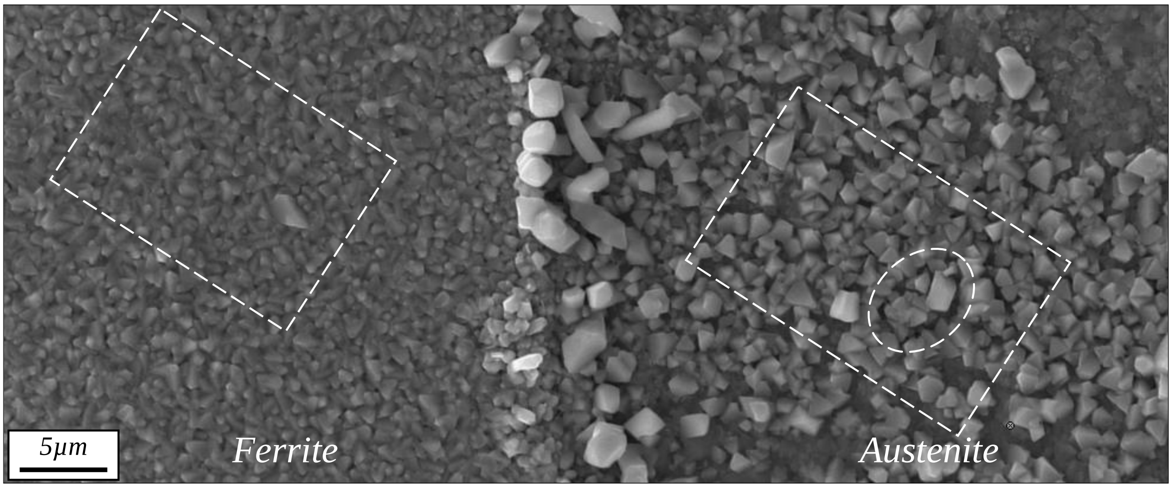

Figure 7.2:- Secondary electron micrograph of the surface oxide formed on S32101 with a 1µm surface finish after oxidation in an ESEM in laboratory air at 266Pa according to the heat treatment shown in Figure 3.6 showing the areas of interest for the ESEM micrographs

Figures 7.3 – 7.4 show a time line of the oxide growth process during the in-situ oxidation of S32101 in the FEGESEM at a temperature of 900°C (N.B. the times are taken from the start of heat-treatment according to the profile shown in Figure 3.6). The two regions of interest are shown in Figure 7.2, by the white boxes. The oxide on the ferrite region was chosen due to its proximity to the distinguishable large bright contrast oxide grain. The austenitic region of interest was chosen due to the presence of a feature which resembled an oxide nodule; visible here as a ring of oxide highlighted by the white oval.

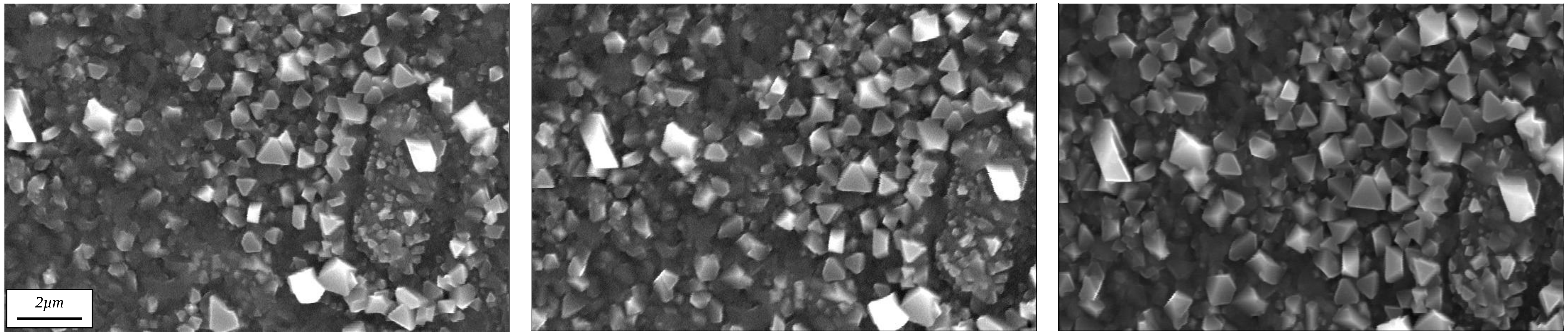

50 minutes *60 minutes* *70 minutes*

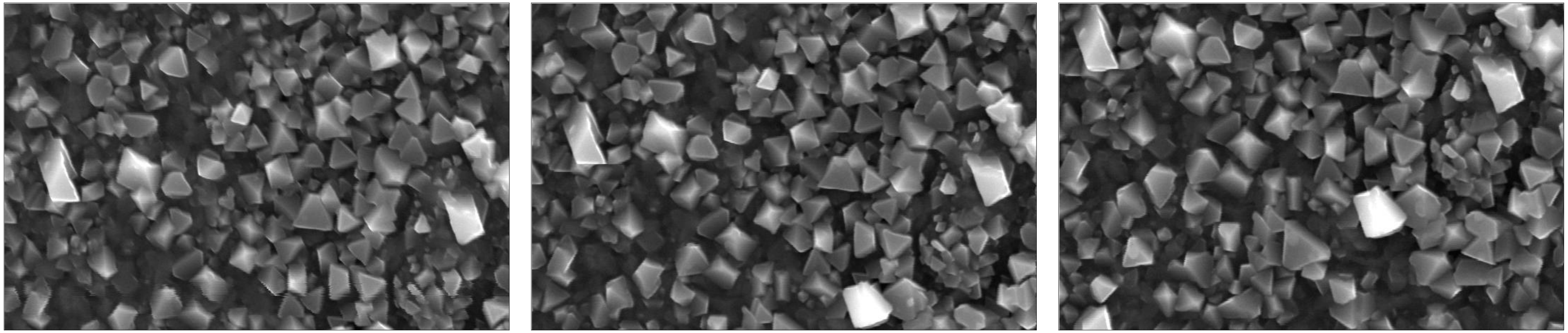

80 minutes *90 minutes* *100 minutes*

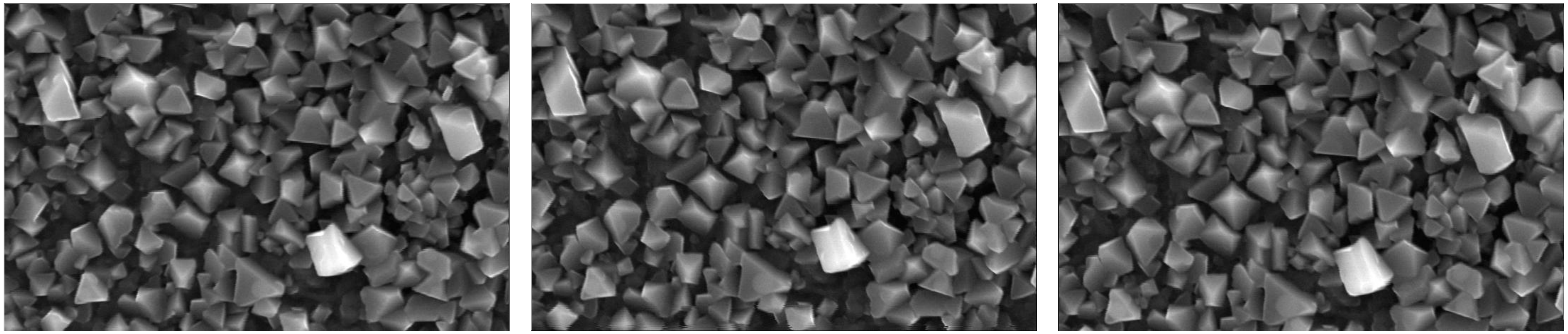

110 minutes *115 minutes* *120 minutes*

Figure 7.3:- Series of secondary electron images captured during in-situ oxidation of the austenitic region of S32101 stainless steel in laboratory air at 266Pa at a temperature of 900°C according to the heat treatment shown in Figure 3.6

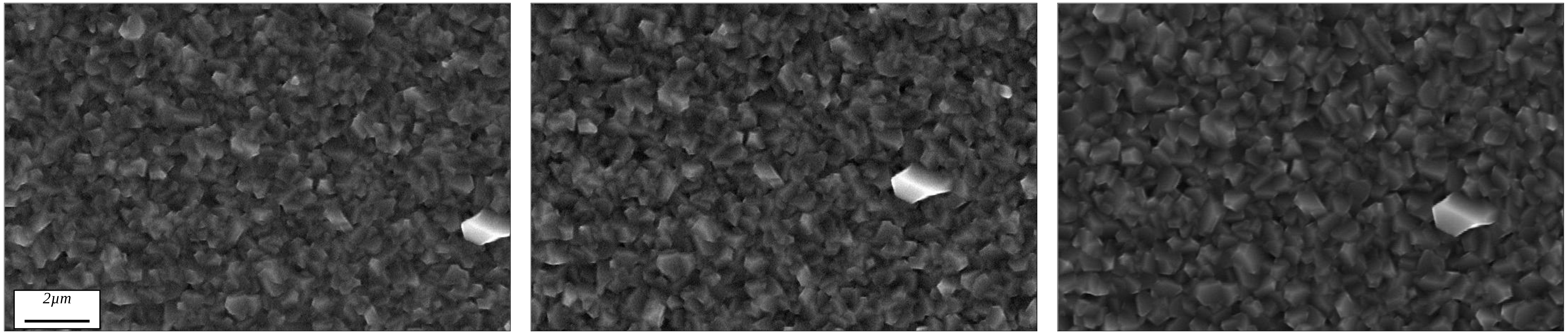

50 minutes *60 minutes* *70 minutes*

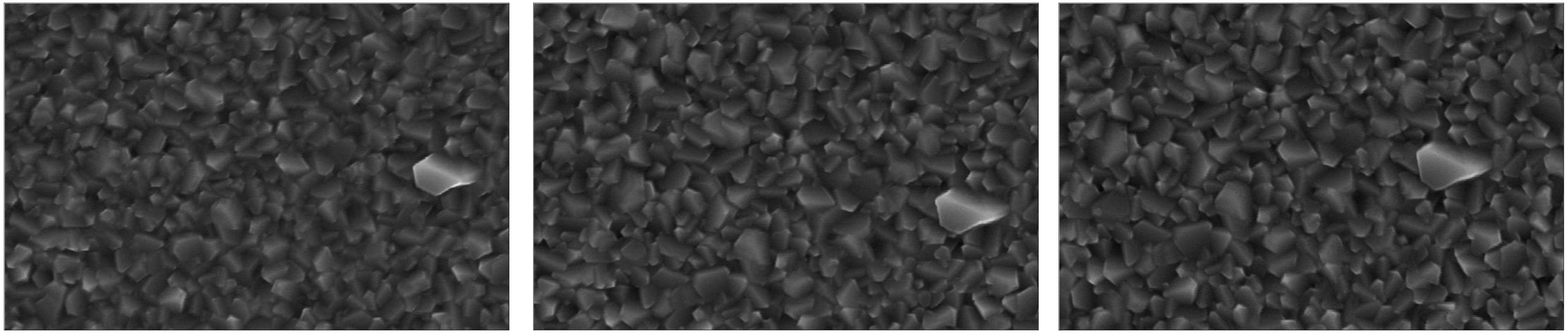

80 minutes *90 minutes* *100 minutes*

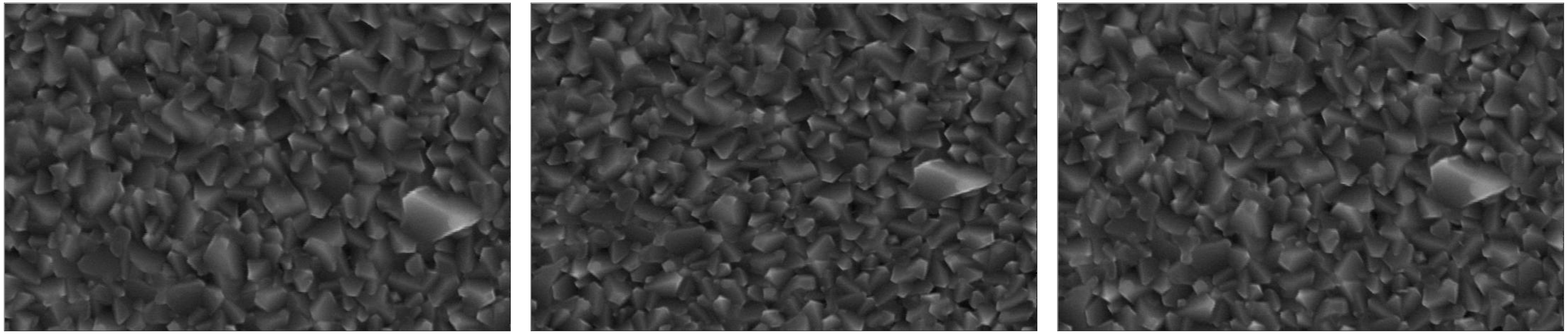

110 minutes *115 minutes* *120 minutes*

Figure 7.4:- Series of secondary electron images captured during in-situ oxidation of the ferritic region of S32101 stainless steel in laboratory air at 266Pa at a temperature of 900°C according to the heat treatment shown in Figure 3.6

Figure 7.3 is a timeline of the growth of the oxide produced on the austenitic phase of S32101 during oxidation in the ESEM. The area shown in this collection of images is shown in context in Figure 7.2. The first image in the sequence was captured after 50 minutes of the heat treatment. The majority of the region consists of a dark base oxide. Upon this base oxide a more facetted, larger grained, brighter contrast oxide has grown to produce discrete nucleation sites distributed over the surface. To the right of the image is a small oval shaped feature which is similar to an oxide nodule. It consists mainly of the finer grained dark base oxide but is encircled by a ring of the brighter more facetted oxide. The range of images shown in the figure reveal a growth process resulting in the oxide observed after 120 minutes of oxidation which consists of a surface almost entirely covered in the facetted oxide crystals. In order to produce an estimation of the growth rate of the oxide crystals under these conditions, the following procedure was applied. A number of crystals were chosen; 5 which were presenting a top view of a square based pyramid and 5 which showed the triangular faces of the crystals (Figure 7.5).

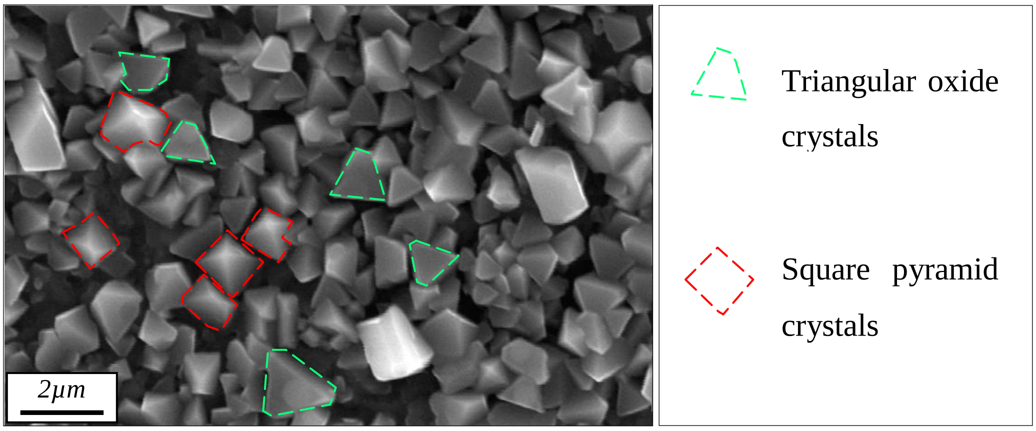

Figure 7.5:- Secondary electron micrographs of the surface oxide formed on S32101 with a 1μm surface finish at 700°C for 5 minutes in laboratory air at 266Pa indicating the measures oxide crystals for volume estimation

It was assumed that each crystal can be equated to an equilateral octahedron as previous results have suggested that the top oxide grains are spinel type oxides which are commonly found to be equilateral octahedron in shape [Bauer and Tvrz (1988)] with a volume given by Equation 7.1.

$$V=\frac{1}{3}\sqrt{2}x^{3} \text{ ---[7.1]}$$

Where x is equal to the length of any edge of the crystal.

The volume and projected area of each of the chosen crystals were calculated at each time in which they were present in the image. The results of this experiment are displayed in Figure 7.6 and suggest that the relationship between oxidation time and crystal volume at these low pressures is linear.

The timeline for oxidation of the ferrite phase of S32101 in the ESEM is shown in Figure 7.4. It is clear from this series of images that growth of the oxide has occurred but to a lesser extent and in a more homogeneous manner than the oxide formed on the austenite phase.

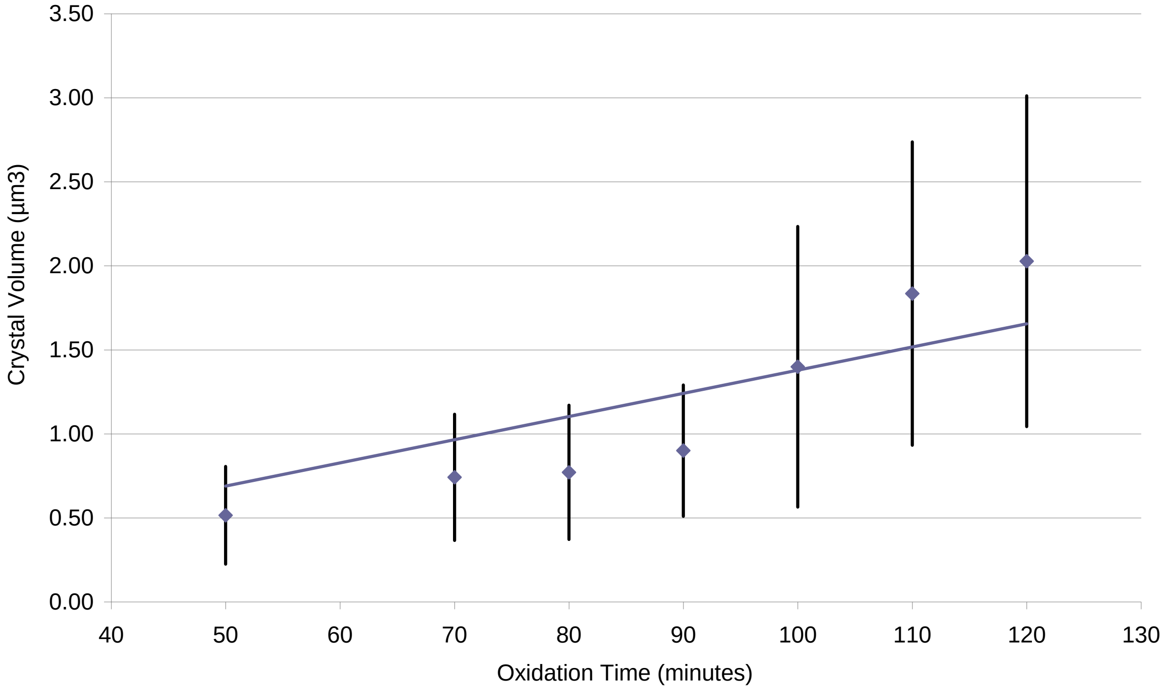

Figure 7.6:- Oxidation time versus average crystal volume of an oxide formed on S32101 after heat treatment according to the procedure shown in Figure 3.6 in an ESEM at 266Pa

7.3 Post ESEM investigation

Following the oxidation procedure in the ESEM, further study of the resulting oxide produced on the ferrite and austenite phases was carried out. Techniques used for this were: field emission gun SEM (FEGSEM), FIB/FEGSEM (both for cross sectioning and site specific TEM sample preparation) and TEM. Chemical analysis was also carried out by the use of EDS.

Figure 7.2 is a secondary electron micrograph of the oxide formed on the S32101 after oxidation in an ESEM. The oxide produced on the ferrite region of the substrate is shown on the left of the image and the austenitic region is shown on the right. The oxide on the ferrite region is finer grained and has a darker contrast whereas the oxide produced on the austenitic side is a large facetted grained phase upon a finer grained oxide. The interface between the two substrate phases has an area of enhanced oxide growth which has formed a ridge of large facetted oxide grains on the surface.

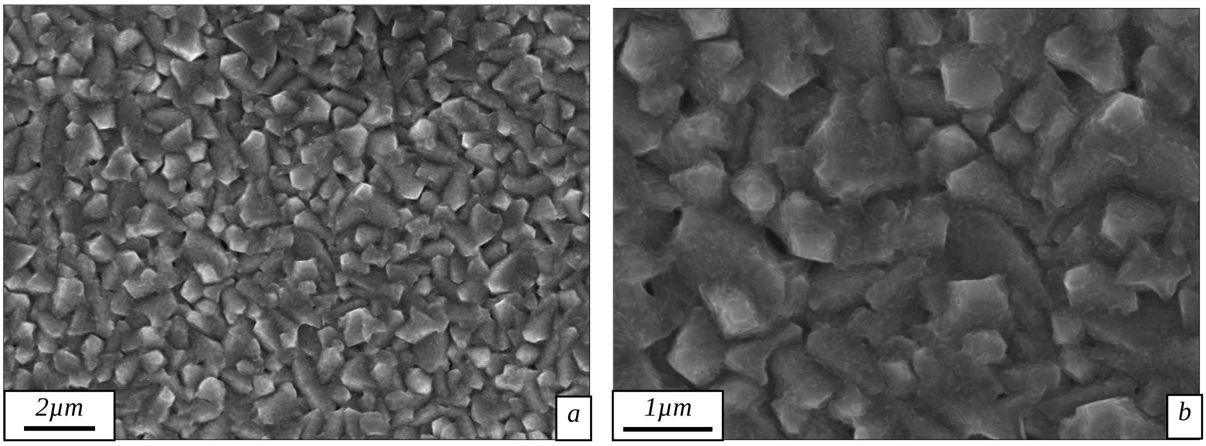

Figure 7.7:- Secondary electron micrograph of a) the surface oxide formed on the ferrite region of S32101 with a 1µm surface finish at after heat treatment routine shown in Figure 3.6 and b) at higher magnification

Figure 7.7 shows secondary electron micrographs of the oxide formed on the ferrite region in Figure 7.2. The surface of this oxide is fairly dense as if the grains have sintered to form a continuous layer. The oxide formed consists of two different grain sizes. The large grains are approximately 1µm in diameter and the smaller grains are 0.5µm. The grains are not smooth but rather textured as if a number of smaller grains are growing on the surface.

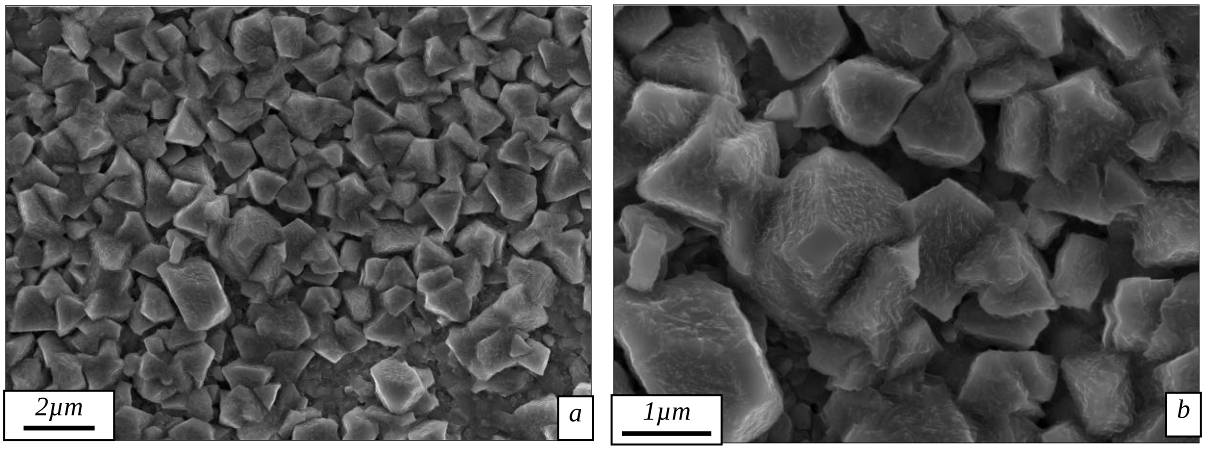

Figure 7.8:- Secondary electron micrograph of a) the surface oxide formed on the austenite region of S32101 with a 1μm surface finish at after heat treatment routine shown in Figure 3.6 and b) at higher magnification

Figure 7.8 are secondary electron micrographs of the oxide formed on the austenite region in Figure 7.2. The top surface of the oxide formed in this region does not seem to be sintered and consequently not as dense as the oxide formed on the surface of the ferrite region. Instead, individual facetted oxide grains measuring approximately 1.5μm in diameter have formed upon a finer grained oxide as small as 100 -500nm in diameter. As with the oxide formed on the ferrite region, the surfaces of the oxide crystals are not smooth.

A secondary electron image and accompanying EDS maps of the oxide formed on an interface between the austenite and ferrite phases is shown in Figure 7.9. There are clear differences between the appearances of the oxides produced on either side of the interface. There is a region of enhanced oxide growth at the boundary between the two phases which is visible due to the brighter contrast. The EDS maps produced of this area reveal that the chemistries of each region are also different. There is a larger iron count on the austenitic region which extends to the edge of the enhanced growth region over the boundary. Chromium is present on either side of the boundary with an increased count in specific regions of the austenitic region which correspond to the areas where the facetted oxides, described previously, have not formed. Areas where the facetted oxides are present show a lower chromium count. The oxide formed at the boundary is lower in chromium content with visible chromium enrichment to either side into both the austenitic region and ferritic region. Manganese reveals a pattern contrary to that of chromium with an overall enhancement of manganese counts on the ferrite side of the boundary. The facetted oxides of the austenite region are manganese enriched with the remainder of the oxide on the austenite region lower in manganese. The oxide formed at the boundary is highly enriched in manganese. Silicon has a low count over the entire analysed region but does show a slight enrichment on the austenitic side of the boundary and a complete absence in the oxide formed over the boundary.

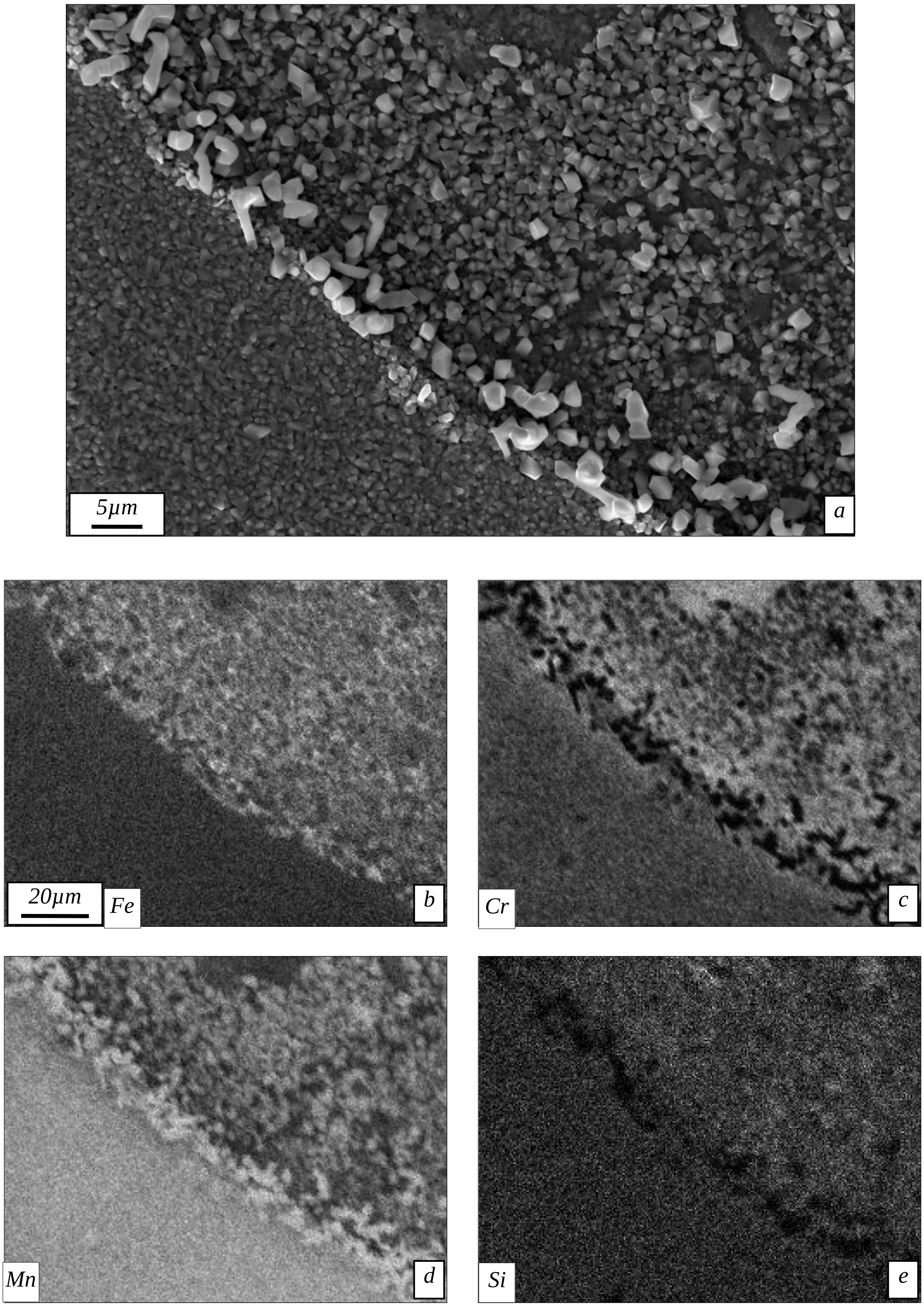

Figure 7.9:- Secondary electron micrograph (a) with accompanying EDS maps of (b) iron, (c) chromium, (d) manganese and (e) silicon of the oxidised interface between the underlying austenite and ferrite boundary of S32101 after in-situ oxidation in an ESEM in laboratory air at a pressure of 266 Pa and a final temperature of 900°C according to the heat treatment shown in Figure 3.6

7.4 Examination of FIB Milled Cross-Sections

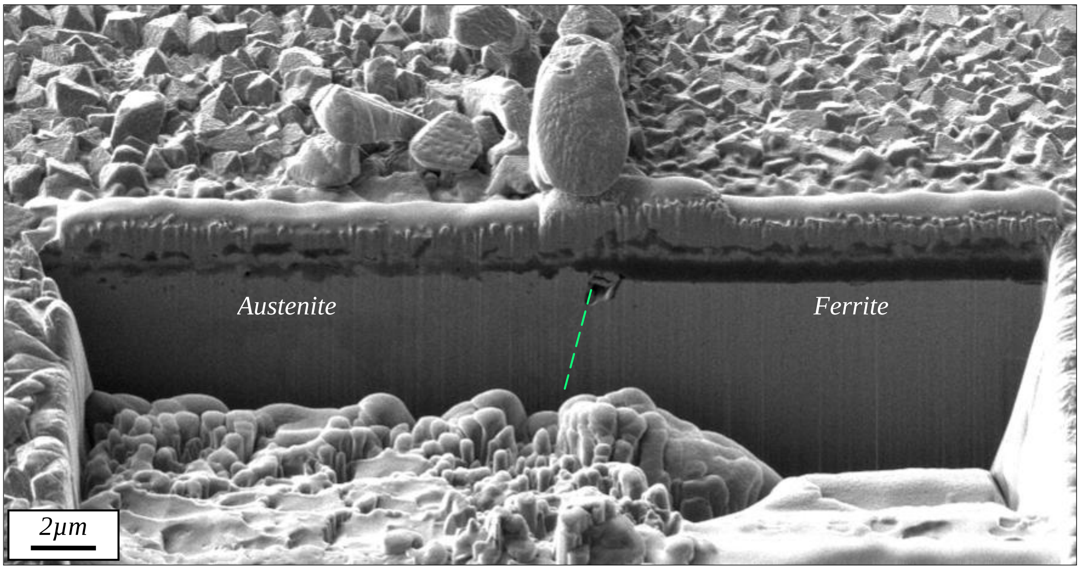

Figure 7.10:- Ion-induced secondary electron micrograph of a cross-section of the oxide produced on the interface of an austenite/ferrite phase boundary in S32101 after in-situ oxidation in an ESEM in laboratory air at 266Pa and at a final temperature of 900°C according to the heat treatment shown in Figure 3.6

In order to study the thickness of the oxides and the relation of the oxide structures to the underlying substrate phase distribution and microstructure, cross-sections were produced using a focussed ion beam (FIB) and images collected using ion-induced secondary electron microscopy (ISEM). Figure 7.10 is an ISEM of a FIB milled cross-section through the oxide formed on the interface of austenite and ferrite phases of an S32101 substrate. The image consists of a number of regions which will require explanation for a reader unfamiliar with FIB milled cross-sections. Due to the geometry within the microscope, the image is taken at an angle of 52° which means that, although the impinging ion beam (used for imaging) is normal to the cross-section, much of the oxidised surface is also visible. In order to protect the top surface of the specimen from damage during milling, a protective layer of metal is applied; in this case the protective metal used was platinum. This protective layer then forms an additional layer in the cross-section as indicated in Figure 7.11. The large bright grain visible towards the top of the image in Figure 7.11 is not an oxide crystal, instead it is an effect of the deposition of platinum onto a rough surface and, as such should not be regarded as an oxide feature.

As shown in Figure 7.10, the oxide surface morphology is different to either side of the boundary. On the ferrite side, the oxide / metal interface is very smooth whereas on the austenite side the interface is very uneven with small regions of penetrating oxide. The oxide on the ferrite side has three layers visible within this image. The lowest layer is dark and is the thickest of the three. The middle layer is a continuous bright contrast band measuring approximately 0.3μm in thickness and 0.5 – 0.7μm from the oxide metal interface. The top layer is a lot less homogeneous which is consistent with the micrographs of the surface in a planar view (Figure 7.9 for example). The oxide formed on the austenite region is far less uniform than that formed on the ferrite region. In some parts there are three layers which are similar to the oxide formed on the ferrite region, however, there are other parts where the oxide is much thinner with only the lower layer present. The results of the cross-section show that the oxides are consistent with the surface in planar view as the facetted oxide crystals are not present over the entire surface.

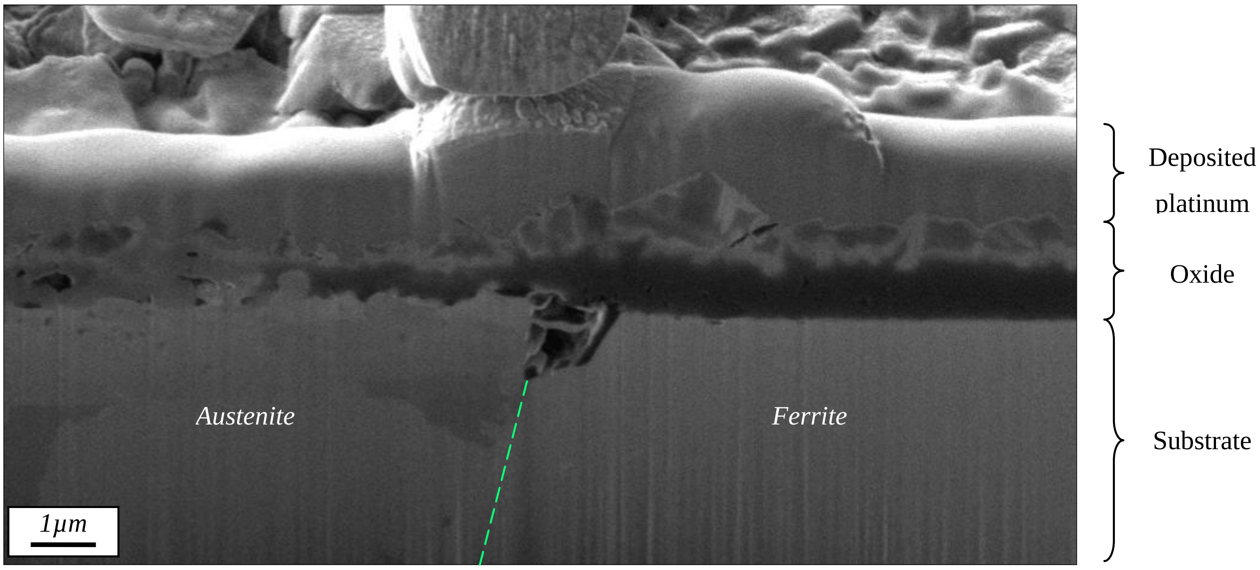

Figure 7.11:- Ion-induced secondary electron micrograph of a cross-section of the oxide produced on the interface of an austenite/ferrite phase boundary in S32101 after in-situ oxidation in an ESEM in laboratory air at 266Pa and at a final temperature of 900°C according to the heat treatment shown in Figure 3.6

Figure 7.11 is a higher magnification ISEM of the same interface as that seen in Figure 7.10. In this image it is very clear that the oxide formed on the ferrite region is thicker than that formed on the austenite region. The layers of oxide on the ferrite region are clearly resolved. At the interface between the two regions, a void has formed in the substrate upon which the manganese rich / chromium poor oxide has formed (Figure 7.9). At this high magnification the structure of the oxide formed on the austenite region is far more disordered than was previously suggested and forms an almost mixed oxide layer.

7.5 Transmission Electron Microscopy of the Phase Boundary

A TEM specimen was taken from the cross-section using the Focussed Ion Beam (FIB) (Figure 7.12). The interface between the two underlying substrate phases is marked with the dashed line. The oxide on the ferritic region is thicker than the oxide formed on the austenitic region and has a clear layered structure with a fine microstructure adjacent to the oxide / metal interface and larger grains towards the outer edge of the scale. The oxide formed on the austenitic region, however, does not have a layered structure but exhibits a single layer mixed phase oxide scale. The oxide formed over the interface consists of a fine grained oxide upon which a large single grain of oxide has formed. This is the largest grain of oxide visible in this field of view. Within the substrate a void is seen on the phase boundary in an area located adjacent to the metal / oxide interface which is lined with an amorphous material.

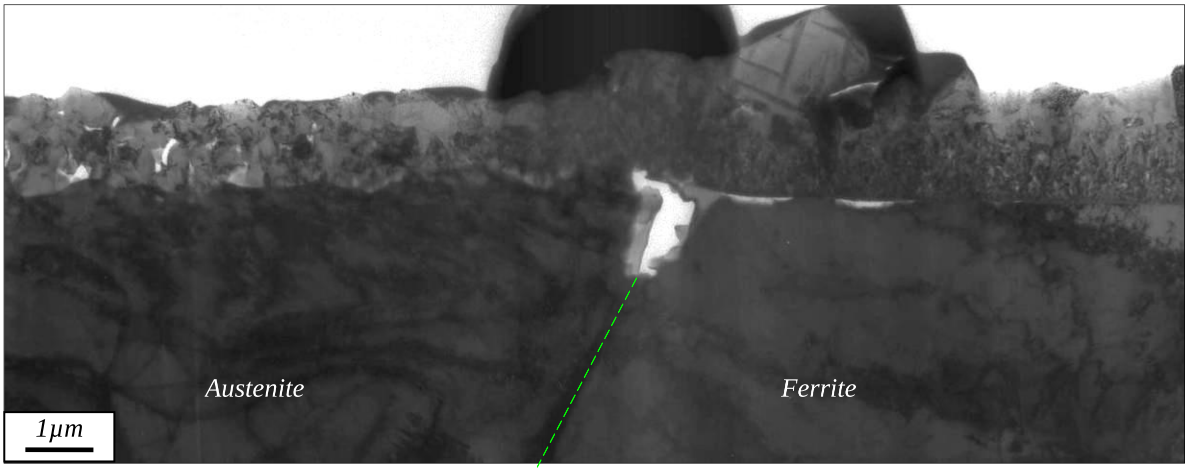

Figure 7.12:- Bright field transmission electron micrograph of a cross-section of the oxide produced on the interface of an austenite/ferrite phase boundary in S32101 after in-situ oxidation in an ESEM in laboratory air at 266Pa and at a final temperature of 900°C according to the heat treatment shown in Figure 3.6

Figure 7.13 shows the oxides formed on the austenitic and ferritic regions of the substrate at higher magnification. The oxide formed on the austenitic region is ~0.8μm thick and consists of grains of differing sizes residing within an oxide layer with no discrete layers discernable. EDS of this layer (Figure 7.14) suggests, however, that there is some chemical gradient within the oxide with the manganese rich oxides (probably MnO) towards the top of the scale and the chromium rich oxides towards the bottom of the scale ($CrMn_2O_3$). There are also a number of pores present within the layer.

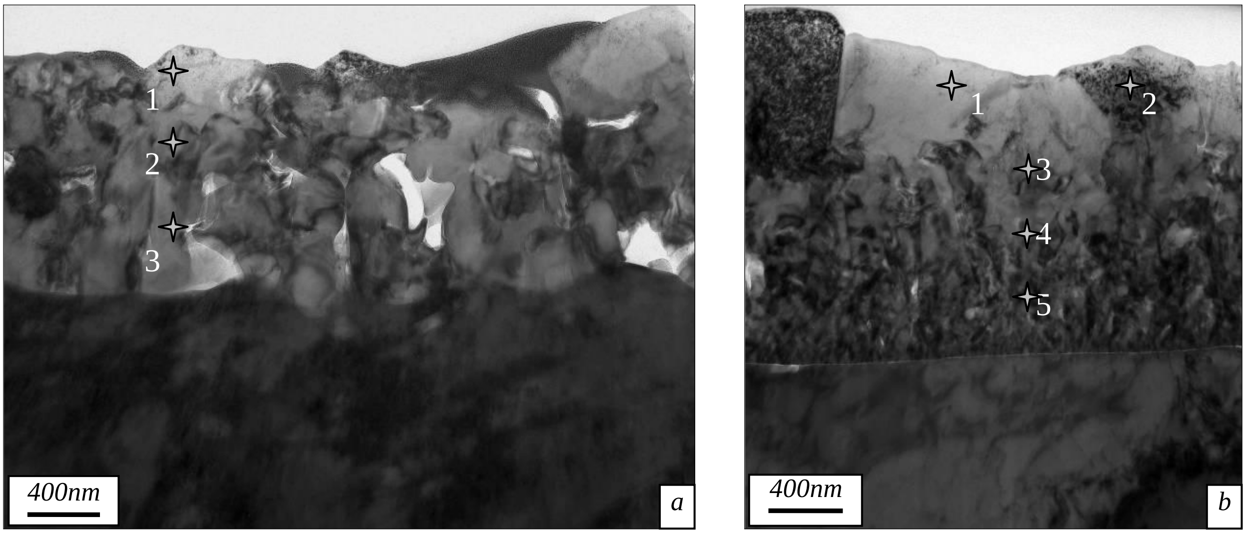

Figure 7.13:- Bright field transmission electron micrographs of oxide formed on a) the austenitic region and b) the ferritic region of S32101 after in-situ oxidation in an ESEM in laboratory air at 266Pa and at a final temperature of 900°C according to the heat treatment shown in Figure 3.6. The numbered stars indicate the locations of collected EDS, displayed in Figures 7.14 – 7.15

The oxide formed on the ferritic region is pore free, measures ~1.5µm thick and consists of two layers: a fine grained region towards the substrate and a coarser grained oxide on the outer surface. EDS of the layers (Figure 7.15) reveals that the layers consist of a top layer which is predominantly manganese oxide (MnO) with a lower layer consisting of a mixed chromium and manganese oxide with a formula close to $CrMn_2O_3$ with little variation in chemistry through its thickness.

The oxide formed over the interface between the austenitic and ferritic regions is shown at higher magnification in Figure 7.16. It can be seen that the large oxide grain is upon a scale consisting of fine oxide grains. EDS has shown that the large oxide grain on the surface of the oxide consists of manganese oxide (50.8At.%Mn 49.2At.% O (MnO)) which is consistent with the results obtained using EDS in the FEGSEM (Figure 7.9) of the oxide formed in the same region.

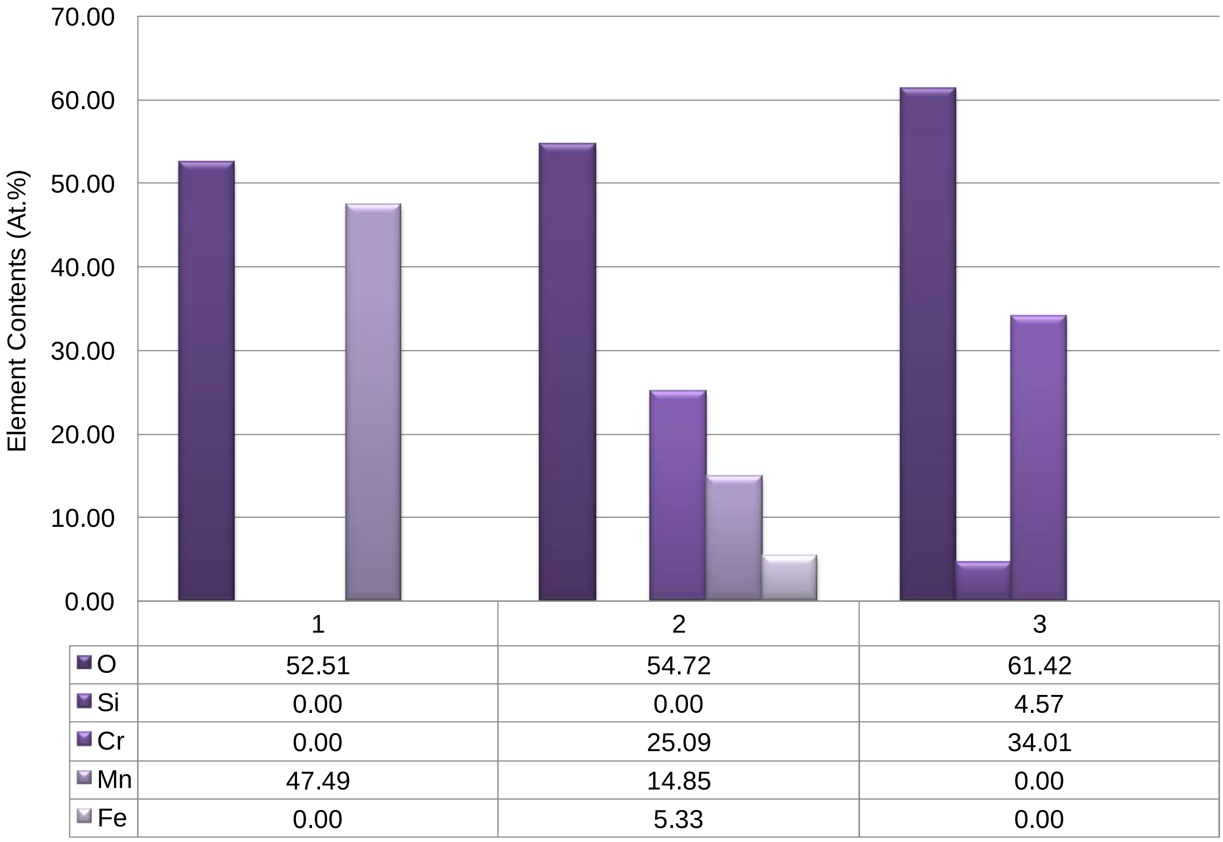

	1	2	3
■ O	52.51	54.72	61.42
■ Si	0.00	0.00	4.57
■ Cr	0.00	25.09	34.01
■ Mn	47.49	14.85	0.00
■ Fe	0.00	5.33	0.00

Figure 7.14:- EDS results of the points taken in Figure 7.13 (a)

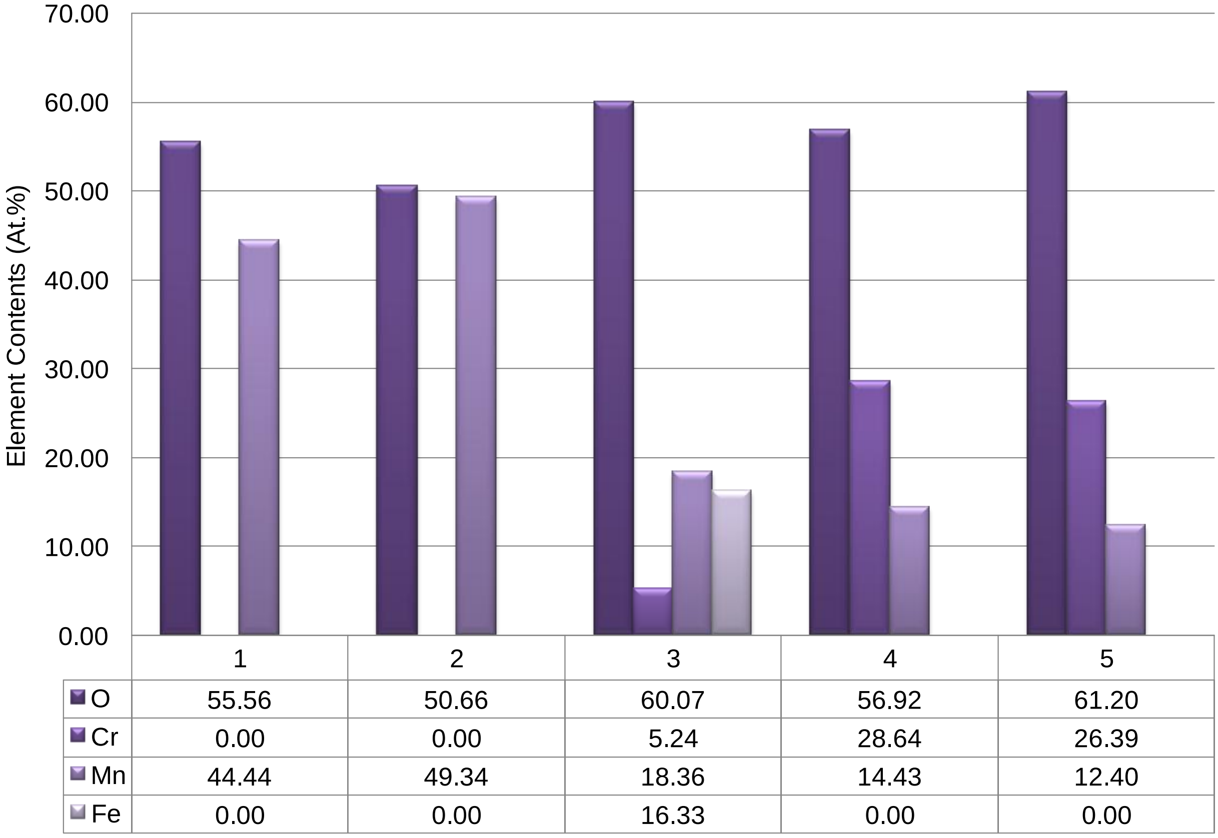

	1	2	3	4	5
■ O	55.56	50.66	60.07	56.92	61.20
■ Cr	0.00	0.00	5.24	28.64	26.39
■ Mn	44.44	49.34	18.36	14.43	12.40
■ Fe	0.00	0.00	16.33	0.00	0.00

Figure 7.15:- EDS results of the points taken in Figure 7.13 (b)

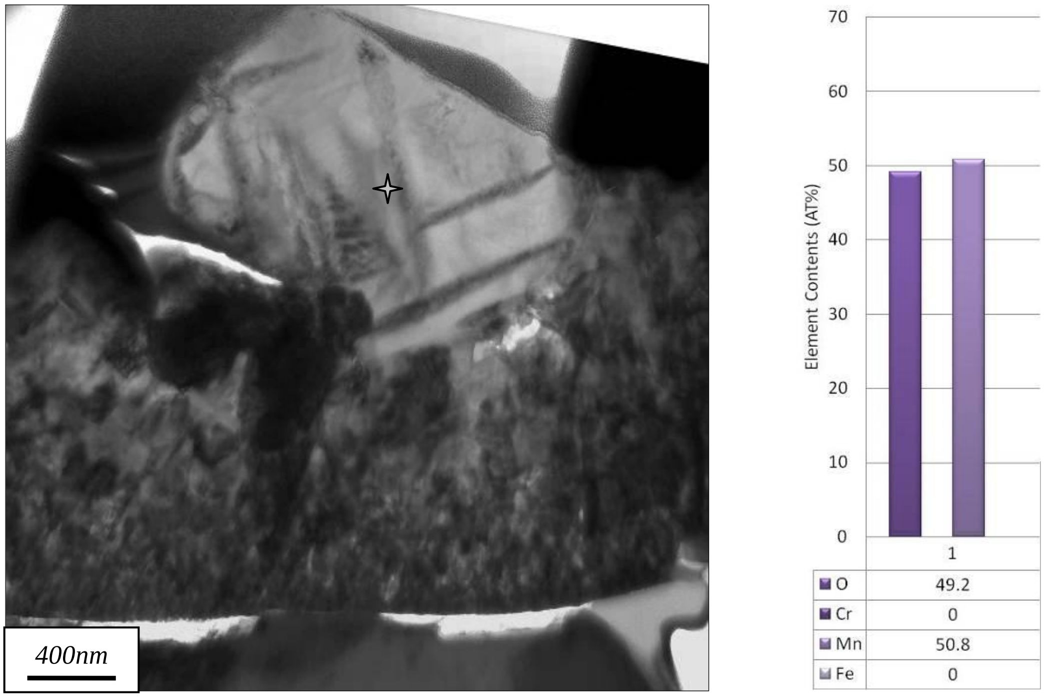

Figure 7.16:- Bright field transmission electron micrograph of oxide formed on the interface of an austenite/ferrite phase boundary in S32101 after in-situ oxidation in an ESEM in laboratory air at 266Pa and at a final temperature of 900°C according to the heat treatment shown in Figure 3.6

8 INITIAL OXIDATION OF DUPLEX STAINLESS STEEL GRADES

8.1 Introduction

S32101 is Outokumpu's low nickel duplex stainless steel grade. After casting, before reheating and subsequent rolling, the surface is ground to remove the surface oxide. For this study, ground specimens were obtained from industry to provide an accurate simulation of the slab's surface prior to reheating.

In order to establish the effect of the early stages of reheat of these industrially ground surfaces, experiments were carried out at temperatures ranging from 700°C – 1200°C at times of 1 and 2 hours. Although these times and temperatures are lower than would be expected during industrial reheat, the results give some indication of the state of the oxide scales during the initial and early stages of industrial reheat.

8.2 S32101 – Industrially Hot Ground

8.2.1 Oxidation at 700°C

After oxidation of S32101 for 1 hour at 700°C in simulated combustion products of propane, the surface oxide shown in Figure 8.1 (a+b) is observed. The surface has a fairly homogeneous covering of small oxide crystals. At higher magnification, however, it is possible to distinguish two types of crystal: there are large grains which measure ~300 – 400 nm in diameter and small grains which are ~100 – 200 nm in diameter. Although the sizes of these crystals are considerably different their shape is very similar with both types of oxide crystals having a facetted structure. After a further hour of oxidation in the same atmosphere, the oxide is similar as those shown in Figure 8.1 (c+d). The two phase oxide structure which was observed after 1 hour of oxidation has been completely covered by the large grained oxide which measures ~300 – 500 nm in diameter. The crystals are facetted in structure and form shapes which can be approximated to equilateral octahedrons.

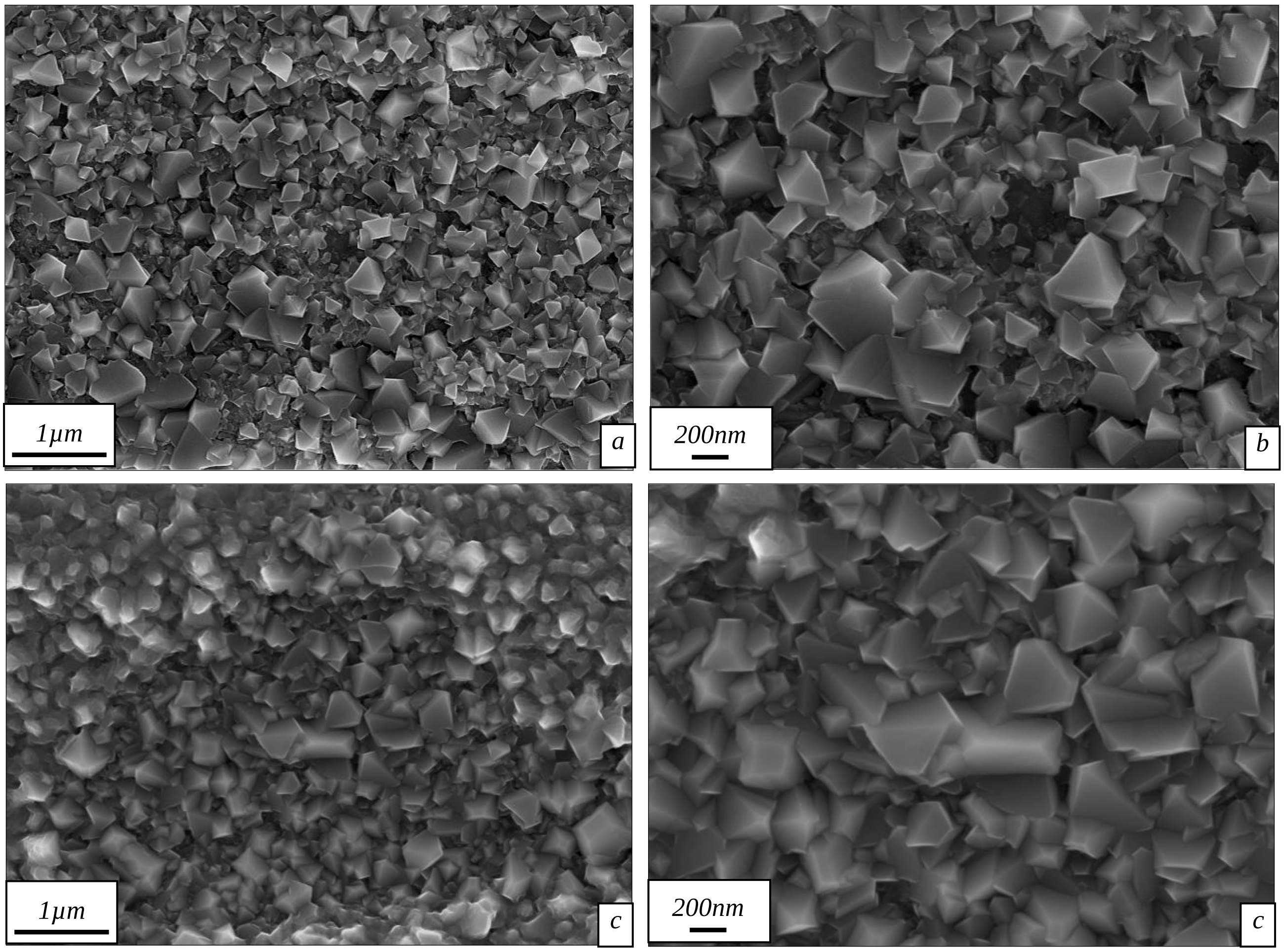

Figure 8.1:- Secondary electron images of the surface oxide formed on industrially ground S32101 after oxidation at a +b) 700ºC for 1 hour and c+d) 700°C for 2 hours in simulated propane combustion products

8.2.2 Oxidation at 800°C

When oxidised at 800°C for 1 hour S32101 produces an oxide surface which can be seen in Figure 8.2 (a+b). At this temperature the oxide growth has produce a much larger grained structure when compared to the oxide produced at 700°C for the same time. In the displayed region, there are two types of oxide present: oxide crystals which are ~300 nm in diameter and two areas which have experienced enhanced growth which have oxide grains measuring 400 – 600 nm in diameter. As with the oxides produced at the lower temperature of 700°C, all the oxide crystals produced have a facetted appearance.

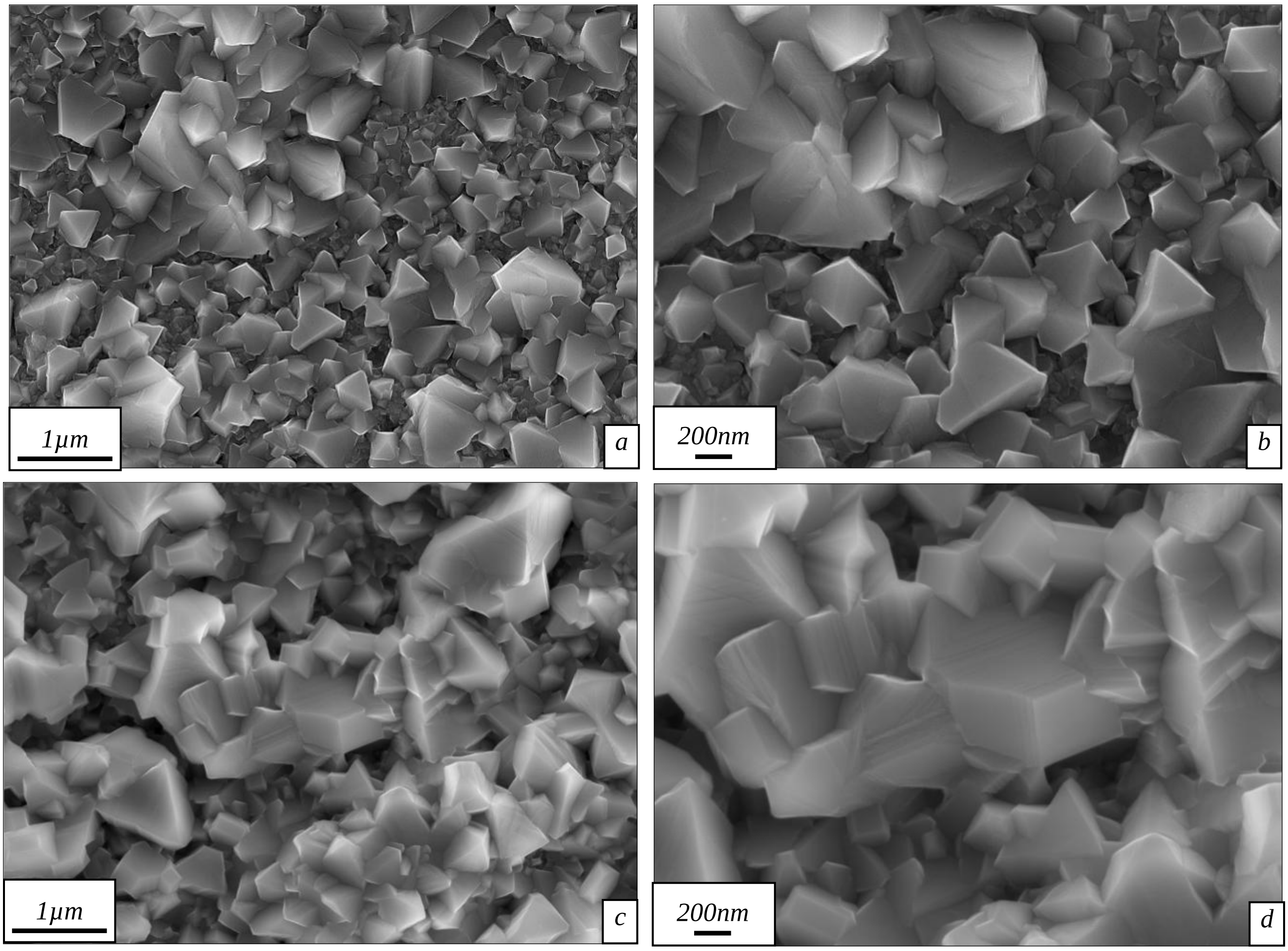

Figure 8.2:- Secondary electron images of the surface oxide formed on industrially ground S32101 after oxidation at (a+b) 800ºC for 1 hour and (c+d) 800°C for 2 hours in simulated propane combustion products

The oxide produced after 2 hours at the same temperature, is shown in Figure 8.2 (c+d). It has a greater coverage of large oxide grains measuring ~1μm in length on top of some smaller crystals. The larger oxide crystals have grown in such a way that they impinge upon each other to produces areas of oxide crystal agglomerates as shown in the higher magnification image of Figure 8.2(d).

8.2.3 Oxidation at 900°C

Figure 8.3 shows the oxide after heat treatment at 900°C for 1 hour. At low magnifications (a) it is clear that the oxide is not completely homogeneous. Instead the majority of the surface is covered in a base oxide with some areas which have experienced enhanced oxide growth. At higher magnification (b) it can be seen that the areas of enhanced oxide growth consist of agglomerates of facetted oxide crystals which have grown to form oxide nodules. The surrounding base oxide is of a similar facetted crystal structure but has a much smaller grain size.

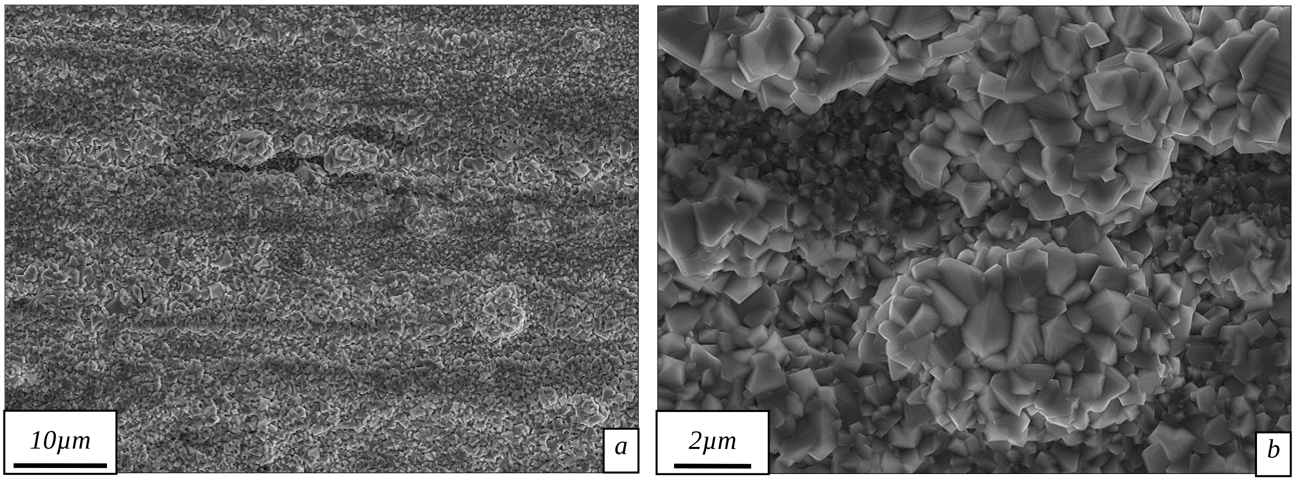

Figure 8.3:- Secondary electron images of a) the surface oxide formed on industrially ground S32101 after oxidation at 900ºC for 1 hour in simulated propane combustion products and b) at higher magnification

Further investigation of the early stage enhanced oxide growth regions was carried out on an oxide formed on industrially ground S32101 after 2 hours at 900°C in simulated combustion products of propane in the tube furnace. The base oxide formed after this heat treatment is shown in Figure 8.4. The visible surface of the oxide consists of a single type of facetted oxide grain which measures approximately 0.5-1µm in diameter.

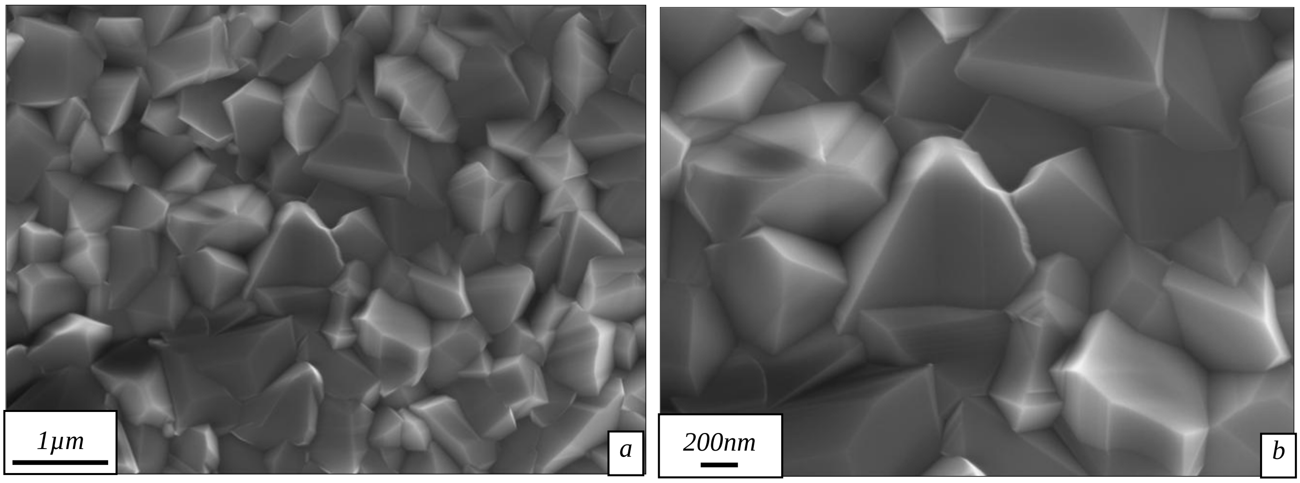

Figure 8.4.:- Secondary electron images of a) the surface oxide formed on industrially ground S32101 after oxidation at 900ºC for 2 hours in simulated propane combustion products showing base oxide and b) at higher magnification

Figure 8.5 is a bright field TEM image of a cross-section of the base oxide. It can be seen that the oxide consists of external oxide layers only. Three oxide layers are present:- the outer oxide (Layer 1) is a large grained material which is approximately 1µm thick at its thickest point. Layer 2 is a fine-grained oxide layer measuring approximately 0.5-0.6µm thick and a layer which has a brighter shade in the micrograph (Layer 3), which has no apparent grain structure and is in the region of 100nm thick. Figure 8.6 is a collection of high resolution EDS maps of an area of the same sample. It is clear from these maps that each of the layers has a different chemical composition. Layer 1 is revealed to consist of only oxygen and manganese, Layer 2 is a chromium rich oxide with modest levels of manganese and Layer 3 is a continuous layer of silicon oxide. After closer inspection of these maps it can be seen that Layer 2 consists of two levels of chromium concentration a high level and a low level. The high level region is mirrored by a lower concentration of manganese suggesting that this layer may in fact be regarded as almost pure chromia. It should also be noted that no significant concentration of iron is observed using EDS mapping in any layer of the oxide scale.

As well as EDS maps of this area, EDS point spectra were also collected. The analysed points are marked in Figure 8.5 with numbered crosses and are displayed in Table 8.1. By comparison of the atomic ratios at each of these points, the oxides can be approximately identified as:- $MnFe_2O_3$, $CrMn_2O_3$ and Si_2O_3 for points 1, 2 and 3 respectively. Examination of the O-Si phase diagram however, [Schnurre, Gröbner and Schmid-Fetzer (2004)], reveals that Si_2O_3 is not a thermodynamically favourable phase and it is possible that the silicon oxide present after this time and temperature of oxidation is in fact, SiO_2.

Table 8.1:- EDS point analysis of an oxide scale formed on industrially ground S32101 after oxidation at 900ºC for 2 hours in simulated propane combustion products

Point		**O**	**Si**	**Mn**	**Cr**	**Fe**
1	Wt%	30.1	-	67.4	-	2.5
	At%	60.0	-	38.9	-	1.4
2	Wt%	34.6	-	22.7	42.7	-
	At%	63.7	-	12.2	24.2	-
3	Wt%	45.6	52.7	-	1.7	-
	At%	59.9	39.4	-	0.7	-

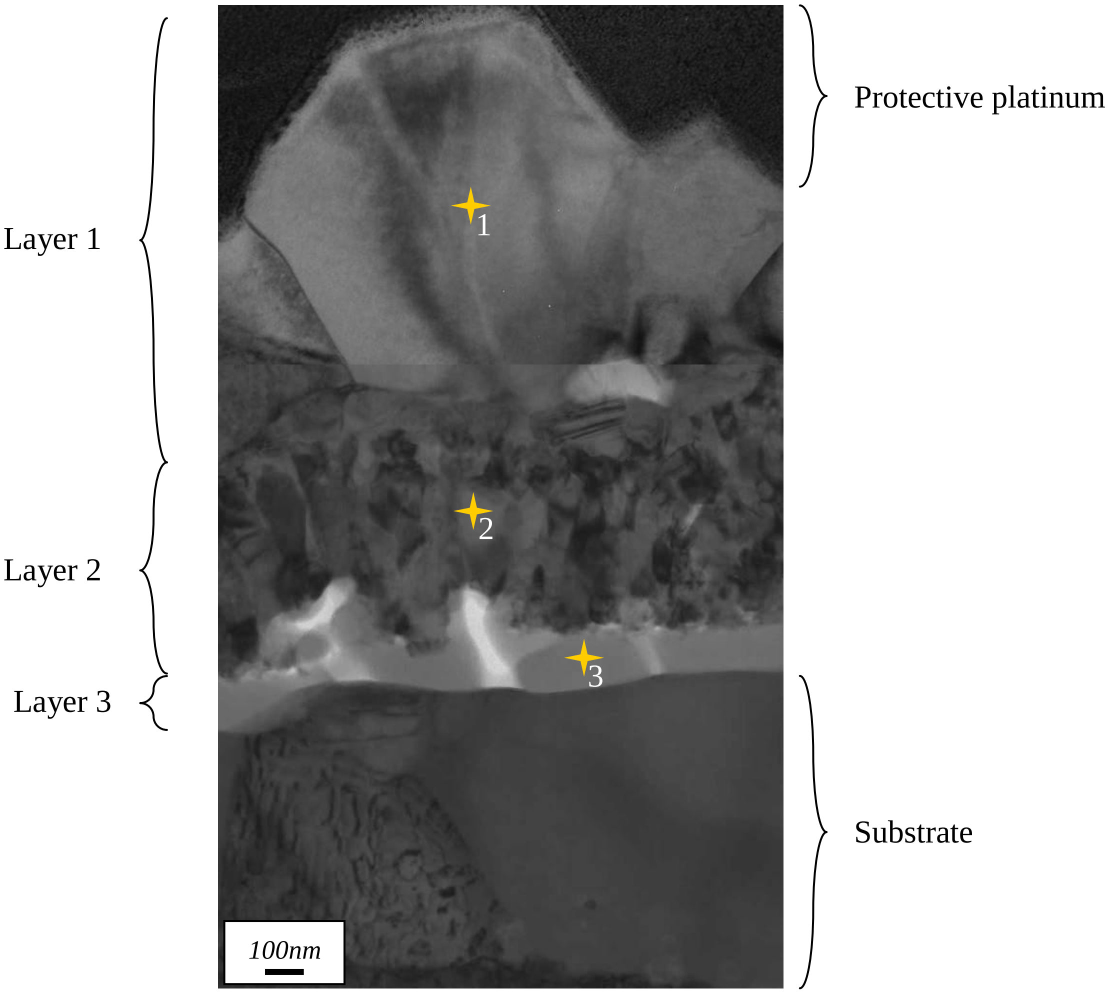

Figure 8.5:- Transmission electron micrograph of a cross-section of the oxide formed on industrially ground S32101 after oxidation at 900ºC for 2 hours in simulated propane combustion products showing EDS analysis points

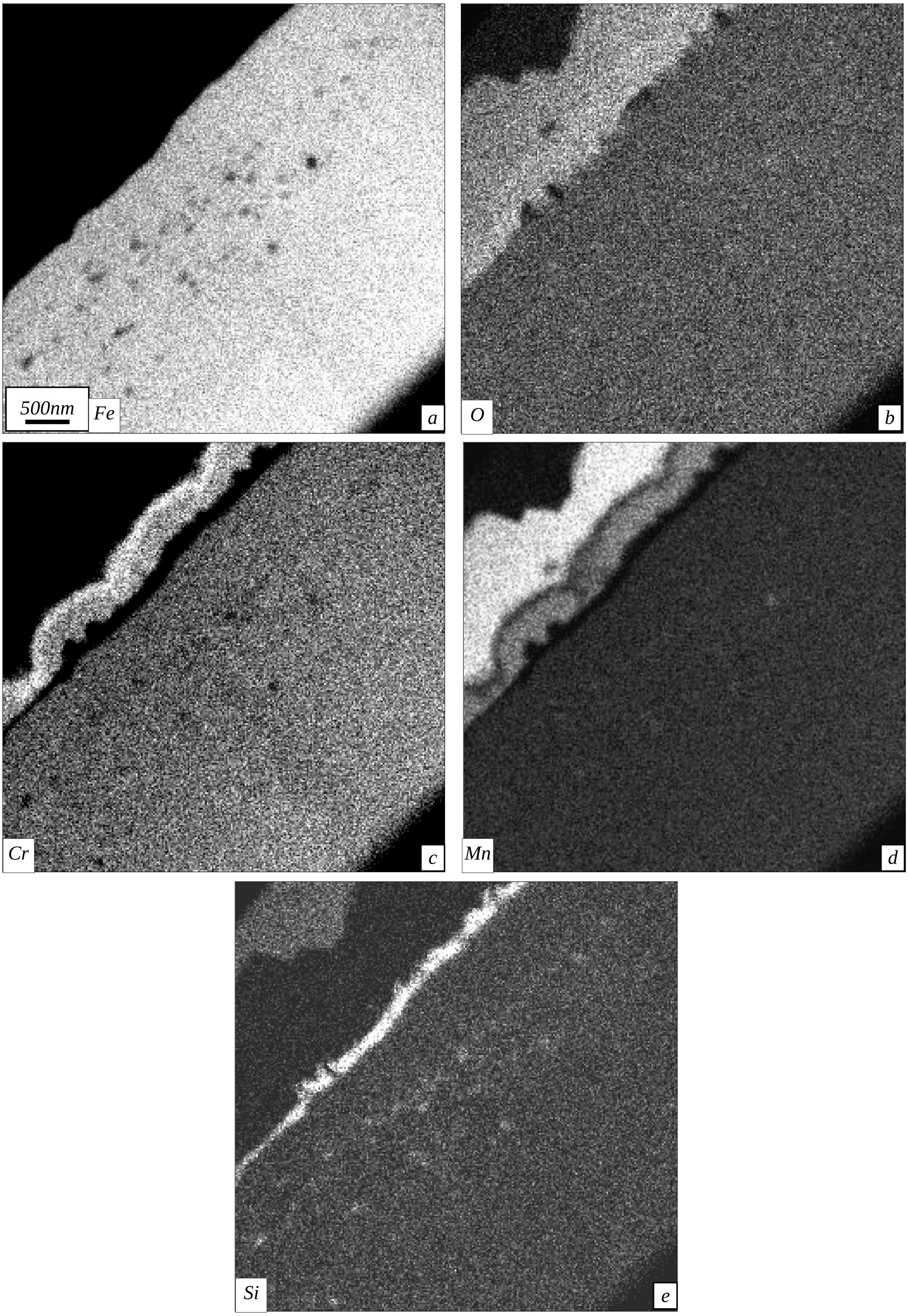

Figure 8.6:- EDS maps of a) iron, b) oxygen, c) chromium, d) manganese, e) silicon and f) image of a cross-section of the oxide formed on industrially ground S32101 after oxidation at 900ºC for 2 in simulated propane combustion products produced by the use of a scanning transmission electron microscope

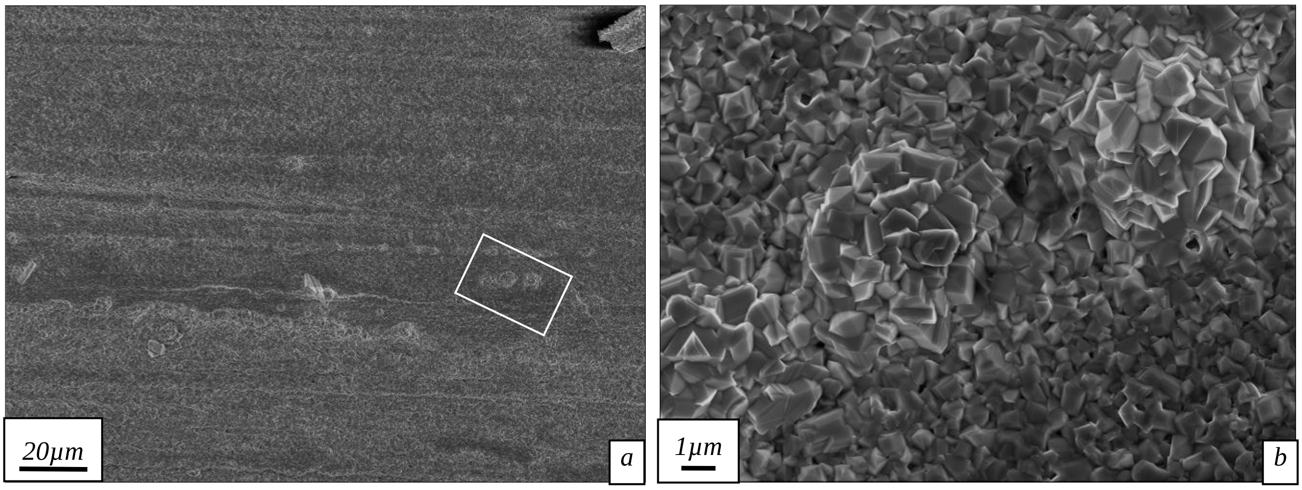

Figure 8.7:- Secondary electron images of surface oxide formed on industrially ground S32101 after oxidation at 900ºC for 2 hours in simulated propane combustion products showing the occurrence of oxide nodules. Rectangle in Figure 8.7(a) indicates the area shown at higher magnification in Figure 8.7(b)

Although the majority of the surface consists of the base oxide structure shown in Figure 8.4, it also has some small oxide features as marked with the white rectangle in Figure 8.7(a). A higher magnification image of the features marked is shown in Figure 8.7(b). This particular region is a line of 3 oxide nodules each measuring approximately 4 – 5 µm in diameter. The upper surfaces of the nodules (i.e. the visible parts in this image) have a similar form to the base oxide shown in Figure 8.4 in that they are formed of an apparent agglomeration of facetted oxide grains. Figure 8.8 is a secondary electron image of an oxide nodule taken at an angle of 52°. It can be seen that it is a steep sided feature and is not an effect of surface undulations or defects.

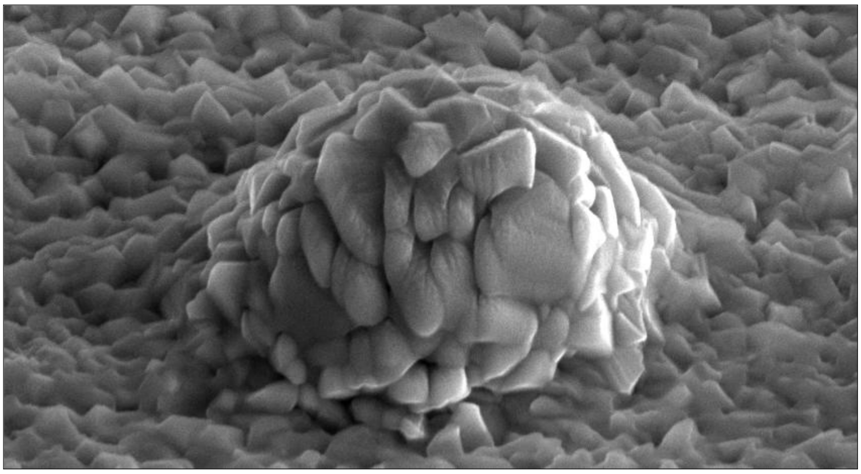

Figure 8.8:- Secondary electron image of surface oxide nodule formed on industrially ground S32101 after oxidation at 900ºC for 2 hours in simulated propane combustion products (52º tilt)

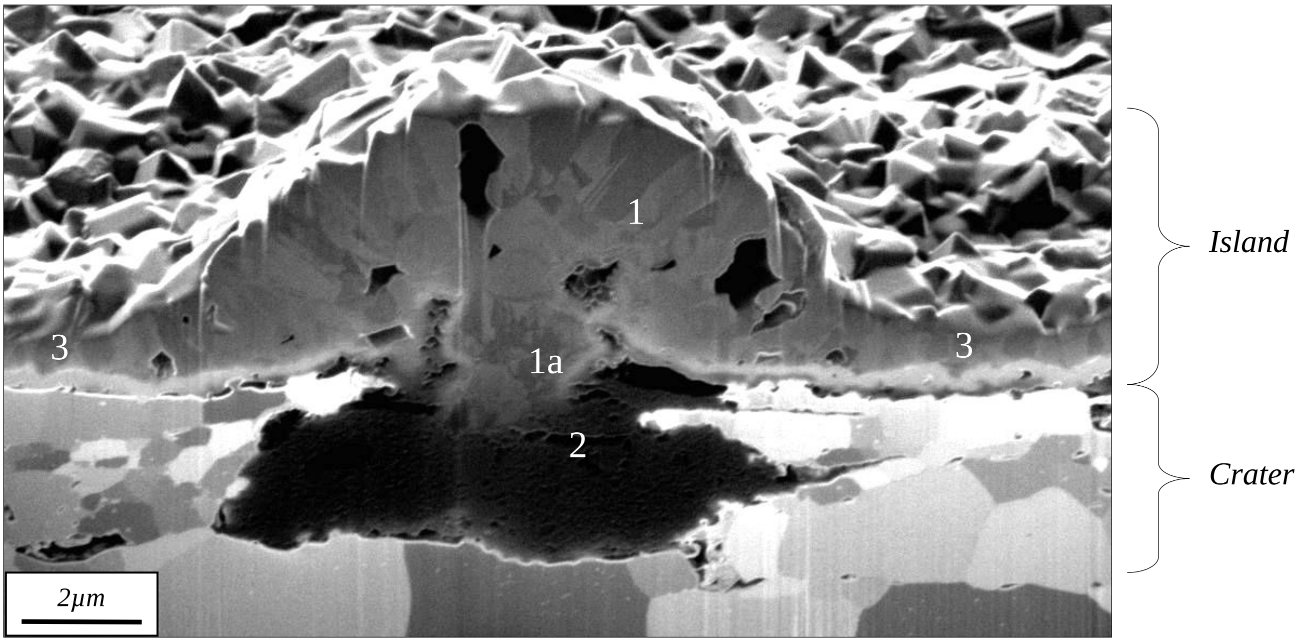

Figure 8.9:- Ion-induced secondary electron image of a FIB milled cross-section of an oxide nodule formed on industrially ground S32101 after oxidation at 900ºC for 2 hours in simulated propane combustion products showing (1)outer island region, (1a) nodule centre where the grain structure is not visible, (2) crater region and (3) base oxide

Figure 8.9 is an ion-induced secondary electron image of an ion-milled cross-section of the small oxide nodule shown in Figure 8.8. This image shows 3 main regions: - the outer island region (1) the inner crater region (2) and the base oxide to either side of the nodule (3). Region 1 is the protruding island region and measures approximately 4μm in height from the original metal surface. Towards the outer edges of the island, the grain structure is clearly revealed (through channelling contrast). The grains are columnar and of a similar size. Towards the centre of the island region (1a) is an area where the grain structure is not visible. Region 2 is a crater which has grown beneath the island. In this image it appears as a black mass. The reason for this dark colour is due to the nature of the ion induced secondary electron imaging technique and is described in detail in Appendix 1 of this thesis. Region 3 is the base oxide to either side of the island region. This region has a two-layer structure. There is a darker contrast outer layer and a brighter inner oxide. The brighter oxide is also present in the island region to its centre where it lifts from the original metal’s surface and its continuity breaks down.

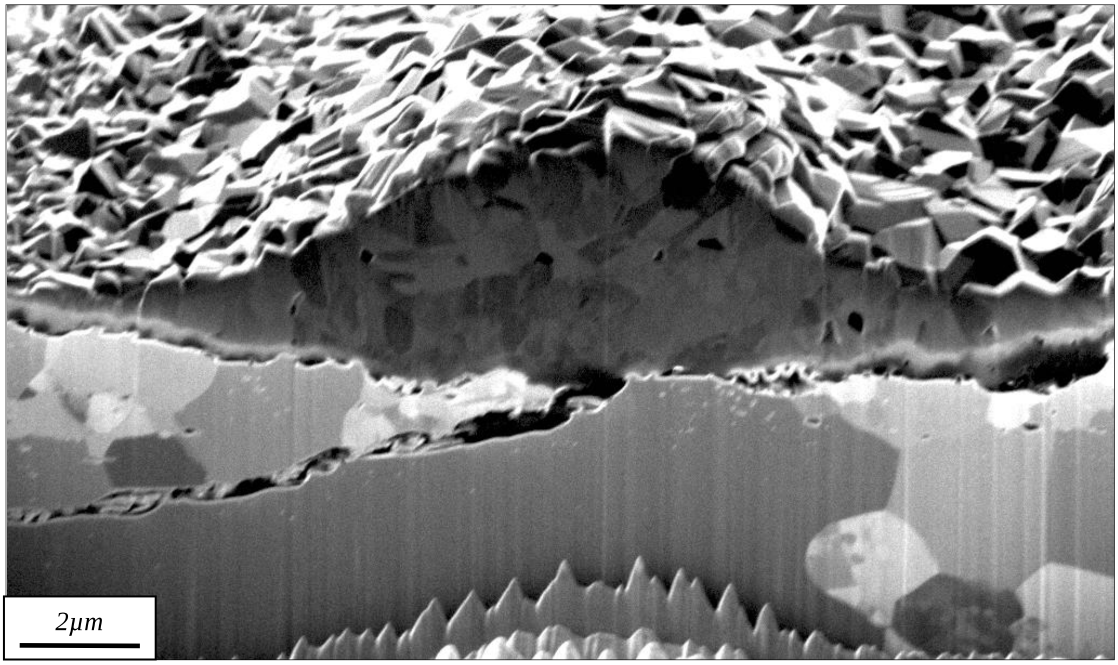

Figure 8.10:- Ion-induced secondary electron image of a FIB milled cross-section of an oxide nodule formed on industrially ground S32101 after oxidation at 900ºC for 2 hours in simulated propane combustion products

Figure 8.10 is an additional ion-induced secondary electron image of an ion-milled cross-section of an oxide nodule formed on industrially ground S32101 after oxidation at 900°C for 2 hours in tube furnace. This particular nodule region is different to the previously shown example, in that there is no crater. Instead it consists of an island part with a similar grain structure to the previous example and a large (apparently oxidised) fissure extending from the substrate to the island's centre. The fissure runs between grains as indicated by the channelling contrast seen in the image, however, it is unknown whether the boundary is a grain boundary or a phase boundary. The bright oxide layer is also present in this example and again it breaks down in the island's centre approximately equidistant from each side of the fissure in the substrate.

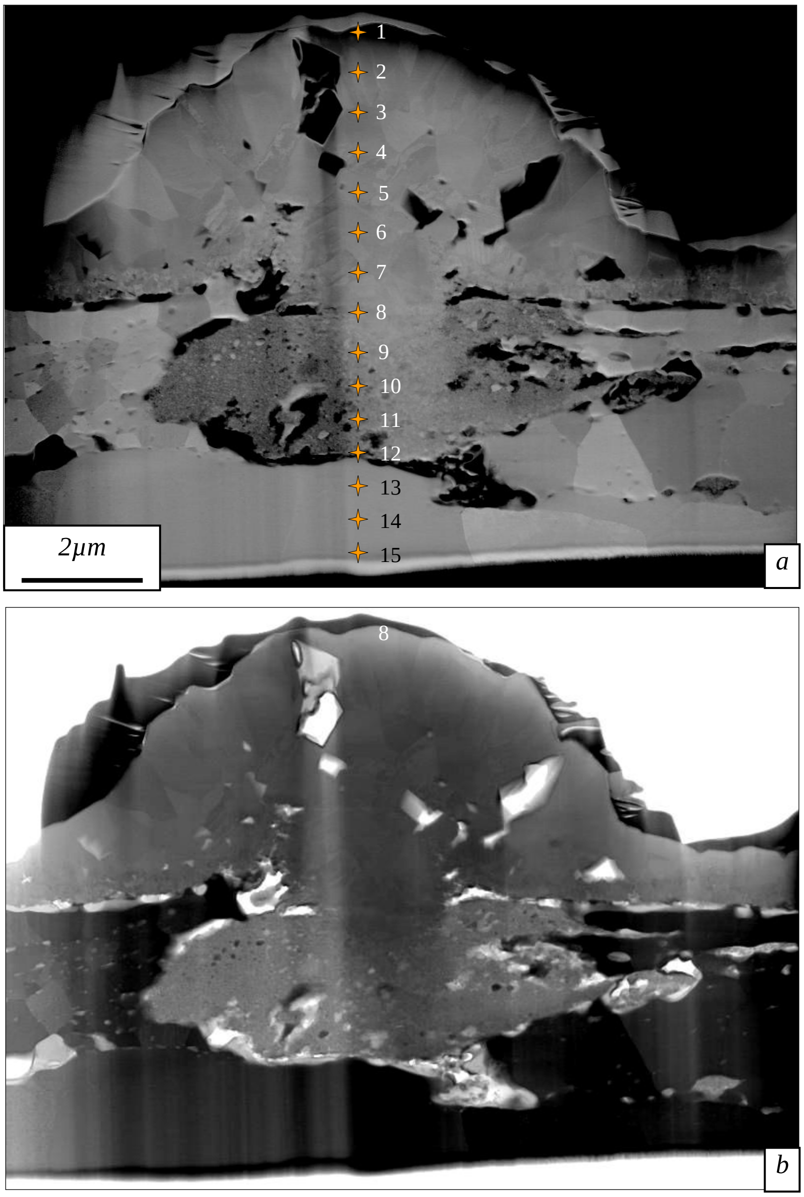

Figure 8.11:- (a) Dark field STEM image showing locations of EDS data collection displayed in Figure 8.14 and (b) a bright field STEM image of an oxide nodule formed on industrially ground S32101 after oxidation in simulated combustion products of propane for 2 hours at 900°C

Figure 8.11 shows a dark and bright field STEM image of the oxide nodule shown in Figure 8.9. Here it can be seen that the bright band in the ion-induced secondary electron image (Figure 8.9) is a fine grained band at the lowest extent oxide adjacent to the oxide / metal interface. The crater region is also extremely fine grained and is surrounded by dark areas which could be voids at the oxide / metal interface. The large oxide grains towards the outer edge of the external island region of the oxide nodule are still visible. The bright field STEM image of the same region shows that many of the dark regions on the dark field image do in fact appear to be voids but many of them are surrounded by a phase which resembles the

SiO_2 shown in Figure 8.5 at the oxide / metal interface. High resolution EDS maps have been taken of this area, the results of which are shown in Figure 8.12.

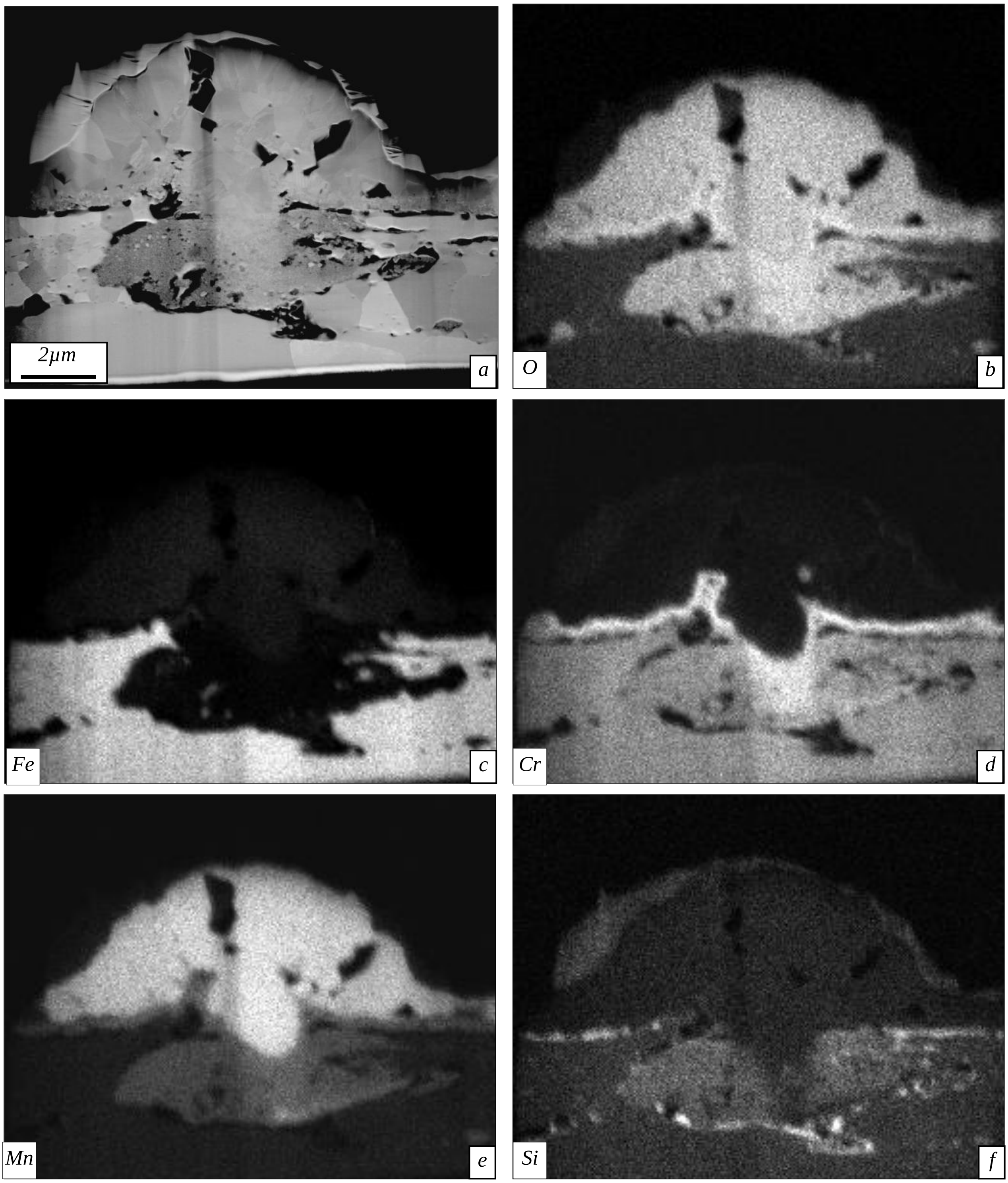

Figure 8.12:- Dark field STEM image(a) and accompanying high resolution EDS maps of (b) oxygen, (c) iron, (d) chromium, (e) manganese and (f) silicon of an oxide nodule formed on industrially ground S32101 after oxidation in simulated propane combustion products for 2 hours at 900°C,

The high resolution EDS maps of the area are shown in Figure 8.12. It is clear from these results that the fine grained band, which is revealed as a bright layer in the ion-induced secondary electron image, is a chromium containing oxide. This high-chromium band then breaks down in the nodule’s centre where the oxide crater is joined to the island. The island itself consists of only manganese and oxygen. Counts of manganese in the chromium rich band are low but still present which is also the case with the oxide found to form in the crater region. The silicon mainly resides at the oxide / metal interface in all regions including: - the base oxide to either side of the nodule, the nodule itself and in positions around the perimeter of the oxide formed in the crater region. It should be noted that the silicon rich layers are continuous when positioned beneath the base oxide and island region but discontinuous when surrounding the crater. As well as forming continuous and discontinuous silica layers, the silicon has also formed within the crater except where the manganese rich island protrudes into the crater.

At higher magnification (Figure 8.13) it can be seen that the chromium rich band breaks down in the nodule’s centre and does not continue into the crater. Instead it comes to quite an abrupt end as it encroaches into the crater. It is also visible from the higher magnification EDS maps that the silicon is situated at many of the apparent voids at the oxide / metal interfaces (indicated by the absence of chromium in Figure 8.13 (c)). EDS spot analysis of the silicon rich layer reveals that it contains ~35 at% silicon and ~65 at% oxygen which suggests that it is SiO_2. There is a clear and abrupt change in chromium and manganese content between the fine grained chromium oxide and the larger grained manganese rich oxide which forms the outer nodule region.

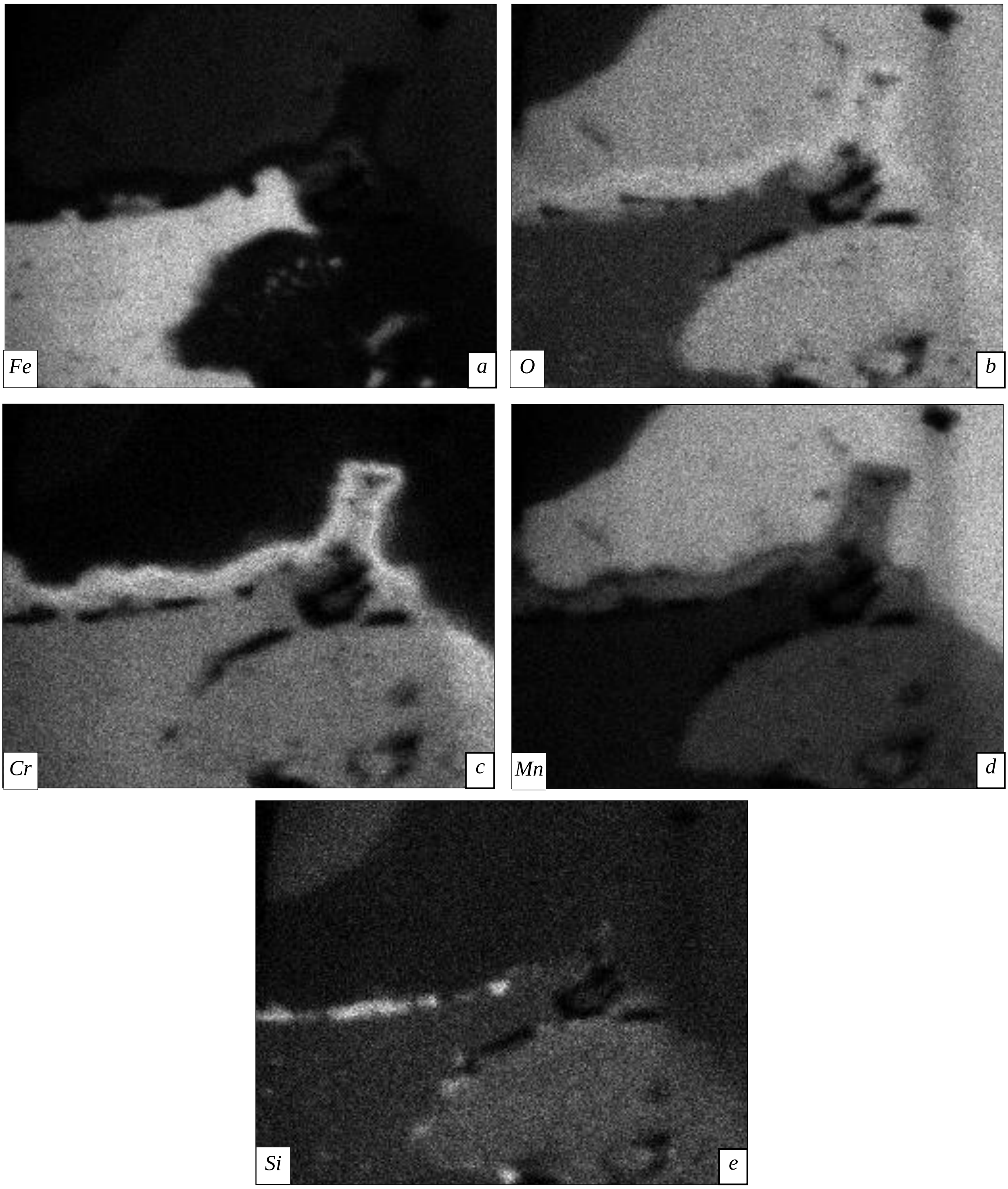

Figure 8.13:- High resolution EDS maps of (a) iron, (b) oxygen, (c) chromium,(d) manganese and (e) silicon of an oxide nodule formed on industrially ground S32101 after oxidation in simulated propane combustion products for 2 hours at 900°C,

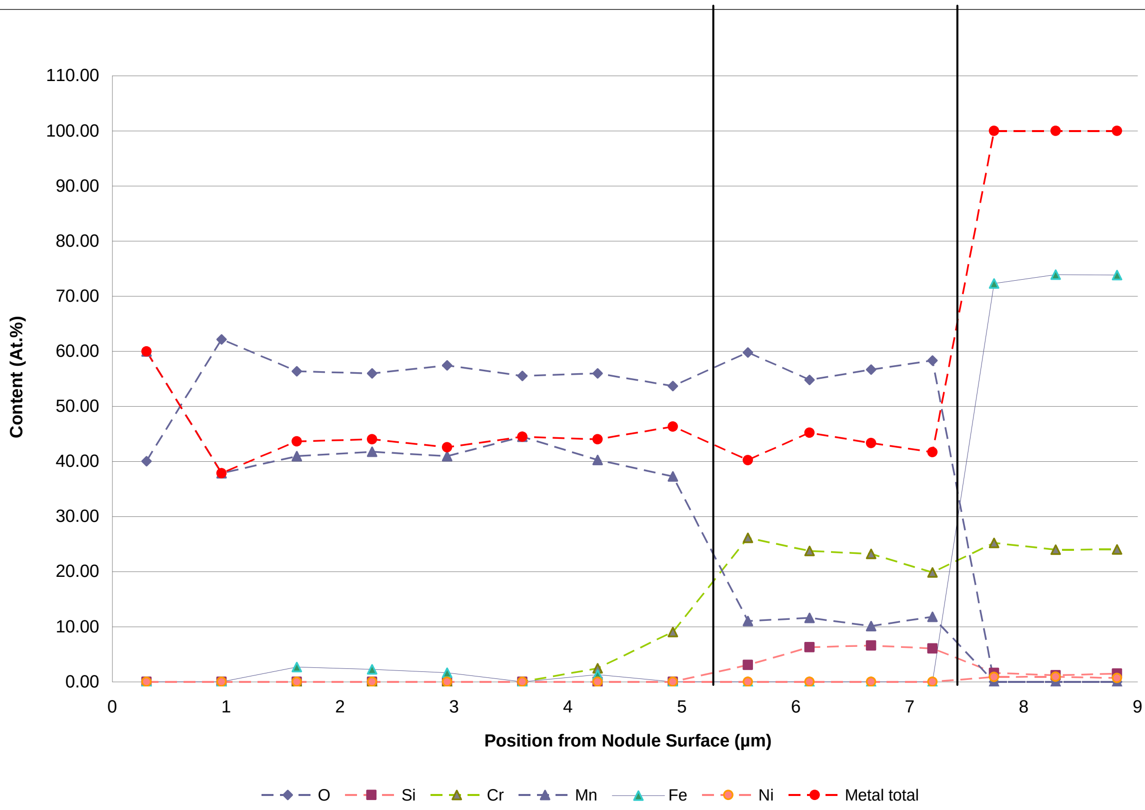

Figure 8.14:- Graph of atomic % versus point number of spot EDS analysis of the points marked in Figure 8.11

EDS spot analyses at the positions shown in Figure 8.11 were carried out on the oxide nodule with the results plotted in Figure 8.14. Through the first 5 µm, the chemical composition of the oxide remains homogeneous with only a slight enrichment of chromium and corresponding depletion of manganese observed at 5 µm which was taken from the interface between the manganese rich outer island region and the chromium rich crater region shown in the high resolution EDS maps of Figure 8.12. The nodule’s upper surface (between 0 and 1 µm) reveals an apparent reversal of the ratio of manganese to oxygen contents. This result, however, should be viewed with some degree of scepticism due to its proximity to the edge of the specimen which may have suffered damage such as excessive thinning during the ion milling process. Between 5 and 7.5 µm the positions were taken from within the chromium rich crater region shown in Figure 8.12. In this region the EDS spots confirm an increase in the amount of chromium present and a decrease in the manganese concentration as well as a small amount of silicon which is at a higher level towards the metal / oxide interface. This particular oxide nodule feature shows no evidence of elemental depletion or enrichment in the substrate immediately below it. From 1 – 7.5 µm, the atomic percentage of metal remains fairly constant between ~45 % with the atomic percentage of oxygen being nearer ~55 % suggesting that the majority of the oxides formed are of the spinel type M_3O_4.

8.2.4 Oxidation at 1000°C

After oxidation for 1 hour at 1000°C, the surface shown in Figure 8.15 is observed. Oxide ridges are formed in the direction of the industrial grinding marks (horizontal in this case) with some spalling of the oxide evident. At higher magnification it is possible to distinguish only one type of oxide crystal which is a highly facetted octahedron shaped crystal. The sizes of the crystals vary with some smaller crystals forming at boundaries between larger crystals. The larger crystals have formed at the tops of the oxide ridges whereas smaller crystals have formed in between the ridges.

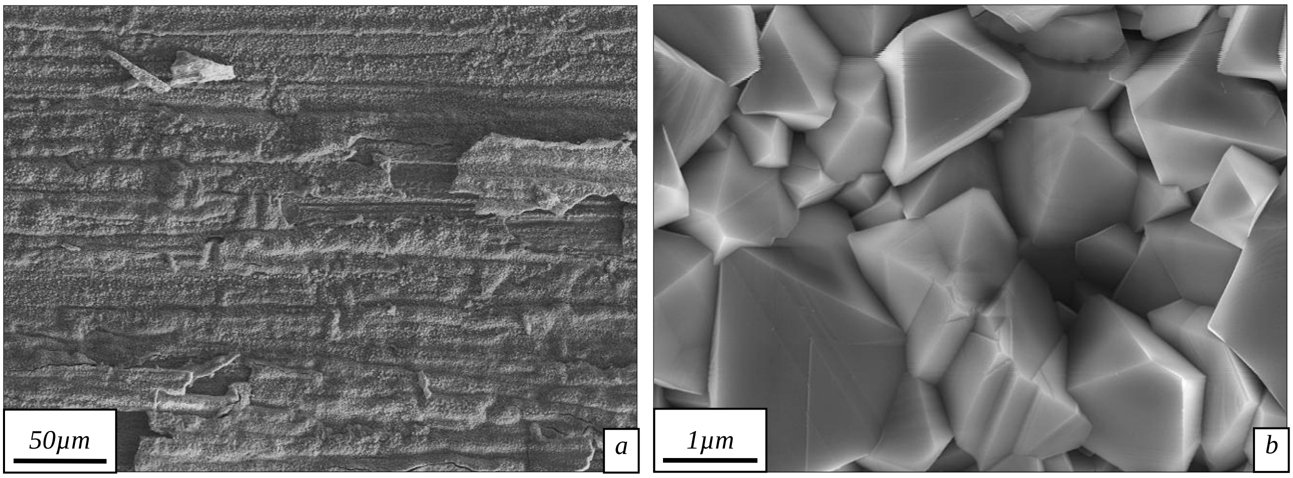

Figure 8.15:- Secondary electron images of a) the surface oxide formed on industrially ground S32101 after oxidation at 1000ºC for 1 hour in simulated propane combustion products and b) at higher magnification

8.2.5 Oxidation at 1100°C

Figure 8.16 shows secondary electron micrographs of the surface of industrially ground S32101 after oxidation at 1100°C for 1 hour in the tube furnace. The overview of the surface shows that there are two types of oxide present. The first is a thin oxide which resembles the marks left by the industrial grinding operation and the second are the large nodular regions. Higher magnification images of the thin and nodular oxides are shown in Figures 8.16 (c) and 8.16 (d) respectively. The thin region has typical facetted oxide grains as well as protrusions of oxide which are much finer grained than the facetted region. The nodular oxide has a far larger grain size but still has a facetted surface.

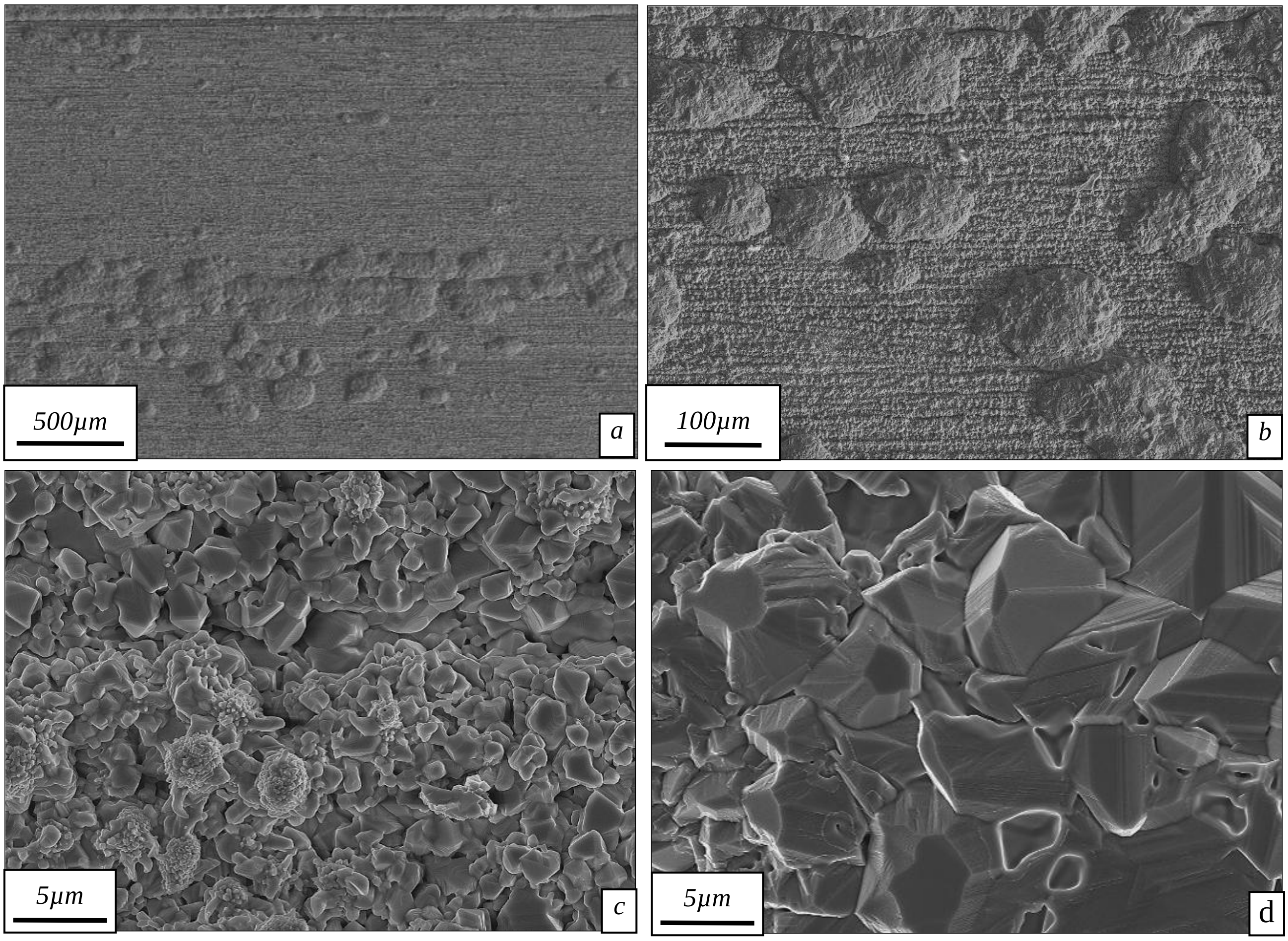

Figure 8.16:- Secondary electron images of the surface oxide formed on industrially ground S32101 after oxidation at 1100ºC for 1 hour in simulated combustion products of propane showing a) low magnification overview of the surface, b) higher magnification of the surface, c) high magnification of the base oxide and d) high magnification of a nodule's surface

In cross-section (Figure 8.17), it can be seen that the nodular island regions are dense oxide structures which are accompanied by an oxide crater which, in this case, extends to approximately 10µm into the surface. To either side of the nodular oxide region is a thinner oxide scale which consists of an oxide which is in contact with the surface and one which forms "loops" of oxide possibly to form the structure in Figure 8.16 which resembles the underlying grinding marks. Large scale oxide nodules are not very common after this heat treatment with the majority of the surface being covered in the base oxide (Figure 8.18). Chemical maps of the nodule shown in Figure 8.17 are displayed in Figure 8.19. The iron map shows that the oxide crater has a band which is devoid of any iron content around its perimeter and that the island is rich in iron. The iron poor band is rich in both chromium and manganese. The chromium map also shows that the crater region is rich in chromium whereas the island has no chromium present; however, this map also reveals that there are two chromium rich features present within the bulk of the island. One is a single isolated entity and the other as a chromium rich vein which extends over the island’s entire width. Similarly, manganese is also present in all chromium rich regions as well as a thin layer on the outer edge of the island. The silicon map reveals very fine silicon rich roots which extend into the substrate. A number of these roots can be associated with the dark features seen in Figure 8.17.

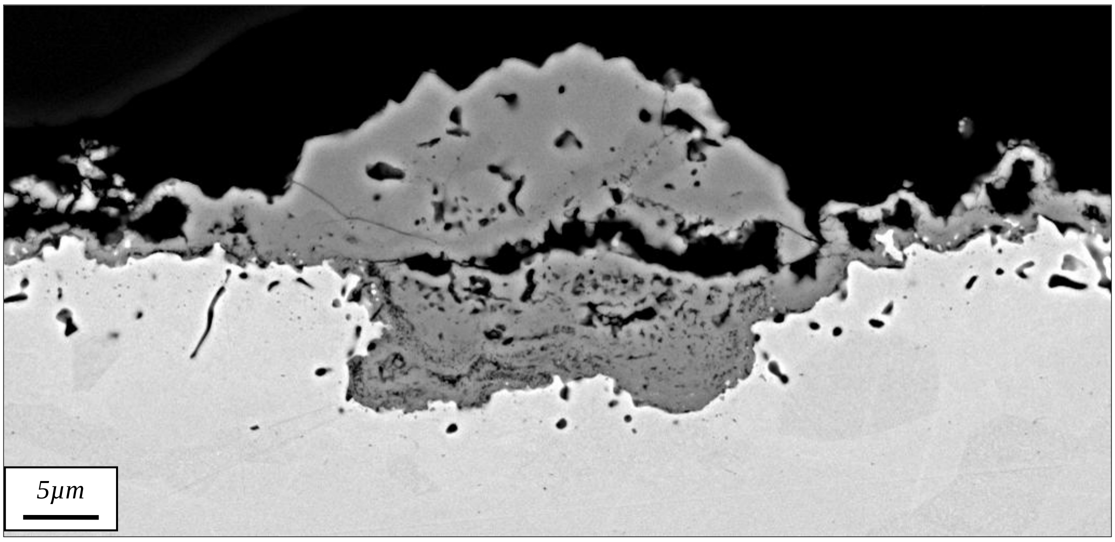

Figure 8.17:- Back scattered electron image of a cross-section of an oxide formed on industrially ground S32101 after oxidation at 1100ºC for 1 hour in simulated propane combustion products

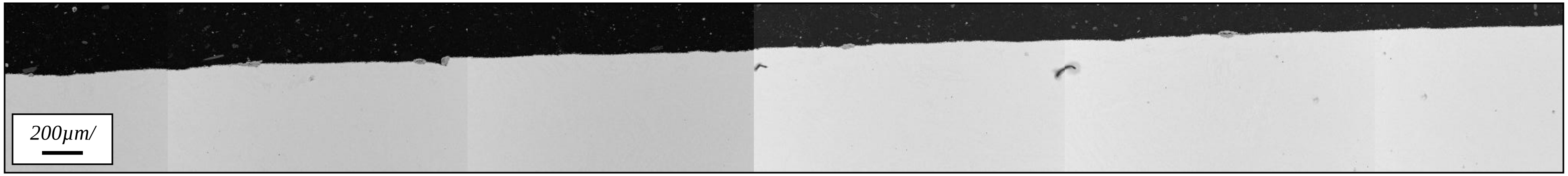

Figure 8.18:- Back scattered electron image of the cross-section of the entire surface of an oxide formed on S32101 after oxidation at 1100°C for 1 hour in t simulated propane combustion products

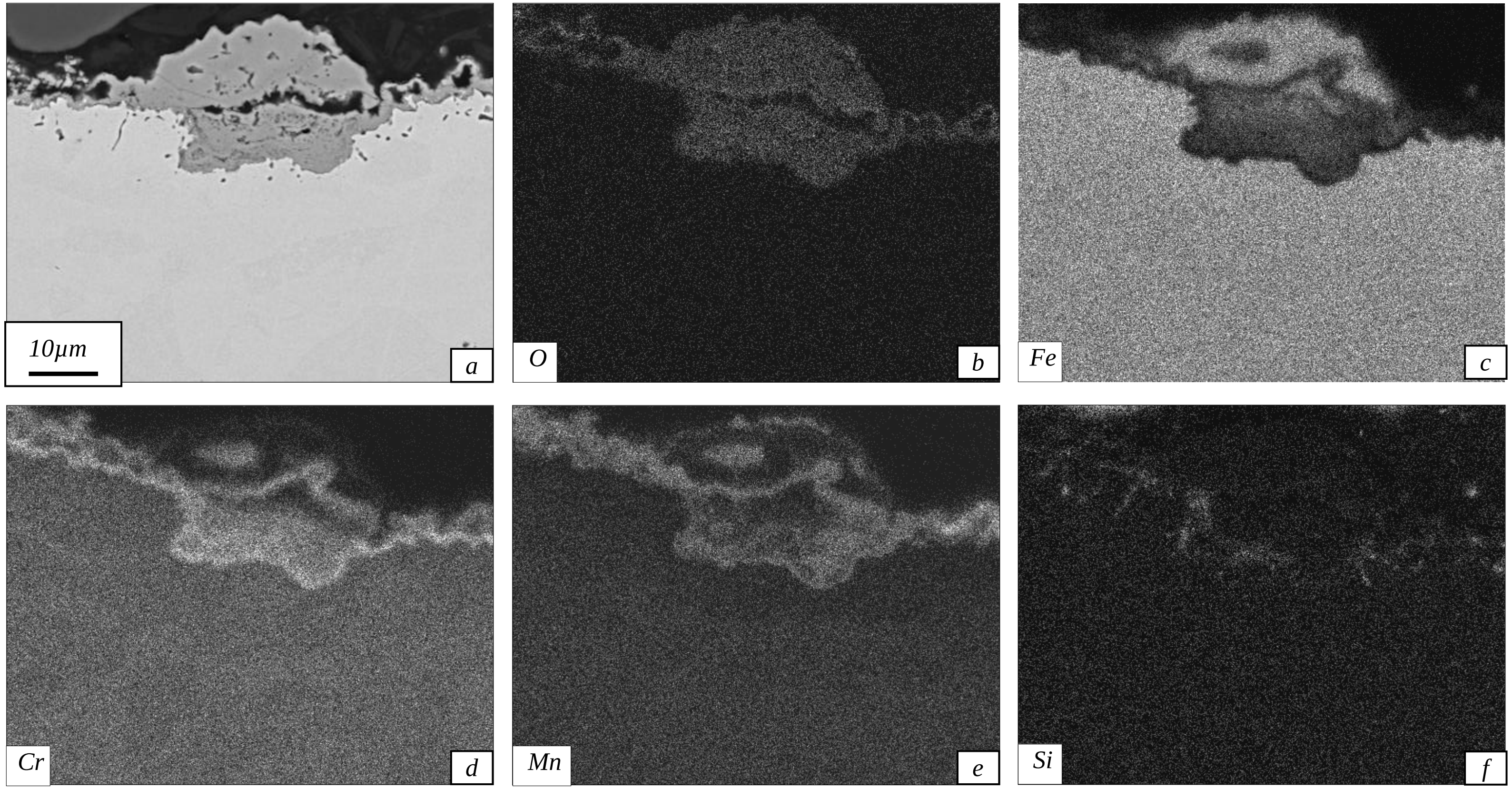

Figure 8.19:- (a) Backscattered electron image with EDS maps of (b) oxygen, (c) iron, (d) chromium, (e) manganese and (f) silicon of an oxide nodule formed on industrially ground S32101 after oxidation in simulated propane combustion products for 1 hour at 1100°C,

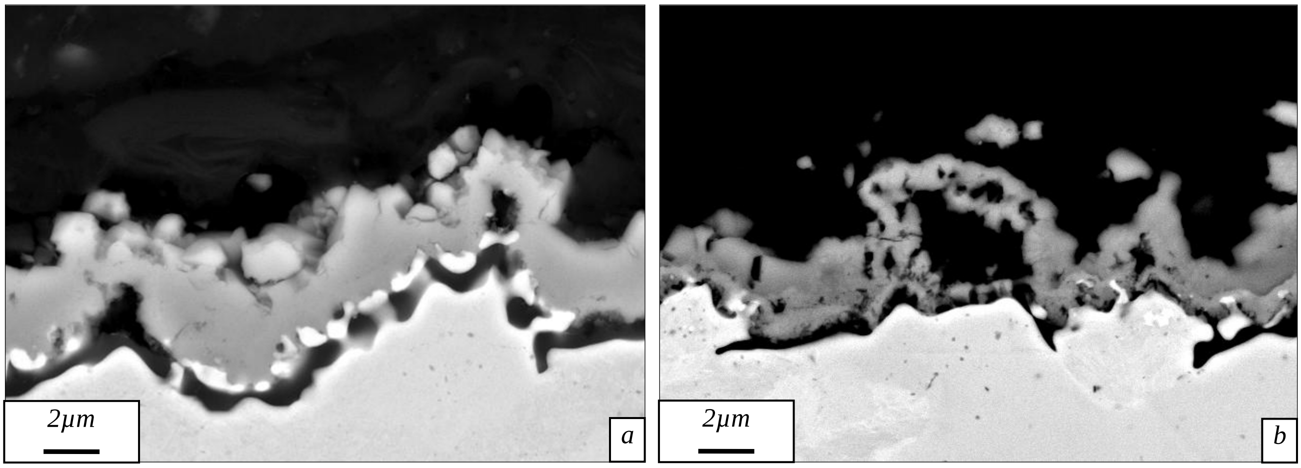

Figure 8.20:- Back scattered electron image of a) a cross-section of an oxide formed on industrially ground S32101 after oxidation at 1100°C for 1 hour in simulated propane combustion products and b) a cross-section of an oxide loop formed in the same conditions

Figure 8.20 are backscattered electron micrographs of a cross-section of the thin oxide. There are two types of the thin oxide: an apparently single layered oxide and areas where the oxide has formed loops. The single layered oxide is in contact with the substrate whereas the oxide loop is not. EDS maps of the oxide loop in Figure 8.20(b) are shown in Figure 8.21. Figure 8.21(a) is a lower magnification backscattered electron micrograph of the oxide loops shown in Figure 8.20 (b). It reveals that the oxide to either side of the loops is apparently dual layer (as indicated by contrast differences within the scale). At the metal / oxide interface there is a dark material which penetrates into the substrate at various positions. The EDS maps show that the dark substance at the oxide / metal interface is silicon rich and that the lower layer of the oxide scale produces only chromium counts. The upper oxide layer is an oxide of manganese. The oxide loop is revealed to consist of a small amount of both chromium and manganese.

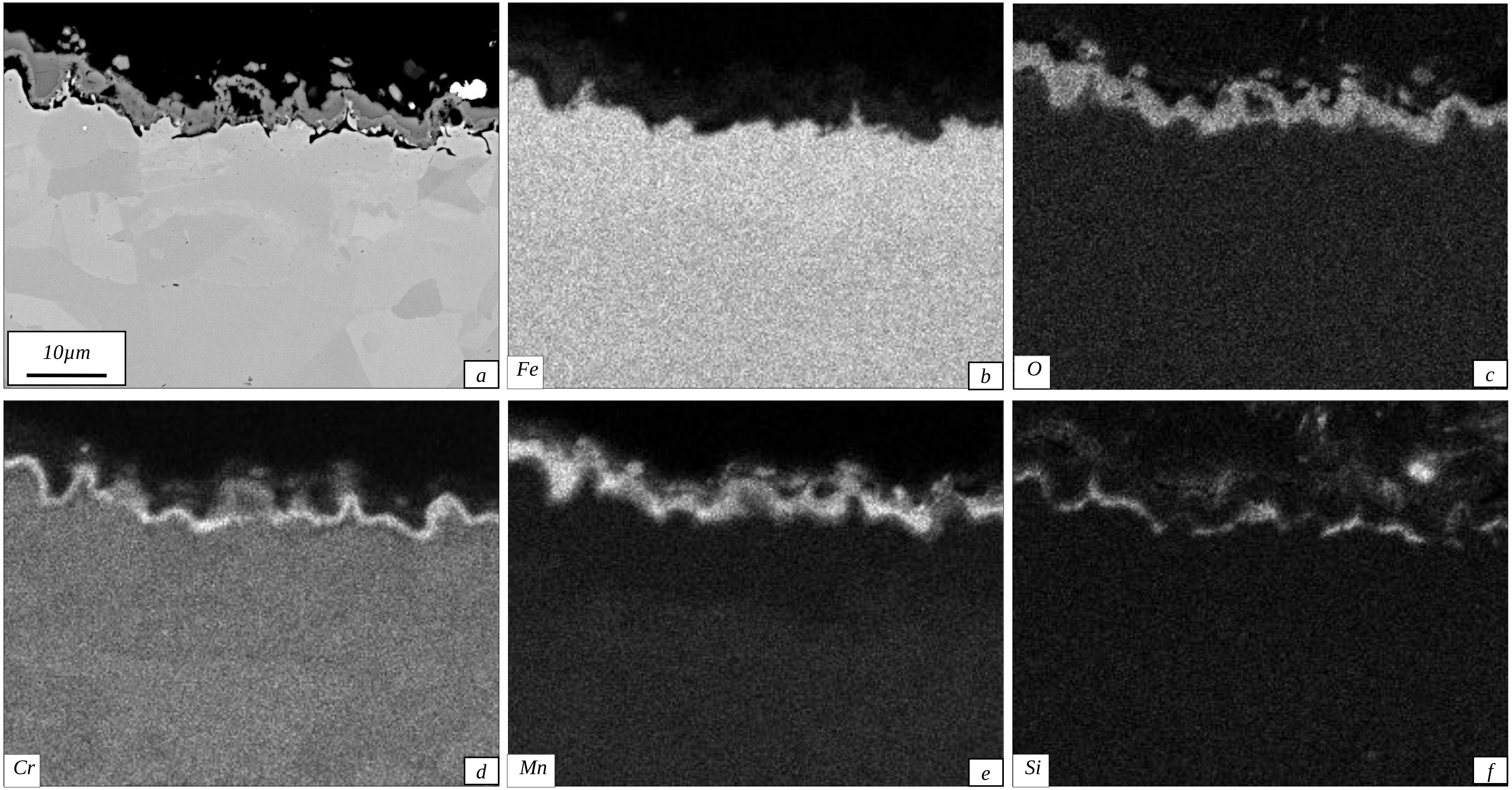

Figure 8.21: a) Backscattered electron micrograph and accompanying EDS maps of b) iron, c) oxygen, d) chromium, e) manganese and f) silicon of an oxide formed on industrially prepared S32101 after oxidation at 1100°C for 1 hour in simulated propane combustion products

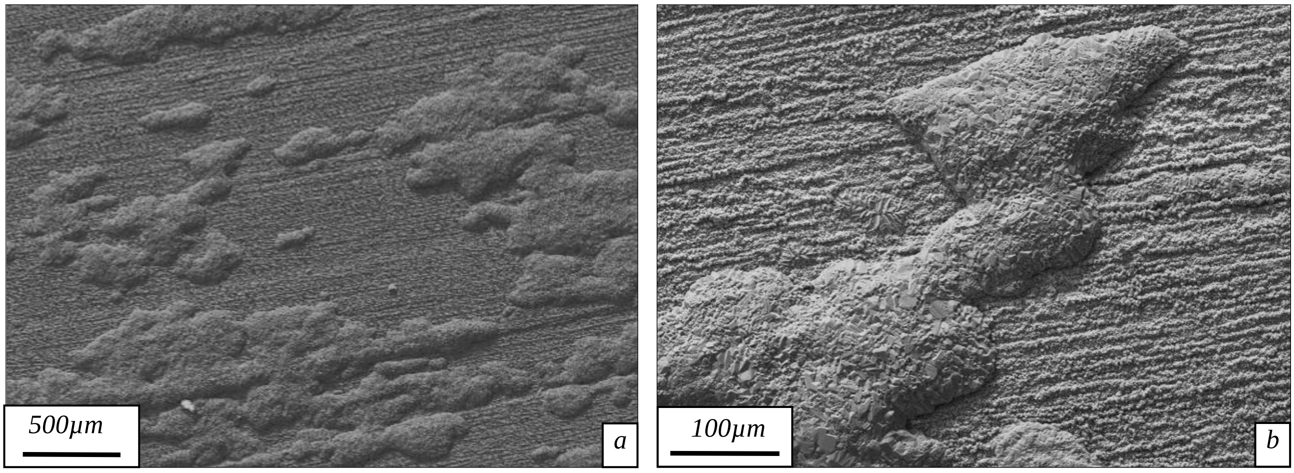

Figure 8.22:- Secondary electron images of the surface oxide formed on industrially ground S32101 after oxidation at 1100ºC for 2 hours in simulated propane combustion products at a) low magnification and b) higher magnification

A further hour of oxidation produces the oxide shown in Figure 8.22. There are again two regions of oxide which are: a base oxide which resembles the underlying grinding marks and areas which has undergone enhanced oxide growth. When compared to the oxide produced in the same conditions for only an hour, the oxide nodules have joined in some places to form large regions of enhanced oxide growth. Very little difference is observed between the oxide morphology produced here and one observed after oxidation at the same temperature for only 1 hour.

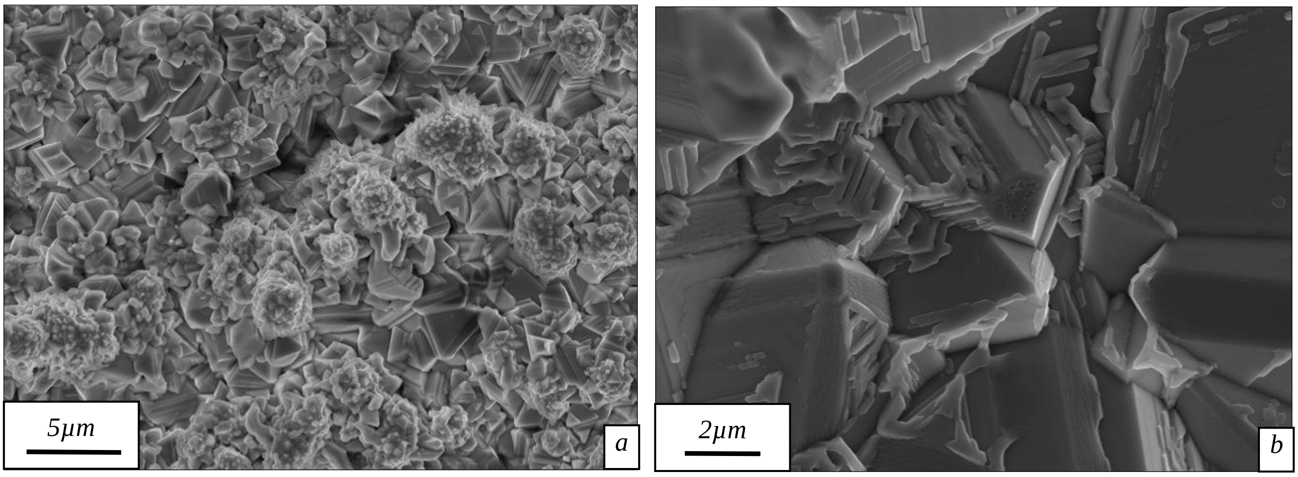

Figure 8.23:- Secondary electron images of the surface oxide formed on industrially ground S32101 after oxidation at 1100ºC for 2 hours in simulated propane combustion products showing a) facetted and globular oxide grains and b) high magnification facetted grains

At higher magnification (Figure 8.23) the oxide produced has a base oxide which is octahedral in shape with globular protrusions growing from its surface. The areas of enhanced oxide growth are highly facetted crystals.

8.3 S32205 – Industrially Hot Ground

8.3.1 Oxidation at 700°C, 800°C and 900°C

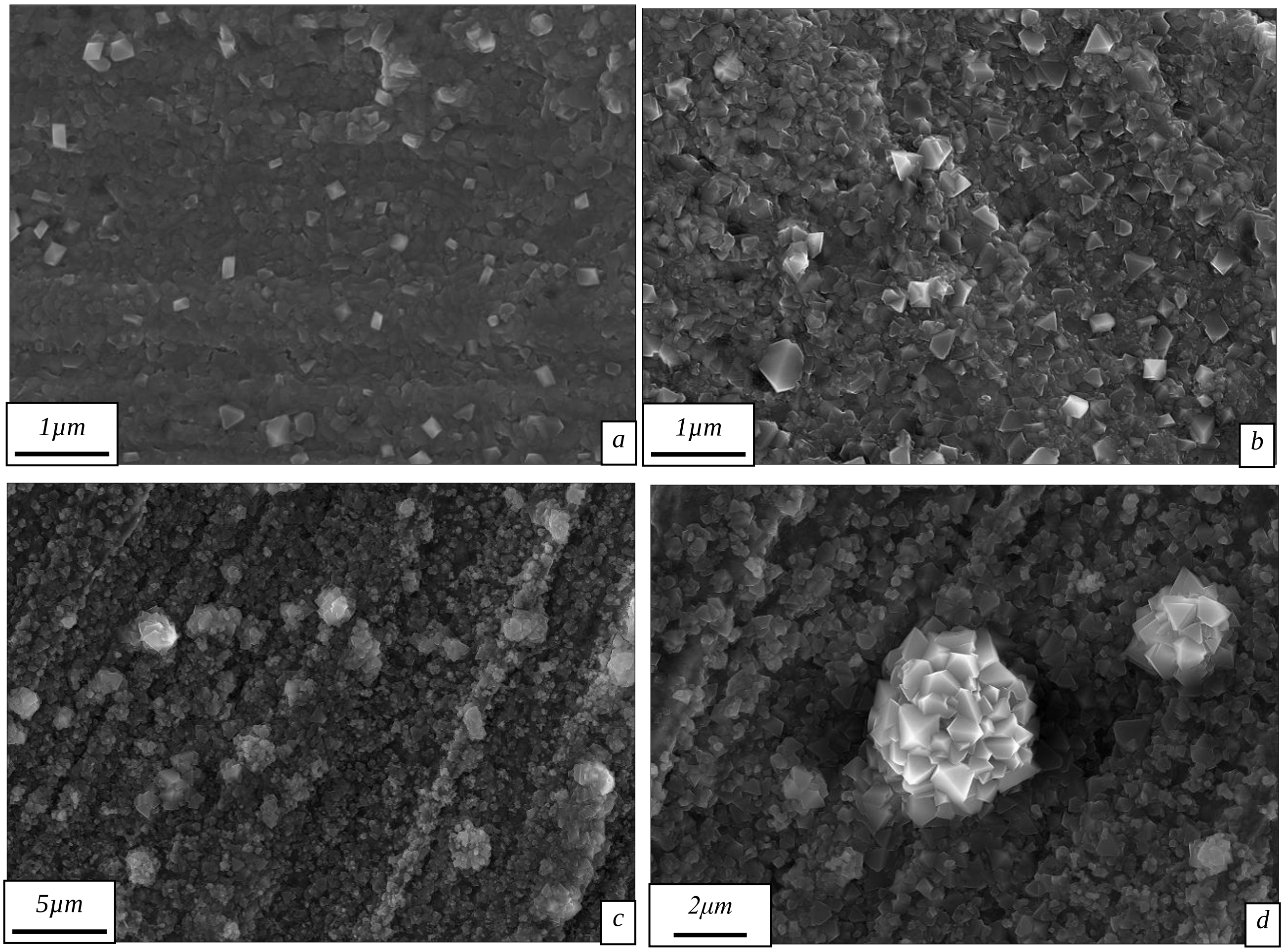

Figure 8.24:- Secondary electron images of surface oxide formed on industrially ground S32205 after oxidation at a) 700°C for 2 hours, b) 800°C for 1 hour and c+d)900ºC for 2 hours in simulated propane combustion products

Figure 8.24 shows secondary electron images of oxide formed on industrially hot ground S32205 in the tube furnace at temperatures of 700°C, 800°C and 900°C. As with many other examples of early stage oxidation reported in this thesis, there are two types of oxide present at the lower of these temperatures (Figure 8.24 a+b):- a fine grained oxide which does not have a facetted structure (dark contrast in these images) and a brighter oxide which are facetted octahedron shaped crystals distributed across the surface of the specimen in a random distribution. The bright octahedron crystals measure ~200nm in length after oxidation at 700°C and are slightly larger after oxidation at 800°C.

Figure 8.24 c + d are secondary electron images showing the result of oxidising S32205 for 2 hours at 900°C in the same atmosphere. This particular specimen showed an oxide which consisted of an underlying base oxide of fine grains and small facetted oxide crystals as well as small areas of enhanced oxide growth which has produced the nodules such as those shown in Figure 8.24 (d). The nodules are formed by an apparent excessive growth of the facetted oxide crystals which are often observed as part of the base oxide.

8.3.2 Oxidation at 1000°C

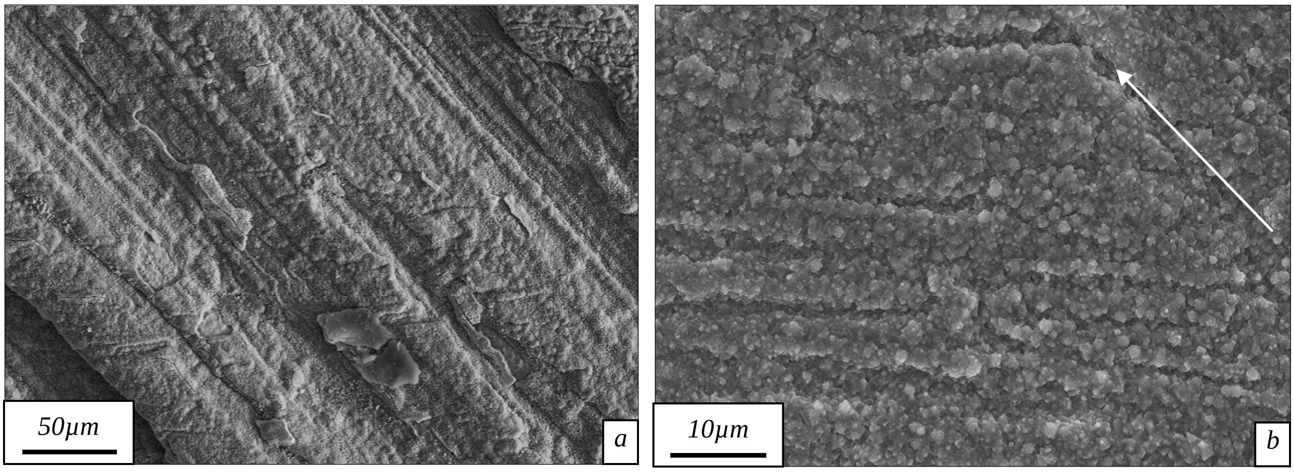

Figure 8.25:- Secondary electron images of a) over view of surface oxide formed on industrially ground S32205 after oxidation at 1000ºC for 1 hour in simulated propane combustion products and b) higher magnification of the base oxide. The arrow indicates the grinding direction of the substrate

After oxidation of S32205 at 1000°C for 1 hour the oxide shown in Figure 8.25 is produced on the surface. At low magnification it is possible to distinguish the grinding marks left by the industrial preparation of the surface. At high magnifications, ridges in the oxide form in a direction almost perpendicular to the grinding direction (grinding direction is indicated by the arrow in Figure 8.25b). The ridges consist of facetted oxide crystals with small protrusions of fine grained oxides from the surface.

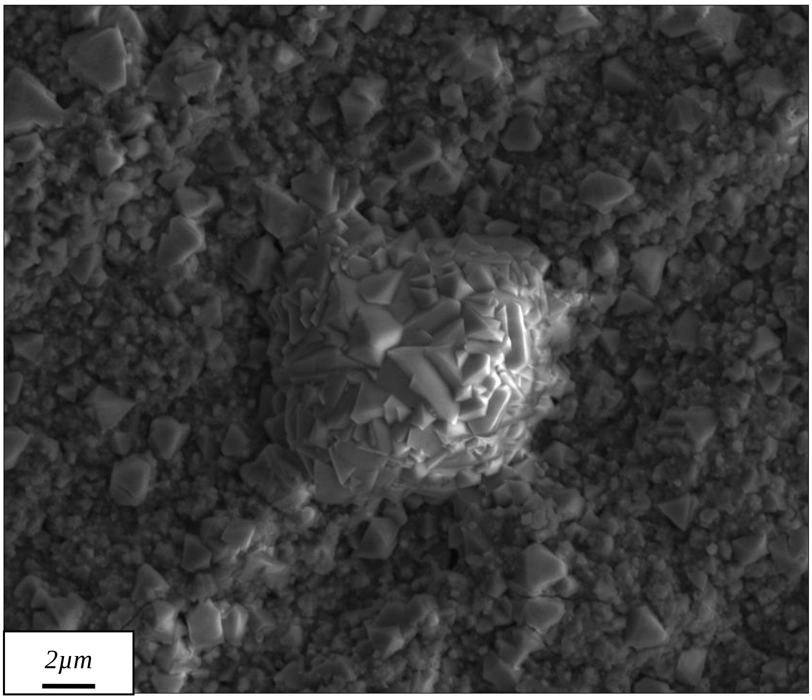

Figure 8.26:- Secondary electron micrograph of an oxide nodule formed on industrially groundS32205 after oxidation at 1000°C for 1 hour in simulated propane combustion products

As well as the oxide ridges on the surface there are occasional small areas of enhanced oxide growth which form oxide nodules such as that shown in Figure 8.26. This particular nodule measures only ~6μm in diameter and as with the majority of the other oxide nodules presented in this thesis, the oxide on the upper surface is made up of facetted grains which are apparently octahedral in shape. The surrounding base oxide is comprised of two different crystal types. The first is a small oxide crystal which is globular in nature and the second is an octahedral type oxide similar to the crystals which form the oxide nodule. A cross-section for TEM examination was produced of this particular area using focused ion beam milling, the result of which is shown in Figure 8.27.

Unlike the nodules formed on S32101, this particular nodule region shows no underlying crater or oxidised boundary of any description. Instead it has formed directly on the metal's surface. The upper edge of the nodule has a thin layer measuring ~0.5 – 1 μm thick of large grains which would make up the surface visible in Figure 8.26. Immediately below this layer are the oxide grains which make up the majority of the nodule. The centre of the nodule is comprised of very fine grains which appear to grow from the centre of the nodule. At the oxide / metal interface there is a void which measures 3 – 4 μm long within which there are a number of areas where an amorphous phase has formed between the metal and the oxide. High resolution EDS maps of this nodule are shown in Figure 8.28.

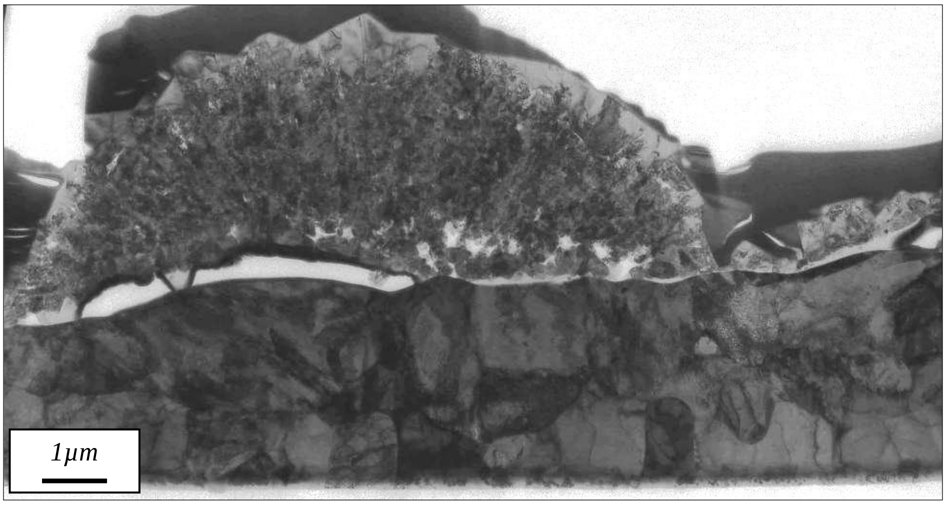

Figure 8.27:- Bright field transmission electron micrograph of a cross-section of an oxide nodule formed on industrially ground S32205 after oxidation at 1000°C for 1 hour in simulated propane combustion products

The high resolution EDS maps of this nodule show that the main portion of the area is a chromium rich oxide. This chromium rich oxide correlates with the fine grained oxide revealed in the bright field TEM image (Figure 8.27). Manganese is detected mostly within the outer grains which make up the top surface of the nodule. As with other examples of nodule growth, these manganese rich oxide grains are also the facetted grains which are visible when examining the surfaces of the oxidised samples, in this example, however, the main difference is that the outer manganese containing layer is very thin. The amorphous oxide visible in the TEM image (Figure 8.27) is indicated as silicon rich in the EDS maps suggesting that there is a small amount of silica present at the metal / oxide interface. There is also a slight enrichment of silicon where the nodule is in contact with the metal.

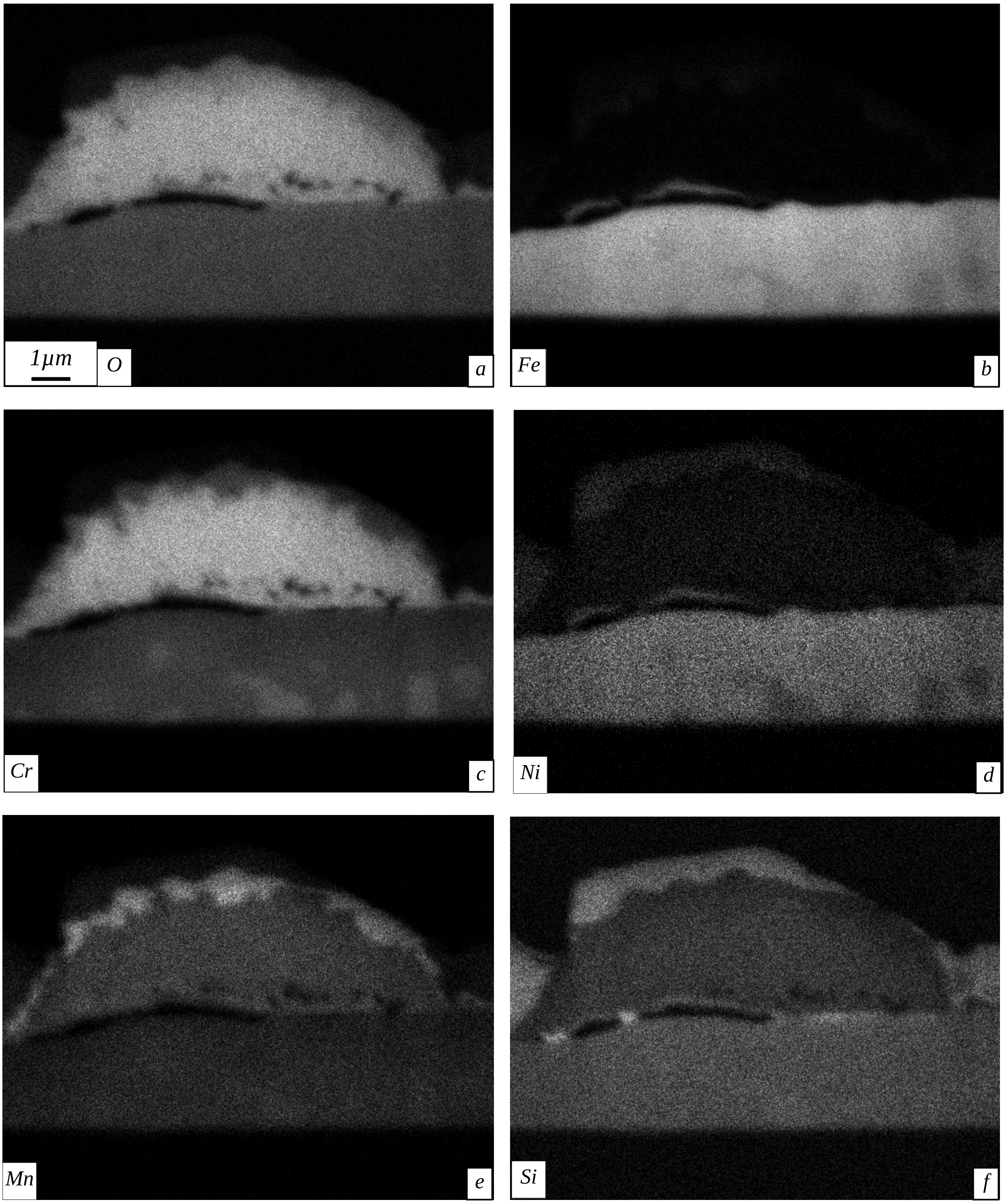

Figure 8.28:- High resolution EDS maps of (a) oxygen, (b) iron, (c) chromium, (d) nickel, (e) manganese and (f) silicon of an oxide nodule formed on industrially ground S32205 after oxidation at 1000°C for 1 hour in simulated propane combustion products

8.3.3 Oxidation at 1100°C

Figure 8.29 shows scanning electron micrographs of the surface of industrially ground S32205 after oxidation at 1100°C for 1 hour in the tube furnace. At low magnification (Figure 8.29(a)) the surface is covered in an oxide which resembles the underlying marks from the grinding operation. It is evident, however, that it consists of oxide ridges which follow the grinding direction. At high magnification it can be seen that the oxide produced consists of two types; the first is a facetted type similar to many other examples shown previously and the second a finer grained oxide whose crystals are close to spherical in shape. These crystals have agglomerated to form oxide protrusions on top of the underlying facetted oxide crystals. In cross section, the two main oxide types are those shown in Figure 8.30. The base oxide is a thin inhomogeneous and disordered oxide film (Figure 8.30(b)). It has localised spalling, cracking and internal oxidation in the form of root type structures. The oxide ridges, which appear as oxide nodules, are ~30 – 40 μm in height and show no considerable oxide crater region (Figure 8.30(a)). Instead there is a small oxide crater beneath a large oxide island with a dense surface layer and a highly disordered centre which is full of voids.

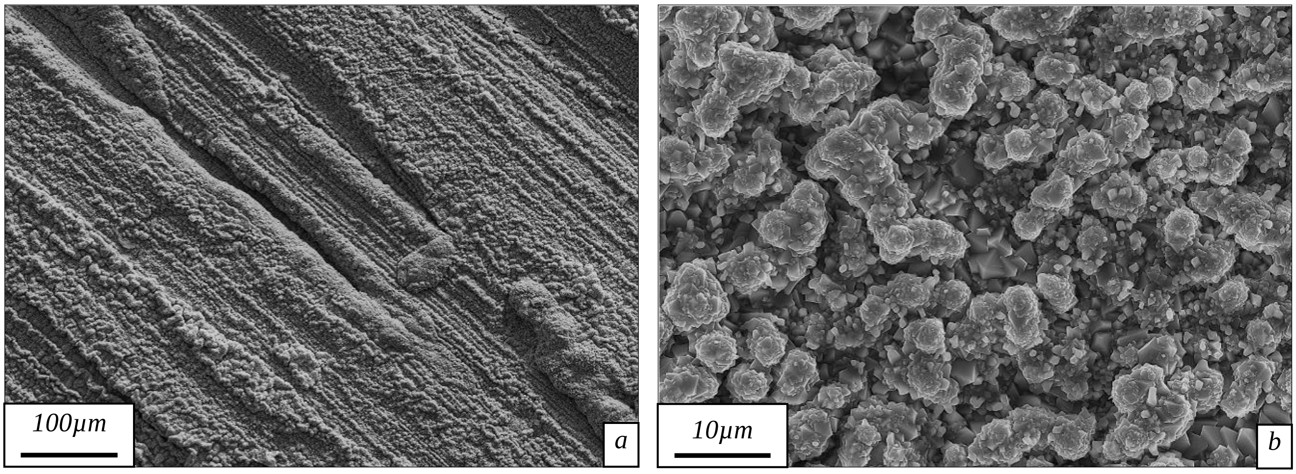

Figure 8.29:- Secondary electron images of a) an overview of the surface of industrially ground S32205 after oxidation at 1100°C for 1 hour in simulated propane combustion products and b) higher magnification of the oxide

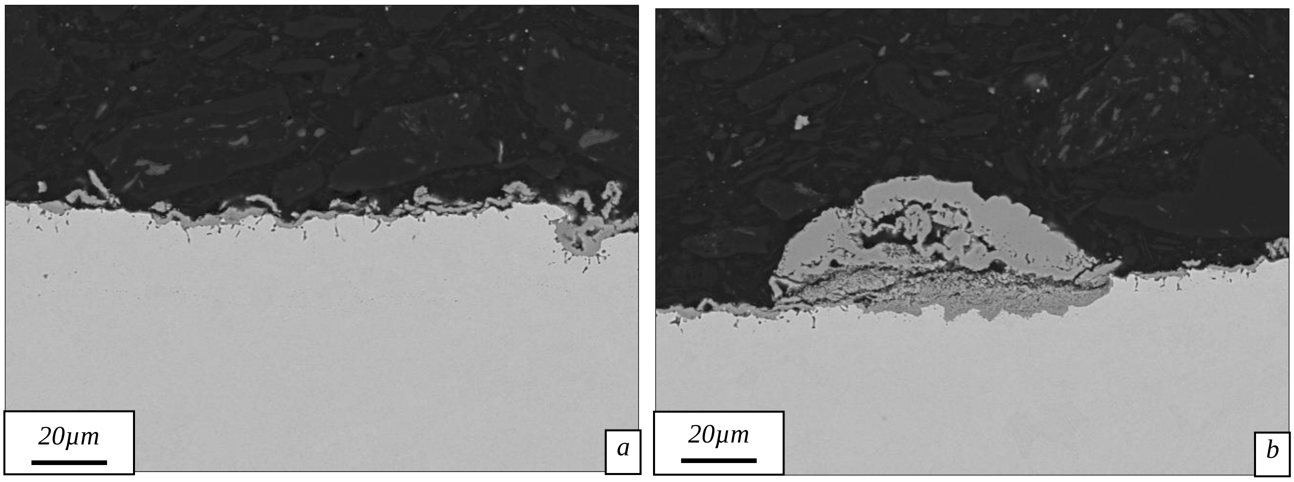

Figure 8.30:- backscattered electron micrographs of a cross section of a) base oxide and b)an oxide nodule formed on industrially ground S32205 after oxidation at 1100°C for 1 hour in simulated propane combustion products

EDS maps of the feature in Figure 8.30(b) are shown in Figure 8.31. The outer surface of the feature is the only iron rich layer. The lower region of the feature is mainly chromium rich with a small quantity of nickel detected in its lower region. Apart from oxygen, chromium is the only element detected in the lowest extent of the crater forming a chromium rich band at the scale / metal interface. As well as this, the base oxide (visible to the left of the image) is also rich in chromium. Silicon is present in very small quantities at the metal / oxide interface. The root type structure visible in the backscattered electron image of the feature is also confirmed as being rich in silicon. As shown in Figure 8.32, nodules are not very common on the surface as the majority of the surface is covered with the base oxide.

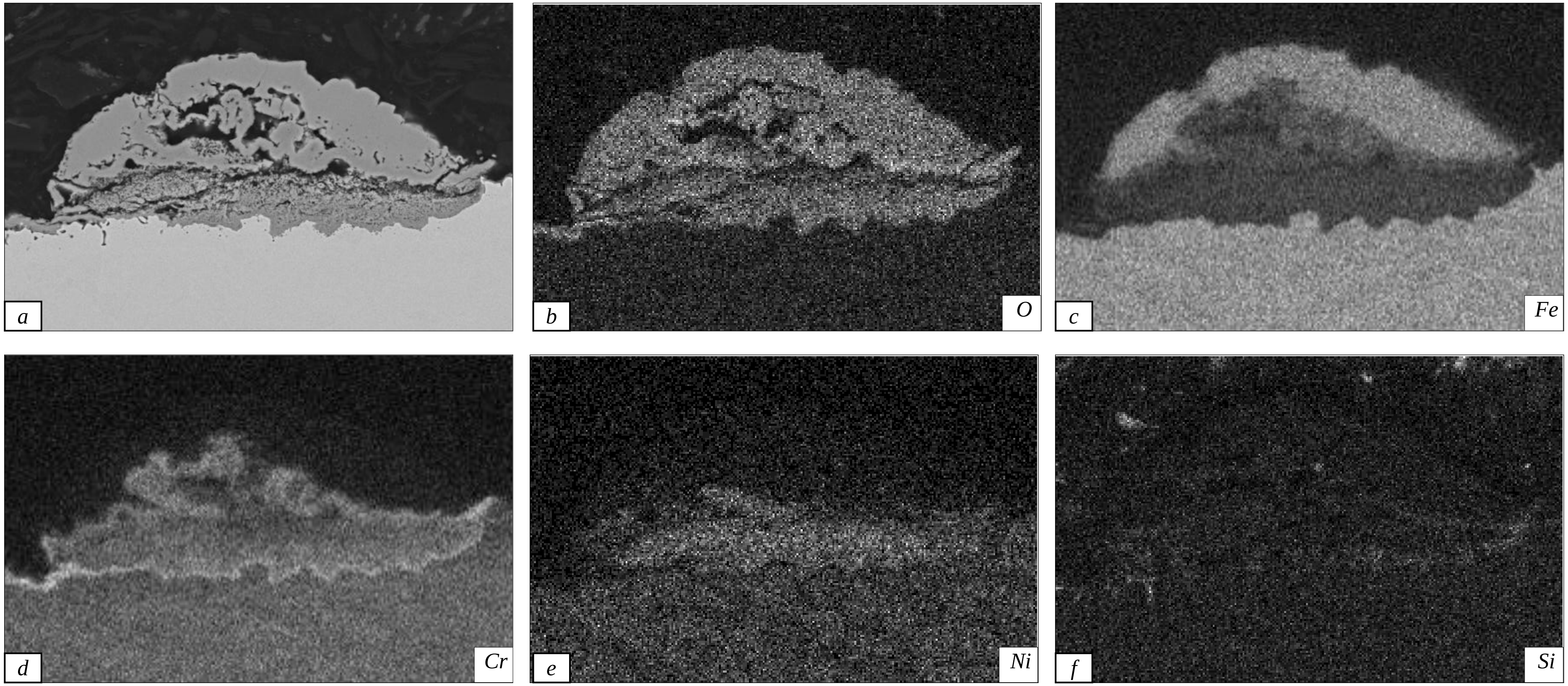

Figure 8.31:- (a) Backscattered scanning electron micrograph with accompanying EDS maps of (b) oxygen, (c) iron, (d) chromium, (e) nickel and (f) silicon taken from a cross-section of an oxide formed on industrially ground S32205 after oxidation in t simulated propane combustion products for 1 hour at 1100°C

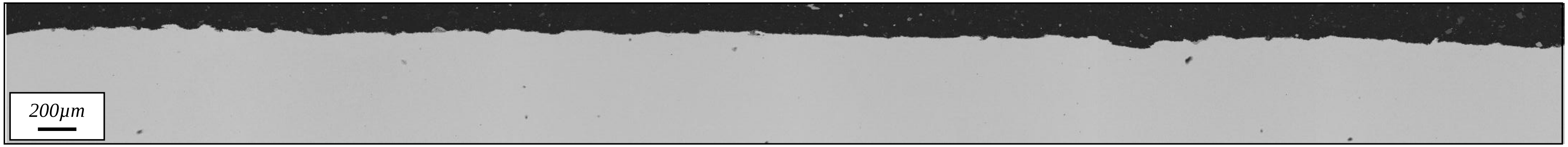

Figure 8.32:- Backscattered scanning electron micrograph of the cross-section of an oxide formed on industrially ground S32205 after oxidation in simulated propane combustion products for 1 hour at 1100°C

8.3.4 Oxidation at 1200°C

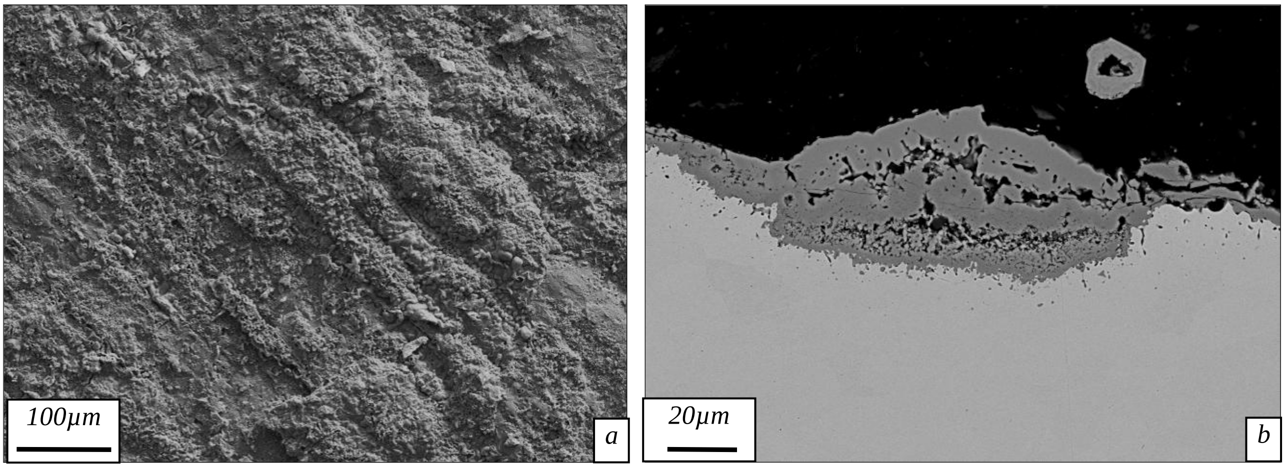

Figure 8.33:- Scanning electron micrograph of a) the surface and b) a cross-section of an oxide formed on industrially ground S32205 after oxidation in simulated propane combustion products for 1 hour at 1200°C

After oxidation of industrially prepared S32205 for 1 hour at 1200°C in the tube furnace, the oxide produced in Figure 8.33 is produced. After this period of oxidation the majority of the surface is covered with an oxide scale. As shown in Figure 8.34, the oxide scale is not completely homogeneous. Instead there are areas which have undergone enhanced oxide growth such as the area shown in cross-section in Figure 8.33(b). This particular area shows a typical oxide nodule in that it has an island region and a shallow crater. The entire nodule from the base of the crater to the tip of the island measures ~40 – 50 μm and ~100 μm wide. Within the nodule there are three distinct layers which can be distinguished by the voids which have formed between them. The bottom layer (Layer 1) is at the base of the crater and forms a border between the oxide in the crater and the metal; it is fine grained and fairly porous. The middle and upper layers (Layer 2 and 3 respectively) are similar in appearance in that they measure ~15 – 20 μm and both show little porosity. EDS mapping of this area (Figure 8.35) reveals that the chemical distribution through this nodule has more layers than is suggested by imaging alone. Layer 3 is predominately iron rich which bleeds into the upper part of layer 2 which consists of mainly chromium oxides. The lowest layer (Layer 1) is comprised of two regions : a nickel and chromium containing region and a chromium rich crater boundary region which is also devoid of any iron.

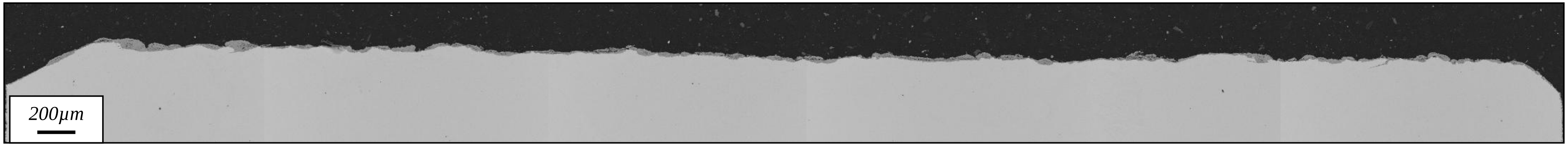

Figure 8.34:- Backscattered scanning electron micrograph of a cross-section of an oxide formed on industrially ground S32205 after oxidation in simulated propane combustion products for 1 hour at 1200°C

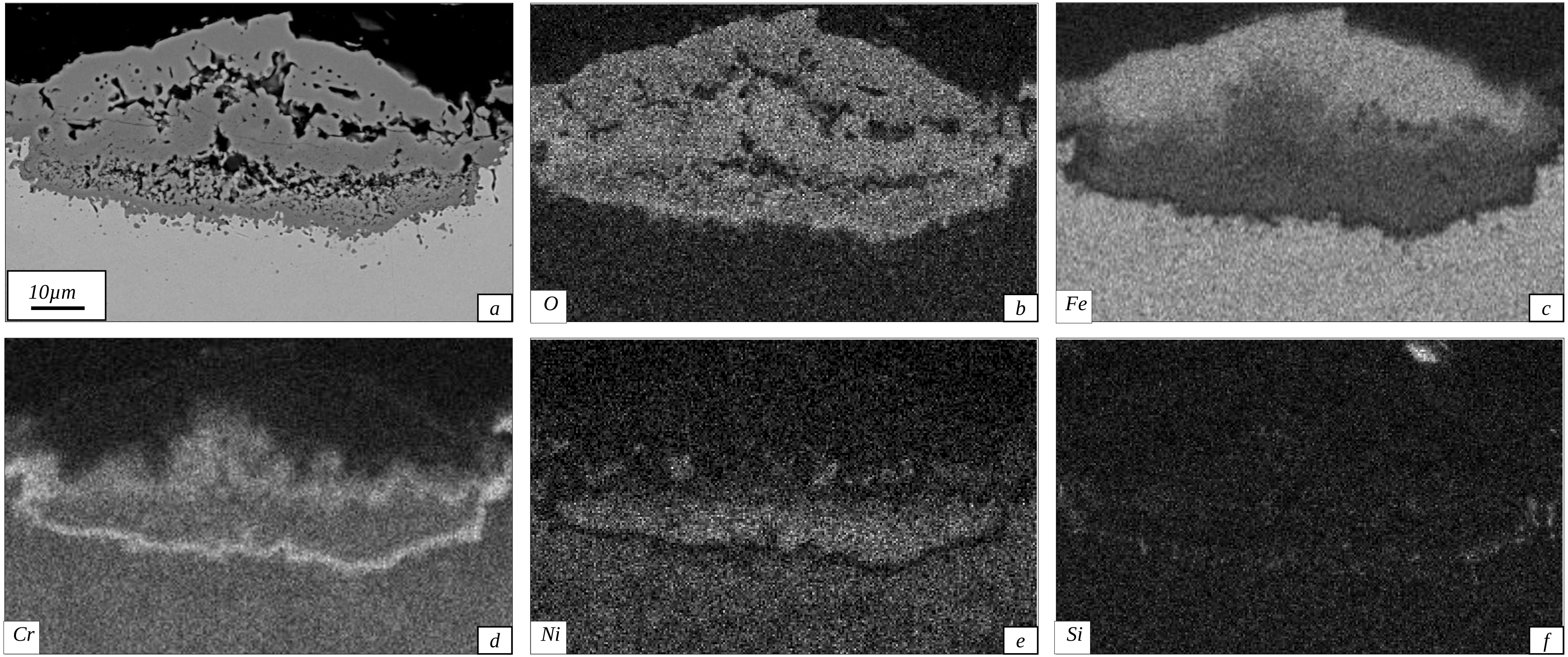

Figure 8.35:- (a) Backscattered scanning electron micrograph with accompanying EDS maps of (b) oxygen, (c) iron, (d) chromium, (e) nickel and (f) silicon taken from a cross-section of an oxide formed on industrially ground S32205 after oxidation in simulated propane combustion products for 1 hour at 1200°C

9 FULL REHEAT OF DUPLEX STAINLESS STEEL GRADES

9.1 S32101 after Industrial Reheat

9.1.1 Hot ground surface

After full reheat procedures of industrially prepared samples of S32101, oxide nodules are seen on the surface. These nodules are of particular interest to industry as they are likely to cause surface imperfections on cold-rolled product. It is therefore, necessary to study the fully formed oxide nodules in both planar and cross-sections in order to understand what contributes to their growth.

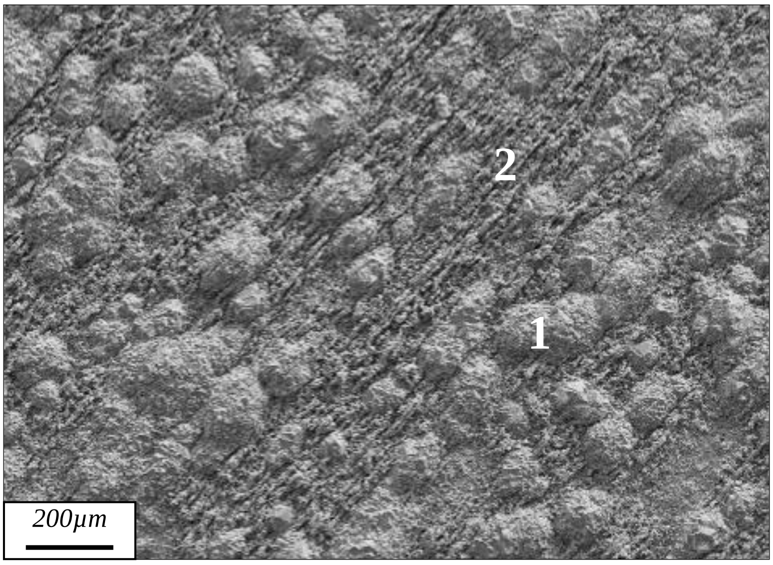

Figure 9.1: secondary electron image of the surface oxide formed on industrially ground S32101 after simulated reheat to a final temperature of 1220°C in the experimental reheat furnace showing (1) oxide nodules and (2) base oxide

Figure 9.1 is a secondary electron image of the surface of S32101 after a full reheat procedure to a final temperature of 1220°C in the experimental reheat furnace. Two types of oxidation can be observed on the surface of this sample: 1) nodular regions whose distribution bears no relationship to the distribution of the austenite and ferrite within the substrate and 2) a thinner oxide which resembles the grinding marks on the surface of the substrate introduced during the industrial grinding operation. A higher magnification image of these two regions are shown in Figure 9.2. It can be seen that the nodular oxides are facetted in structure whereas the oxides seen in region 2 are more granular.

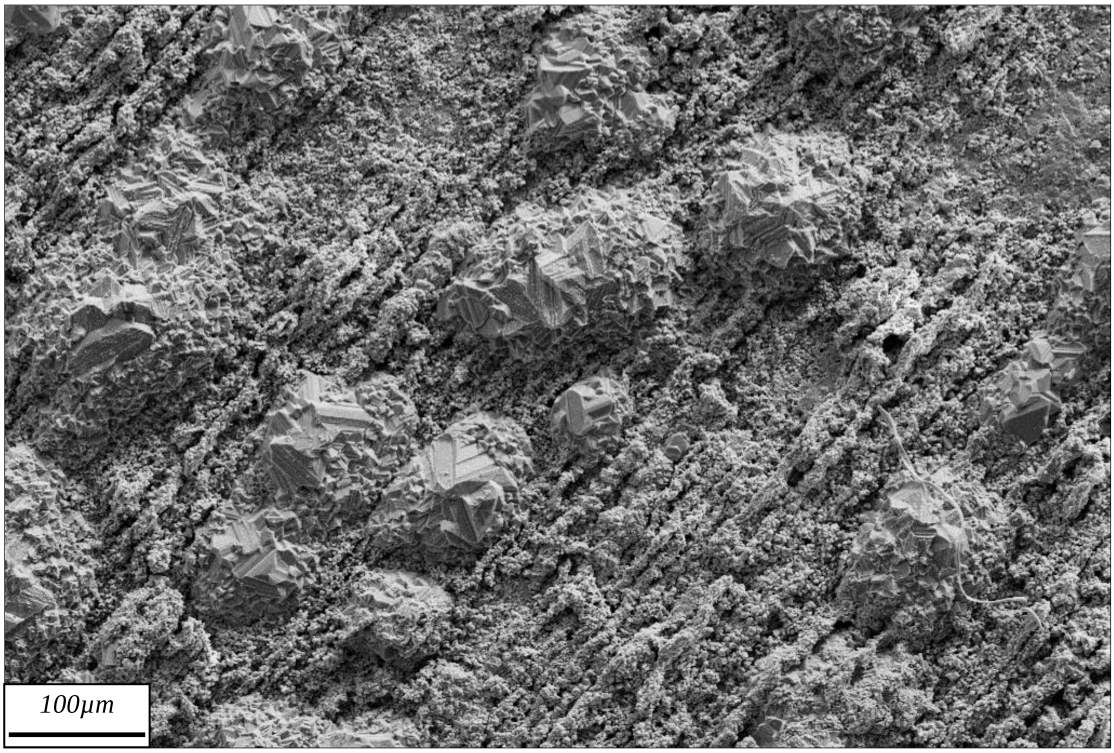

Figure 9.2: secondary electron image of the surface oxide formed on industrially ground S32101 after simulated reheat to a final temperature of 1220°C in the experimental reheat furnace

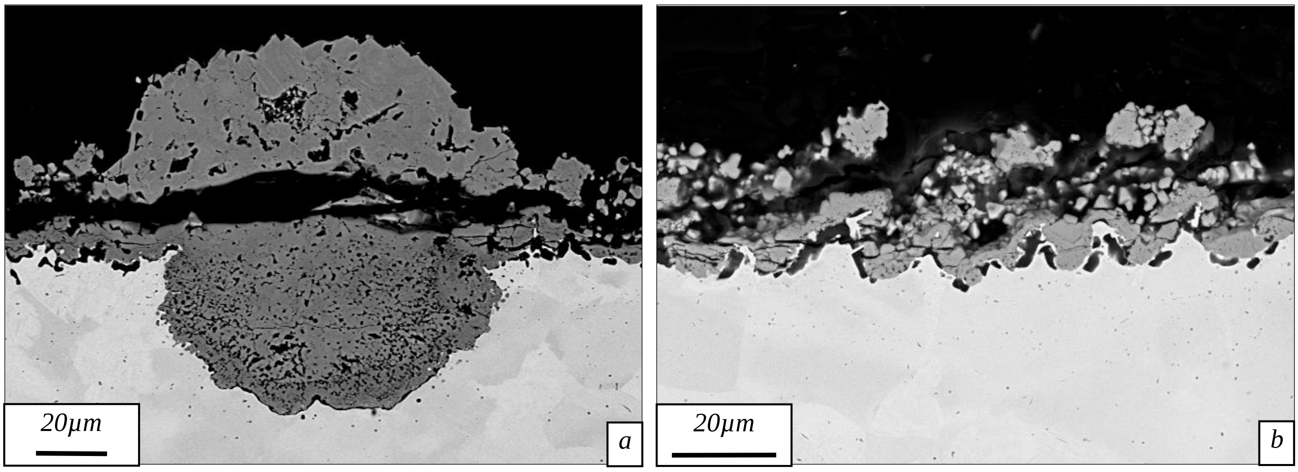

Figure 9.3: Backscattered electron image of a cross-section of a) an oxide nodule and b) the base oxide formed on industrially ground S32101 after simulated reheat to a final temperature of 1220°C in the experimental reheat furnace

Figure 9.3(a) is a backscattered electron image of a cross-section of a typical oxide nodule formed on the surface taken from the area marked in Figure 9.10. The nodule has an external part (referred to as the "island") and an internal oxide (referred to as the "crater"). The island region is a lot less porous, than the finer-grained crater region. To either side of the nodule there is an oxide which is similar to that shown in Figure 9.3(b) which is the oxide present in the area marked "2" in Figure 9.1. This oxide is very uneven with surface undulations. The oxide is poor and damaged above the interface which may be as a result of taking a cross-section of an inhomogeneous surface as seen in Figure 9.2.

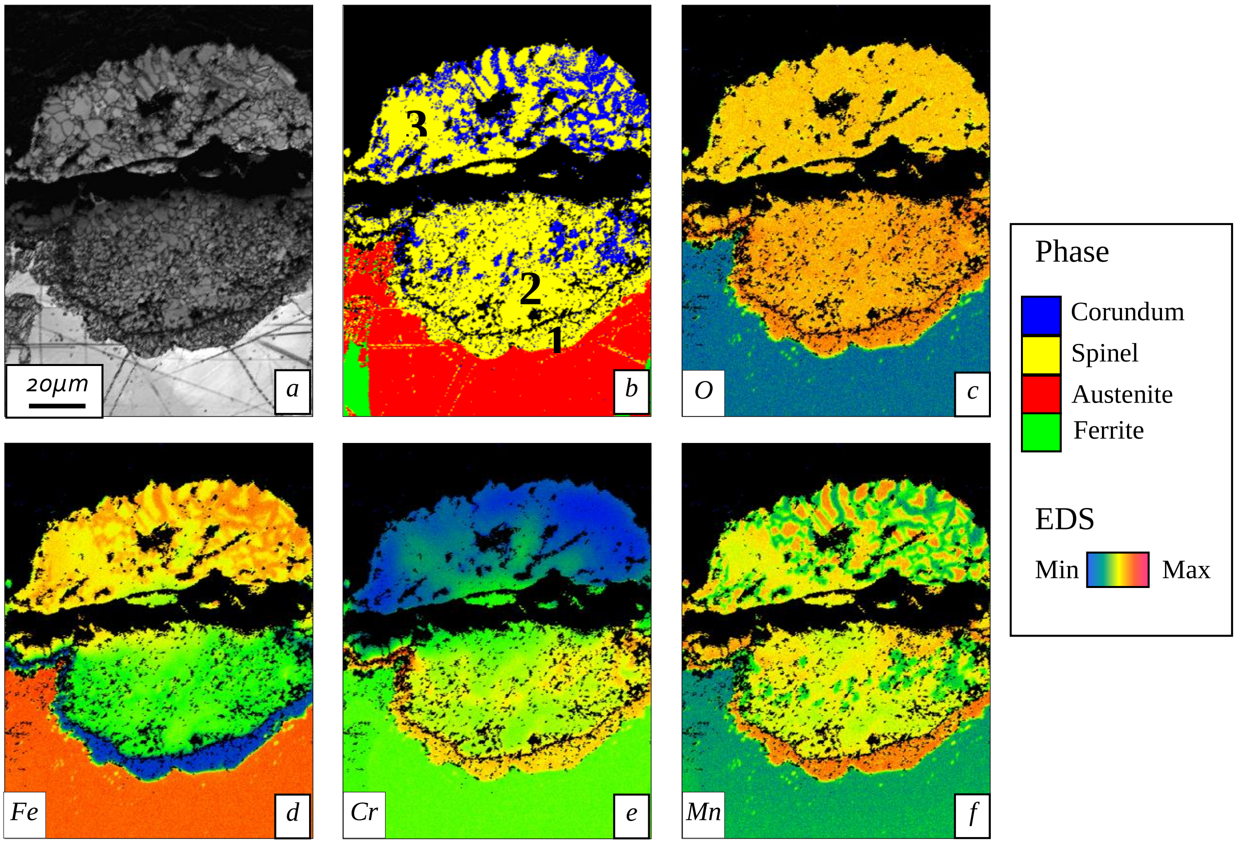

Figure 9.4: EBSD / EDS maps of a) Image quality, b) Phase, c) Oxygen, d) Iron, e) Chromium and f) manganese in a nodule formed on industrially ground S32101 after simulated reheat to a final temperature of 1220°C in the experimental reheat furnace

Figure 9.4 is a montage of simultaneously collected EBSD and EDS maps of the nodule shown in Figure 9.3. These maps clearly show that the crater region has two main constituent parts which are divided by a dark line in the image quality map: a band which borders the crater (1) and the bulk of the crater itself (2). Both the band and the bulk consist of mainly spinel type oxides whereas the island (3) is a mixture of spinel and corundum type oxides in roughly equal quantities. The chemical distribution in the nodule is complex. The band (1) is a spinel type oxide which is lacking in iron but enriched in both chromium and manganese. The bulk of the crater (2) is a mixed spinel with contents of iron, chromium and manganese. However, within the bulk there are a few packets of corundum type oxides whose chromium content is slightly higher than the spinel and whose manganese content is lower. The island part of the nodule has two phases: an iron and manganese rich spinel and an iron rich corundum type oxide, presumably haematite. This particular oxide nodule is located on an austenitic region of the substrate material.

9.1.2 Industrially prepared lab size specimens

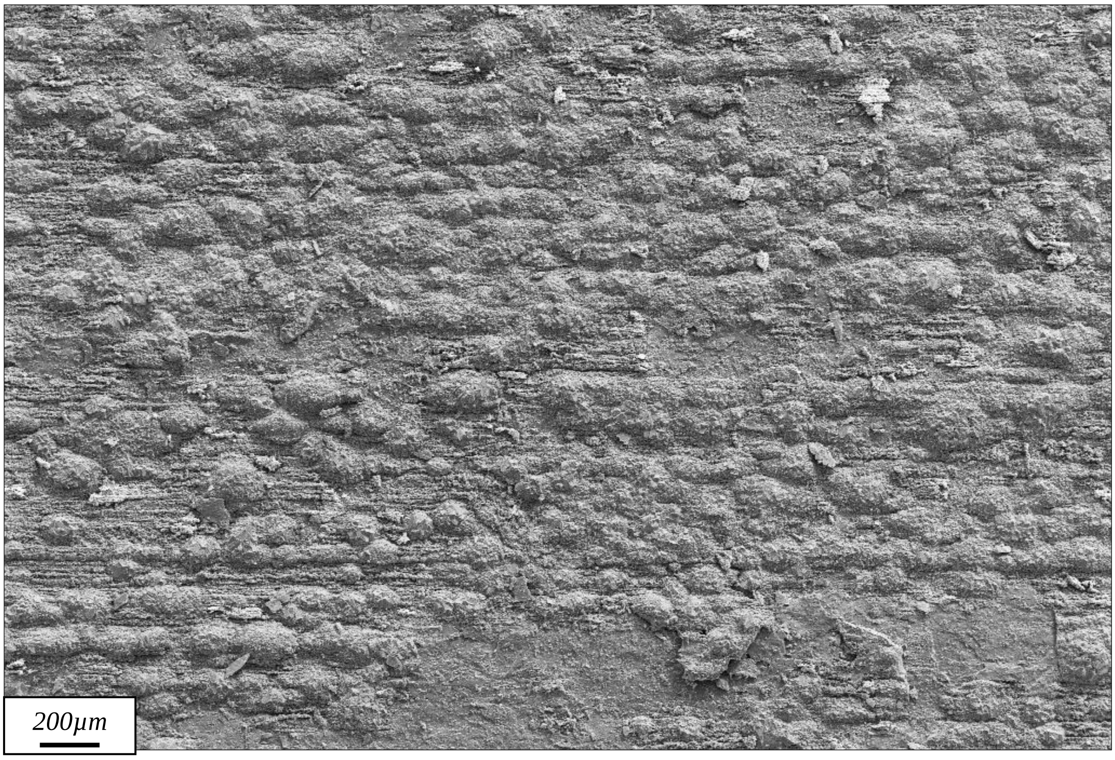

Figure 9.5: Secondary electron images of the surface oxide formed on industrially ground S32101 after simulated reheat to a final temperature of 1220°C in the experimental reheat furnace

Industrially hot ground small-scale specimens were also heated in the reheat furnace. Figure 9.5 is a secondary electron micrograph of the surface of industrially ground S32101 after reheat to a final temperature of 1200°C in the reheat furnace. As seen on other examples, the surface is made up of two distinct regions: a base oxide which resembles the grinding marks and a nodular oxide region. In this case the grinding plane is horizontal. The nodular regions follow the grinding marks to some extent with series' of nodules joining together along the grinding direction to form long ridges of oxide. In this example the majority of the surface is covered in the nodular type oxides with only small areas of base oxide visible.

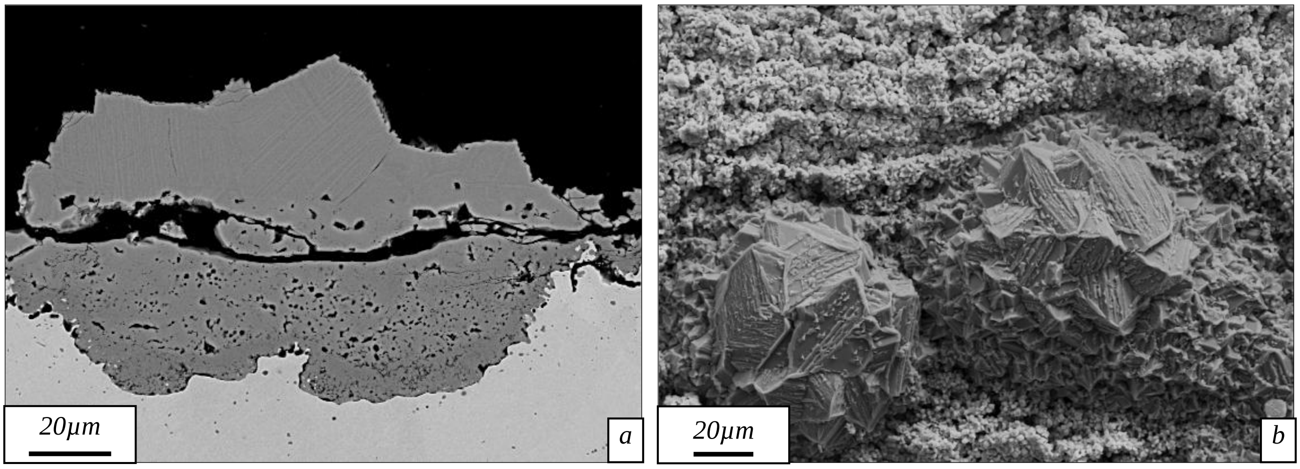

Figure 9.6:a) Back scattered electron image of a cross-section and b) secondary electron image of an oxide formed on industrially ground S32101 after simulated reheat to a final temperature of 1220°C in the experimental reheat furnace

An overview of the entire specimen’s surface in cross-section is shown in Figure 9.11. When compared to the same view of a large specimen’s surface (Figure 9.10), there are many more complete oxide nodules on the surface, which consist of both an outer and an inner part, on the laboratory scale specimen. Besides the large difference in complete oxide nodules, the size and general appearance of the oxide nodules are very similar. In high magnification cross-section (Figure 9.6), the nodular regions are similar to other examples presented. The island region is lacking in porosity but the crater region shows a high degree of porosity. When viewed at higher magnification (Figure 9.6(b)), the surface has facetted nodules surrounded by the base oxide which is finer grained and seems to follow the grinding marks which were present prior to oxidation.

Figure 9.7(a) is an optical micrograph of the oxide nodule shown in Figure 9.6(a). No further information is revealed regarding the crater region of the nodule when compared to the SEM image but the island region is very different. There are two distinct shades of oxide. The dark shade makes up the majority of the oxide in the island region and acts as a matrix to the second lighter-shade phase. Within a single grain (Figure 9.7(b)) of the matrix oxide (marked with a red line) there are a series of thin, parallel seams which give the impression of growing from the edges of the grain. The oxide seams formed on the left edge of the grain are thicker to the bottom-left hand edge suggesting that it is this boundary from which the seams are growing.

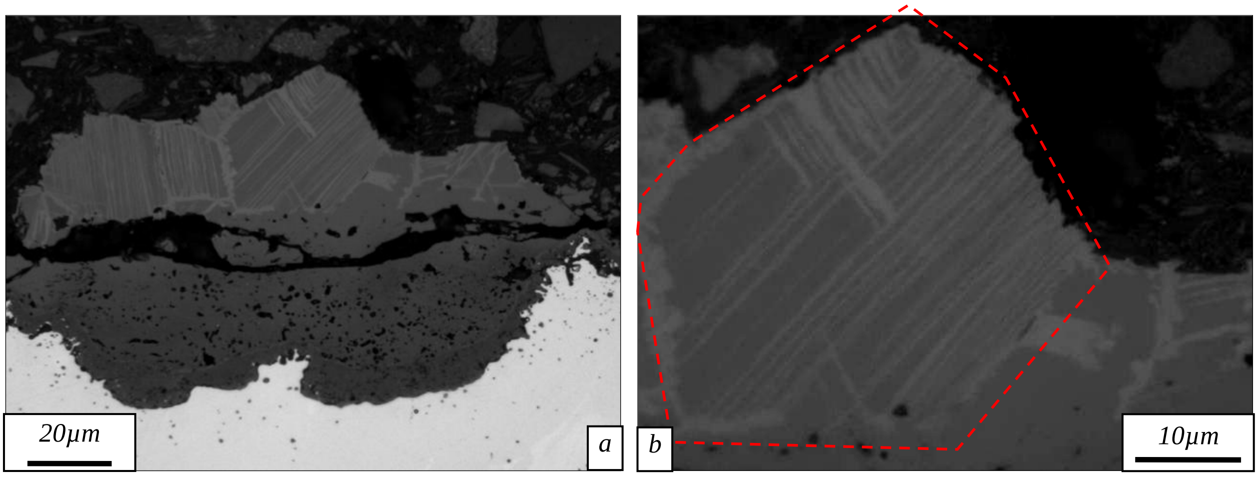

Figure 9.7: Optical micrograph of a cross-section of an oxide formed on industrially ground S32101 after simulated reheat to a final temperature of 1220°C in the experimental reheat furnace the red area indicates a needle phase growing in the outer layer of the oxide nodule

9.1.3 Laboratory prepared surfaces

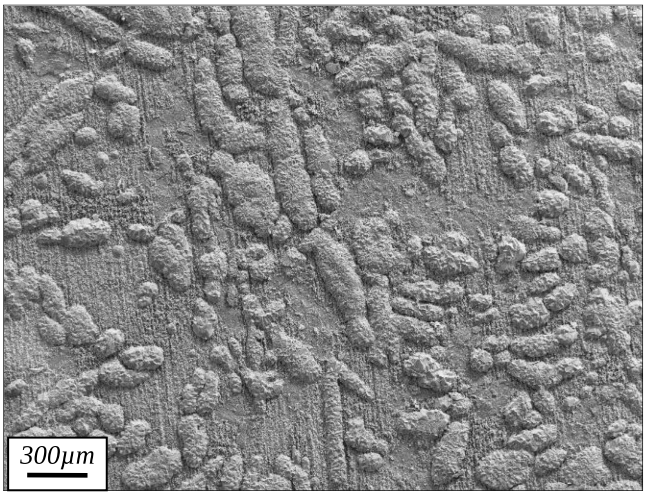

Figure 9.8: Secondary electron images of the surface oxide formed on laboratory ground (80Grit) S32101 after simulated reheat to a final temperature of 1220°C in the experimental reheat furnace

Laboratory size coupons of S32101, prepared to a finish of 80grit, were oxidised in the reheat furnace for comparison of sample surface finishes. Figure 9.12 is an overview of the cross-section of the sample's surface oxide. When compared to Figure 9.10 and Figure 9.11, it can be see that the oxide produced has a number of nodules closer to the number seen in Figure 9.10 but that their breadth is greater. Figure 9.8 is a secondary electron micrograph of a laboratory size specimen with an 80 Grit surface finish which has been oxidised for a reheat cycle to a final temperature of 1220°C in the reheat furnace. The surface has features in the base oxide which are parallel to one another (in the vertical direction in this image), which can be attributed to the grinding marks prior to oxidation. The second features on the surface are island features with a similar distribution and morphology to the underlying austenitic region of the duplex stainless steel's microstructure (Figure 3.1). Figure 9.9 is a higher magnification micrograph of a typical oxide island feature on the surface of the specimen. It is a facetted nodule where some of the individual grains have a stepped surface surrounded by the oxides resembling the grinding marks.

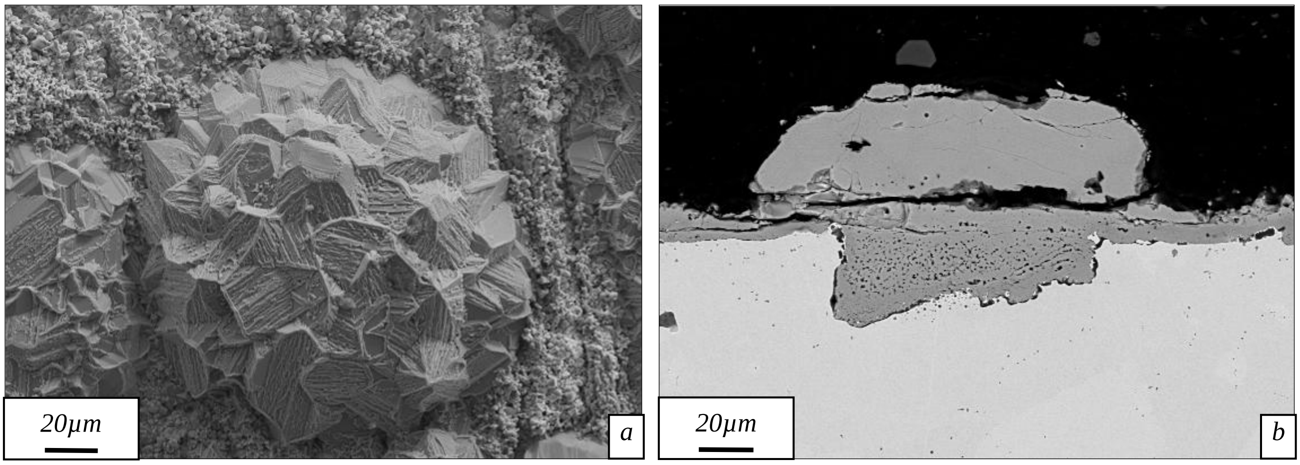

Figure 9.9: a) Secondary electron image of the surface oxide and b) backscattered electron image of a cross-section of an oxide formed on laboratory ground (80Grit) S32101 after simulated reheat to a final temperature of 1220°C in the experimental reheat furnace

A cross-section of a typical island feature is shown in Figure 9.9(b). The island part of the nodule feature is approximately 35μm in height and the crater part extends to approximately the same depth into the substrate material. The majority of the crater is fairly porous except for the region immediately below the island and a band extending around the crater's perimeter which both show very little porosity. Around the crater's perimeter is a dark substance which has, in other specimens, been shown to be silica. It should be noted that this silica is not so prevalent to either side of the oxide nodule.

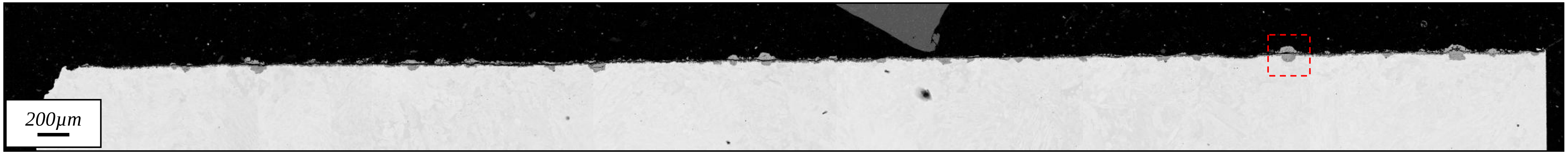

Figure 9.10:- Back scattered electron image of the cross-section of the entire surface of an oxide formed on industrially ground large specimens S32101 after a full reheat procedure to a maximum temperature of 1220°C in the experimental reheat furnace

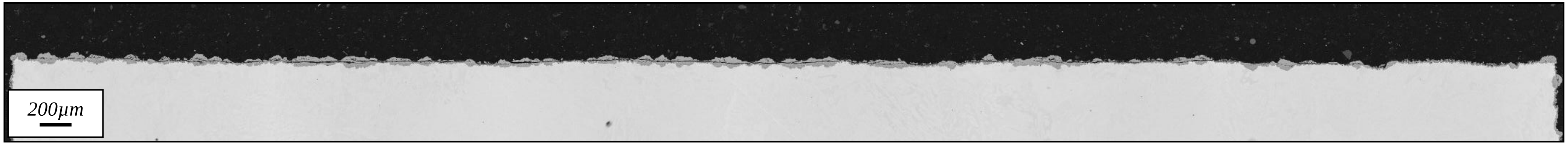

Figure 9.11:- Back scattered electron image of the cross-section of the entire surface of an oxide formed on industrially ground laboratory specimens S32101 after a full reheat procedure to a maximum temperature of 1220°C in the experimental reheat furnace

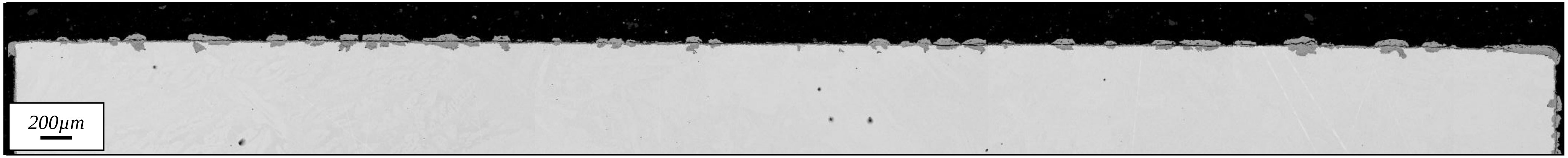

Figure 9.12:- Back scattered electron image of the cross-section of the entire surface of an oxide formed on laboratory prepared (80 Grit) S32101 after a full reheat procedure to a maximum temperature of 1220°C in the experimental reheat furnace

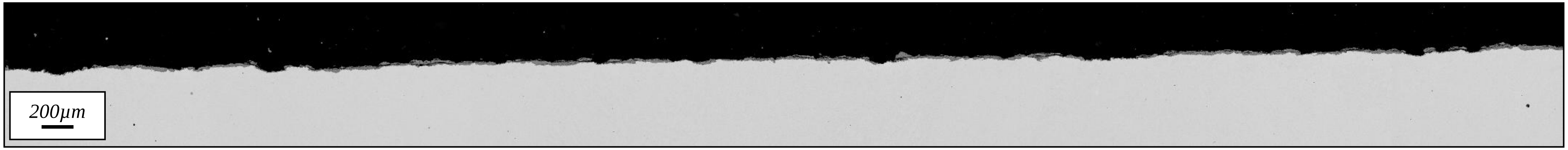

Figure 9.13:- Back scattered electron image of the cross-section of the entire surface of an oxide formed on industrially ground S32205 after a full reheat procedure to a maximum temperature of 1220°C in the experimental reheat furnace

9.2 S32205 after industrial reheat

9.2.1 Industrially ground sample

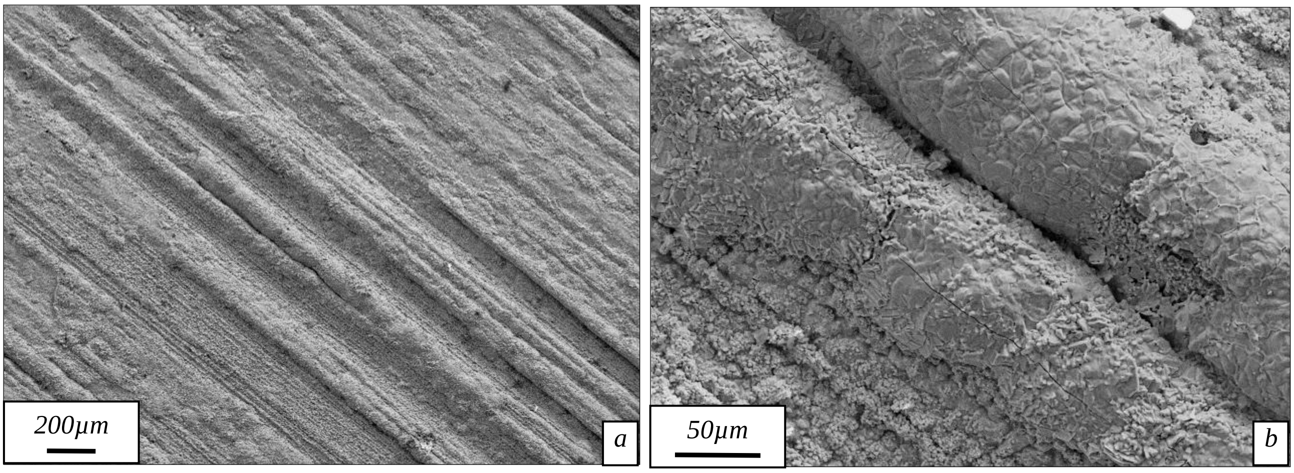

Figure 9.14: Secondary electron images of a) overview of the surface oxide formed on industrially ground S32205 after simulated reheat to a final temperature of 1220°C in the experimental reheat furnace and b) higher magnification of the oxide ridges

Figure 9.14 shows the oxide produced on the surface of industrially prepared S32205 after oxidation to a final temperature of 1220°C in the reheat furnace. Oxidation of this grade in the reheat furnace does not produce oxide nodules in the same way as S32101. Instead, at low magnifications, the oxide is fairly homogeneous with a number of oxide ridges visible in the grinding direction. At higher magnification the surface is seen to have two types of oxide present: a base oxide and large oxide ridges which have a smooth surface made up of many grains. In cross-section (Figure 9.13) no oxide nodules are visible. Instead an oxide covers the surface which is quite uniform.

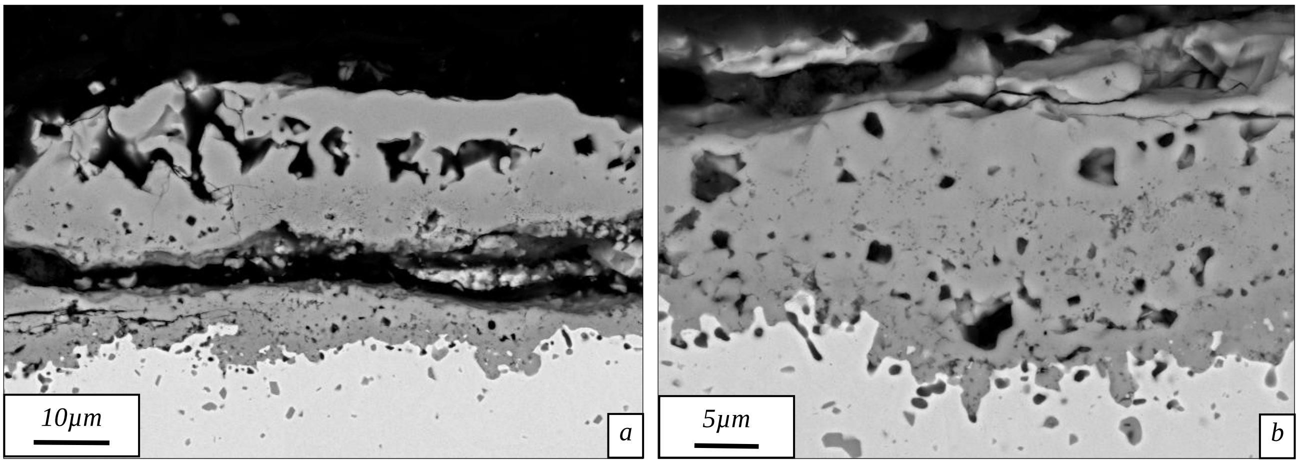

Figure 9.15: Backscattered electron images of a) a cross-section of the oxide formed on industrially ground S32205 after simulated reheat to a final temperature of 1220°C in the experimental reheat furnace and b) higher magnification of the oxide / metal interface

Figure 9.15 is a backscattered electron image of a cross-section of a typical area of oxide formed on S32205 after simulated reheating in the reheat furnace to a final temperature of 1220°C. The oxide shown in this region is ~ 35 – 40 µm. From this image it is possible to suggest that the lowest layer of oxide is fine-grained and porous. Into the substrate below the oxide are a number of internal oxide particles. Above the large gap (presumably a crack formed during cooling) there is an apparently dual layer oxide scale. The lowest layer adjacent to the large gap is similar to the oxide in contact with the metal and the outer layer is marked by the absence of small pores and the presence of large voids which were probably produced by polishing and grain pull-out, suggesting that this layer is easily damaged. Figure 9.16 is a montage of simultaneously collected EBSD / EDS maps of a typical area of oxide formed on S32205 after oxidation in the reheat furnace at a maximum temperature of 1220°C. The image quality map reveals that the lower oxide region is fine grained and the outer oxide consists of larger grains. This particular region has smaller, equiaxed grains in the lower region and larger grains at the oxide’s surface. The chemical distribution within this region of oxide is quite complex. There are at least three distinct, chemically different regions. To the lowest extent of the oxide there is a band of oxide measuring ~2 – 3µm thick which is the highest chromium and oxygen content and the lowest iron content. Chromium content is then reduced in the remainder of the lower oxide zone which also has moderate concentration of iron, manganese and nickel. Above the crack, a gradient of chromium is observed to ~2 – 3µm into the external oxide. This chromium gradient corresponds to the smaller equiaxed grains shown in the image quality map. The outer oxide is mainly iron rich with two grains showing very low counts of any element other than iron and oxygen. In the middle of the outer oxide there are two grains which show moderate levels of nickel, manganese and iron.

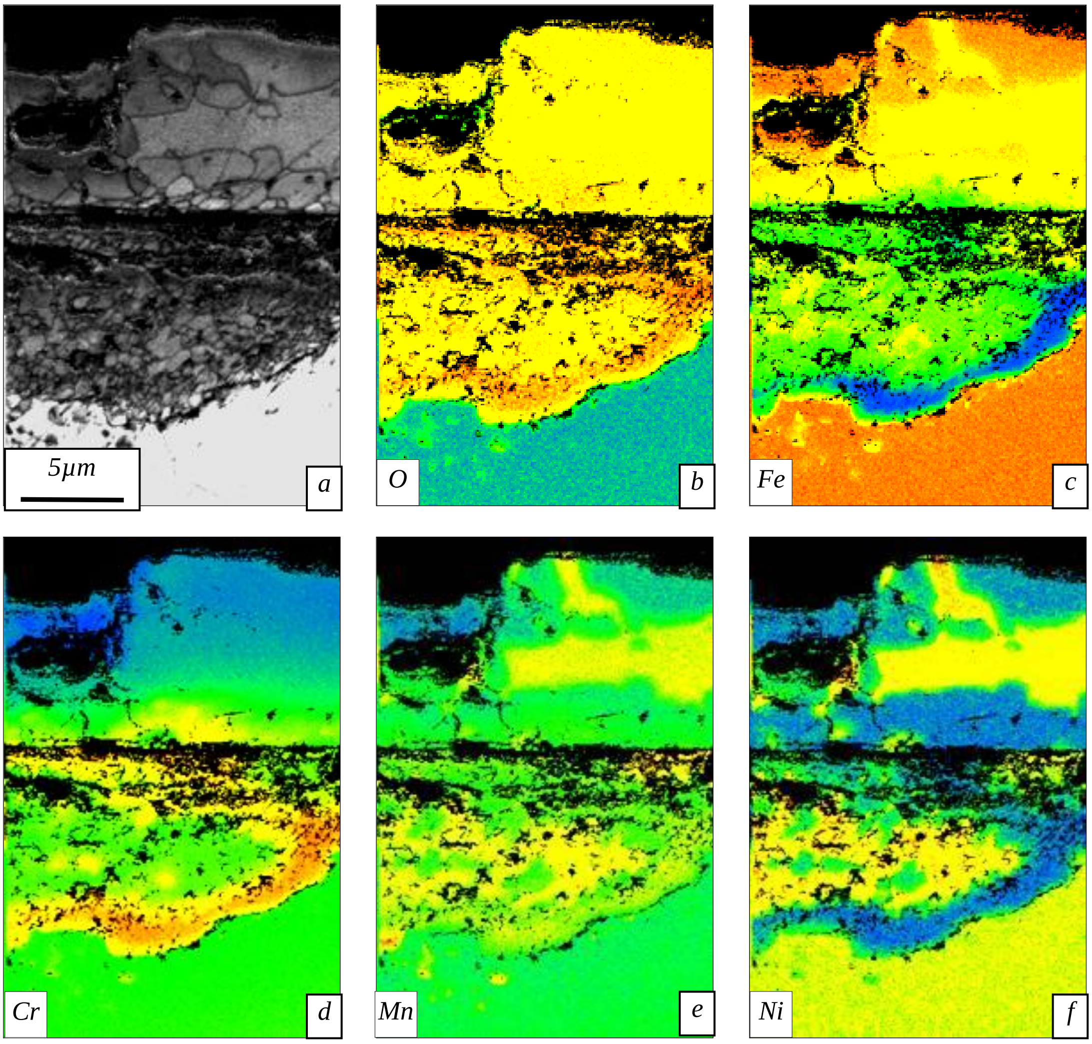

Figure 9.16: EBSD / EDS maps of a) Image quality, b) oxygen, c) iron, d) chromium, e) manganese and f) nickel in an oxide formed on industrially ground S32205 after simulated reheat to a final temperature of 1220°C in the experimental reheat furnace

10 OXIDATION OF POLISHED LABORATORY SAMPLES

10.1 Introduction

In order to study the effect of the underlying phase distribution on oxide nodule morphology, oxidation experiments were carried out on samples prepared with a reference surface. The surface chosen was polished to a 1µm diamond finish. Oxidising a surface with this finish meant that the surface, when compared to the surface which was industrially ground, was free of surface ridges or undulations and also relatively free of mechanical damage which may lead to recrystallisation.

10.2 Polished S32101

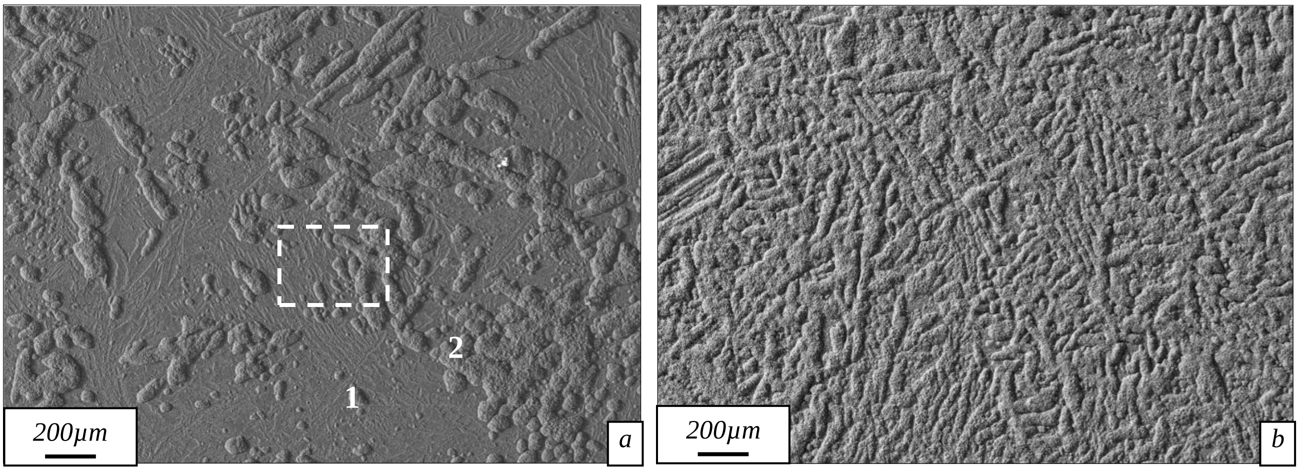

Figure 10.1: Secondary electron image of the surface of polished S32101 after oxidation at 1000°C for (a) 1 hour with a white rectangle indicating the area of EDS analysis shown in Figure 10.4 and (1) indicating the base oxide and (2) indicating the nodular oxide and (b) 2 hours in simulated combustion products of propane

Figure 10.1 shows the effect of oxidising samples of polished S32101 at 1000°C for 1 and 2 hours in the tube furnace. After oxidation for 1 hour the surface has two main regions visible: base oxide (1) and areas which have experienced enhanced oxide growth to form regions of oxide islands on the surface (2). It can be suggested at this point that, due to the distribution of the oxide islands, they reside upon the austenitic phases of the underlying substrate. After this short period of oxidation it is clear that not all of the austenite present has formed oxide islands. After oxidation for a further hour, however, the surface has a greater proportion of oxide islands. Although obvious that they cover a greater proportion than 50% of the surface (approximate proportion of the austenite phase), they still resemble the morphology of the austenite regions of the substrate.

Figure 10.2 and 10.3 are backscattered electron images of cross-sections of the entire surface oxides formed on polished S32101 after oxidation in the tube furnace at 1000°C for 1 and 2 hours respectively. After oxidation for 1 hour the surface is ~30% covered in oxide nodules which are spaced in an apparently random distribution over the surface of the specimen. After oxidation for a further hour the surface is almost completely covered by oxide nodules with a few small areas where no nodules are present. When compared to the nodules shown in Figure 9.10 – 9.12, they are far smaller but cover a greater proportion of the oxidised surface.

A montage showing a secondary electron image and EDS maps of the surface of polished S32101 after oxidation at 1000°C for 1 hour in the tube furnace is presented in Figure 10.4. The region shown relates to the area marked in Figure 10.1(a). The two main regions are visible: thin oxide region (1) and the oxide islands (2). The EDS of this area shows that the islands have a very interesting chemical make-up. The centre / top of the oxide islands are made up of iron oxides with a ring of manganese and chromium oxides at their perimeters. Region 1 also consists of two chemically different oxides. For example the thin oxide area displayed in Figure 10.2 consists of two topographically different oxides. One is thin and the other appears to be thicker. The thicker of the two consists of oxides of manganese whereas the thinner oxide has been shown to contain mainly chromium suggesting that it may have protective properties.

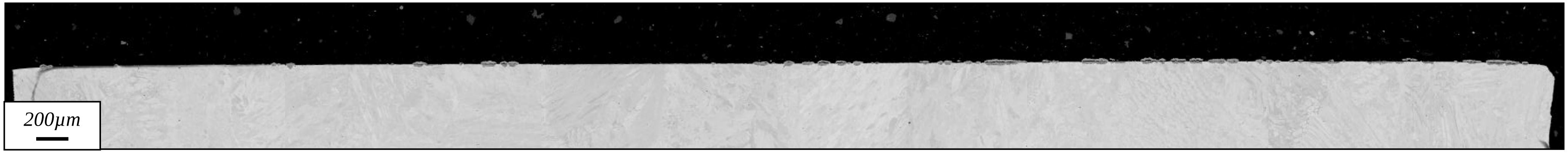

Figure 10.2:- Back scattered electron image of the cross-section of the entire surface of an oxide formed on laboratory polished (1µm) S32101 after oxidation at 1000°C for 1 hour in simulated propane combustion products

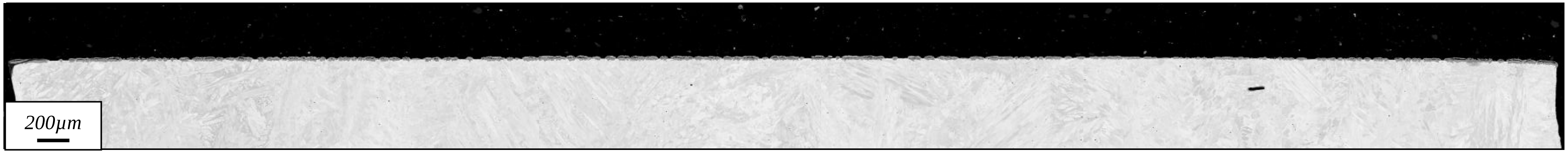

Figure 10.3:- Back scattered electron image of the cross-section of the entire surface of an oxide formed on laboratory polished (1µm) S32101 after oxidation at 1000°C for 2 hours in simulated propane combustion products

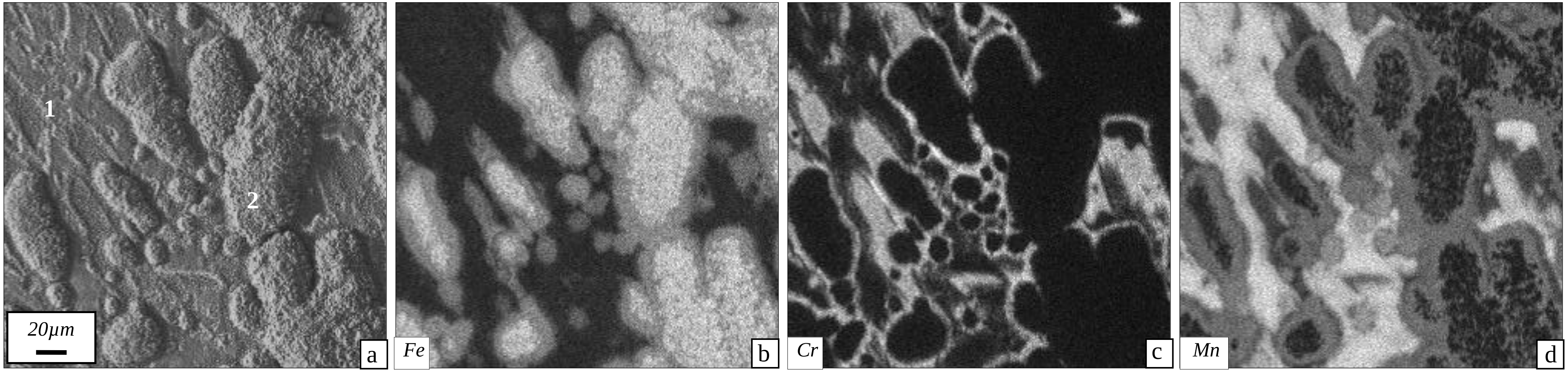

Figure 10.4: EDS of the surface of polished S32101 after oxidation at 1000°C for 1 hour in simulated propane combustion products showing (a) Secondary electron image, (b) iron, (c) chromium and (d) manganese

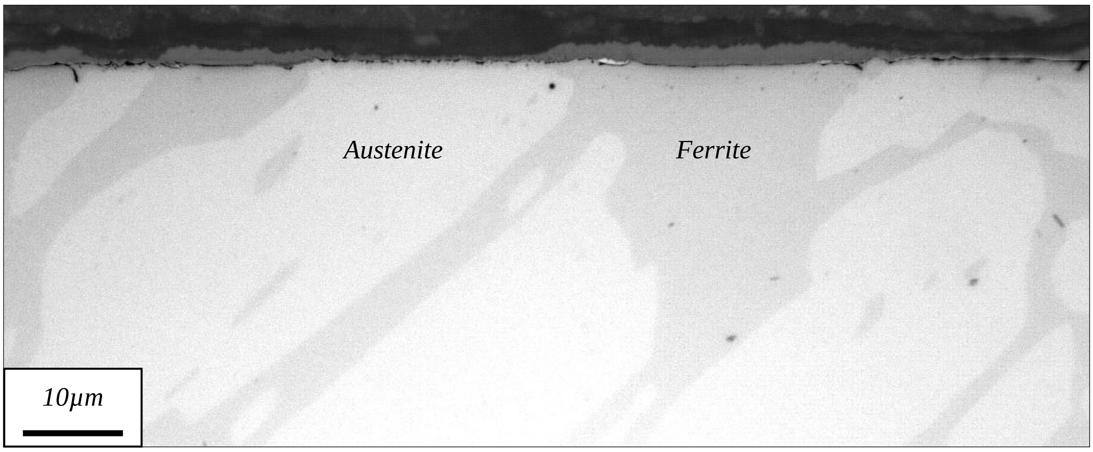

Figure 10.5: Optical micrograph of polished S32101 after oxidation at 1000°C for 1 hour in simulated propane combustion products showing thicker oxide on ferrite and thinner oxides on austenite regions

The regions which show the thinner oxides (shown in Figures 10.1 and 10.2) have already been shown to contain two chemically different oxides. Figure 10.5 is an optical micrograph of a cross-section of the thin base oxide. It shows that the thicker oxide forms on the ferrite phase of the substrate whereas the thinner oxide tends to form on the austenitic grains.

Figure 10.6 is a backscattered electron image and corresponding EDS maps of an oxide formed across a phase boundary. The oxide formed on the ferrite phase has a roughly constant thickness of ~2μm whereas the oxide formed on the austenitic phase is less homogeneous and has formed small asperities of oxide which has produced a rough surface. In the centre of the marked area is an oxide root extending to ~2μm into the substrate following the route of the phase boundary. EDS of this area reveals that the thick oxide is a dual layer oxide consisting of an inner layer of a chromium manganese oxide and an outer layer of manganese oxide. The oxide formed on the austenite phase, however, shows only one oxide layer which is a mixed chromium manganese oxide. Silica is found at the interface between the oxide and substrate on both phases. It is apparent, however, that this silica layer is far more homogeneous on the ferrite phase. The root is also silicon rich.

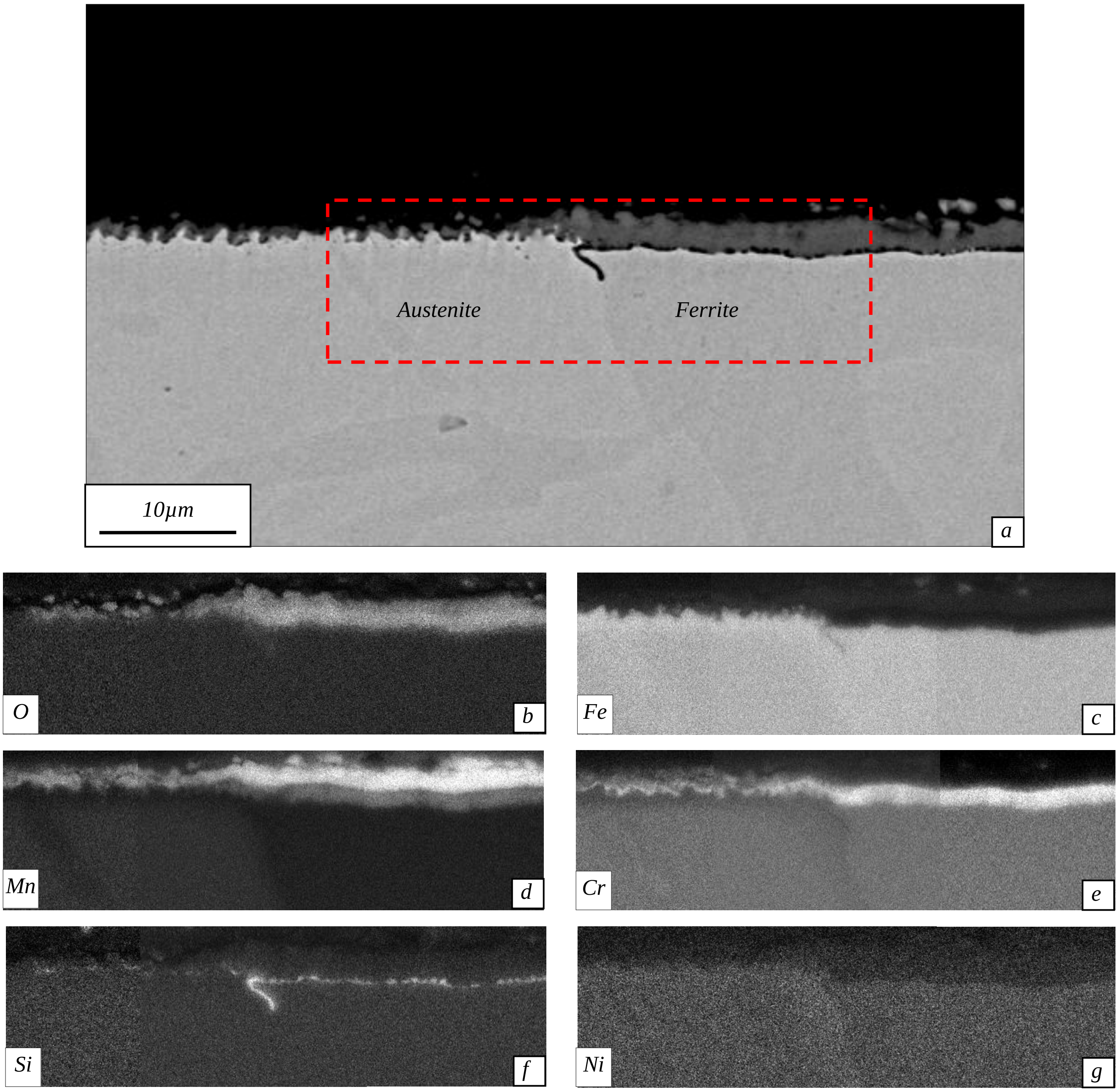

Figure 10.6: a) Backscattered electron image of polished S32101 after oxidation at 1000°C for 1 hours in simulated propane combustion products showing oxide produced at an austenite / ferrite phase boundary with EDS maps of b) oxygen, c) iron, d) manganese, e) chromium, f) silicon and g) nickel

Figure 10.7 shows a backscattered electron image of an oxide island and is accompanied by corresponding EDS maps of iron, chromium and manganese. The nodule shows an island / crater morphology. The island is situated upon an austenitic region of the substrate and shows two easily distinguishable regions. The first is the outer layer which is approximately 10μm thick over its entire length and has a complete lack of porosity. Within the boundaries of this layer is an inner oxide region which is more porous and in some places does not come into contact with the outer layer which means that a large void exists in the centre of the island, between the outer and inner oxides. The crater region shows a very high degree of porosity at its centre. The perimeter of this highly porous region is encased by a less porous oxide which is ~2µm thick. EDS maps of this nodule show that the crater is chromium rich with the non-porous perimeter showing the highest concentration. The middle of the island region is revealed to be almost entirely oxides of iron. Manganese oxides are shown to be present on the edges of the island (in agreement with Figure 10.2) and thetop part of the inner oxide of the island.

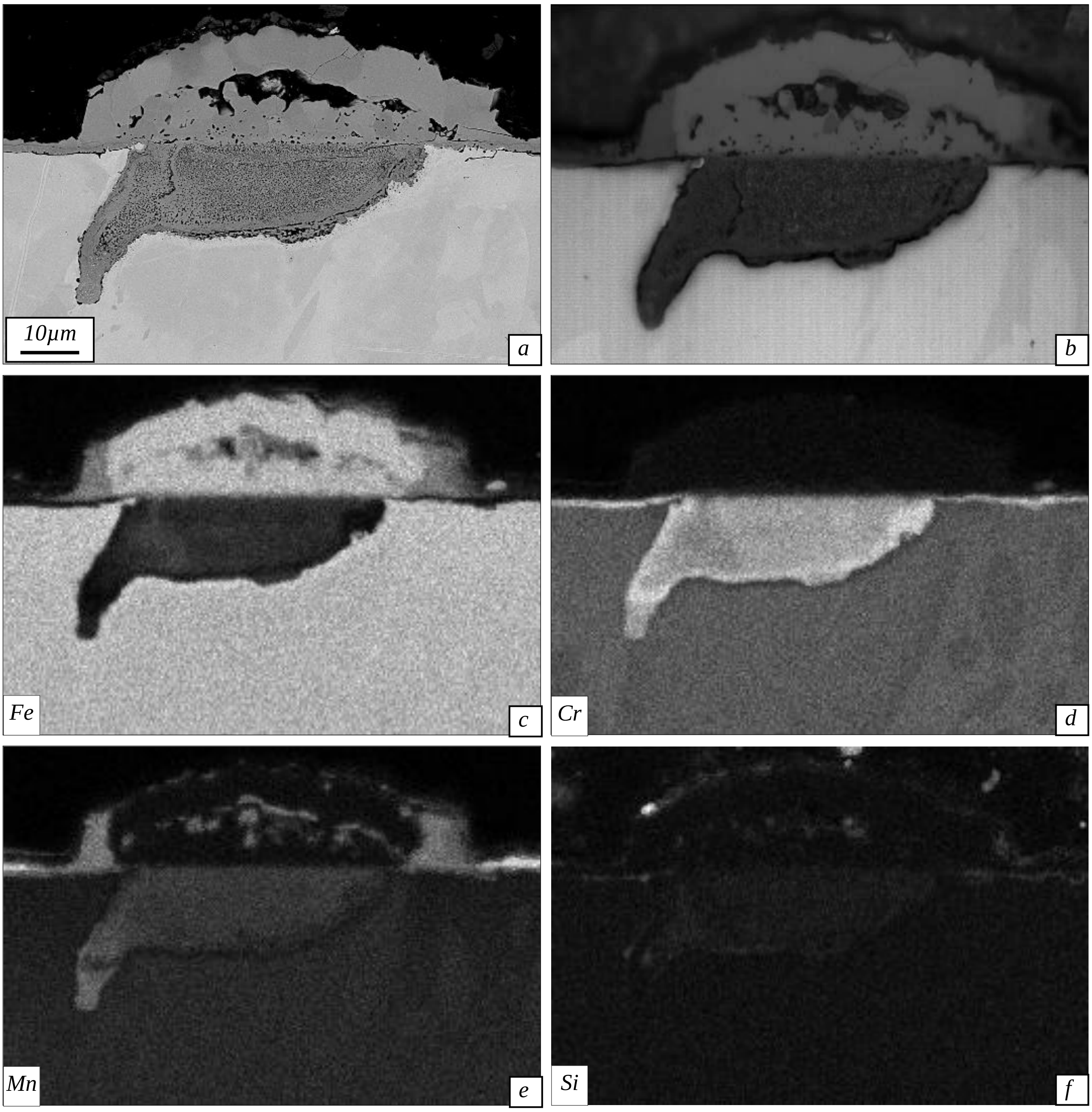

Figure 10.7: a) backscattered electron image and b) optical micrograph and accompanying EDS of a cross section of polished S32101 after oxidation at 1000°C for 1 hour in simulated propane combustion products showing (c) iron, (d) chromium, (e) manganese and f) silicon

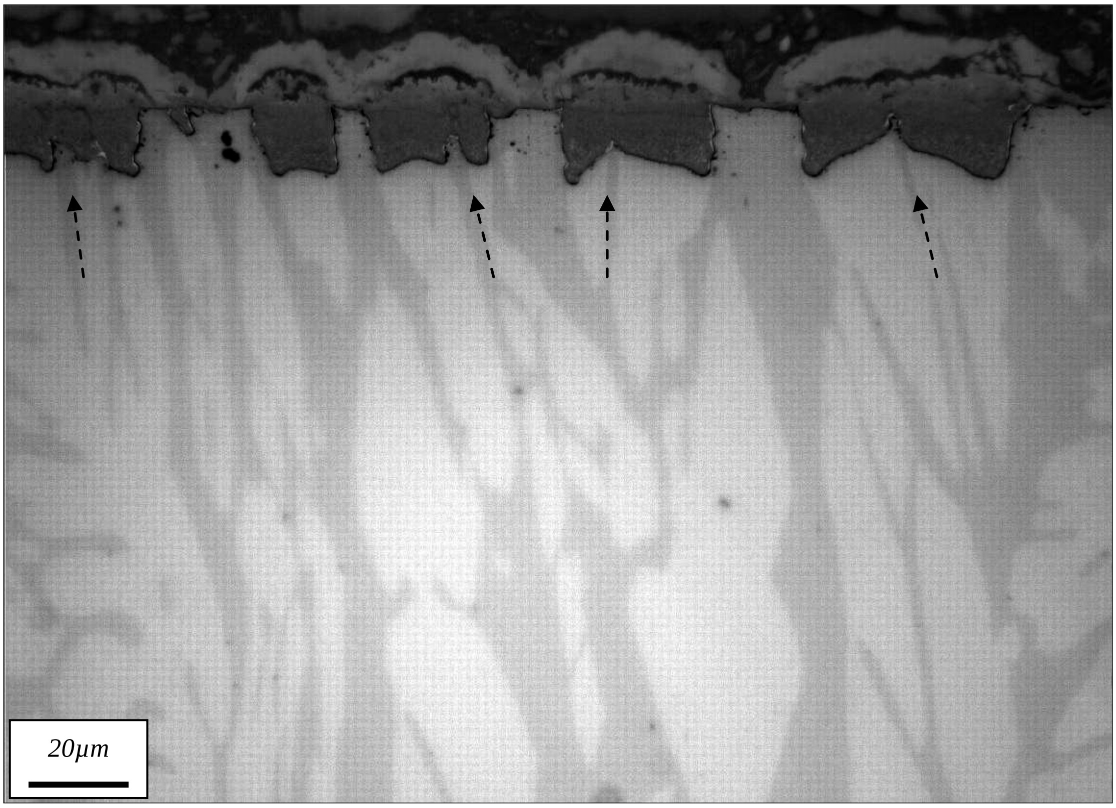

Figure 10.8: Optical micrograph of polished S32101 after oxidation at 1000°C for 2 hours in simulated propane combustion products showing oxide nodules on austenite regions

Figure 10.8 is an optical micrograph of a cross-section of an oxide scale formed on polished S32101 after oxidation at 1000°C for 2 hours. The nodules are the same in appearance to that shown in Figure 10.7. What is very clear from this particular micrograph is that the boundaries of the oxide craters do not extend beyond the austenite phase boundary within the substrate. Even where there are small intrusions of ferrite into the craters' bases (as indicated by the arrows) the growth of the crater is suppressed.

Figure 10.9 is a cross-section of an oxide nodule after oxidation of a polished surface of S32101 for 2 hours at 1000°C in the tube furnace. This micrograph reveals a crater during its growth process. On the surface of the substrate is an oxide island similar to the island shown after oxidation for 1 hour previously (Figure 10.7). The two areas are identical with the outer oxide, inner oxide layer and a gap between the two. The crater region has a porous structure to a depth of approximately 8 – 10μm and a chromium rich healed layer at the majority of its perimeter. At the extreme bottom of the crater is a region which in not healed and, because of this apparent lack of healing, can be assumed to be growing into the adjacent austenite region (as revealed by a lower chromium count).

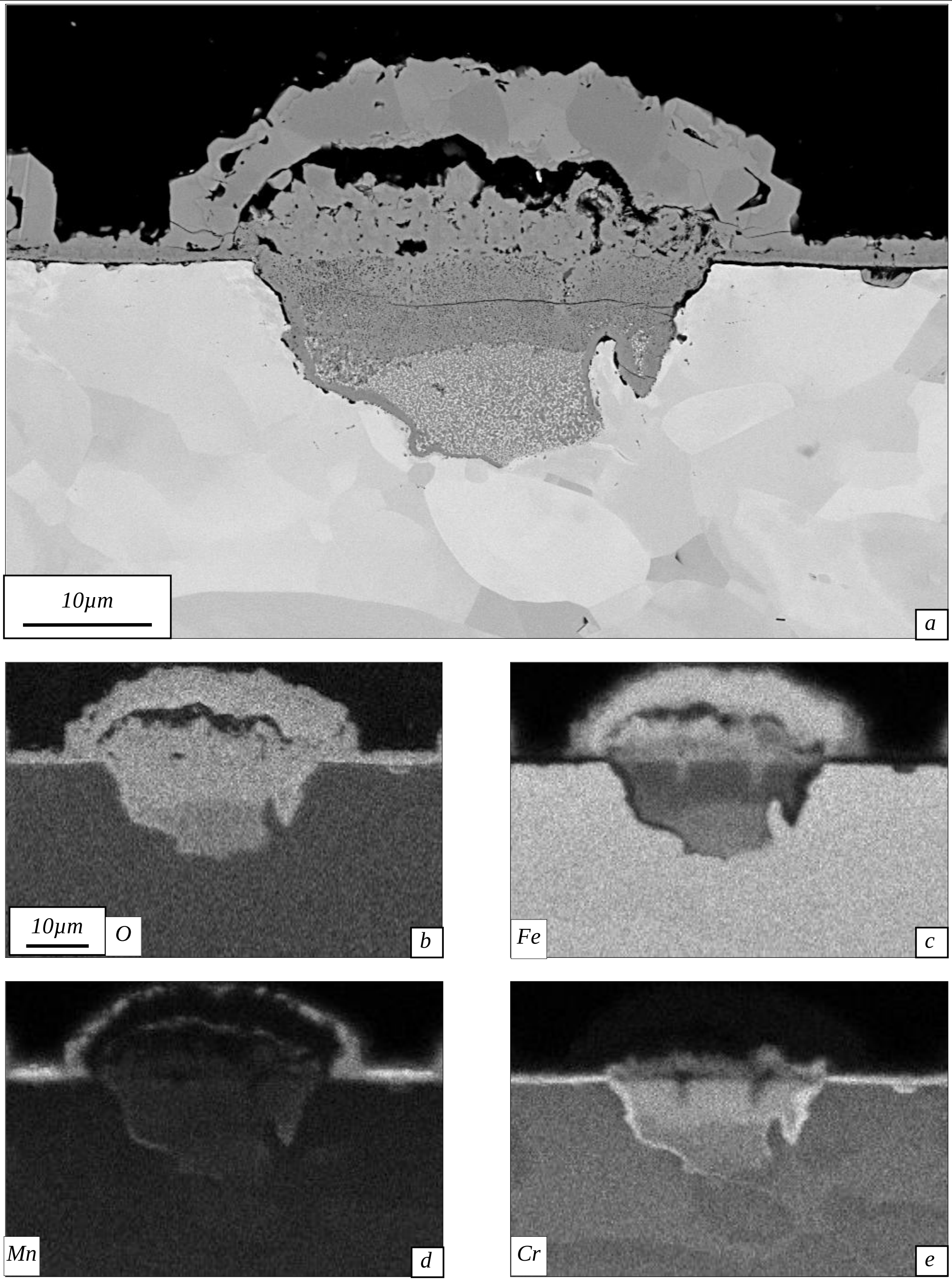

Figure 10.9 a) Backscattered electron image of polished S32101 after oxidation at 1000°C for 2 hours in simulated propane combustion products with EDS maps of b) oxygen, c) iron, d) manganese and e) chromium

10.3 Polished S32205

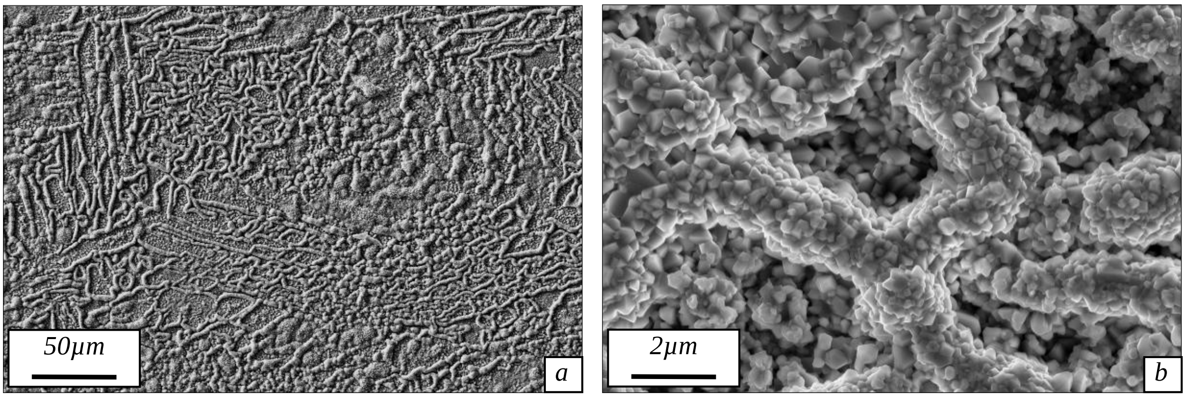

Figure 10.10:- Scanning electron micrographs of the surface an oxide formed on polished S32205 after oxidation in simulated propane combustion products for 2 hours at 1000°C showing (a) low magnification overview and (b) high magnification image of the surface

Figure 10.10 shows the oxide produced on S32205 duplex stainless steel after polishing to a 1µm surface finish and oxidising in the tube furnace for 2 hours at 1000°C. The oxide produced on this sample has a number of oxide types visible on the surface. The first forms oxide ridges which follow the boundaries of the phases within the substrate. The second is the oxide which has formed within these boundaries which is a fine grained facetted oxide and the last type are small oxide nodules as shown in Figure 10.11.

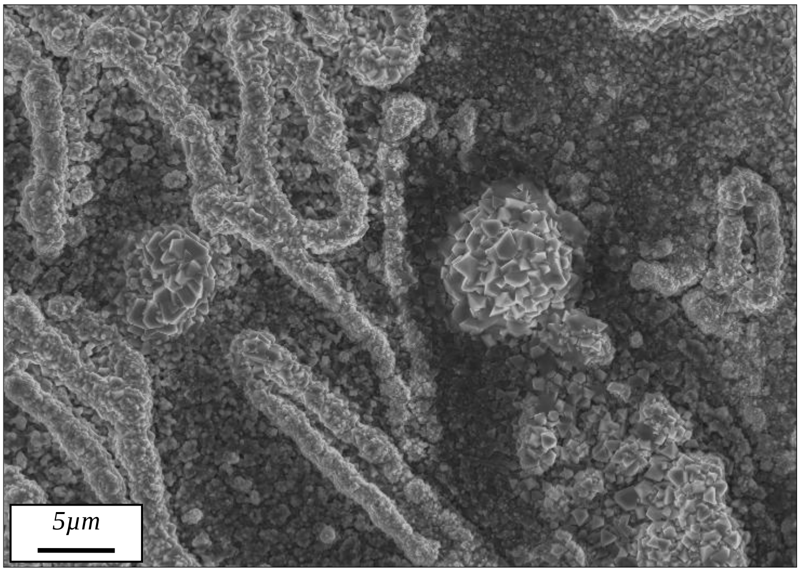

Figure 10.11:- Scanning electron micrograph of the surface an oxide formed on polished S32205 after oxidation in simulated propane combustion products for 2 hours at 1000°C

Both oxide nodules shown in Figure 10.11 have formed in a position which is detached from the oxide ridges. The oxide crystals which form these nodules are facetted in structure and seem to take the octahedron shape adopted by many other oxide crystals reported in previous sections.

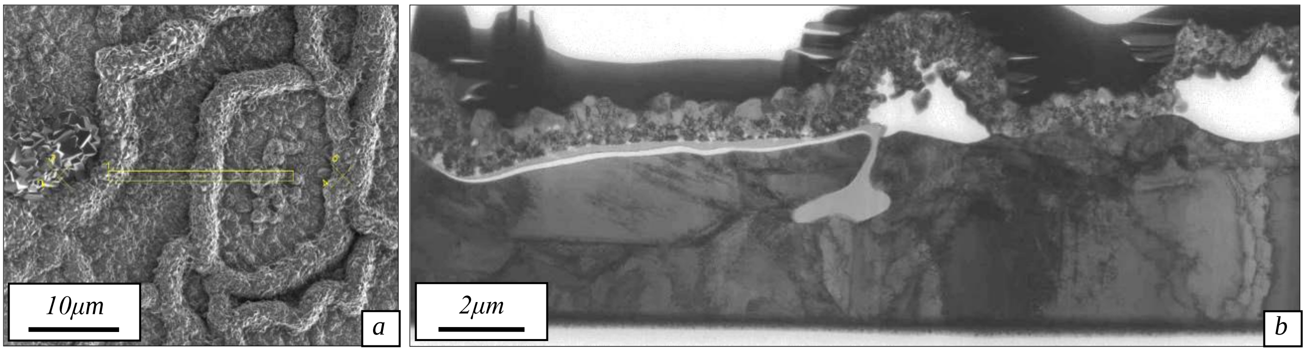

Figure 10.12:- a) Secondary electron image of the surface showing area for TEM thin foil preparation and b) TEM bright field micrograph of the thin foil produced by FIB milling of an oxide produced on S32205 after oxidation at 1000°C for 2 hours in simulated propane combustion products

A TEM thin foil was produced of the oxide ridges in the area shown in Figure 10.12(a) by the use of FIB. A resulting bright field transmission electron micrograph is shown in Figure 10.12(b). The oxide ridges are, infact, loops of oxide rather than solid elongated oxide nodules as was previously suspected. To the left of the main oxide ridge shown in this image is a thin oxide scale which measures ~1.5 – 2 µm thick which is shown at higher magnification in Figure 10.13 together with a higher magnification bright field TEM micrograph of the oxide ridge itself. Beneath the oxide ridge is a large void which creates the loop of oxide. In the substrate a large area of an amorphous phase is observed which joins a layer of the amorphous phase beneath the oxide scale to the left of the image.

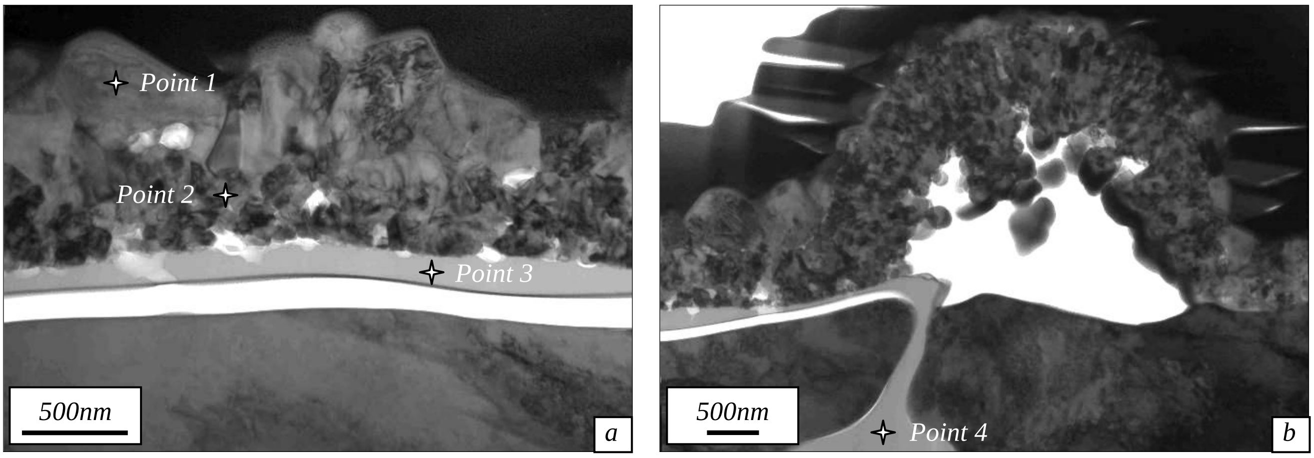

Figure 10.13:- Bright field TEM images of a) base oxide and b) oxide ridge taken from the area shown in Figure 5.61(a) of the oxide formed after 2 hours at 1000°C in simulated propane combustion products. Points 1 – 4 indicate positions for EDS data collection

The thin oxide scale consists of three oxide layers. The first is a relatively large grained oxide towards the outer edge of the scale, a fine grained middle layer and a final amorphous layer which is separated from the substrate by a thin void evident from the bright white contrast. The oxide ridge consists wholly of a fine grained oxide with a large void between the ridge and the substrate. From this high magnification image it is possible to see that the amorphous phase follows a grain or phase boundary into the substrate and forms a large area of the amorphous phase within the substrate. EDS of this area was taken at the positions marked in Figure 10.13. Point 1 was taken in the upper part of the base oxide and was found to be manganese rich $(MnCr)_2O_{3.}$ Point 2, taken from the fine-grained region of the oxide was found to be almost pure Cr_2O_3 with a small quantity of manganese. The amorphous phase (point 3 and 4), both underlying the base oxide and within the large sub-surface area, was identified as silica (~66at% oxygen and ~33at% silicon).

11 DISCUSSION – OXIDATION OF DUPLEX STAINLESS STEELS

11.1 Introduction

In this chapter, the results relating specifically to the oxidation of duplex stainless steels will be discussed with reference to the literature. This section will outline the oxidation of duplex stainless steels from the initial oxidation stages (drawing from results obtained using in-situ observation), through the early oxidation stages and finally the oxide produced after simulation of the full industrial reheat procedure.

The phenomena treated here will include the base oxide formation and microstructure, distribution of oxide nodules on the surface after full reheat and after heat treatments in simulated propane combustion products, the effect of surface finishes on the oxidation and the process of oxide nodule formation on these grades.

11.2 Initial oxidation of S32101

The experiments conducted in the environmental SEM were crucial to the understanding of the effect of the underlying microstructure of duplex grades on the oxide produced.

The ESEM experiments have shown that the ferrite phase oxidises at a faster rate than the austenitic phase from the outset of heat treatment with a more feature-full oxide produced on the ferrite after as little as 5 minutes oxidation (Figure 7.1). The cross-sections of the oxides to either side of the phase boundary have also revealed that the oxide formed on the ferrite phase is thicker than on the austenite side, again confirming the difference in the oxidation rate of the two substrate phases. There are also differences between the morphologies of the oxide formed on either side of the boundary. The oxide on the austenite phase has facetted grains on the upper surface which have not formed a continuous layer whereas on the ferrite phase the oxide is a dense continuous layer.

As shown in Figures 7.3 and 7.4, there is an expected increase in the crystal size on both phases as the duration of heat treatment increases. The morphology of the crystals, however, does not change. The oxide formed on the austenite phase remains inhomogeneous and that formed on the ferrite phase retains its continuous upper oxide layer. One implication of these observed differences in oxide density is that the oxide formed on the austenite region may have less of a protective nature than the oxide formed on the ferrite phase. The formation of a dense, impenetrable oxide layer prevents the ingress of oxygen to the metal's surface thus protecting the metal from further oxidation. As the oxide on the austenite region has areas where the thickness varies, it can be suggested that it may not be as protective as the dense and apparently sintered oxide formed on the ferrite phase as shown schematically in Figure 11.1.

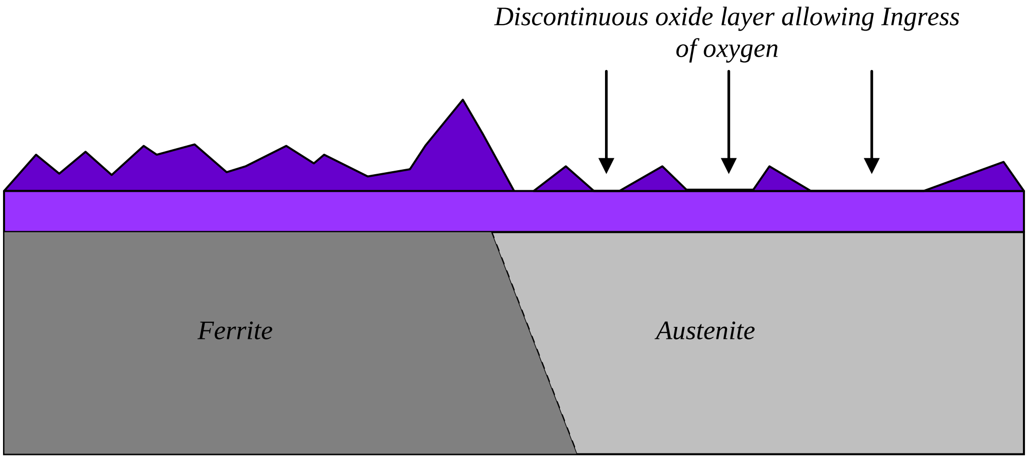

Figure 11.1:- Schematic of the initial oxide formed on S32101 in the ESEM experiment

The differences in oxidation rate of the two substrate phases lead to differences in the thickness of the oxides on the two regions. This can be explained by two possible mechanisms. It is known that chromium is a ferrite former and so will be present in slightly greater proportions in the ferrite phase than in the austenite region. Results have shown that this is the case, with differences observed in EDS maps of similar areas (e.g. Figure 10.9). The actual levels of chromium have been determined to be ~21 wt% in the austenite regions and ~23 wt% in the ferrite regions (Table 3.2). The difference in chromium contents therefore, is unlikely to produce such noticeable differences. It is more likely that the differences are due to a variation in diffusion rates in the different phases.

It is known that diffusion rates of some elements are faster in ferrite than austenite [Gunn, 1997]. As oxidation is a diffusion based process, this means that, at a particular temperature, formation of a unit of oxide on the ferrite region would occur at a faster rate than the formation of the same unit of oxide on the austenite region. After this short period of oxidation time and at the relatively low temperatures involved during the ESEM experiment, the differences in oxidation rate have the effect of producing a thin oxide on the austenite region and a thicker oxide on the ferrite region. This would imply that if oxidation of the two phases was allowed to proceed without the influence of any effect other than diffusion rates, then the oxide on the austenite phase would produce the same oxide as that produced on the ferrite region, but after a longer heat treatment. The oxide band visible at the perimeter of the austenite region in Figure 7.1(b) suggests that an oxide similar to the ferrite region is in the process of forming which, if correct, would confirm that the main differences in oxides produced between the austenite and ferrite regions are related to diffusion rate in the substrate.

There is a large manganese rich oxide grain which has formed over the boundary between the phases (Figure 7.11 and 7.16). Grain and phase boundaries are known to provide pathways for increased diffusion rates. This allows oxidation at the phase boundaries to be enhanced which will produce the larger oxide grains observed at the perimeter of the austenite phase by the end of the ESEM experiment. The enhanced growth of manganese oxide at the boundary implies that the phase boundary is acting as a diffusion path primarily for manganese towards the surface of the material. This is further suggested by the observation that there is no noticeable difference between the thickness of the fine grained chromium rich oxide over the phase boundary.

The EDS maps taken from this specimen type i.e. from a planar view, should be treated with some degree of scepticism. The fact that both the iron and the chromium (the major constituents of the alloy) are enriched in the thinner parts of the oxide (i.e. the areas lacking large facetted grains) means that it may be an effect of the volume sampled by EDS as the thin oxide is less than 1µm thick. Manganese reveals a pattern contrary to that of chromium with an overall enhancement of manganese counts on the ferrite side of the boundary. As manganese is not a major constituent of the alloy (present only to a value of ~5wt.%), and that no iron or chromium is observed in the ferrite region, this is a real result. The facetted oxides of the austenite region are also manganese enriched with the remainder of the oxide on the austenite region lacking in manganese. The oxide crystals formed at the boundary are highly enriched in manganese. Silicon has a low count over the entire analysed region but does show a slight enrichment on the austenite side of the boundary and a complete absence in the oxide formed over the boundary.

11.3 Oxidation during the Early Stages

During the early stages of oxidation, many different phenomena were observed on duplex stainless steels. The two most significant phenomena are the production and growth of the base oxide (i.e. the non-nodular oxide) and the formation of early stage oxide nodules on the surface. Both of these will be discussed and comparisons between the duplex grades will be made.

11.3.1 Base Oxide Formation

The base oxide is produced after short oxidation times at low temperatures and can generally be thought of as a thin, uniform oxide scale which forms before any additional feature becomes prominent (e.g. oxide nodules). It is how the heat treatment affects this base oxide which will determine what features will form, where they are located and how severe they will be. It is therefore important to understand how the base oxide forms.

As discussed in Section 11.2, facetted, octahedral oxide grains can be associated with spinel type oxides [Bauer and Tvrz (1988)]. It is these shaped crystals which are present on the upper surface of the oxides produced after heat treatment of both S32101 and S32205 although they tend to be more prominent on the S32101. These oxide grains are found on both the austenite and ferrite regions on ground surfaces. Comparison of the micrographs in Figure 8.1 and 8.24, for example, show the difference in the early stage oxidation of the two metals even after oxidation at 700°C. The surface of the oxide formed on the S32101 is completely composed of facetted oxide grains which can be assumed to be spinel type oxides, however, the oxide formed on the S32205, at the same time and temperature, has only a few small, isolated, facetted oxide grains on the surface.

Manganese can have a detrimental effect on the formation of a protective oxide on chromium containing steels as it forms a more stable oxide than chromium and has a higher diffusivity in iron alloys than chromium [Morasco and Young (1990)]. This means that the manganese rapidly oxidises prior to the formation of the protective chromium rich oxide. Results presented in this thesis (e.g. Figures 8.14, 8.28 and 8.31) and within the literature have shown that manganese rich oxides are commonly found on the upper surface of the oxide. This is due to the effect explained by [Morasco and Young (1990)] from a study of Fe-Cr-Mn alloys. As the manganese is rapidly oxidised to form a chromium and manganese spinel, the underlying substrate is depleted in manganese until it has a composition comparable to a Fe-Cr alloy. At this stage, the chromium is then oxidised to produce protective chromia. However, the manganese spinel will not stop growing because, as been shown by [Wild(1977)], manganese has a greater rate of diffusion in chromia than chromium does, which means that, providing there is sufficient supply of manganese in the underlying substrate, the oxide produced will be dual layered with a manganese rich outer oxide and chromium rich inner oxide. Examples of the manganese rich oxides shown in this thesis are all octahedral in shape suggesting that they are either spinel type oxides (such as $CrMn_2O_4$) or cubic oxides such as MnO which agrees with the literature for manganese containing steels.

This goes some way to explaining the differences observed in the early stage oxidation of S32101 and S32205. The main differences in chemistry between the two metals are that they contain a nominal concentration of 21.5 wt.% and 22 wt% chromium and 5 wt.% and 0 wt.% manganese respectively. The differences in chromium concentration are not of a large enough magnitude to explain the better oxidation resistance of the S32205, but due to the fact that minor additions of manganese can have dramatic effects on the oxidation rate of chromium containing alloys [e.g. Holcomb and Alman (2006) and Morasco and Young (1990)] the large difference in manganese content will be a significant factor.

11.3.2 Early Stage Nodule Formation

After full reheat of duplex stainless steels (particularly S32101), oxide nodules form on the surface. Due to their depth of penetration into the surface of the metallic substrate (e.g. Figure 9.3), removal of these oxide nodules may prove difficult using mechanical descaling methods for a number of reasons;tThe oxide in the crater region may not be fully removed (Figure 11.2(b)) which will leave an imperfection in the surface of the metal reducing the quality of the surface of the final cold rolled product. Even if the nodules were completely removed a large pit would remain (Figure 11.2(c)) and in order to remove this, a large amount of useful metal would need to be removed by further grinding of the surface (Figure 11.2(d)).

As well as this effect on product yield, the presence of oxide nodules during rolling will increase the surface roughness of the materials which will lead to increase wear of the rolls [Li and Sellars (1996) and Munther and Lenard (1998)]. The formation of oxide nodules also has implications for lower temperature service applications where oxide nodules are vulnerable to spallation [Perez (2001)]. In order to fully understand the formation of these oxide nodules, experiments were carried out in the initial stages of oxidation using the simulated propane combustion products. Results of heat treatments in the reheat furnace (which produce full reheat nodules) will be discussed in the Section 11.4.

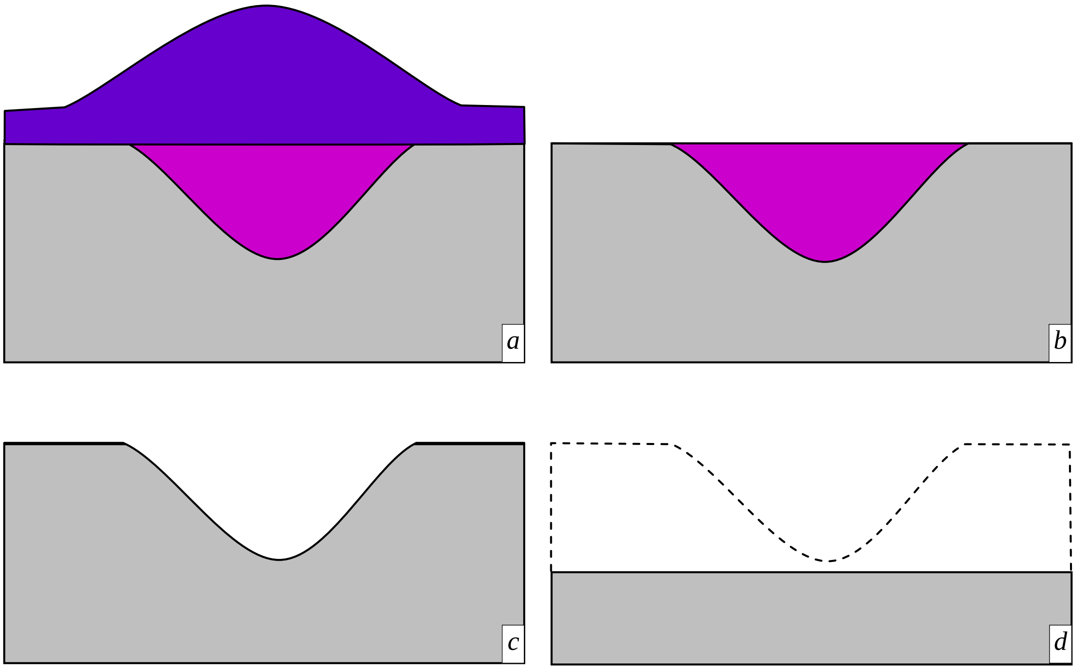

Figure 11.2:- Schematic of the effect of nodule formation on the production of an acceptable surface finish on duplex grades indicating (a) the general appearance of an oxide nodule, (b) an oxide nodule with the island removed, (c) the remaining pit after removal of the crater and (d) the amount of material losses which are required to completely remove the oxide nodule

Early stage oxide nodules have been observed after heat treatments on both S32101 and S32205 at all temperatures above 900°C. The use of dual bean FIB has been extremely useful in the preparation of site specific cross-sections (Figure 8.9) and TEM samples (Figure 8.11). The particular oxide nodule displayed in these figures is a good example of a typical oxide nodule formed on industrially prepared S32101 duplex stainless steel during oxidation at 900°C for 2 hours. Interestingly there is a chromium rich fine-gained oxide band present in the nodule which breaks down in its centre. The second nodule type formed on this grade after the same heat treatment is displayed in Figure 8.10. It has a different appearance to the nodule shown in Figure 8.9 as it has no crater region. Instead it consists only of an island region. Underneath the island the substrate contains an apparently oxidised boundary which intersects the substrate’s surface at the nodule’s centre. It is unknown whether this band is simply a grain boundary or if it is a boundary between phases. This boundary may act as a diffusion path for any elements entering the nodule.

As with the previous example of initial nodular oxidation, there is a thin band which has a lighter contrast which, as confirmed by EDS (Figure 8.12), corresponds to chromium enrichment within the base oxide and the nodule itself. This band extends to approximately 1/3 of the width of the nodule on either side leaving approximately 4µm of the nodule with no protective chromium present (this is where the boundary intersects the surface of the substrate). It is, however, unknown whether this break in the chromium rich band is a cause of the initial nodule oxidation site or an effect of excessive growth of chromium poor oxide. From the current results, however, it is feasible to produce a sequence of possible nodule formation steps (Figure 11.3). It is known that stainless steel obtains its stainless property from the production of a thin chromia layer which forms during the initial oxidation stages (Figure 11.3 (a)). From the results obtained it can be suggested that grain / phase boundaries in the substrate provide diffusion paths for elements from the substrate to the oxide scale producing a small area of local breakaway oxidation occurring on the surface (Figure 11.3 (c+d)). This small area will then grow to form a nodule on the surface similar to that seen in Figure 8.10. After further oxidation the nodule will grow in height and also form a crater area beneath it (Figure 11.3 (d-f)). The oxide nodule shown in Figure 8.10 is believed to be in the state represented by the schematic shown in Figure 11.3(d) whereas the oxide nodule shown in Figure 8.9 is thought to be at a more advanced stage of oxidation and is better represented by Figure 11.3(f)

Although not as frequent as on S32101, initial nodule oxide growth sites have also been identified on the S32205 substrate. An example of this is shown in Figures 8.27 and 8.28. As discussed is Section 11.3, the manganese contents of the two duplex grades are significantly different. The S32205 nominally contains no manganese although it will be present as an impurity. The EDS maps of the nodule shown in Figure 8.28 reveal that the upper most grains are manganese oxide (with small quantities of chromium) but that the majority of the nodule consists of fine grained chromium rich oxides. The formation of this nodule therefore does not show any evidence to suggest that a protective oxide layer has failed or that any other element has begun to oxidise, instead there has been enhanced growth of a chromium rich oxide leading to the formation of the nodule. This could be explained by the presence of a pathway for fast diffusion. In duplex grades this could include: phase boundaries, grain boundaries or something introduced by the industrial grinding operation. S32205 is ground at a low temperature compared to the S32101 so strain induced recrystallisation would not occur until the reheat stage. This would mean that the diffusion in the upper layers of the substrate could be affected by both the introduced dislocations [Lloyd, Saunders, Kent and Fursey (1977)] and the high grain boundary density after recrystallisation during the reheat. The micrograph shown in Figure 8.27 contains many grain boundaries which suggests that the recrystallisation may have contributed to the nodule growth.

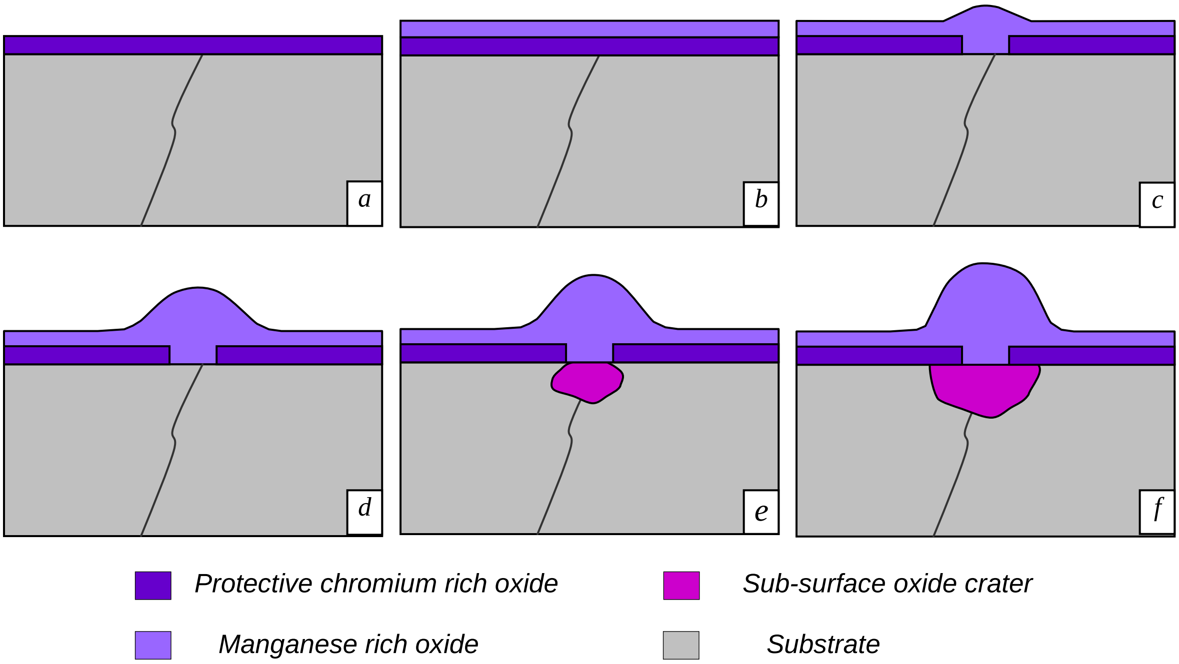

Figure 11.3:- Schematic of nodule formation during the oxidation of duplex stainless steel. (a) thin protective oxide forms, (b) a secondary oxide layer may form, (c) protective properties are lost due to chemical breakdown of protective chromia, (d) oxide nodule forms on the surface, (e) small crater forms below the oxide nodules and continues to grow and (f) a full oxide nodule and crater is produced

The nodule shown in Figure 8.17 and 8.18 is in a much later stage of growth but provides evidence to suggest that nodule formation may be dependant on the formation and subsequent breakage of a protective chromium rich oxide. This nodule has a chromium rich band through its centre. The band is revealed as having similar counts to the apparently protective base oxide to either side of the oxide nodule. As this nodule has an associated chromium / manganese rich oxide crater, it can be suggested that this loop has cracked (due to the volumous nature of Cr_2O_3), revealing a chromium depleted substrate as reported by Evans, Hilton, Holm and Webster (1980). The reason that the crack in the protective oxide band is not visible is an effect of sampling using non site-specific cross-sectioning. As it would be less likely that a protective oxide is produced upon the depleted layer, a local breakaway nodule has formed on the surface (Figure 11.4).

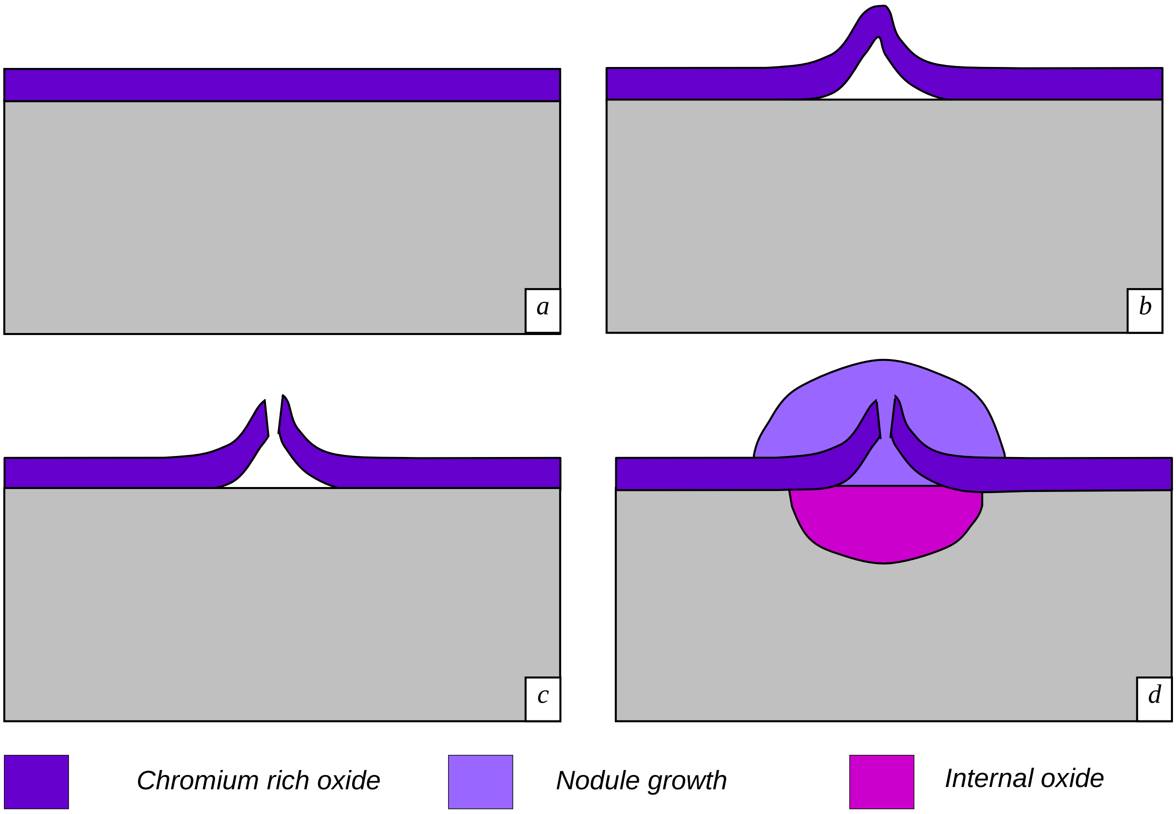

Figure 11.4: Sequence of possible initial nodule formation steps showing (a) formation of a protective base oxide, (b) loop of oxide forming due to a larger volume of oxide to metal, (c) oxide loop cracking due to mechanical stress build-up and (d) full nodule formation

11.4 Oxide Scales Produced after Full Reheat

During real industrial reheating operations, the surface finish of both of the duplex grades studied in this thesis is 32 grit. This finish is produced by hot grinding of the S32101 and by cold grinding of the S32205. This process is carried out after casting in order to remove the surface of the as-cast slab in an attempt to reduce surface imperfections. Together with the correct surface finish, the specimens discussed here were all oxidised in the Avesta experimental reheat furnace in an attempt to obtain the most industrially comparable results possible.

One of the most striking results is that there is a large difference in the surface oxide between the S32101 and the S32205 after heat treatment for the same time and at the same temperature (Figures 9.1 and 9.14 respectively). The S32101 shows a surface with a base oxide which resembles the underlying grinding marks with many oxide nodules on the surface and the S32205 shows a surface which is far more uniform. The S32205 does, however, have large oxide ridges in the grinding direction which the S32101 does not.

In cross-section the oxide nodules formed on the S32101 are chemically similar to the oxide ridges formed on the S32205 (as shown by comparison of Figures 9.4 and 9.16) suggesting that both alloys encounter a similar stage of breakaway oxidation during reheat. The main difference is the formation of oxide nodules on S32101 which are absent after reheat of S32205. The main difference between the two alloys is that S32101 has a nominal 5 wt% manganese whereas S32205 has 0wt%. As discussed previously, manganese has a detrimental effect on iron – chromium alloys which leads to the formation of oxide nodules on the surface of the S32101.

11.5 Oxidation of Polished Duplex Stainless Steel

When compared to the oxidation of ground duplex S32101 for the same time and temperature (Figure 8.15), the oxide produced on polished S32101 after heat treatment at 1000°C for 1 hour in the tube furnace (Figure 10.1) is much more dependant on the underlying substrate microstructure. The distribution of the oxide islands resemble the underlying austenite distribution and, as shown in Figure 10.8, the oxide craters also penetrate only into the austenitic regions forming oxide nodules on and into the austenitic phase of the substrate. These nodules are produced due to the local breakdown of protective oxide properties which has resulted in catastrophic oxide growth in these regions.

It is well known that localised spalling of protective oxide scales can lead to localised breakaway regions on stainless steels [Evans, Hilton, Holm and Webster (1983), Wood (1970)] and oxidation of duplex stainless steels has been suggested to produce a chromium depletion in the underlying substrate leading to a solely austenitic region present below the oxide scale [Li, Jiang and Riquier (2005), Riquier and Zhang (2004)]. In contrast to these findings no evidence has been found to suggest that local breakaway oxidation of S32101 depends on spallation, and oxidation does not induce a phase change on a polished surface.

Instead, oxides of different thicknesses and chemical composition form on the austenite and ferrite phases within the substrate during the early stages of oxidation (Figure 10.5 and 10.6). These initial oxides then govern the formation of local breakaway regions on the austenitic phase (Figures 10.7, 10.8 and 10.9) whilst the oxide on the ferritic phase remains thin and apparently protective in agreement with earlier work [Li *et al*. (2005)].

During the early stages of oxidation, thin oxides form on both of the substrate phases. The ferritic regions tend to form three layers of oxide: a continuous silica layer at the base, a chromium / manganese oxide and a manganese oxide upper layer. The austenitic regions on the other hand form only two layers: a manganese / chromium oxide layer and a discontinuous silica layer which resides within asperities at the oxide / metal interface. Continuous silica layers (as seen at the base of the oxide on the ferritic regions) have previously been shown to either promote the growth of protective oxides [Evans, Hillton, Holm and Webster (1980)] or hinder overall oxide growth [Evans *et al*. (1983), Bamba, Wouters, Galerie, Charlot and Dellali (2006), Kumar and Douglass (1976)]. Evidence from the present study has shown that the silica first promotes the growth of a thicker more protective oxide (in the early stages) and then may prevent further growth which would otherwise lead to breakaway oxide growth during the later stages. The thinner oxide seen on the austenitic region has a discontinuous silica layer at the oxide/metal interface which has been shown by other authors [Evans *et al*. (1980)] to be deleterious to an oxide's protective properties. Previous work [Bamba *et al*. (2006)] has shown that additions of silicon to an iron-chromium alloy up to 1wt.% can have a noticeable difference on the oxidation behaviour. A silicon free alloy produced breakaway regions consisting of iron rich nodules whereas 0.5wt.% and 1wt.% silicon alloys showed no breakaway iron rich nodules. Another study [Evans *et al*. (1980)] showed that there is an optimum value for silicon content where contents below and above that value produce a faster growing oxide. It is known that silicon is a ferrite former and so will be of a greater proportion in the ferrite region (i.e. the non-nodular region). Results have shown that the silicon content in the ferrite grains is consistently higher than a comparable austenite region. Although the differences seem slight, it has been shown that small changes in silicon content can have a large effect on the oxides produced. Another possible reason for the differences observed between the phases is that diffusion rates in the ferrite phase are faster than those observed in the austenite phase. This would allow faster formation of oxides of all elements contained within the alloy. The result of this would be a faster forming chromium-rich protective oxide. It follows as well that this would also allow the formation of a more complete silica layer on the ferrite region which would add to the protective nature of the oxide. A similar effect has been seen by Tholence and Norell (2008) who found that ferritic steel form a protective layer of silica during oxidation whereas an austenitic grade did not.

During the later stage of the presented results, local breakaway oxidation occurs on the austenite region. In the range of times and temperatures studied, this breakaway nodule formation is only observed in the austenite region. The difference is due to the retention of the protective nature of the thicker chromium-rich oxide layer in addition to the continuous silica layer at the oxide / metal interface. As diffusion rates in ferrite are higher than in the austenite region, a protective oxide would be retained even after scale cracking or delamination. This cracking is known to occur in chromia due to the voluminous nature of chromia in comparison to the underlying alloy. This cracking then exposes the underlying, chromium depleted metal to the oxidising atmosphere leading to chemical failure of the protective chromium rich oxide. Iron rich oxides then form allowing internal oxidation of elements in the underlying metal to take place forming a crater. As the metal at the crater growth front is constantly being depleted of chromium (by oxidation), it grows unhindered until it encroaches upon the ferrite phase where it is healed by the increased supply of chromium. This effect is clearly illustrated by Figure 10.9 which shows a crater growing into the substrate but healed (by high chromium oxides) where contact with the ferrite phase is established. Re-healing has been discussed by other authors in relation to breakaway oxidation [Evans *et al*. (1980) Evans *et al*. (1983), Wood (1970)].

In summary, the substrate phases produce two different oxides in the early stages: a thin oxide on the austenite and a thicker oxide on the ferrite. It is proposed that due to the fast rate of diffusion in the ferrite phase, a protective chromium rich oxide forms. As well as this chromium layer, a continuous silica layer produced at the base of the oxide forms which also encourages protective behaviour of the oxide. On the austenite phase however, a protective oxide does not form which allows the development of nodules consisting of iron oxides with chromium rich craters. These craters then grow unimpeded until then impinge upon the neighbouring ferrite regions where they heal with a high chromium oxide thus prohibiting further growth of the crater into the substrate (Figure 11.4). This process is shown schematically in Figure 11.5.

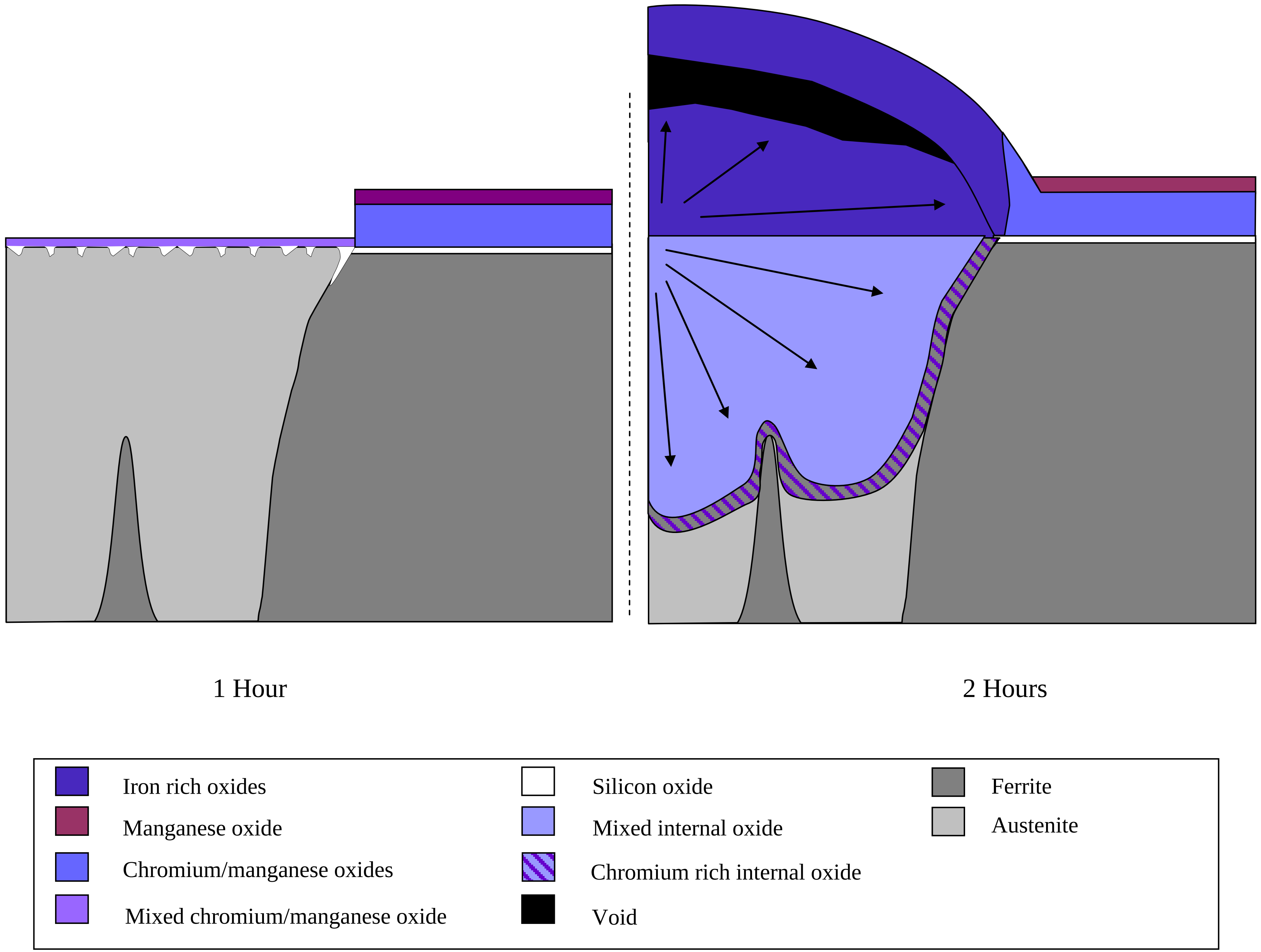

Figure 11.5: Schematic of the formation of oxide nodules on the surface of polished S32101 during reheat

11.6 Differences between Polished and Ground Duplex Stainless Steels

Comparison of the results of oxidation trails on polished and industrially prepared specimens of S32101 revealed that industrially ground specimens, such as that shown in Figure 9.5, tend to have oxide nodules forming in seemingly random locations along the direction of grinding. The industrially prepared surfaces where grinding damage is reduced such as the surface finished to 80 grit as shown in Figure 9.8 or the polished specimens described in Chapter 7 have oxide nodule distributions which are highly dependant on the underlying phase distribution.

A simple explanation of this phenomenon is that the grinding process causes a smearing effect between the two phases which destroys the surface phase distribution and so produces a more random oxide morphology.

Figures 8.9 and 8.10 show oxide nodules formed on hot ground S32101 after heat treatment and they reveal that there are grains towards the upper surface of the substrate which can be seen to be as small as 0.5 – 1µm in diameter. The differences observed during these experiments are probably due to recrystallisation caused during the heat treatment because of the strain induced by the grinding process. Although hand grinding is relatively undamaging (when compared to industrial grinding procedures) it has been shown that grinding of a ferritic stainless steel using 600 grit silicon carbide paper can cause damage to a depth of 1 – 2 µm [Ostwald and Grebe (2004)] and that damage of this type can induce recrystallisation of the upper layer of the substrate when heated [Grabke, Müller-Lorenz, Strauss, Pippel and Woltersdorf (1998)]. This recrystallisation will have a number of possible effects on the oxide scales produced during the reheat procedure. The most recognisable effect is the production of a finer grain size towards the upper surface of the substrate which is known to improve resistance to oxidation in chromia forming alloys [Peng, Yan, Zhou and Wang (2005)]. This increases the number of grain boundaries which will increase the diffusion rates of elements through the upper surface of the substrate. This means that the oxide formation is far less dependant on the substrate composition below this recrystallised region as elements can be transported from other parts of the substrate. This process would have the effect of reducing the influence of the underlying substrate phase distribution on the location of the oxide nodules and also slowing overall oxide growth due to the increased transport of elements to produce a protective oxide. This is also suggested by Douglass, Gesmondo and de Asmundis (1986) who found that oxidation of an electropolished Fe-Mn-Cr specimen was much faster than that of a ground specimen. They attributed this to the high diffusion rates through the cold worked region of both manganese and chromium which promotes the formation of a protective oxide. The more prominent formation of oxide nodules on polished specimens may be an effect of overall increased oxidation rate when compared to industrially ground specimens.

It was noted by Li *et al*. (2005) and Lille (2006) that during oxidation of duplex stainless steels, the area of the substrate directly below the oxide scale undergoes a phase transformation to produce a layer of ferrite or austenite. A phase change has also been reported by Wang and Chang (2002) who studied the oxidation of a Fe-Mn-Al alloy where manganese is the austenite stabiliser. The phase to which the underlying substrate transforms is dependent on the composition of the substrate material. In alloys where manganese is an important austenite stabiliser (such as in S32101) the depletion will encourage the formation of a ferrite layer. Where chromium is an important ferrite former particularly in a nickel containing alloy then depletion of chromium and enrichment of nickel at the oxide / metal interface will produce an austenite layer. In duplex grades, which contain large amounts of chromium but only small amounts of manganese, the most likely occurrence is that the substrate will be depleted in manganese thus producing the ferritic layer beneath the oxide. As with the formation of a fine-grained layer, this transformation will again allow faster bulk diffusion rates (due to the faster diffusion in ferrite than austenite) and so increase the oxidation rate which will in turn reduce the phase dependence. However, this could also have a beneficial effect on the oxidation rate at the later stages of oxidation. Within the ferrite region, chromium concentration will be higher which may encourage a protective oxide to form.

11.7 Summary of Oxidation of Duplex Stainless Steel

In summary, the oxidation of duplex stainless steel during industrial reheat processes produces nodular oxide growths. It is important to understand the growth of these nodules as they may have a detrimental effect on the stainless steel's surface finish. From the evidence gained during this thesis it is feasible to produce a timeline of the nodule growth mechanism.

In the initial stages the ferrite will form a thicker and more protective oxide due to higher rates of diffusion of both manganese and chromium. This can be further enhanced by the presence of cold working in the substrate from, for example, surface grinding operations. The introduction of the cold work introduces dislocations and promotes recrystallisation which both will enhance the diffusion rates. As manganese has a higher diffusivity through chromium rich oxides than chromium does, oxides of manganese will be found on the outer edge of the scale from the initial stages.

After the initial stages of oxidation, the oxide scale will continue to evolve with the upper manganese rich crystals growing to form octahedron shaped grains on the surface. Beneath this layer, a chromium-rich oxide layer will have formed which will prevent catastrophic oxidation from occurring. However, if this layer breaks, either by mechanical or chemical failure, an oxide nodule will form at the site. As the oxide nodules grow in size, a large crater will be formed which grows unhindered until an increased supply of chromium heals at its base and prevents any further growth. On a polished surface, oxide nodules always form on the austenite phase before the ferrite phase due to a more protective oxide scale being present on the ferrite region. The craters will grow only into the austenite phase until they impinge upon the ferrite phase where the increase in chromium causes the healing and prevents further growth.

12 CONCLUSIONS

A study into the oxidation behaviour of austenitic grades, 304 and 316L, and duplex grades, S32101 and S32205, has been conducted. Heat treatment temperatures have ranged from 700°C to 1300°C for times of up to 5 hours in oxidising atmospheres of ambient air or simulated combustion products of propane.

12.1 Austenitic Stainless Steels (304 and 316L)

- Oxidation of austenitic grades in ambient air can produce a layered sub-surface oxide structure which forms when protective oxide layers form and then fail due to chromium depletion in the substrate. This allows the ingress of oxygen and the subsequent formation of an additional chromium rich oxide layer.
- Oxidation of austenitic grades produces external scale layers which consist of a mixture of corundum and spinel structures. The chemical distribution though these layers consists of a lower layer of chromium rich oxides followed by an intermediate layer of iron and nickel oxides and a final upper layer of haematite.
- Within the outer layers of some oxides formed, a phase change occurs from spinel type oxide (which can be approximated to magnetite) to haematite. The change produces haematite which forms in a needle like structure from the outer edge of the oxide grains along a specific crystal plane.
- Particulate internal oxides have been shown to form in austenitic grades when temperatures are in excess of 1200°C and are more prevalent when the cooling rate is slowed. A number of these particles have been shown to be dendritic in nature which suggests the formation of a liquid phase during the oxidation process. The dendritic particles are rich in silicon and hence, together with the temperature of formation, it can be suggested that these dendrites are due to the formation of liquid fayalite which solidifies on cooling to produce the dendrites observed.
- Oxidation of as-cast austenitic stainless steel does not have a significant effect on the oxide scale produced after reheating. However, in some cases an internal oxide banding

is observed which is produced when oxides are formed in the dendritic as-cast microstructure of the substrate.

- Iron-rich oxide nodules are observed when oxidation of austenitic grades is carried out in simulated combustion products of propane gas. These are probably formed when the protective oxide fails due to stresses produced in the scale during growth revealing an underlying chromium depleted substrate.

12.2 Duplex Stainless Steels (S32101 and S32205)

- ESEM investigation of oxidation of S32101 has shown that the ferrite phase oxidises at a greater rate than the austenite phase from the outset of oxidation. This causes a dense and relatively thick, continuous upper oxide layer to form on the ferrite phase and a discontinuous and thinner layer to form on the austenite phase.
- Oxidation of polished duplex stainless steel surfaces produces nodules in positions which are highly related to the underlying phase distribution. Nodular oxide and accompanying craters, are formed on the austenite phase only and a thinner three-layer structure is formed on the ferrite phase. This is due to a faster rate of diffusion in the ferrite phase which allows the formation of a protective oxide in the early stages with a thinner less protective oxide on the austenite region. The protective oxide on the ferrite phase consists of a thick chromium rich oxide layer and a thin but continuous silica layer at the metal – oxide interface. After further oxidation, the austenite phase exhibits local breakaway oxidation whereas the ferrite phase does not.
- Oxidation of duplex grades in the early stages produces oxides consisting of fine-grained oxide layers in the first instance with larger grained manganese rich grains in the later stages of oxidation. These form due to the fact that manganese has a faster rate of diffusion through the chromia than chromium does resulting in a dual layer oxide scale.
- Initial oxide nodules form on duplex stainless steels when the, protective chromium rich oxide fails (either mechanically of chemically) revealing a chromium-depleted substrate which allows the formation of a manganese rich oxide nodule. There is also evidence to suggest that these initial nodule sites form on substrate grain or phase boundaries.

- Full reheat of duplex grades results in a nodular surface oxide consisting of iron-rich oxide nodules with oxide craters which extend into the substrate. At the perimeter of the crater region there is a chromium rich band which is assumed to re-heal the protective properties and hinder further growth of the oxide nodule.
- Phase dependence is not seen on ground substrates due to the damage induced during the grinding operation. This damage is responsible for modification of the upper substrate layers which causes a greater supply of chromium to the oxide layer and allows it to remain protective and uniform for a longer period of heating.

13 FURTHER WORK

This thesis has presented results showing which oxide types and microstructures can be expected to form on austenitic and duplex stainless steels under a number of oxidation conditions. In order to fully appreciate the effect of oxides on the manufacture of stainless steels, further work is required to quantify the descalability of the oxides produced. This could be achieved in a number of ways including: the inverted blister test (as described in Chapter 2), the impact of the oxide scales by a projectile or deformation of the metal after oxidation. These techniques will cause spallation of the produced oxide scales. The amount of spallation could then be compared to the microstructure of the oxides to establish the optimum conditions for the formation of a highly descalable oxide structures.

In order to design more effective descaling procedures for specific alloys, a systematic variation of the contents of alloying elements such as silicon and manganese could be carried out. This would allow a better understanding of the effect of each individual element on the microstructure and, if carried out with descaling experiments, the mechanical properties of the oxide formed. The information obtained from such a study would allow manufacturers to establish whether a slight alteration in composition of a grade (within tolerances) could lead to difficulties in the manufacturing process.

Further work could also address a later stage in the production of stainless steel: annealing. This process lasts a significantly shorter period of time than reheat (in the order of a few minutes) and is carried out at much lower temperatures (~900°C). These conditions yield thinner and more adherent oxide scales. In order to remove these oxides, chemical descaling or pickling is commonly carried out. Differences in the oxide scale produced can affect this pickling. If the substrate is dual phase (such as duplex stainless steel), differences in local chemistry could cause inhomogeneous effects which could lead to difficulties during chemical descaling. Future studies should study the microstructural differences in these annealing scales and relate this to their relative descalablity.

14 REFERENCES

H. Asteman, J.E. Svensson and L.G. Johansson, “Evidence for chromium evaporation influencing the oxidation of 304L: The effect of temperature and flow rate”, Oxidation of Metals, **57**, 193, 2002.

H. Asteman, J.E. Svensson and L.G. Johansson, “Effect of water-vapor-induced Cr vaporization on the oxidation of austenitic stainless steels at 700 and 900 degrees C - Influence of Cr/Fe ratio in alloy and Ce additions”, Journal of the Electrochemical Society, **151**, B141, 2004.

.

H. Astemann, J.E. Svensson, L.G. Johansson and M. Norell, “Indication of chromium oxide hydroxide evaporation during oxidation of 304L at 873 K in the presence of 10% water vapour”, Oxidation of Metals, **52**, 95, 1999.

H. Asteman, J.E. Svensson, M. Norell and L.G. Johansson, “Influence of water vapor and flow rate on the high-temperature oxidation of 304L; Effect of chromium oxide hydroxide evaporation”, Oxidation of Metals, **54**, 11, 2000.

E.C. Bain and W.E. Griffiths, “An introduction to the iron chromium-nickel alloys”, Transactions of the American Institute of Mining and Metallurgical Engineers, **75**, 166, 1927.

G. Bamba, Y. Wouters, A. Galerie, F. Charlot and A. Dellali “Thermal oxidation kinetics and oxide scale adhesion of Fe-15Cr alloys as a function of their silicon content”, Acta Materialia, **54**, 3917, 2006.

S.N. Basu and G.J. Yurek, “Effect of Alloy Grain-Size and Silicon Content on the Oxidation of Austenitic Fe-Cr-Ni-Mn-Si Alloys in Pure O_2”, Oxidation of Metals, **36**, 281, 1991.

J. Bauer and F. Tvrz, “A Field Guide in Color to Minerals, Rocks and Precious Stones”, Chartwell Books, 1988.

J. Beddoes and M.J. Bibby, Principles of Metal Manufacturing Processes, Arnold, New York, 1999.

D.J.M. Bevan, J.P. Shelton, and J.S. Anderson, “Properties of Some Simple Oxides and Spinels at High Temperatures, Journal of the Chemical Society, Nov, 1729, 1948

M. Biochenko, “Continuous Casting of Steel”, Butterworths, London, 1961.

S. Birosca, D. Dingley and R.L. Higginson, “Microstructural and Microtextural Characterisation of Oxide Scale on Steel using Electron Backscatter Diffraction”, Journal of Microscopy, **213**, 235, 2003.

N. Birks, G.H. Meier and F.S. Pettit, “Introduction to the High Temperature Oxidation of Metals, 2nd Edition”, Cambridge University Press, Cambridge, 2006.

A. Bruckman and G. Simkovic, Concerning Mechanism of Scale Growth Due to Cation Diffusion in Fe2O3 and CuS, Corrosion Science, **12**, 595, 1972.

P. Bolsaitis and M. Kahlweit, “Internal Oxidation of Cu-Si Alloys”, Acta Metallurgica, **15**, 765, 1967.

J.M. Camp and C.B. Francis ”The Making, Shaping and Treating of Steel”, United States Steel Company, 1951.

D. Caplan and M. Cohen, “High Temperature Oxidation of Some Iron – Chromium Alloys”, Journal of Metals, **10**, 1058, 1952.

D. Caplan and M. Cohen, “High Temperature Oxidation of Chromium-Nickel Steels”, Corrosion, **15**, 141t, 1959.

S.Y. Cheng, S.L. Kuan and W.T. Tsai “Effect of Water Vapour on Annealing Scale Formation of 316 SS”, Corrosion Science, **48**, 634, 2006.

Y.M. Chiang, D. Bernie, and W.D. Kingery, “Physical Ceramics: Principles for Ceramics Science and Engineering”, John Wiley & Sons, Inc., New York, 1997.

D.L. Douglass, F. Gesmundo and C. de Asmundis, The Air Oxidation of an Austenitic Fe-Mn-Cr Stainless Steel fro Fusion Reactor Applications, Oxidation of Metals, **25**, 235, 1986.

H.E. Evans, D.A. Hilton, R.A. Holm and S.J. Webster, “The Development of Localized Pits during Stainless Steel Oxidation”, Oxidation of Metals, **14**, 235, 1980.

H.E. Evans, D.A. Hilton, R.A. Holm and S.J. Webster, “Influence of Silicon Additions on the Oxidation Resistance of a Stainless Steel”, Oxidation of Metals, **19**, 1, 1983.

J.M. Francis and J.A. Jutson, “The Role of Silicon in Determining the Oxidation Resistance of an Austenitic Steel”, Materials Science and Engineering, **4**, 84, 1969.

H. Fujikawa, T. Morimoto and Y. Nishiyama, “Direct Observation and Analysis of the Oxide Scale Formed on Y-Treated Austenitic Stainless Steels at High Temperature”, Materials at High Temperatures, **17**, 293 2000.

G. Gedge, “Building Bridges”, Materials World, **14**, 19, 2006.

L.A. Giannuzzi and F.A. Stevie, “Introduction to focused ion beams :instrumentation, theory, techniques, and Practice”, New York, 2005.

H.J. Grabke, E.M. Müller-Lorenz, S. Strauss, E. Pippel and J. Woltersdorf, “Effects of Grain Size, Cold Working, and Surface Finish on Metal-Dusting Resistance of Steels”, Oxidation of Metals, **50**, 241, 1998.

E. Gregory and E.N. Simons, “Steel Working Processes: Principles and Practice of Forging, Rolling, Pressing, Squeezing, Drawing and Allied Methods of Metal Forming”, Odhams Books Limited, 1964.

R.N. Gunn, “Duplex Stainless Steels”, Abington Publishing, Cambridge, England, 1997.

M. Halvarsson, J.E. Tang, H. Asteman, J.E. Svensson and L.G. Johansson “Microstructural Investigation of the Breakdown of the Protective Oxide Scale on a 304 Steel in the Presence of Oxygen and Water Vapour at 600 Degrees C”, Corrosion Science, **48**, 2014, 2006.

A,N, Hansson and M.A.J. Somers, “Influence of Oxidation Environment on Scale Morphology and Oxidation Rate of Fe-22Cr”, Materials at High Temperature, **22**, 223, 2005.

J.B. Heywood, “Internal combustion engine fundamentals”, McGraw-Hill Book Co. Singapore, 1988.

R.L. Higginson and C.M. Sellars, "Worked Examples in Quantitative Metallography”, Maney Publishing, 2003.

D.T. Hoelzer, B.A. Pint and I.G. Wright, “A Microstructural Study of the Oxide Scale Formation on ODS Fe-13Cr Steel”, Journal of Nuclear Materials, **283**, 1306, 2000.

G.R. Holcomb and D.E. Alman, “The effect of manganese additions on the reactive evaporation of chromium in Ni-Cr alloys”, Scripta Materialia, **54**, 1821, 2006.

V.R. Howes, “Oxide Growth and Spalling on Fe-Cr Alloys Studied by Hot Stage Microscopy, Corrosion Science, **8**, 729, 1968.

F.J. Humphreys, “Characterisation of fine-scale microstructures by electron backscatter diffraction (EBSD)”, Scripta Materialia, **51**, 771, 2004.

M. Imagumbai and H. Kajioka, “Application of Solidification Theory with Small-Supercooling to Morphology of Dendritic Inclusions in Steel”, Iron and Steel Institute of Japan, **36**, 1022, 1996.

C. Issartrel, H. Buscail, E. Caudron, R. Cueff, F. Riffard, S.E. Messki, P. Jacquet and M. Lambertin, “Nitridation Effect on the Oxidation of an Austenitic Stainless Steel AISI 304 at 900°C”, Applied Surface Science, **225**, 14, 2004.

A.S. Khanna, “Introduction to High Temperature Oxidation and Corrosion”, ASM International, USA, 2002.

P. Kofstad, “High Temperature Corrosion”, Elseveir Applied Science Publishers Ltd., 1988.

M. Krzyzanowski, W. Yang, C.M. Sellars and J.H. Beynon, “Analysis of Mechanical Descaling: Experimental and Modelling Approach”, Materials Science and Technology, **19**, 109, 2003.

O. Kubaschewski, “IRON – Binary Phase Diagrams”, Springer – Verlag, Berlin/Heidelberg, and Verlag Stahleisen mbH, Düsseldorf, 1982.

I. Kvernes and M. Oliviera, “High Temperature Oxidation of Fe-13Cr-xAl Alloys on Air / H_2O Vapour Mixtures”, Corrosion Science, **17**, 237, 1977.

A, Kumar and D.L. Douglass, “Modification of the Oxidation Behaviour of High-Purity Austenitic Fe-14Cr-14Ni by the Addition of Silicon”, Oxidation of Metals, **10**, 1, 1976.

L-F. Li, Z-H. Jiang and Y. Riquier, “High-temperature Oxidation of Duplex Stainless Steels in Air and Mixed Gas of Air and CH4”, Corrosion Science, **47**, 57, 2005.

Y.H. Li and C.M. Sellars, “Cracking and Deformation of Surface Scale During Hot Rolling of Steel”, Materials Science and Technology, **18**, 304, 2002.

F. Liu, J.E. Tang, T. Jonsson, S. Canovic, K. Segerdahl, J.E. Svensson and M. Halvarsson, “Microstructural investigation of protective and non-protective oxides on 11% chromium steel”, Oxidation of Metals, **66**, 295, 2006.

C. Lille, Private communication, 2006.

G.O. Lloyd, S.R.J. Saunders, B. Kent and A. Fursey, “Breakaway Oxidation of Fe-10%Cr and Fe-20%Cr at Temperatures up to 600°C”, Corrosion Science, **17**, 269, 1977.

R.A. Lula, “Stainless Steel”, American Society for Metals, Ohio, United States of America, 1986.

A.L. Marasco and D.J. Young, “The Oxidation of Iron Chromium Manganese Alloys at 900-Degrees C”, Oxidation of Metals, **36**, 157, 1991.

H.M. McCullough, M.G. Fontana and F.H. Beck, “Formation of Oxides on Some Stainless Steels at High Temperatures”, Transactions of the American Society for Metals, **43**, 404, 1951.

K, McNee, Private Communication 2005.

K. McNee and D. Dulieu, Private Communication 2005.

J.P. McCaffrey, M.W. Phaneuf, L.D. Madsen, “Surface damage formation during ion-beam thinning of samples for transmission electron microscopy”, Ultramicroscopy, **87**, 97, 2001

I.A. Menzies and D. Mortimer, “Oxidation of Chromium Diffusion Coatings on Iron – Chromium Volatility and Experimental Methods”, Corrosion Science, **6**, 517, 1966.

L. Mikkelsen and S. Linderoth, “High Temperature Oxidation of Fe-Cr-Alloy in O_2-H_2-H_2O Atmospheres; Microstructure and Kinetics”, Materials Science and Engineering, **361**, 198, 2003.

L.A. Morris, in handbook of Stainless Steels, D. Peckner, I.M. and Bernstein, eds., McGraw-Hill, Texas, 1977.

J. Mougin, M. Dupeux, L. Antoni and A. Galerie, “Adhesion of Thermal Oxide Scales Grown on Ferritic Stainless Steels Measured using the Inverted Blister Test”, Materials Science and Engineering, **359**, 44, 2003.

S. Mrowec and K. Przybylski, “Self-Diffusion and Defect Structure in Cobaltous Oxide”, Oxidation of Metals, **11**, 383, 1977

P.A. Munther and J.G. Lenard, “The Effect of Scaling on the Interfacial Friction in Hot Rolling of Steels”, Journal of Materials Processing Technology, **88**, 105, 1998.

R.L. Newton, “Definitions and Causes of Continuous Casting Defects”, Percy Lund, Humphries and Co. Ltd, 1967.

J. Orloff, “High resolution focused ion beams :FIB and its applications : the physics of liquid metal ion sources and ion optics and their application to focused ion beam”, New York, 2002.

C. Ostwald and H.J. Grabke, “Initial Oxidation and Chromium Diffusion. I. Effects of Surface Working on 9 – 20% Cr Steels, Corrosion Science, **46**, 1113, 2004.

N. Otsuka, Y. Nishiyama and T. Kudo, “Breakaway Oxidation of TP310S Stainless-Steel Foil Initiated by Cr Depletion of the Entire Specimen in a Simulated Flue-Gas Atmosphere”, Oxidation of metals, **62**, 121, 2004.

N. Otsuka, S. Yoshiaki and H. Fujikawa, “Internal-External Transition for the Oxidation of Fe-Cr-Ni Austenitic Stainless Steels in Steam”, Oxidation of Metals, **32**, 13, 1989.

Outokumpu1, The Future of Bridges is Duplex, http://www.outokumpu.com/pages/Page____35770.aspx?docid=210573, first accessed 27/11/2006.

Outokumpu2, An LDX2101® Breakthrough in Pressure Vessels, http://www.outokumpu.com/pages/Page____35636.aspx?docid=210635 aspx first accessed 27/11/2006.

I. Panas, J-E. Svensson, H. Asteman, T.J.R. Johnson and L-G. Johansson, “Chromic acid evaporation upon exposure of Cr_2O_3(s) to H_2O(g) and O_2(g) – mechanism from first principles, Chemical Physics Letters, **383**, 549, 2004”

R. Peraldi and B.A. Pint, “Effect of Cr and Ni Contents Behaviour of Ferritic and Austenitic Model Alloys in Air with Water Vapour”, Oxidation of Metals, **61**, 463, 2004.

F.J. Perez, M.J. Cristobal, G. Arnau, M.P. Hierro and J.J. Saura, “High-Temperature Oxidation Studies of Low Nickel Austenitic Stainless Steel. Part I: Isothermal Oxidation”, Oxidation of Metals, **55**, 105, 2001.

R Peraldi and B.A. Pint, “Effect of Cr and Ni Contents on the Oxidation Behaviour of Ferritic and Austenitic Model Alloys in Air and Water Vapour”, Oxidation of Metals, **61**, 463, 2004.

F.J. Pérez, F. Pedraza, C. Sanz, M.P. Hierro and C. Gómez, “Effect of Thermal Cycling in the High Temperature Oxidation Resistance of Austenitic Stainless Steel”, Materials and Corrosion – Werkstoffe und Korrosion, **53**, 231, 2002.

X. Peng, J. Yan, Y. Zhou and F. Wang, “Effect of Grain Refinement on the Resistance of 304 Stainless Steel to breakaway Oxidation in Wet Air”, Acta Materialia, **53**, 5079, 2005.

R. Pettersson, L. Liu and J. Sund, “Cyclic Oxidation Performance of Silicon-Alloyed Stainless Steel in Dry and Moist Air”, Corrosion Engineering, Science and Technology, **40**, 211, 2005.

V. Randle, “Theoretical Framework fro Electron Backscatter Diffraction”, in Electron Backscatter Diffraction in Materials Science, Springer, 2000.

F. Riffard, H. Buscail, E. Caudron, R. Cueff, C. Issartrel, and S. Perrier, “Yttrium Sol-Gel Coating Effects on the Cyclic Oxidation behaviour of 304 Stainless Steel”, Corrosion Science, **45**, 2867, 2003.

Y. Riquier and H. Zhang, “L’oxydation à haute température des asiers inoxydables austéno-ferritiques”, La Revue Métallurgie, **101**, 855, 2004. (in French)

S. Rubanov and S. Munroe, “FIB-induced damage in silicon”, Journal of Microscopy, **214**, 213, 2004.

A.C.S. Sabioni, A.M. Huntz, F. Silva and F. Jomard, “Diffusion of Iron in Cr2O3: Polycrystals and Thin Films”, Materials Science and Engineering, **392**, 254, 2004.

I. Saeki, H. Konno and R. Furuichi, “The Initial Oxidation of Type 430 Stainless Steel in O2-H2O-N2 Atmospheres at 1273 K”, Corrosion Science, **38**, 19, 1996.

Y. Sakai, T. Yamada, T. Suzuki and Ichinokawa, “Contrast mechanisms of secondary electron images in scanning electron and ion microscopy”, Applied Surface Science, **145**, 96, 1999

A.J. Sedriks, Corrosion of Stainless Steel, John Wiley & Sons, New York, 1979.

S.M. Schnurre, J. Gröbner and R. Schmid-Fetzer, “Thermodynamics and Phase Stability in the Si-O System, journal of Non-Crystalline Solids, **336**, 1, 2004.

A.U. Seybolt, “Observations on the Fe-Cr-O System”, Journal of the Electrochemical Society, **107**, 148, 1960.

K. Segerdahl, J.E. Svensson and L.G. Johansson “The high temperature oxidation of 11% chromium steel: Part II - Influence of flow rate”, Materials and Corrosion – Werkstoffe und Korrosion, **53**, 479, 2002.

W. Sherwood and S.R. Shatynski, “The Effect of Temperature on Oxide Scale Adherence During Descaling Operations”, Surface Technology, **21**, 39, 1983.

W.W. Smeltzer, “Diffusional Growth of Multiphase Scales and Sub-scales on binary Alloys: A Review”, Materials Science and Engineering, **87**, 35, 1987.

G.J. Stokkers, A. Van Silfhout, G.A Bootsma, T. Fransen and P.J. Gellings, “Interaction of Oxygen with an AISI 314 Stainless Steel Surface by Ellipsometry and Auger Electron Spectroscopy in Combination with Ion Bombardment”, Corrosion Science, **23**, 195, 1983.

F.H. Stott, G.C. Wood and J. Stringer “The Influence of Alloying Elements on the Development and Maintenance of Protective Scales”, Oxidation of Metals, **44**, 113, 1995.

C.S. Tedmon, “Effect of Oxide Volatilization on Oxidation Kinetics of Cr and Fe-Cr Alloys”, Journal of the Electrochemical Society, **113**, 766, 1966.

F. Tholence and M. Norell, “High Temperature Corrosion of Cast Alloys in Exhaust Environments. II—Cast Stainless Steels”, Oxidation of Metals, **69**, 37, 2008.

K. Vepulanont, “Kinetics and Structure of Oxide Scale Formation on Stainless Steels Under Simuated Gas-Fired Furnace Conditions”, MPhil thesis, University of Sheffield, 2006.

C.A. Volkart and M.A. Minor, “Focused Ion Beam Microscopy and Micromachning”, Materials Research Society Bulletin, **32**, 389, 2007.

C. Wagner, “Beitrag zur Theorie des Anlaufvorgangs”, Zeitschrift für Physikalische Chemie., **B21**, 25, 1933.

C.J. Wang and Y.C. Chang, “Formation and growth morphology of nodules in the high-temperature oxidation of Fe-Mn-Al-C alloy”, Materials Chemistry and Physics, **77**, 738, 2003.

G.D. West, S. Birosca and R.L. Higginson, “Phase Determination and Microstructure of Oxide Scales Formed at High Temperature”, Journal of Microscopy, **217**, 122, 2004.

R.K. Wild, “High Temperature Oxidation of Austenitic Stainless Steel in Low Oxygen Pressure”, Corrosion Science, **17**, 87, 1977.

I.M. Wolff, L.E. Iorio, T. Rumpf, P.V.T. Scheers, and J.H. Potgieter, “Oxidation and Corrosion Behaviour of Fe-Cr and Fe-Cr-Al Alloys with Minor Alloying Additions”, **241**, 264, 1998.

G.C. Wood, “Structures of Thick Scales on Alloys, in Oxidation of Metals and Alloys”, In: Oxidation of Metals and Alloys (Conference), Metals Park, Ohio, 1970.

G.C. Wood and M.G. Hobby, “Composition Changes During the Healing of Oxide Scales on an Austenitic Stainless Steel”, Journal of the Iron and Steel Institute, **203**, 54, 1965.

A. Yamauchi, K. Kurokawa and H. Takahashi “Evaporation of Cr2O3 in atmospheres containing H2O”, Oxidation of Metals, **59**, 517, 2003.

H.J. Yearian, H.E. Boren and R.E. Warr, “Structure of Oxide Scales in Nickel-Chromium Steels”, Corrosion, **12**, 561t, 1956.

H.J. Yearian, W.D. Derbyshire and J.F. Radavich, “The Formation of Oxide Films on Chromium and 18 Cr-8 Ni Steels”, Corrosion, **13**, 507t, 1957.

H.J. Yearian, E.C. Randell. E.C, and T.A. Longo, “The Structure of Oxide Scales on Chromium Steels”, Corrosion, **12**, 515t, 1955.

B. Zhao, E. Jak and P.C. Hayes, “The Effect of MgO on Liquidus Temperatures of Fayalite Slags”, **30B**, 1017, 1999.

ADVANCED ANALYTICAL TECHNIQUES

Electron backscatter diffraction

When an electron beam strikes the surface of a highly polished sample, making an angle of 20° to the surface, a Kikuchi pattern is produced. The incident electron beam being inelastically scattered in all directions by the lattice planes produces the Kikuchi pattern. Since the electrons arrive at a plane at many different Bragg angles the electrons are scattered in a cone like pattern. If a collector screen is positioned to intersect the path of these diffracted electrons then it will detect two lines; one cone from the top and one from the bottom of the plane. These lines are very nearly straight and so appear to be parallel, (Figure A1.1). The Kikuchi bands give information on the lattice planes; each Kikuchi band will have a distinct width and will therefore correspond to a crystallographic plane, where the bands overlap it corresponds to a zone axis and intersection of several bands correspond to a major axis (Figure A1.2). The pattern, therefore, provides a substantial amount of information about the crystal structure of the material which can provide a means for characterising the material [Randle, (2000)]. Using optimum materials and SEM conditions, it is possible to obtain an effective spatial resolution of 10nm [Humphreys (2004)].

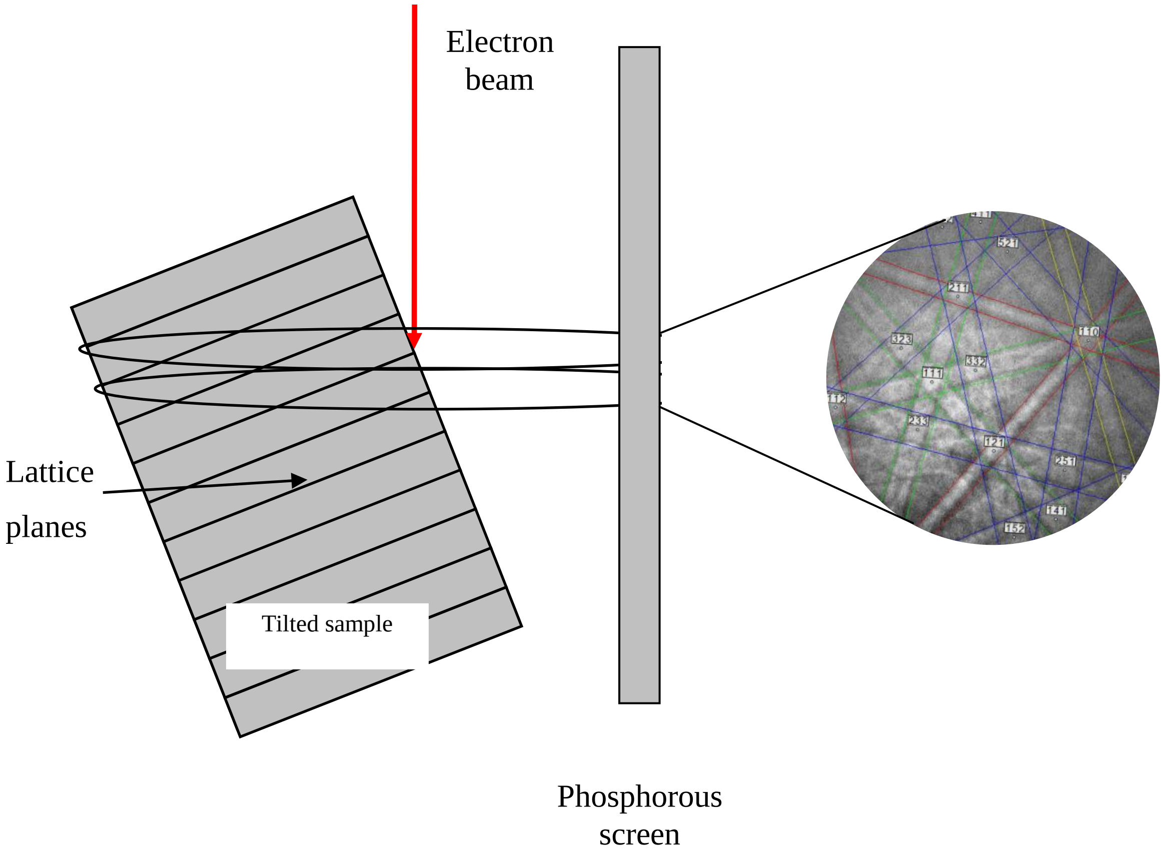

Figure A1.1: Schematic Diagram Showing the Formation of a diffraction pattern in EBSD

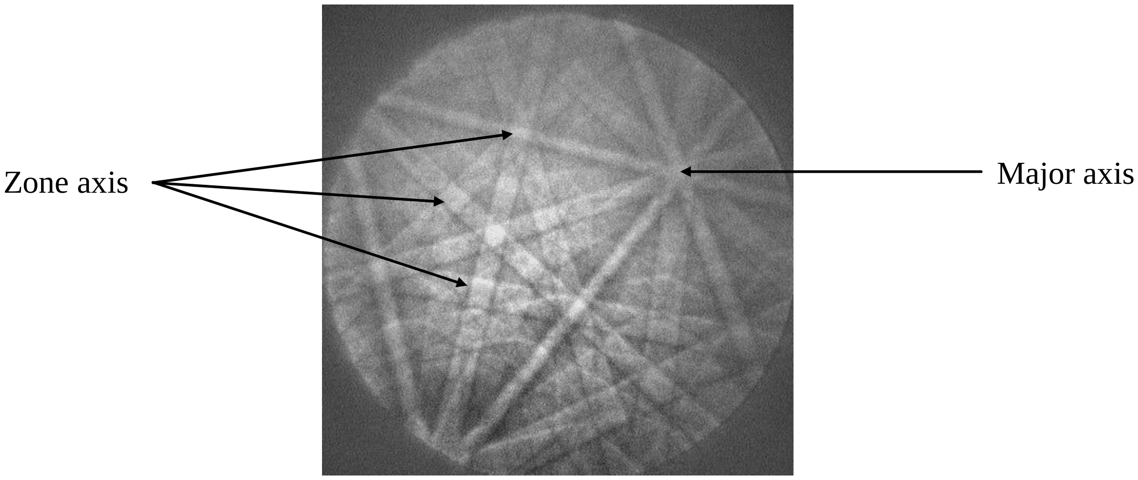

Figure A1.2: Example of a diffraction obtained using EBSD

Focussed Ion beam – Solid Interaction

When Focussed ion beams interact with a solid, scattering occurs in one of two ways: elastic and inelastic scattering. Elastic scattering results in the displacement of lattice atoms, material sputtering or defect production in the material. Inelastic scattering leads to the release of a number of signals from the material, these include:- Secondary ions, secondary electrons, X-rays and in some cases, light. The most commonly collected and most useful signal is the secondary electron signal. This is due to the fact that secondary electron yield is approximately 1 secondary electron for every 1 impinging ion making it a very abundant signal [Orloff, Utlaut and Swanson (2002)].

The feature which is made use of for cross-section and TEM sample preparation is sputtering of material which can occur when an inbound ion transfers sufficient momentum to a target atom that it is subsequently freed from the material. This process has been optimised in recent years and now allows machining on a very small scale.

Origin of Contrast in Ion Induced Secondary Electron Images

When a beam of ions impinges upon the surface of a material, secondary electrons can be produced at a rate of approximately one electron for each striking ion [Orloff et al. (2002)] (this can increase with beam voltage). The yield of secondary electrons is also related to the orientation of a polycrystalline material relative to the ion beam which leads to channelling contrast in ion induced secondary electron images. Channelling contrast is achieved when a grain is oriented in such a way that the low indexed axis is parallel to the incident ions from the focused ion beam and is shown schematically in Figure A1.3 (a) (for a channelled ion) and Figure A1.3 (b) (for an ion which is not channelled). This channelling causes the ions to enter the material via the channels between the atom columns which enables them to travel to a depth much greater than would usually be achieved before interacting with the target atoms. Interactions of the ions with the material in this case occur at a much greater depth from the surface which means fewer secondary electrons can escape [Gianuzzi and Stevie (2006)]. A comparable number of electrons will be produced as the ions collide with the atoms, but those secondary electrons that are produced from a greater depth will lose their energy during interactions on their way to the target’s surface and will be unable to escape the surface and hence are unable to be detected. This produces a lower secondary electron count at the detector and consequently a darker grain (Figure A1.3(a) and (b)).

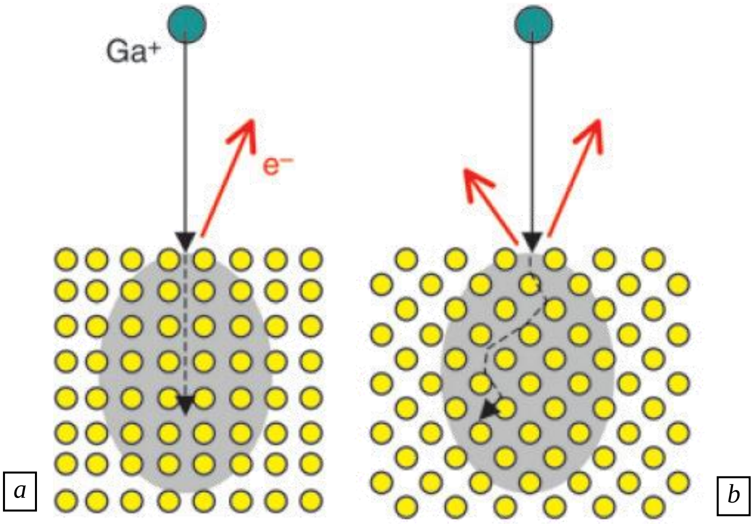

Figure A1.3:- Schematic of ion-beam solid interaction showing (a) the case where the impinging ion is channelled between atom columns. This means that the ion can travel a greater distance before a collision which results in a lower secondary electron emission at the surface and (b) the case where the ion is not channelled which means that a greater number of secondary electrons are generated near the surface so the grain will appear bright. (after Volkert and Minor (2007))

As well as channelling contrast, atomic weight can produce contrast in ion induced secondary electron images. Sakai, Yamada, Suzuki and Ichinokawa (1999), studied a sample with strips of materials successively larger in atomic mass and compared the contrast achieved by electron imaging and ion imaging. It was found that the contrast was reversed when imaging with ion induced secondary electrons, with the highest atomic mass appearing as a darker shade and the lowest atomic mass appearing as a brighter shade. The reason for this difference is related to the range of ion travel (the distance into the material the ions travel) which is related to the atomic mass as shown in Figure A1.4. Figure A1.4 shows a computer simulated depth of penetration model which reveals that the peak depth of ion travel into a surface depends on the atomic number. The shaded area is outside the sample’s surface and so can be considered to be reflected ions. It can be seen that as atomic mass (M_2) increases, the loss due to ion reflection (shaded area of the graph) increases (i.e. secondary electron yield decreases). In summary a material with a greater atomic mass will appear darker than one which has a lower atomic mass; the reverse of what may be expected when using impinging electrons [Sakai *et al.* (1999)].

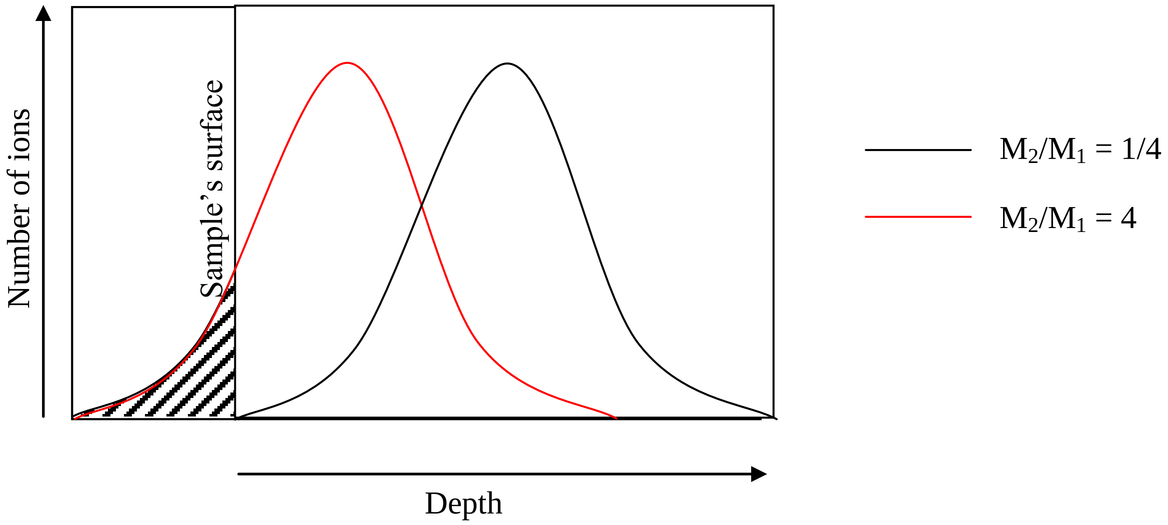

Figure A1.4:-Calculated range of impinging ions with varying target atom (M_2) :impinging particle mass (M_1) ratio. The shaded region represents the reflected particles.(Adapted from Sakai et al (1999))

Charging is another mechanism by which contrast can be derived in ion induced secondary electron imaging. Bright edges are a familiar sight when imaging a non-conducting specimen in a scanning electron microscope. This is caused by the build up of negatively charged electrons on the specimen which repel secondary electrons making the number of electrons counted at that point higher. When imaging using ion induced secondary electrons, a sample would be charged with positively charged ions which will then attract the secondary electrons reducing the number of electrons reaching the detector. Therefore a charging region in an ion beam instrument would appear dark when secondary electrons are collected; the opposite of what is seen in an electron microscope.

Ion Induced Damage

As the ions travel into the sample they gradually lose their energy (through interaction with the atoms in the material) and eventually come to rest as an implanted ion in the atomic structure of the material. The impinging ions cause some atoms to be displaced from their lattice positions which can lead to the production of an amorphous layer. Monte-Carlo simulation of penetrating gallium ions into crystalline silicon substrate has shown that at 30KeV the amorphised region extends to a depth of approximately 20 - 25 nm after milling at typical milling angles [Rubanov and Munroe (2004), McCaffrey(2001)]. TEM samples are usually prepared by milling each side of the thin foil so the actual extent of the damage is a 20 – 25nm layer on each side. If using TEM for analysis of crystal structures, chemistry or phase identification, these implanted ions and amorphised regions can alter lattice parameters or phase identification respectively. According to [Zeigler (2006)], there are many different types of damage which can be introduced by an impinging ion beam. The four most relevant types are: Displacement, vacancy production, interstitial production and replacement collisions.

EFFECT OF SURFACE FINISHES

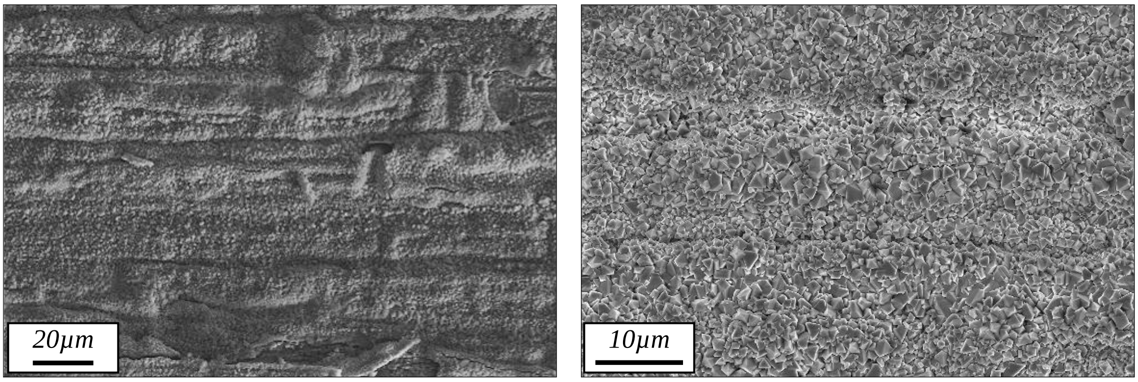

Figure A2.1:- Oxide formed on S32101 after preparation to an 80Grit finish and oxidation in simulated propane combustion products for 1 hour at 1000°C

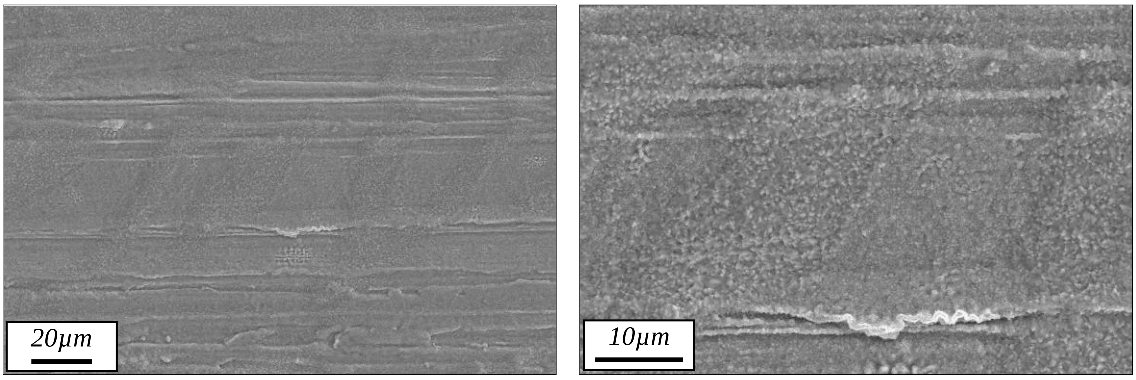

Figure A2.2:- Oxide formed on S32101 after preparation to a 240Grit finish and oxidation in simulated propane combustion products for 1 hour at 1000°C

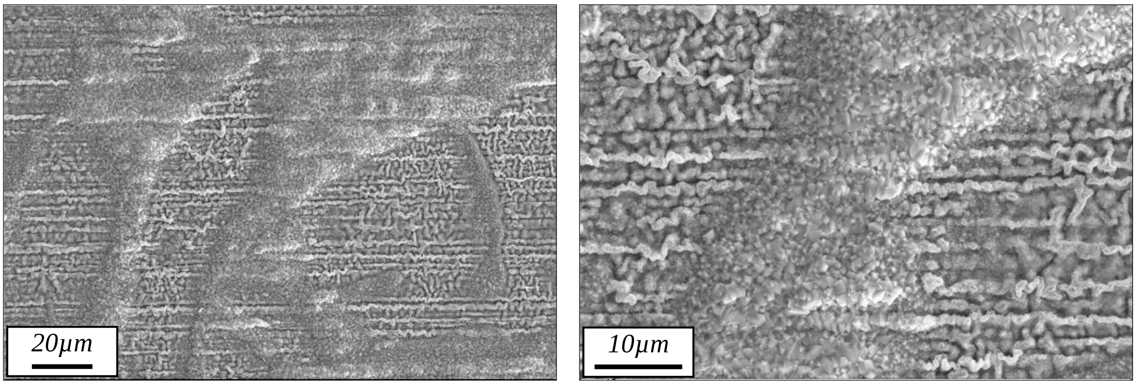

Figure A2.3:- Oxide formed on S32101 after preparation to an 800Grit finish and oxidation in simulated propane combustion products for 1 hour at 1000°C

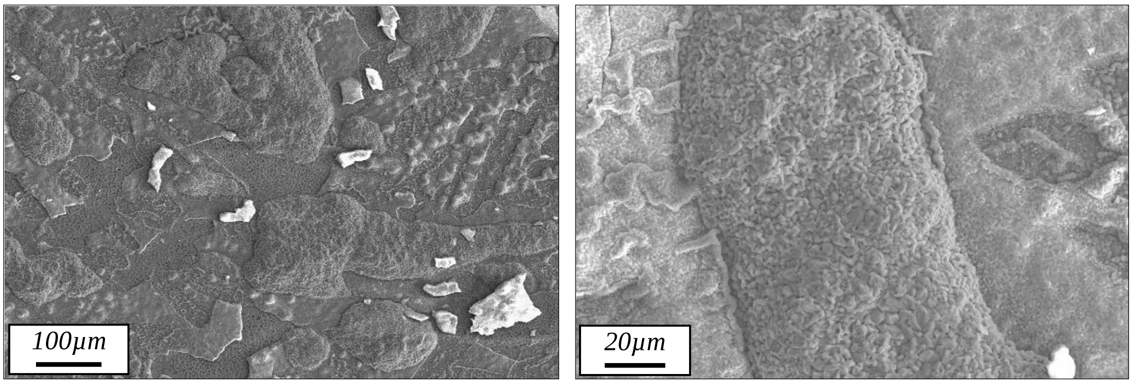

Figure A2.4:- Oxide formed on S32101 after preparation to a 2400Grit finish and oxidation in simulated propane combustion products for 1 hour at 1000°C

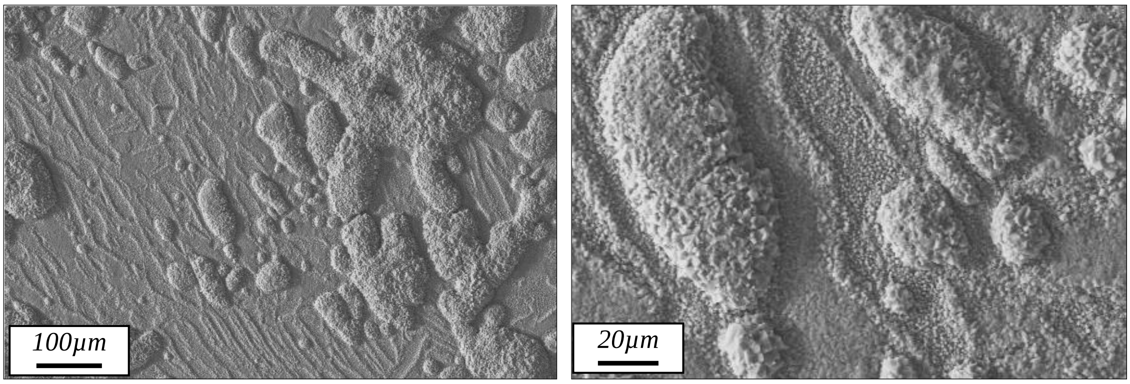

Figure A2.5:- Oxide formed on S32101 after preparation to a 1µm finish and oxidation in simulated propane combustion products for 1 hour at 1000°C

Figures A2.1 – A2.5 show oxide scales formed on S32101 after heat treatment in simulated propane combustion products at 1000°C for 1 hour with differing surface finishes. The surfaces were prepared using an industrially ground initial finish which was then laboratory ground using successively finer grades of silicon carbide paper until the desired finished was achieved. The specimens were then cleaned using methanol and oxidised in the tube furnace according to Chapter 3 of this thesis. The specimens were examined using a Leo 1530VP Field Emission Gun Scanning Electron Microscope.

In A2.1 the surface is covered in an oxide which shows no sign of the underlying phase distribution. In Figure A2.2, it is apparent that different oxides are formed on each phase with less densely packed oxide forming on the austenite phase. On an 800Grit surface, (Figure A.2.3), the oxides are very dissimilar with a facetted oxide forming on the ferrite phase and a rumpled looking oxide forming on the austenite phase. When a surface prepared to a finish of 2400Grit is oxidised, oxide nodules are found to form on the austenite phase only which is also the case on a polished surface (as shown in Chapter 10).

The results of this small study showed that the effect of the underlying phase distribution on the position of the formation of oxide nodules is increased as remnant surface preparation damage is removed.

SUITABLILITY OF SIMULATION

In order to establish the suitablity of the tube furnace, experiments were carried out to determine how comparable the results obtained were to the results obtained using the Avesta furnace.

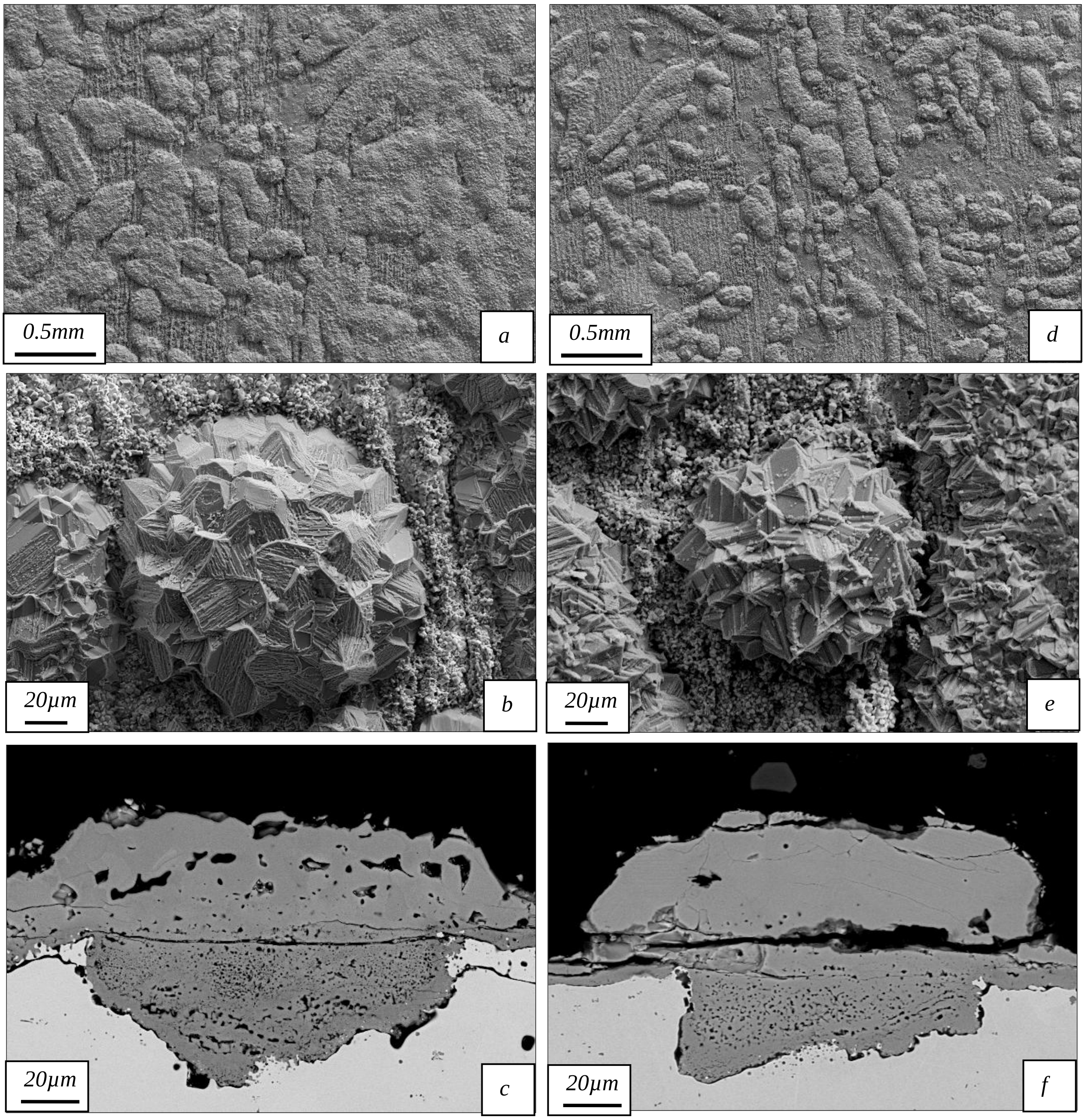

Figure 3.6: Comparison of the resulting oxides formed after oxidation of S32101 prepared to an 80 grit finish for a reheat cycle to a final temperature of 1200°C in Furnace 3 (a,b and c) and Furnace 1 (d, e and f)

Figure 3.6 reveals the results of these tests. Figures 3.6(a) is an overview of the sample's surface in planar view, 3.6(b) is a higher magnification image of the resulting oxide nodules 3.6(c) is a metallographically prepared cross-section of an oxide nodule formed on S32101 after a full reheat cycle in the tube furnace simulation and Figures 3.6(d)(e) and (f) show the resulting planar and cross-sectional views of the oxide formed on S32101 after the same reheat procedure in the Avesta furnace. It is clear from these views that, although there are differences in size and shape of some of the oxide nodules, the tube furnace produces similar results to the Avesta furnace and so is considered to be a satisfactory simulation.